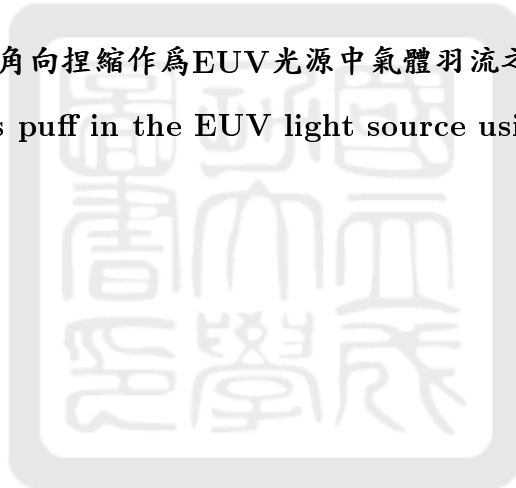


國立成功大學
太空與電漿科學研究所
碩士論文

National Cheng Kung University
Institute of Space and Plasma Sciences
Master Thesis

利用角向捏縮作為EUV光源中氣體羽流之研究
Study of the gas puff in the EUV light source using a theta pinch



研究生 (Author) : 劉嘉楷 Jia-Kai Liu
指導老師 (Advisor) : 張博宇博士 Dr. Po-Yu Chang
中華民國一百一十一年六月 June, 2022

國立成功大學

碩士論文

利用角向捏縮作為EUV光源中氣體羽流之研究

Study of the gas puff in the EUV light source using a theta pinch

研究生：劉嘉楷

本論文業經審查及口試合格特此證明

論文考試委員：

曲宏宇

林明緯

張博宇

指導教授：

張博宇

單位主管：



(單位主管是否簽章授權由各院、系(所、學位學程)自訂)

中華民國 111 年 6 月 7 日

摘要

本論文主要是產生氬氣羽流，將用於產生極紫外光光刻所需的光源。極紫外光光刻技術被認為是這一代半導體工藝中最先進的技術之一，我們想藉由角向捏縮電漿羽流來產生極紫外光光刻光源，當電漿羽流的溫度到達約30 eV，就會輻射出極紫外光。為了驅動角向捏縮，我們建造了一個1 kJ的脈衝功率系統，該系統可以提供峰值 135 ± 1 kA的電流、 1592 ± 3 ns的上升時間和大約600 MW的輸出功率，然後，藉由小型脈衝功率系統驅動電弧放電，使氬氣游離產生氬氣電漿羽流。因此，我們使用裝有不同氣壓的緩衝氣瓶的脈衝氣閥產生氬氣羽流，並且使用紋影系統(Schlieren system)拍攝氣體羽流，探討在不同情況下的流動變化。在實驗中，我們使用了24 V和12 V的脈衝氣閥，並且以不同的實驗設計對兩者分別進行測試。在24 V脈衝氣閥的實驗中，結果顯示，脈衝氣閥設置在距離凸透鏡前20 cm、垂直於桌面的紋影遮光刀鋒、25°C的氣體溫度、V5A的收縮發散噴嘴以及5 atm氣壓差的實驗設置下，成效最好；在12 V脈衝氣閥的實驗中，結果顯示，無收縮發散噴嘴以及5 atm氣壓差的實驗設計下，成效最好。除此之外，12 V的脈衝氣閥出口直徑為5.5 mm，比24 V的大，所以12 V的影像對比程度大於24 V的影像。因此，如果我們想要透過紋影影像清楚觀察到氣體羽流或電漿羽流的流動變化，較大的脈衝氣閥的出口直徑是比較好的。

關鍵字: 極紫外光、放電電漿、角向捏縮、氣體羽流、收縮發散噴嘴、Schlieren系統

Abstract

In this thesis, we are working on generating the gas puff which will be used in an extreme ultraviolet (EUV) light source for EUV lithography. EUV lithography is considered as one of the most advanced technology in this generation of semiconductor process. We would like to generate the EUV lithography light source by compressing the plasma plume with a theta pinch. The temperature of the plasma plume potentially reaches ~ 30 eV and radiates the EUV light. To drive the theta pinch, we have built a 1-kJ pulsed-power system which can provide a pulsed current with a peak current of 135 ± 1 kA, a rise time of 1592 ± 3 ns, and a peak power of ~ 600 MW. And then, a plasma plume will be generated by a plasma gun which ionized an Argon gas puff via arc discharge driven by a small pulsed-power system. The gas puff was generated by a pulsed valve with a gas reservoir with different gas pressure. Images of the gas puff were taken by a Schlieren system. We studied how gas puff propagated differently with different conditions. The gas puff was generated by either a 24-V pulse valve or a 12-V pulse valve. Then, we have tested many experimental setups with both of them. We found that the condition of the pulse valve set at 20 cm from the convex lens, the vertical knife-edge in Schlieren system, the 25°C gas temperature, the V5A Convergent-divergent nozzle (CDN), and the 5-atm pressure difference was the best in experiments using the 24-V pulse valve. Furthermore, the condition without Convergent-divergent nozzle (CDN) and the 5-atm pressure difference was the best in experiments using the 12-V pulse valve. However, the output diameter of the 12-V pulse valve is 5.4 mm, which is larger than that of the 24-V pulse valve. Therefore, the contrast of the image in the 12-V pulse valve was higher than in the 24-V pulse valve. It shows that the larger output diameter of the pulse valve is better if we would like to observe either the gas puff or the plasma plume clearly through the schlieren images.

Keywords: Extreme ultraviolet (EUV), Discharge-produced plasma (DPP), Theta pinch, Gas puff, Convergent-divergent nozzle, Schlieren system

致謝

很慶幸兩年多前的自己能夠來到成大就讀電漿所，並且順利加入張博宇教授所領軍的Pulsed-Plasma Laboratory (PPL)實驗室。回憶起當年生疏的模樣，就彷彿昨天似的刻刻皆於我腦海裡揮之不去，永遠不會忘記第一次與張博宇教授的「面試」，那種沒有距離感的聊天打破我對於師生間距離的界定，也讓我明白何謂亦師亦友，並使我不畏懼提出任何問題；永遠不會忘記實驗室裡的每個成員，從學弟、同儕、學長姊，大家團結一心，不留一手的傳承自己的專業，好讓我不至於徬徨在陌生的領域，更勇敢去接受任何挑戰；永遠不會忘記第一次親自使用脈衝功率系統，在期待與緊張相互矛盾下完成實驗；永遠不會忘記那些曾經淚水與歡笑交織譜出關於我與PPL的雋永樂章；永遠不會忘記.....；永遠不會忘記.....。

在這段為期兩年多的碩士生涯，我很榮幸能參與到脈衝功率系統的建置，看著系統在大家的努力下日趨完善，那份象徵PPL精神的成就感，相信參與過的你定能明白。而在自己研究領域的方面，雖稱不上一帆風順，但我想也算是滿載而歸，從對電路一竅不通到能夠自主完成，在紋影系統(Schlieren system)方面，我更是吃足了苦頭，三顧茅廬的詢問光電所吳品頡教授，經過多次的失敗改良，最後在張博宇教授的提點之下才順利完成，走得艱辛但實屬值得！期望PPL在張博宇教授的揮軍之下，能發揚光大、擴張領土。

最後先感謝兩年多後的自己沒有放棄，仍然堅持走到這裡；謝謝張博宇教授兩年多前的選擇，才造就了現在的我；謝謝PPL實驗室裡的所有夥伴，沒有你們的歡笑陪伴，我也沒辦法這麼勇敢；謝謝遠在宜蘭卻心繫著我的家人，一路不畏風雨的支持著我，讓我跌彈斑鳩後能東山再起；謝謝所有身邊愛我、關心我的人，有你們的存在，是我此生最幸福的事。謝謝大家！

Contents

1	Introduction	1
1.1	The extreme ultraviolet lithography	1
1.1.1	Plasma plume	2
1.1.2	Theta pinch	3
1.2	The pulsed-power system	4
1.3	The convergent-divergent nozzle (CDN)	5
1.4	Schlieren system	7
1.5	The goal and the outline of the thesis	8
2	The pulsed-power system	10
2.1	The structure of the pulsed-power system	10
2.2	The spacer of the rail-gap switch	12
2.3	The Rogowski coil of the pulsed-power system	17
2.3.1	The motivation of upgrading the Rogowski coil	18
2.3.2	The design of the new Rogowski coil	19
2.3.3	The mount of the new Rogowski coil	23
2.3.4	The calibration of the new Rogowski coil	24
2.3.5	Calibration results	25
2.3.6	Output of the pulsed-power system	27
2.4	Summary	28
3	The gas puff	29
3.1	The construction of the gas-gun system	29
3.2	The pulse-valve system	30
3.2.1	The 24-V pulse-valve system	30
3.2.2	The 12-V pulse-valve system	33
3.2.3	The pulse-valve opening-time measurements	34
3.3	The reservoir system	39
3.4	The convergent-divergent nozzles(CDN)	41
3.5	The procedure of operating the gas-gun system	42

3.6	Summary	43
4	Schlieren system	44
4.1	The design of the Schlieren system	44
4.2	The improvement of the Schlieren system	45
4.3	Summary	53
5	Experimental results	54
5.1	Analyzing procedure	54
5.1.1	Width of the gas puff	54
5.1.2	Opening angle of the gas puff	60
5.1.3	Tilted angle of the Convergent-divergent nozzle (CDN)	61
5.1.4	Contrast of the differential image	62
5.2	The 24-V pulse valve	63
5.2.1	Different locations of the pulse valve setting	64
5.2.2	Different Schlieren knife-edge settings	70
5.2.3	Different temperature of the gas puff	73
5.2.4	Different convergent-divergent nozzles (CDN)	78
5.2.5	Different pressure of the argon gas	85
5.2.6	Summary	95
5.3	12-V pulse valve	96
5.3.1	No convergent-divergent nozzle (CDN), 0.5-atm pressure difference . . .	97
5.3.2	No convergent-divergent nozzle (CDN), 1-atm pressure difference . . .	100
5.3.3	V7 convergent-divergent nozzle (CDN), 0.5-atm pressure difference . . .	102
5.3.4	V7 convergent-divergent nozzle (CDN), 1-atm pressure difference . . .	104
5.3.5	V8 convergent-divergent nozzle (CDN), 0.5-atm pressure difference . . .	106
5.3.6	V8 convergent-divergent nozzle (CDN), 1-atm pressure difference . . .	108
5.3.7	Summary	110
5.4	Summary	111
6	Future works	112
7	Summary	114

References	117
A Appendix	118
A.1 The pulsed-power system	118
A.1.1 The reports of the Rogowski coil calibration	118
A.1.2 The drawing of the Coaxial Outer for the Rogowski coil	123
A.1.3 The photos of the Rogowski coil	124
A.1.4 The procedure of opening/closing the lid of the vacuum chamber	125
A.1.5 The procedure of milling Electrodes	127
A.1.6 The drawing of the spacer of the rail-gap switch	128
A.2 The gas puff	137
A.2.1 The procedure of operating the gas-gun system	137
A.2.2 The 24-V pulse valve opening-time measurements	138
A.2.3 The drawing of the Convergent-divergent nozzles (CDNs)	142
A.2.4 The simulation of CDNs	147
A.3 Schlieren system	154
A.3.1 The first version of the 12-V LED holder	154
A.3.2 The second version of the 12-V LED holder	155
A.4 Experimental results	156
A.4.1 Different locations of the pulse valve setting	156
A.4.2 Different temperature of the gas puff	159
A.4.3 Different convergent-divergent nozzles (CDNs)	162
A.4.4 Different pressure of the argon gas	165
A.4.5 No CDN, 0.5-atm pressure difference	171
A.4.6 No CDN, 1-atm pressure difference	173
A.4.7 V7 CDN, 0.5-atm pressure difference	175
A.4.8 V7 CDN, 1-atm pressure difference	177
A.4.9 V8 CDN, 0.5-atm pressure difference	180
A.4.10 V8 CDN, 1-atm pressure difference	182
A.5 The vendors of all components	184
A.6 Folder of data	185

List of Figures

1	Downsizing the semiconductors is hard because of the optical diffraction[1]. . . .	1
2	(a) The schematic of EUV light generated by heating the laser-produced plasma (LPP)[1]. (b) The schematic of EUV light generated by compressing the discharge-produced plasma (DPP)[2].	2
3	(a) The schematic of the gas puff generator[2]. (b) The schematic of a plasma gun[2].	3
4	The schematic of the theta pinch.	4
5	(a) The schematic of each wing pulsed-power system. (b) Current output of our pulsed-power system.	5
6	(a) The configuration of the Convergent-divergent nozzle (CDN)[3]. (b) The diagram of the Convergent-divergent nozzle (CDN)[4].	7
7	The experimental setup of our Schlieren system.	8
8	(a) The schematic of light deflection[5]. (b)Image of the light source at the knife-edge[5].	8
9	The CAD drawing of the pulsed-power system.	11
10	Enlarged CAD drawing of the cylindrical vacuum chamber, rail-gap switch, and transmission line.	11
11	The CAD drawing of the rail-gap switch.	12
12	(a) Enlarged CAD drawing of HV, grounded electrodes, and knife-edge electrode. (b) The CAD drawing of the spacer with the rail-gap switch.	13
13	The engineering drawing of the old spacer.	14
14	The engineering drawing of the new spacer.	14
15	The architecture of the spacer.	15
16	The parts of the spacer.	16
17	(a) The architecture of the 91-screws spacer. (b) The architecture of the 37-screws spacer.	17
18	The principle of the Rogowski coil working.	17
19	The cross-section drawing of the vacuum chamber.	18

20	(a) The old version of the Rogowski coil. (b) The new version of the Rogowski coil.	18
21	The cross-section of the coaxial cable.	19
22	The drawing of the Rogowski coil working.	20
23	The cross-section drawing of the Rogowski coil in the coaxial transmission line. .	21
24	The production of the Rogowski coil.	23
25	The sectional drawing of the coaxial outer and Rogowski coil.	24
26	(a) Rogowski coil PE holder. (b) Cable ties.	24
27	The Rogowski coil was calibrated with the Pearson current monitor.	25
28	The result of the Rogowski coil curve fitting.	26
29	The relationship between input current and output voltage.	26
30	The Rogowski coil measured the current from the 1-kJ pulse-power system. . .	27
31	The current measurement from both of south and north wings triggered. . . .	28
32	The CAD drawing of the pulsed-valve system.	30
33	(a) The figure of the 24-V pulse valve. (b) The figure of the 12-V pulse valve. .	30
34	The cross-section drawing of the 24-V pulse valve.	31
35	(a) The circuit of the relay (FOD3184). (b) The circuit of the 24-V pulse-valve control box.	32
36	(a) The 24-V pulse-valve control box. (b) The layout drawing of the 24-V pulse-valve control circuit.	32
37	The cross-section drawing of the 12-V pulse valve.	33
38	(a) The circuit of the 12-V pulsed-valve control box. (b) The 12-V pulsed-valve control box.	34
39	The experimental setup of the 24-V pulse valve sound measurement.	35
40	The sound recording of the time delay setting at 1 s.	35
41	The 1-s time delay result of cutting data with Matlab.	36
42	The relation of the time delay between function generator setting and pulsed-valve opening.	38
43	The curve fitting result of the time delay.	38
44	The CAD drawing of the reservoir system.	39

45	(a) The figure of the reservoir. (b) The cross-section drawing of the reservoir. . .	40
46	The relation of the air in the reservoir at 50-ms and 100-ms time delay between the amount of gas substance remaining and pressure difference setting.	41
47	The optical pathway diagram of the Schlieren system.	45
48	(a) The schematic of the signal of the gas puff without the knife edge. (b) The schematic of the signal of the gas puff with the knife edge.	45
49	(a) Schematic of the first version of the experimental setup. (b) The first version of the Schlieren image of the gas puff.	46
50	(a) Schematic of the second version of the experimental setup. (b) The second version of the Schlieren image of the gas puff.	47
51	Schematic of chromatic aberration.	47
52	(a) Schematic of the third version of the experimental setup. (b) The third version of the Schlieren image of the gas puff.	47
53	(a) Schematic of the fourth version of the experimental setup. (b) The fourth version of the Schlieren image of the gas puff.	48
54	(a) Schematic of the fifth version of the experimental setup. (b) The fifth version of the Schlieren image of the gas puff.	48
55	(a) The convex side of first lens face the light source. (b) The flat side of first lens face the light source.	49
56	Schematic of the sixth version of the experimental setup.	49
57	(a) The sixth version of the Schlieren image of the gas puff. (b) The horizontal line profile of the seventh version of the image.	50
58	Schematic of the seventh version of the experimental setup.	50
59	(a) The seventh version of the Schlieren image of the gas puff. (b) The horizontal line profile of the seventh version of the image.	51
60	Schematic of the eighth version of the experimental setup.	51
61	(a) The eighth version of the Schlieren image of the gas puff. (b) The horizontal line profile of the eighth version of the image.	52
62	Schematic of the ninth version of the experimental setup.	52

63	(a) The ninth version of the Schlieren image of the gas puff. (b) The horizontal line profile of the ninth version of the image.	53
64	(a) The RGB-scale of the schlieren image without gas puff. (b) The RGB-scale of the schlieren image with gas puff.	55
65	(a) The grayscale of the schlieren image without gas puff. (b) The grayscale of the schlieren image with gas puff.	55
66	The double-precision value of the differential image.	56
67	(a) The horizontal line profiles of the image. (b) The intensity signal difference of the image at 190 pixels.	56
68	The target wave of the intensity signal difference.	57
69	(a) The valley of the target wave. (b) The curve fitting result of the valley. . . .	58
70	(a) The peak of the target wave. (b) The curve fitting result of the peak. . . .	58
71	(a) The curve fitting result overlay with the original wave. (b) The curve fitting result of the target wave.	59
72	(a) The horizontal line profile of the Convergent divergent nozzles (CDN). (b) The intensity signal difference of the Convergent divergent nozzles (CDN). . . .	60
73	The slope of the propagating path of the gas puff.	61
74	The slope of the propagating center of the gas puff.	62
75	(a) The vertical line profile of the image. (b) The signal intensity difference of the location of the vertical line profile.	63
76	(a) The horizontal line profile of the image. (b) The signal intensity difference of the location of the horizontal line at 199 pixels.	63
77	(a) V5A CDN. (b) V5B CDN. (c) V6 CDN.	64
78	(a) Schematic of the location set at 20 cm from the convex lens of the experimental setup. (b) Schematic of the location set at 42 cm from the convex lens of the experimental setup.	65
79	(a) The horizontal line profile of the image in the pulse valve 20 cm from the convex lens case. (b) The signal intensity difference of the location of the horizontal line at 186 pixels.	65

80	(a) The horizontal line profile of the image in the pulse valve 42 cm from the convex lens case. (b) The signal intensity difference of the location of the horizontal line at 145 pixels.	66
81	The slope of the propagating path of the gas puff in the pulse valve 20 cm from the convex lens case.	67
82	The slope of the propagating center of the gas puff in the pulse valve 20 cm from the convex lens case.	67
83	The slope of the propagating path of the gas puff in the pulse valve 42 cm from the convex lens case.	68
84	The slope of the propagating center of the gas puff in the pulse valve 42 cm from the convex lens case.	69
85	The grayscale of the schlieren image with tilted knife-edge. Left one is the image without gas puff and right one is the image with gas puff.	70
86	The signal difference of the schlieren image in knife-edge set oblique to the optical table case.	71
87	The grayscale of the schlieren image with horizontal knife-edge. Left one is the image without gas puff and right one is the image with gas puff.	71
88	The signal difference of the schlieren image in knife-edge set horizontal to the optical table case.	72
89	The grayscale of the schlieren image with a vertical knife-edge. Left one is the image without gas puff and right one is the image with gas puff.	72
90	The signal difference of the schlieren image in knife-edge set vertical to the optical table case.	73
91	(a) The horizontal line profile of the image in 15C–gas puff case. (b) The signal intensity difference of the location of the horizontal line at 150 pixels.	74
92	(a) The horizontal line profile of the image in 25°C–gas puff case. (b) The signal intensity difference of the location of the horizontal line at 169 pixels.	75
93	The slope of the propagating path of the gas puff in 15–gass puff case.	75
94	The slope of the propagating center of the gas puff in 15–gass puff case.	76
95	The slope of the propagating path of the gas puff in 25–gass puff case.	77

96	The slope of the propagating center of the gas puff in 25—gass puff case.	77
97	(a) The horizontal line profile of the experimental setup with V5A CDN case. (b) The signal intensity difference of the location of the horizontal line at 210 pixels.	79
98	(a) The horizontal line profile of the experimental setup with V5B CDN case. (b) The signal intensity difference of the location of the horizontal line at 85 pixels.	79
99	(a) The horizontal line profile of the experimental setup with V6 CDN case. (b) The signal intensity difference of the location of the horizontal line at 208 pixels.	80
100	The slope of the propagating path of the experimental setup with V5A CDN case.	81
101	The slope of the propagating center of the experimental setup with V5A CDN case.	81
102	The slope of the propagating path of the experimental setup with V5B CDN case.	82
103	The slope of the propagating center of the experimental setup with V5B CDN case.	83
104	The slope of the propagating path of the experimental setup with V6 CDN case.	84
105	The slope of the propagating center of the experimental setup with V6 CDN case.	84
106	(a) The horizontal line profile of the experimental setup at 5-atm pressure dif- ference case. (b) The signal intensity difference of the location of the horizontal line at 170 pixels.	85
107	(a) The horizontal line profile of the experimental setup at 6-atm pressure dif- ference case. (b) The signal intensity difference of the location of the horizontal line at 184 pixels.	86
108	(a) The horizontal line profile of the experimental setup at 7-atm pressure dif- ference case. (b) The signal intensity difference of the location of the horizontal line at 183 pixels.	86
109	(a) The horizontal line profile of the experimental setup at 8-atm pressure dif- ference case. (b) The signal intensity difference of the location of the horizontal line at 185 pixels.	87

110	(a) The horizontal line profile of the experimental setup at 9-atm pressure difference case. (b) The signal intensity difference of the location of the horizontal line at 185 pixels.	88
111	The slope of the propagating path of the experimental setup at 5-atm pressure difference case.	88
112	The slope of the propagating center of the experimental setup at 5-atm pressure difference case.	89
113	The slope of the propagating path of the experimental setup at 6-atm pressure difference case.	90
114	The slope of the propagating center of the experimental setup at 6-atm pressure difference case.	90
115	The slope of the propagating path of the experimental setup at 7-atm pressure difference case.	91
116	The slope of the propagating center of the experimental setup at 7-atm pressure difference case.	92
117	The slope of the propagating path of the experimental setup at 8-atm pressure difference case.	93
118	The slope of the propagating center of the experimental setup at 8-atm pressure difference case.	93
119	The slope of the propagating path of the experimental setup at 9-atm pressure difference case.	94
120	The slope of the propagating center of the experimental setup at 9-atm pressure difference case.	95
121	(a) V7 CDN. (b) V8 CDN.	97
122	(a) The horizontal line profile of the experimental setup without CDN at 0.5-atm pressure difference case. (b) The signal intensity difference of the location of the horizontal line at 70 pixels.	98
123	The slope of the propagating path of the experimental setup without CDN at 0.5-atm pressure difference case.	99

124	The slope of the propagating center of the experimental setup without CDN at 0.5-atm pressure difference case.	99
125	(a) The horizontal line profile of the experimental setup without CDN at 1-atm pressure difference case. (b) The signal intensity difference of the location of the horizontal line at 71 pixels.	100
126	The slope of the propagating path of the experimental setup without CDN at 1-atm pressure difference case.	101
127	The slope of the propagating center of the experimental setup without CDN at 1-atm pressure difference case.	101
128	(a) The horizontal line profile of the experimental setup with V7 CDN at 0.5-atm pressure difference case. (b) The signal intensity difference of the location of the horizontal line at 180 pixels.	102
129	The slope of the propagating path of the experimental setup with V7 CDN at 0.5-atm pressure difference case.	103
130	The slope of the propagating center of the experimental setup with V7 CDN at 0.5-atm pressure difference case.	103
131	(a) The horizontal line profile of the experimental setup with V7 CDN at 1-atm pressure difference case. (b) The signal intensity difference of the location of the horizontal line at 180 pixels.	104
132	The slope of the propagating path of the experimental setup with V7 CDN at 1-atm pressure difference case.	105
133	The slope of the propagating center of the experimental setup with V7 CDN at 1-atm pressure difference case.	105
134	(a) The horizontal line profile of the experimental setup with V8 CDN at 0.5-atm pressure difference case. (b) The signal intensity difference of the location of the horizontal line at 200 pixels.	106
135	The slope of the propagating path of the experimental setup with V8 CDN at 0.5-atm pressure difference case.	107
136	The slope of the propagating center of the experimental setup with V8 CDN at 0.5-atm pressure difference case.	107

137	(a) The horizontal line profile of the experimental setup with V8 CDN at 1-atm pressure difference case. (b) The signal intensity difference of the location of the horizontal line at 199 pixels.	108
138	The slope of the propagating path of the experimental setup with V8 CDN at 1-atm pressure difference case.	109
139	The slope of the propagating center of the experimental setup with V8 CDN at 1-atm pressure difference case.	109
140	The schematic of the plasma plume generator.	112
141	(a) The design of the Helmholtz coil. (b) The side view of the Helmholtz coil. .	113



List of Tables

1	The diagnostics of our pulsed-power system.	5
2	The comparison between the first version and second version of the Rogowski coils.	22
3	The comparison of the Rogowski coil fixing methods.	24
4	The information of the pulse valves.	34
5	The deviation of the time delay setting at 1 s.	37
6	The deviation of the time delay setting.	37
7	The size of the different convergent-divergent nozzles.	42
8	The 24-V pulse valve experimental setup with Convergent-divergent nozzle (CDN) in different conditions.	64
9	The comparisons of the 24-V pulse valve set at different position.	69
10	The comparisons of the different schlieren knife set.	73
11	The comparisons of the 24-V pulse valve set at different temperatures.	78
12	The comparisons of the experimental setup with different CDN.	85
13	The comparisons of the experimental setup at different pressure.	95
14	The 12-V pulse valve experimental setup in different conditions.	97
15	The comparison results of the 12-V pulse valve experimental setups in different conditions.	110
16	The output diameter of the pulse valves.	111

1 Introduction

We are studying gas puff in the extreme ultraviolet lithography(EUV) light source using a theta pinch. It is to understand how the gas puff performs differently under different conditions, including different temperatures of the gas puff, different pressure differences between the reservoir and the atmospheric pressure, different convergent-divergent nozzles (CDN), and different schlieren knife-edge directions. In this chapter, all the main characters of this thesis are introduced. In section 1.1, EUV lithography[6] and our design of the EUV light source will be introduced. In section 1.2, the pulsed-power system will be introduced. In subsection 1.3, the convergent-divergent nozzle will be introduced. In section 1.4, the Schlieren system will be introduced. Finally, the goal of the thesis is given in section 1.5.

1.1 The extreme ultraviolet lithography

The empirical rule describing the development of the semiconductor industry over at least fifty years is Moore's Law[7][1] stating that the number of transistors on a microchip double about every two years, though the cost of computers is halved. The critical dimension (CD) has been reduced along with Moore's law these years. Then, the line width of the mask defines the component size of the semiconductors. When the linewidth of the mask is in the order of the optical wavelength used in the lithography, the component size can't be downsized because of the optical diffraction as shown in figure 1[1].

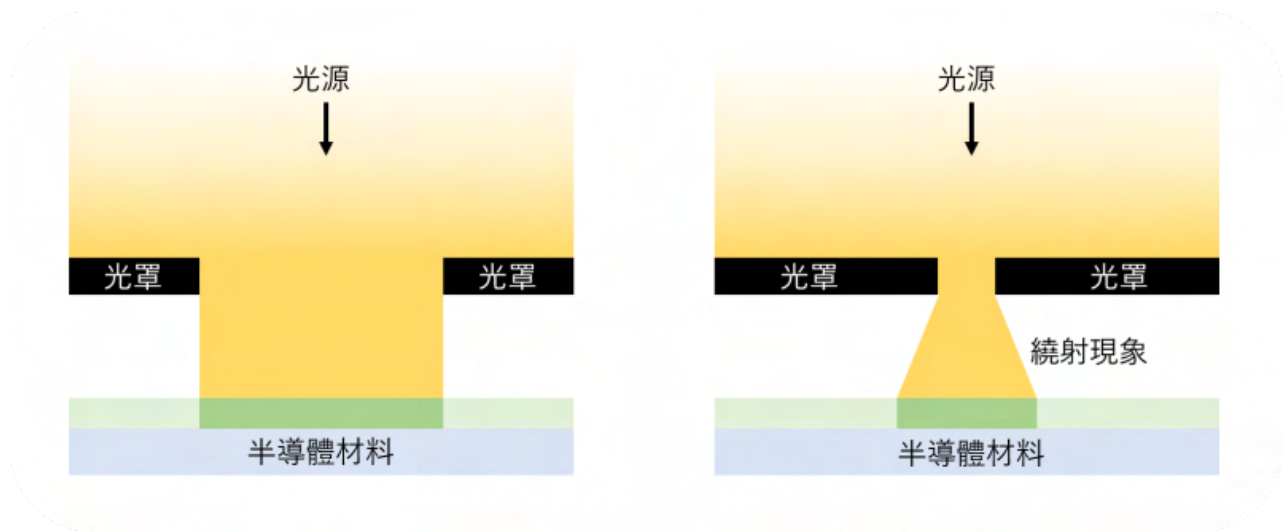


Figure 1: Downsizing the semiconductors is hard because of the optical diffraction[1].

In order to reduce the diffraction effect, a shorter optical wavelength is needed. For example, Taiwan Semiconductor Manufacturing Company Limited (TSMC)[8] starts using a light source at 13.5 nm for Extreme ultraviolet lithography (EUVL)[9][10]. The EUV light is generated by the laser-produced plasma (LPP) heated by the CO₂ laser as shown in figure 2(a)[1]. On the other hand, we are developing an EUV light source using the 1-kJ pulsed-power system with diagnostics shown in figure 2(b). The gas puff is injected by the pulse valve with a glass tube. Then, an arc discharge current between the pair of electrodes is used to ionize the gas puff for generating the plasma plume. Finally, a Helmholtz coil driven by our 1-kJ pulsed-power system will compress the plasma plume as a theta pinch. The plasma plume is heated via adiabatic compression and radiates EUV light when the temperature reaches ~ 30 eV. Our development of EUV light source is potentially more efficient than those on the market because of the higher conversion efficiency and is also cheaper.

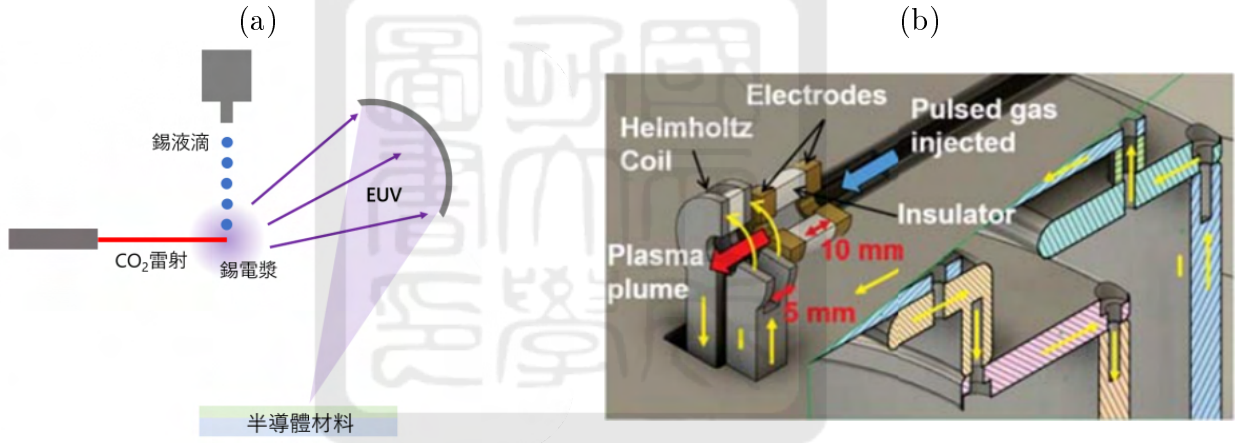


Figure 2: (a) The schematic of EUV light generated by heating the laser-produced plasma (LPP)[1]. (b) The schematic of EUV light generated by compressing the discharge-produced plasma (DPP)[2].

1.1.1 Plasma plume

Before generating the plasma plume, a gas puff needs to be provided first. Figure 3(a) is the schematic of the gas puff generator. It consists of an Argon gas cylinder, a manual valve, a gauge, a relief valve, a reservoir, and a pulse valve. When the gas is provided from the gas cylinder, the manual valve with a gauge is used to control the working pressure in the gas line. A pressure of 6 \sim 10 atm will be used. Moreover, the relief valve works for ensuring that the pressure does not go beyond our working pressure. The reservoir is set for stabilizing the gas output pressure. Finally, the pulse valve will provide a gas puff in a short period of time.

The plasma plume is generated by a plasma gun, which consists of two ring electrodes parallel to each other with an insulator in between as shown in figure 3(b). When a gas puff is provided, the quartz tube guides the gas puff to the plasma gun. The voltage across the electrodes will be provided by a small pulsed-power system with a $1\text{-}\mu\text{F}$ capacitor C. We will charge the capacitor up to 5 kV. When the gas puff propagates through the gap, an arc discharge is initiated via self breakdown. As a result, the gas puff becomes a plasma plume.

The speed and the propagated differently of the gas puff are really important for us to synchronize the plasma plume and the theta pinch. It is why we need to study the gas puff.

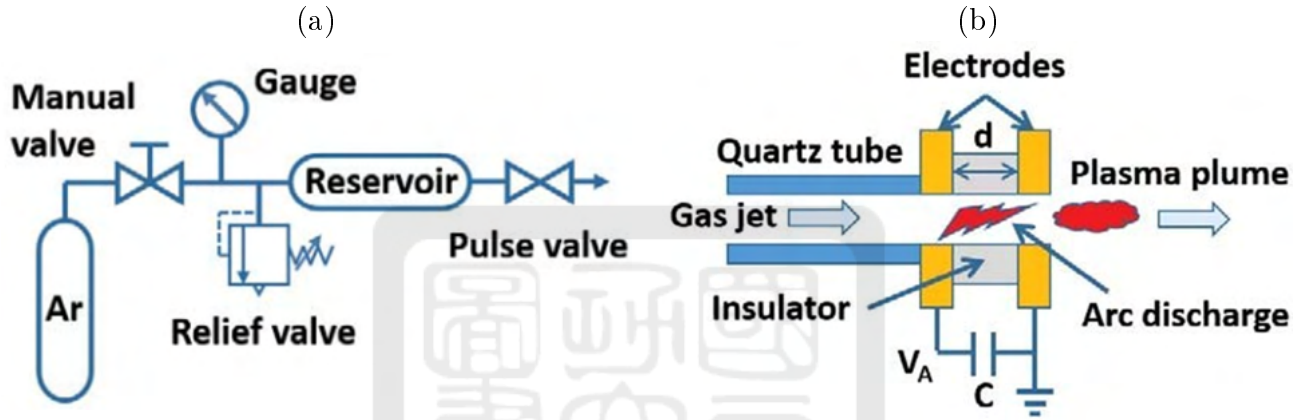


Figure 3: (a) The schematic of the gas puff generator[2]. (b) The schematic of a plasma gun[2].

1.1.2 Theta pinch

In order to compress the plasma plume, a theta pinch is used. Figure 4 is the schematic of the theta pinch. When a time-varying current goes through the ring coil in the azimuthal direction shown as the blue arrows, a time-varying magnetic field is generated in the z direction shown as the black arrows. Afterward, a time-varying plasma current in the reversed azimuthal direction is induced by the time-varying magnetic field shown as the green arrows. The Lorentz force, i.e., $\vec{J} \times \vec{B}$ forces, is generated in the radial direction toward the center as shown in the top view of the figure 4. As a result, the plasma plume is compressed by the theta pinch. If the plasma is magnetized or the compressing speed is fast enough, the plasma plume is compressed adiabatically. Therefore, the plasma plume is heated adiabatically during the compression.

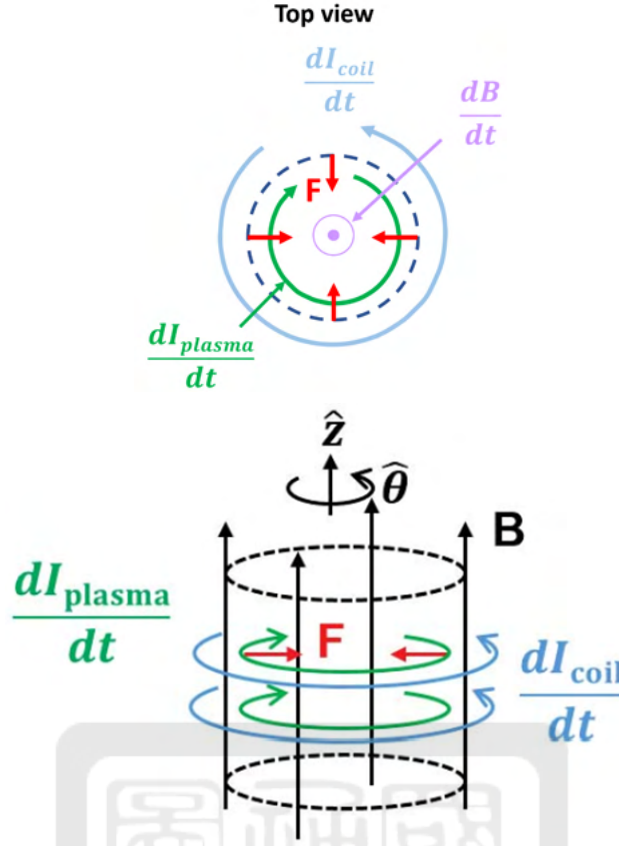


Figure 4: The schematic of the theta pinch.

1.2 The pulsed-power system

The pulsed-power system is built for driving the Helmholtz coil which can provide a pulsed magnetic field of at least 3 Tesla for the theta pinch. It consists of twenty $1\text{-}\mu\text{F}$ capacitors, two rail-gap switches, two parallel-plate transmission lines, one coaxial transmission line, and a cylindrical vacuum chamber. The pulsed-power system is separated into two wings located on the opposite sides of the chamber. One is called the north wing and the other is called the south wing. Each wing consists of five bricks of capacitors connected in parallel, one rail-gap switch, and one parallel-plate transmission line as shown in figure 5. Therefore, the capacitance of one wing is $2.5\text{ }\mu\text{F}$ and the total system is $5\text{ }\mu\text{F}$. During the experiment, the capacitors are charged to 20 kV storing total energy of 1 kJ. The output current and the rise time are 135 ± 1 kA and 1592 ± 3 ns, respectively, as shown in figure 5(b). The summary of the parameters of our pulsed-power system is shown in table 1.

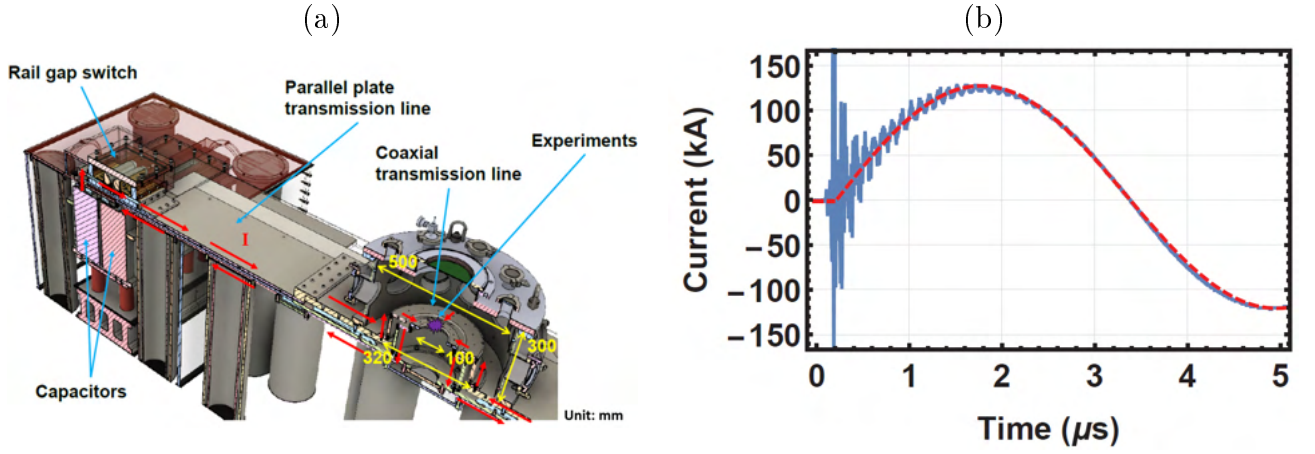


Figure 5: (a) The schematic of each wing pulsed-power system. (b) Current output of our pulsed-power system.

Table 1: The diagnostics of our pulsed-power system.

Capacitance	$5 \mu\text{F}$
V_{charge}	20 kV
Energy	1 kJ
I_{peak}	$135 \pm 1 \text{ kA}$
Rise time	$1592 \pm 3 \text{ ns}$
Inductance	$205 \pm 4 \text{ nH}$
Resistance	$10.0 \pm 0.2 \text{ m}\Omega$

1.3 The convergent-divergent nozzle (CDN)

In order to generate the gas puff which propagates forward without too much side-expansion, a convergent-divergent nozzle (CDN) is used. For more than fifteen years, aerospace technologies have grown. Convergent-divergent nozzles (CDN) are used in rockets, scramjets, and ramjets to accelerate the exhausted gas and produce thrusts according to Newton's third law of motion. Figure 6(a) is the configuration of the CDN where p_c is the gas pressure of the chamber, T_C is the temperature of the gas and p_b is the background pressure[3]. Then, gas flows through the CDN from a chamber of high gas pressure, e.g., our reservoir (Swagelok Corporation, 304L-HDF4-50) to one of lower pressure, e.g., atmospheric pressure. The reservoir is big enough so that the velocity and pressure of the gas are almost stable here. Gas flows from the reservoir into the converging section of the CDN, passes the throat, and then through the diverging section. Finally, the gas exhausts into the ambient as a jet called a gas puff.

Figure 6(b) is the temperature, pressure, and the Mach number diagram of the CDN[4]. In order to study the gas velocity in the divergent section, the conservation of mass equation is

used:

$$\dot{m} = \rho V A = \text{constant} \quad (1)$$

where \dot{m} is the mass flow rate, ρ is the gas density, V is the gas velocity and A is the cross-sectional flow area. Differentiating Eq. 1 and dividing it by $\rho V A$, we get:

$$\frac{d\rho}{\rho} + \frac{dV}{V} + \frac{dA}{A} = 0 . \quad (2)$$

On the other hand, the conservation of momentum equation provides

$$\rho V dV = -dp . \quad (3)$$

It means that the fluid element is accelerated by the pressure difference. Further, the isentropic flow equation shows:

$$\frac{dp}{p} = \gamma \frac{d\rho}{\rho} , \quad (4)$$

$$dp = \gamma \frac{p}{\rho} d\rho , \quad (5)$$

where γ is the ratio of the specific heat. Furthermore, the equation of state in ideal gas shows:

$$p = \rho R T \quad (6)$$

where R is gas constant and T is temperature. Combining Eq. 5 with Eq. 6 and $a^2 \equiv \gamma R T$ where a is the speed of sound, we get

$$dp = a^2 d\rho . \quad (7)$$

Combining Eq. 7 with Eq. 3 and using the definition of Mach number $M \equiv \frac{V}{a}$, we obtain:

$$-M^2 \frac{dV}{V} = \frac{d\rho}{\rho} . \quad (8)$$

Finally, we combine Eq. 2 with Eq. 8 and get:

$$(1 - M^2) \frac{dV}{V} = -\frac{dA}{A} . \quad (9)$$

Therefore, a subsonic gas flow ($M < 1$) is accelerated in a convergent section, and a supersonic gas flow ($M > 1$) is accelerated in the divergent section of the CDN. Thus, the gas puff flows without too much side expansion after leaving the CDN. We used a code of Matlab [3] provided in section A.2.4 to simulate our CDNs set in different conditions.

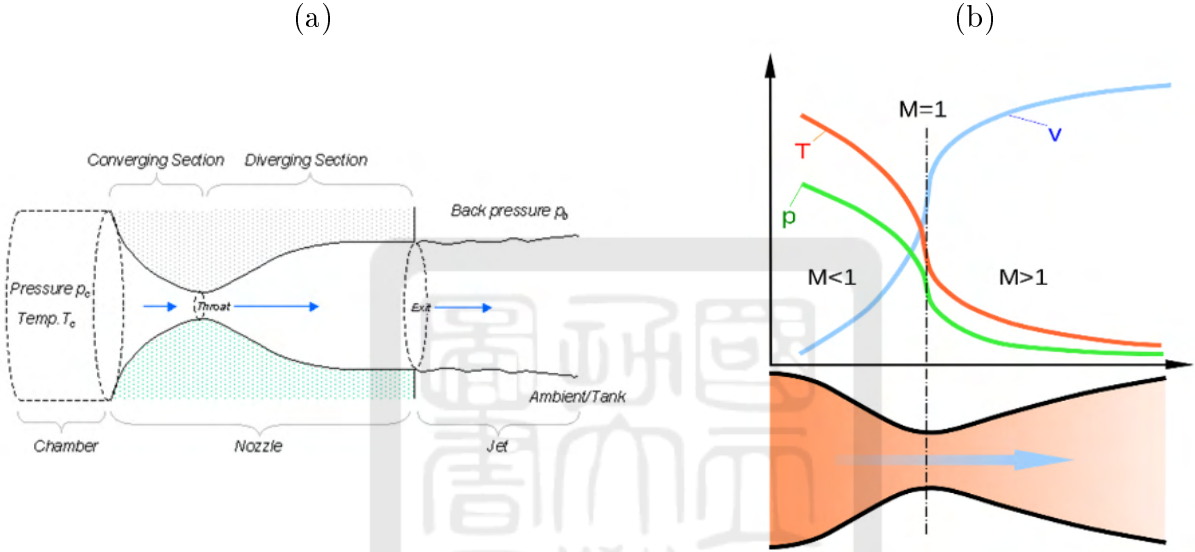


Figure 6: (a) The configuration of the Convergent-divergent nozzle (CDN)[3]. (b) The diagram of the Convergent-divergent nozzle (CDN)[4].

1.4 Schlieren system

Schlieren system[11] is the most common way to observe the density gradient of fluid. In order to observe the gas puff, we built a Schlieren system as shown in figure 7. The gas puff is set as the region of interest and the vertical knife-edge is used to block parts of the light. When a light passes through and is refracted by the gas puff, the edge of the gas puff is enhanced. Therefore, the sensitivity of the Schlieren system is the key of our experiments.

The sensitivity of the Schlieren system is defined by the contrast of the schlieren images. According to geometric optics, the intensity of the output light is related to how large the knife-edge blocks parts of the light at the focal point of the convex lens. To describe how a Schlieren image works, our green led light source is simplified to a rectangle as shown in figure 8[5] with a size of $a_0 \times b_0$. Assuming that the knife-edge blocks part of the rectangular so that

only the region $a_k \times b_0$ passes through the focal point. Assuming that I_0 is the intensity of the image without the knife edge, then the intensity with the knife edge is $\frac{a_k}{a_0} I_0$. When the light passes through the gas puff, the light is refracted so that the rectangular shifts with Δa on the focal point. In other words, an area of $(a_k \pm \Delta a) \times b_0$ passes through the knife-edge. As a result, the intensity of the screen is

$$I_{\text{screen}} = \frac{a_k \pm \Delta a}{a_k} I_0. \quad (10)$$

Since Δa is dependent on the density gradient, the larger density gradient in the gas puff is, the greater Δa is. If a knife-edge that blocks more light initially, i.e., a_k is smaller, the sensitivity of the Schlieren system is higher.

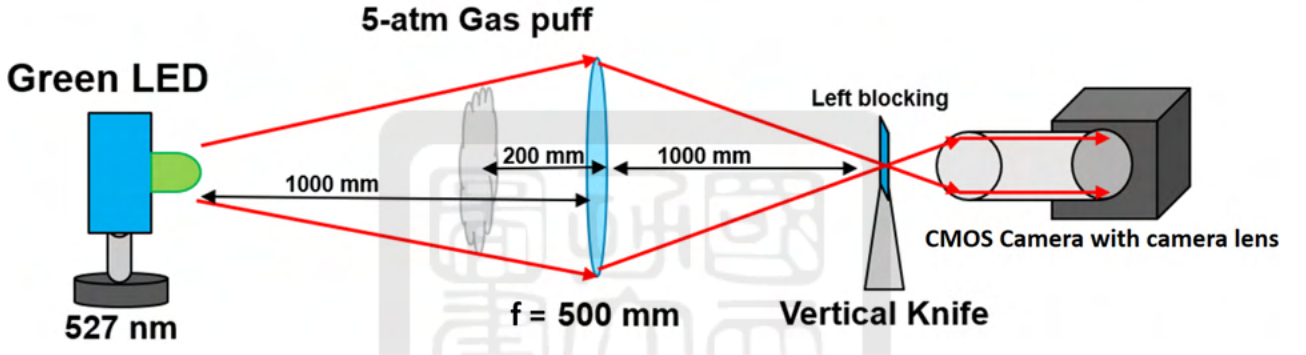


Figure 7: The experimental setup of our Schlieren system.

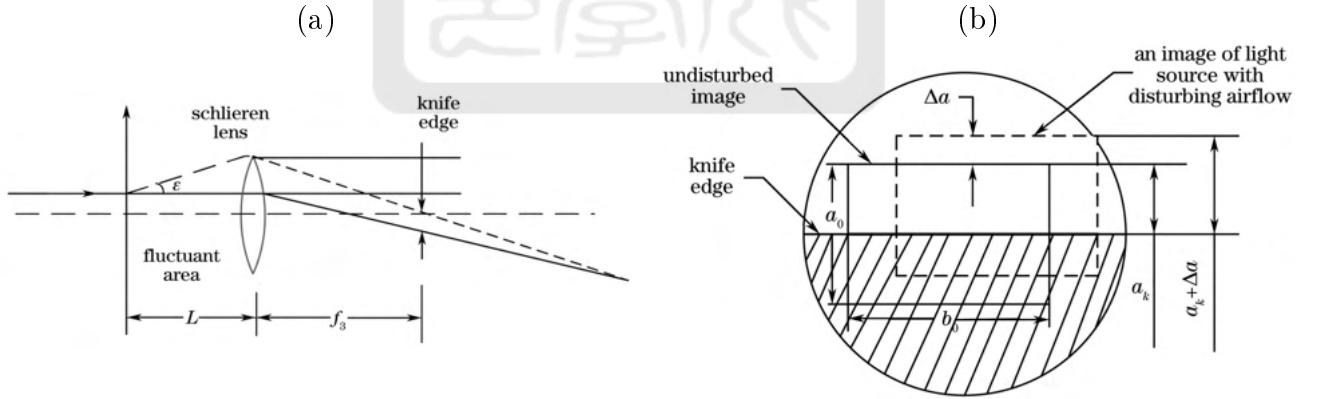


Figure 8: (a) The schematic of light deflection[5]. (b) Image of the light source at the knife-edge[5].

1.5 The goal and the outline of the thesis

The goal of the thesis is to study the gas puff which will be used in an EUV light source. In particular, how the gas puff expands with different experimental conditions is studied. In addition, in order to measure the parameters of the pulsed-power system, we built a Rogowski

coil with 130-turns aluminum tape as the curved solenoid in the Rogowski coil. Chapter 2 will introduce the work about the pulsed-power system and the Rogowski coil. Chapter 3 will introduce how the gas puff is provided. In order to observe the gas puff, we built a Schlieren system. In chapter 4, the design of the Schlieren system will be introduced. Studies of how gas puff propagates will be given in chapter 5. Finally, future works and the summary are given in chapters 6 and 7, respectively.



2 The pulsed-power system

In order to compress the plasma, a pulsed-power system is used to provide the energy with high power. We would like to use the pulsed-power system to drive a Helmholtz coil which can provide a 3-Tesla pulsed magnetic field for compressing the plasma. In this chapter, the pulsed-power system is introduced. The structure of the pulsed-power system will be introduced in Section 2.1. Then, the spacer of the rail-gap switch used to control the spacing between electrodes will be introduced in Section 2.2. Since the size of the old version Rogowski coil was too large, we built a smaller one that can be fixed in the system. The new Rogowski coil will be introduced in Section 2.3. A summary is given in Section 2.4.

2.1 The structure of the pulsed-power system

The pulsed-power system can provide energy for all experiments. Figure 9 is the computer-aided design (CAD) drawing of the pulsed power system. The pulsed-power system consists of twenty $1\text{-}\mu\text{F}$ capacitors, two rail-gap switches, two parallel-plate transmission lines, one coaxial transmission line, and a cylindrical vacuum chamber. The system can provide a pulsed current with a peak of $135 \pm 1\text{ kA}$ with a rise time of $1592 \pm 3\text{ ns}$. Twenty $1\text{-}\mu\text{F}$ capacitors, which are used to store the energy, are divided into two groups. They are at two opposite sides of the cylindrical vacuum chamber, called the south and the north wing. The capacitance of one wing is $2.5\text{ }\mu\text{F}$. Therefore, the total capacitance of the pulsed-power system is $5\text{ }\mu\text{F}$. Capacitors are charged to 20 kV storing total energy of 1 kJ .

Figure 10 is the enlarged CAD drawing of the cylindrical vacuum chamber, the rail-gap switch, and the transmission line. The outer cylinder of the coaxial transmission line connects with the top plate of the parallel-plate transmission line, and the inner one connects with the bottom plate of the parallel-plate transmission line. The rail-gap switch consists of the rail-like electrodes and the knife-edge electrode. One of the rail-like electrodes is connected to the top plate of the parallel-plate transmission line. The other rail-like electrode is connected to the capacitors. The bottom plate of the parallel-plate transmission line is connected to the capacitor bank. When the system is triggered, the current from capacitors passes through the top plate of the parallel-plate transmission line. After passing through the top plate of the parallel-plate transmission line, the current will enter the cylindrical vacuum chamber. The

load for the experiment is set between the outer cylinder of the coaxial transmission line and the inner one of the coaxial transmission line. The current would pass through the load and back to the inner cylinder of the coaxial transmission line. Then, the current passes through the bottom plate of the parallel-plate transmission line and back to the capacitor bank.

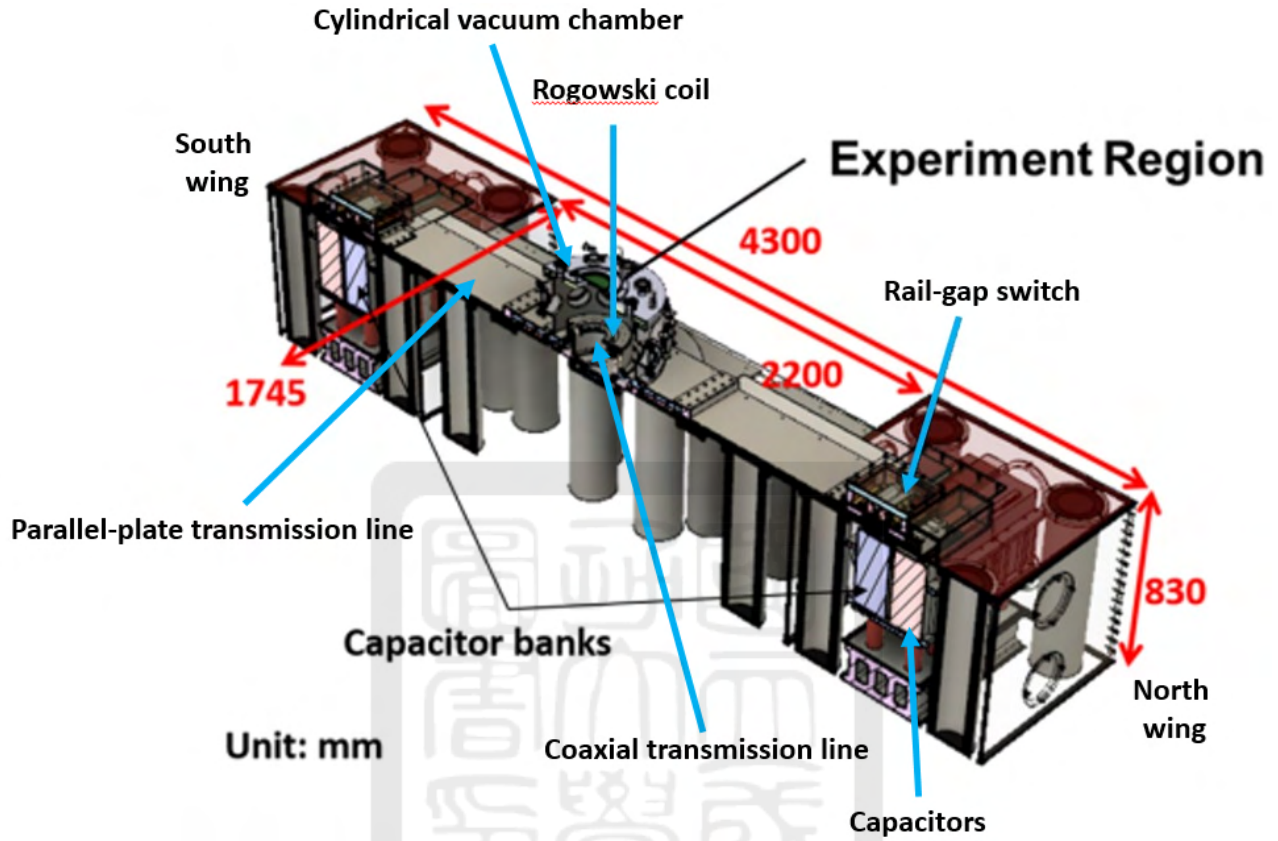


Figure 9: The CAD drawing of the pulsed-power system.

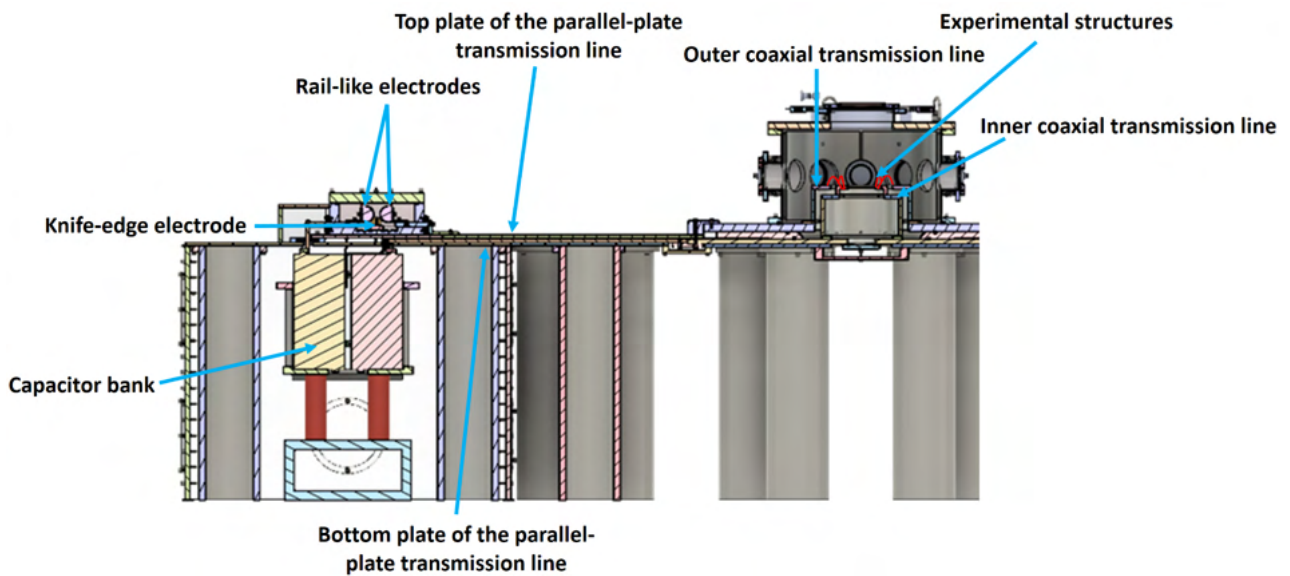


Figure 10: Enlarged CAD drawing of the cylindrical vacuum chamber, rail-gap switch, and transmission line.

2.2 The spacer of the rail-gap switch

Figure 11 is the cut view of the CAD drawing of the rail-gap switch with low inductance. The inductance of the rail-gap switch is 230 ± 10 nH which was measured by the former student Ming-Cheng Jheng[12]. The rail-gap switch consists of two rail-like electrodes and a knife-edge electrode in between. One of the rail-like electrodes is connected with the capacitors and the other one is connected with the top plate of the parallel-plate transmission line. The electrode near the capacitors is called the high voltage (HV) electrode and the other one is called the grounded electrode.

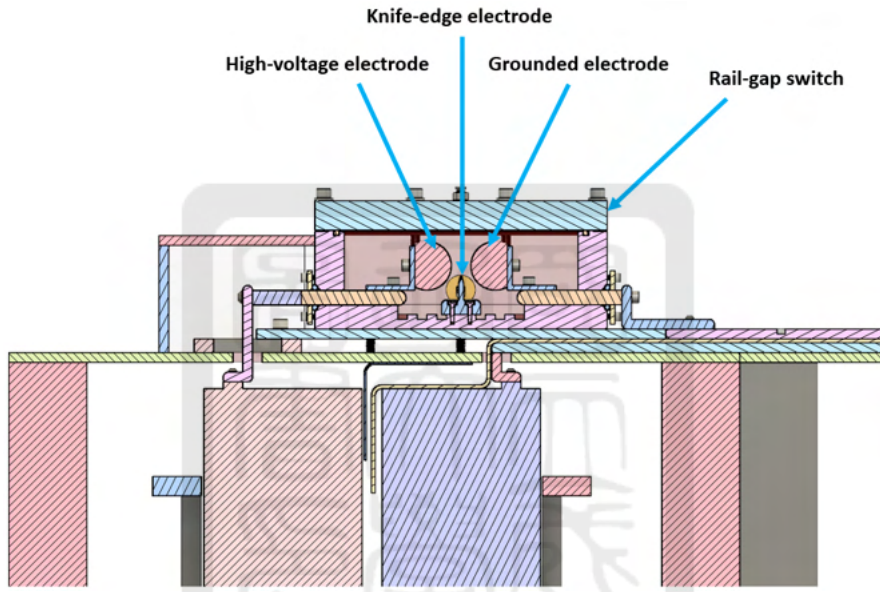


Figure 11: The CAD drawing of the rail-gap switch.

Figure 12(a) is the enlarged CAD drawing of the HV electrode, the grounded electrode, and the knife-edge electrode. The length of the cylindrical part of the HV electrode and the grounded electrode is 300 mm. The length of the knife-edge including the rounded edge on the side is 300 mm. The gap between the grounded electrode and the knife electrode is smaller than the gap between the HV electrode and the knife electrode. The Figure 12(b) is the CAD drawing of the rail-gap switch with the spacer. We use the spacer to control the gap distance between the HV electrode and grounded electrode when we assemble the rail-gap switch. The spacer is removed after the positions of all electrodes are all set.

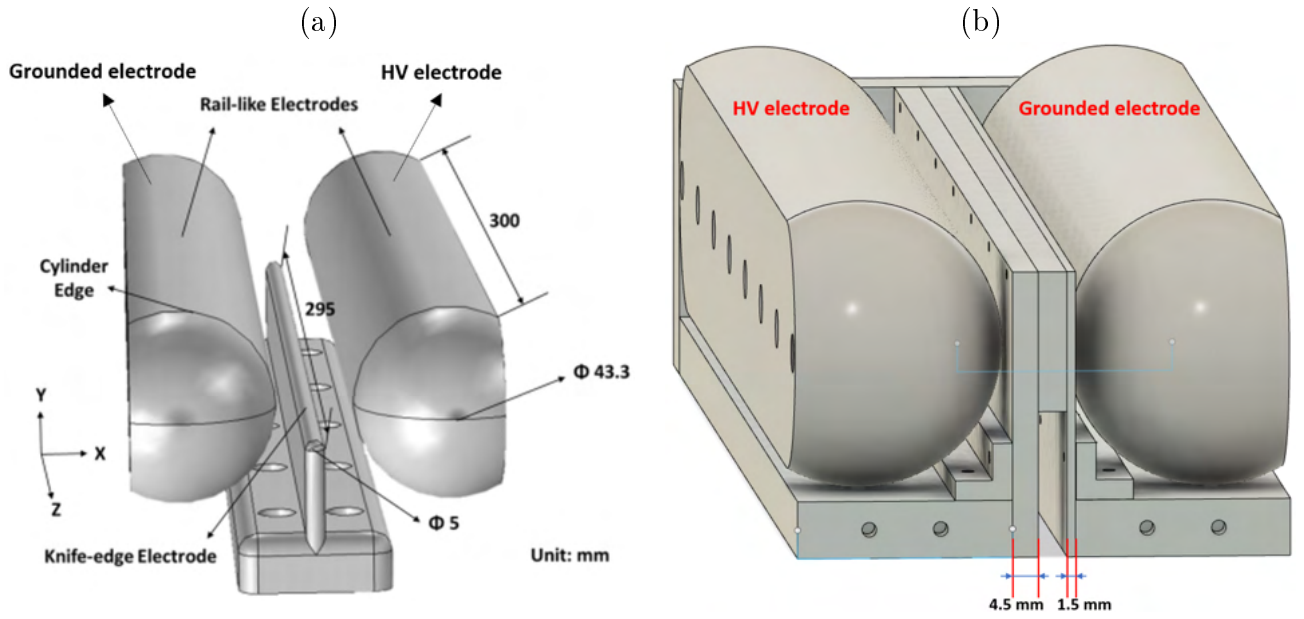


Figure 12: (a) Enlarged CAD drawing of HV, grounded electrodes, and knife-edge electrode. (b) The CAD drawing of the spacer with the rail-gap switch.

Figure 13 is the engineering drawing of the old version of the spacer. The gap distance between the HV electrode and grounded electrode was 21 mm because the designed working voltage of the pulsed-power system was 50 kV at the beginning. However, the actual working voltage is only 20 kV. On the other hand, the old version of the spacer was made all in one. The internal stress will cause the body of the spacer to deform. Because of these reasons, we built a new spacer for the rail-gap switch as shown in figure 14. The gap distance of the new spacer between the HV electrode and grounded electrode is 11 mm. Further, we divide the body of the spacer into eight pieces. The advantage of the new spacer is the adjustable construction. For example, the gap distance of the new spacer between the HV electrode and grounded electrode can be adjusted by using plates with different thicknesses.

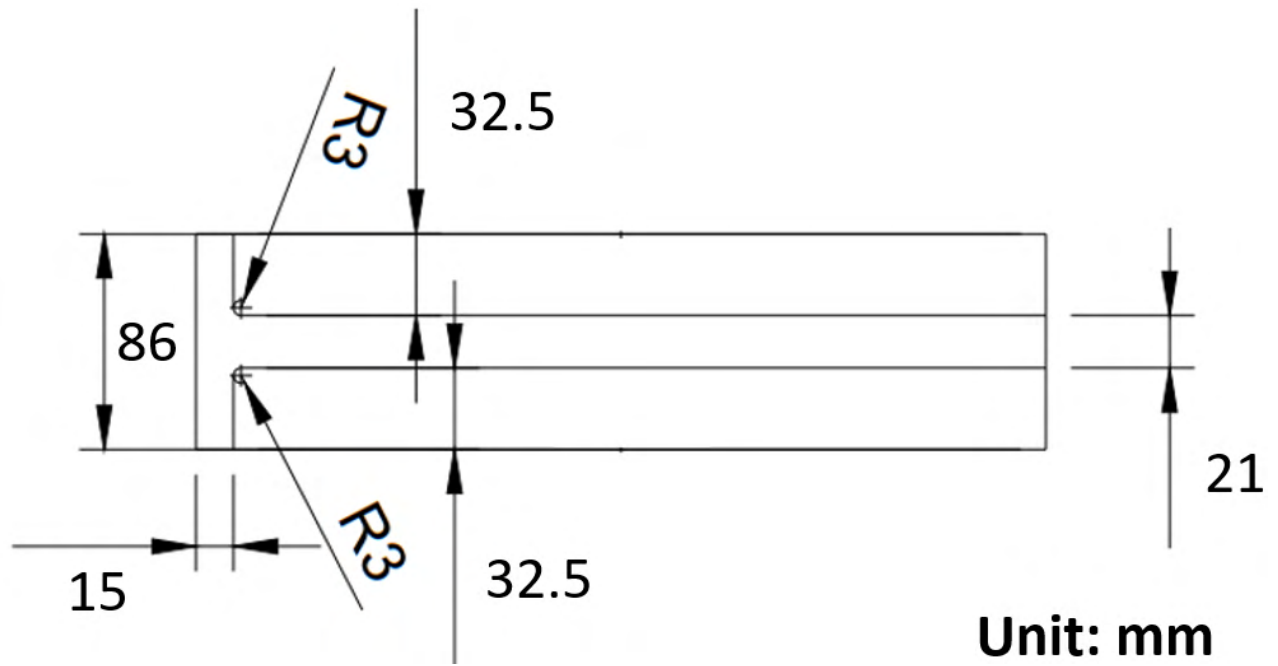


Figure 13: The engineering drawing of the old spacer.

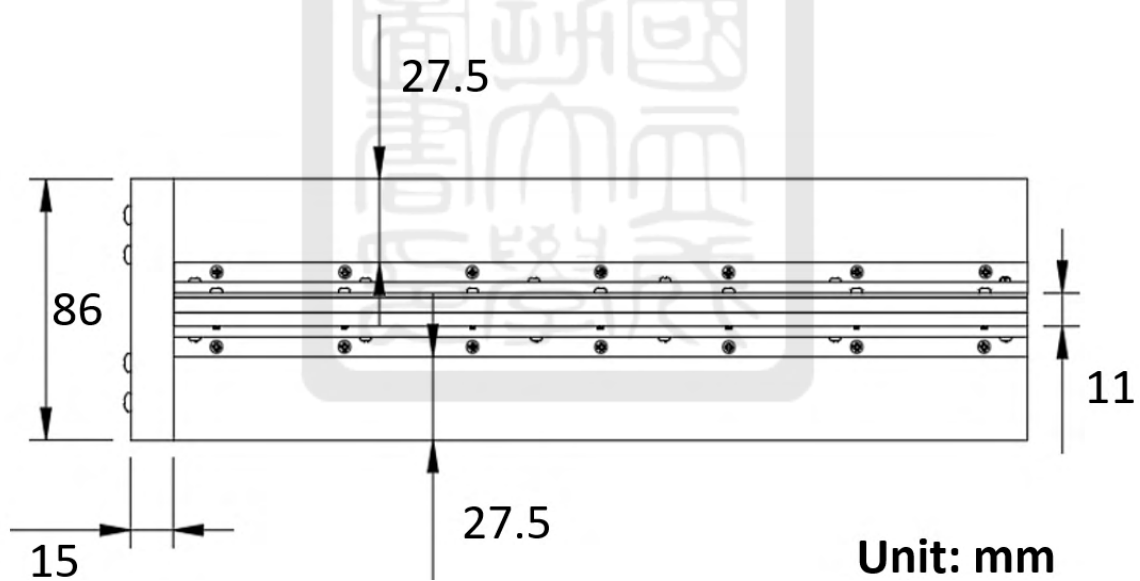


Figure 14: The engineering drawing of the new spacer.

Figure 15 is the 3D model of the new spacer. The spacer was assembled from eight pieces all made of stainless steel. Each part of the spacer is introduced in details down below:

(1) Figure 16(a) is the base of the spacer. The spacer has two bases. They are cuboids with 300 mm in length, 37.5 mm in width, and 10 mm in height. These pieces are used to support other parts above the bases.

(2) Figure 16(b) is the L-holder of the spacer. The spacer has two L-holders. They are used to fasten two walls on the bases. This piece is made by removing a cuboid with a cross-section

of $6.5 \text{ mm} \times 6.5 \text{ mm}$ from a cuboid with a cross-section of $10 \text{ mm} \times 10 \text{ mm}$. The length of the piece is 300 mm.

(3) Figure 16(c) is the thin wall of the spacer. The spacer has one thin wall. It is a rectangular plate with 300 mm in length, 50 mm in width, and a thickness is 1.5 mm. This piece is used to determine the gap distance between the grounded electrode and the knife-edge electrode. If we want to change the gap distance, we will replace the wall with a different thickness.

(4) Figure 16(d) is the thick wall of the spacer. The spacer has one thick wall. It is a rectangular plate with 300 mm in length, 50 mm in width, and a thickness is 4.5 mm. This piece is used to determine the gap distance between the HV electrode and the knife-edge electrode. If we want to change the gap distance, we will replace the wall with different thickness.

(5) Figure 16(e) is the bridge of the spacer. The spacer has one bridge. It is a rectangular plate with 300 mm in length, 24.5 mm in width, and the thickness is 5 mm. The thickness is the same as that of the knife-edge electrode. This piece is used to connect the thin wall to the thick wall.

(6) Figure 16(f) is the back holder of the spacer. The spacer has one back holder. It is a cuboid with 86 mm in length, 50 mm in width, and 15 mm in thickness. This piece is used to fasten two bases.

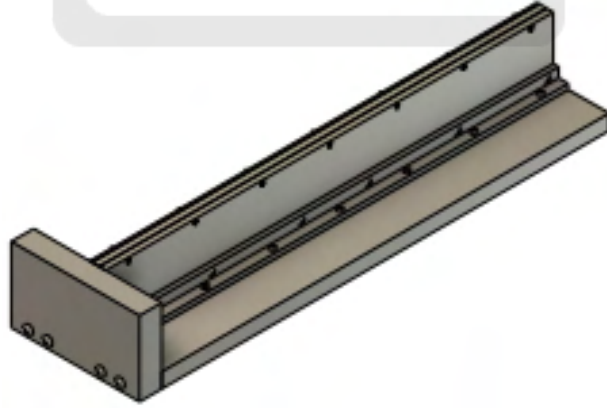


Figure 15: The architecture of the spacer.

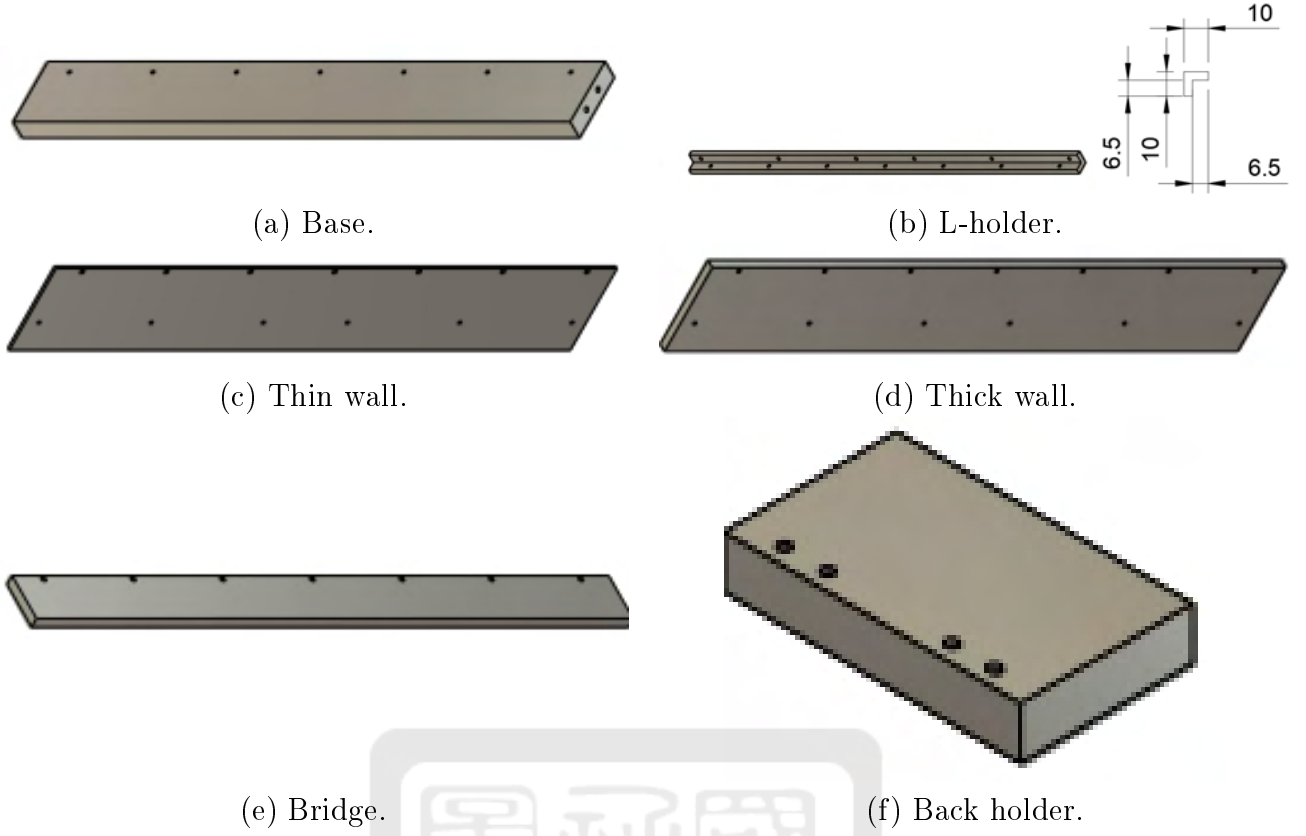


Figure 16: The parts of the spacer.

The shape of the spacer is a bulge shape. Each piece of the spacer is fastened with each other by M2 and M3 screws. We can change the thick and thin walls of the spacer with different thicknesses to adjust the gap distance between the HV electrode and grounded electrode. When we would like to adjust the rail-like switch from the north wing to the south wing, we only need to move the back holder from one side to the other side of the spacer. The engineering drawings of all pieces are provided in section A.1.6.

The spacer is designed using Fushion 360. We divided the structure of the spacer into many parts first. Then, we decided the size of each part and it was made by Sanpon iron co., ltd. Figure 17(a) is the 91-screws spacer. It is the first version of the new spacers. Since this version needs too many through holes for screws, the cost is too much. Thus, we designed the second version with fewer screws as shown in figure 17(b). It only uses 37 screws for fixing all pieces.

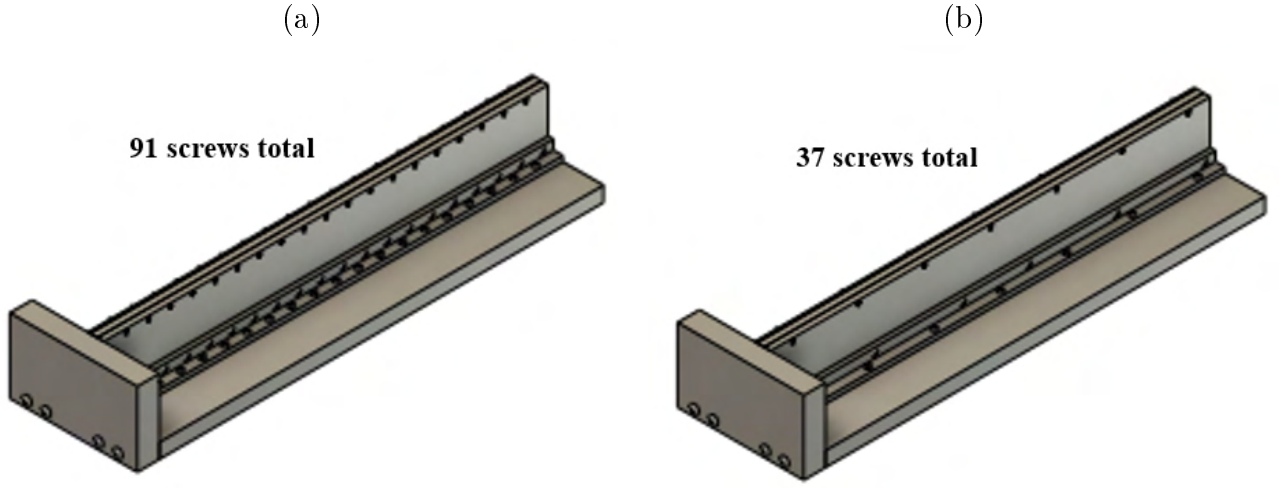


Figure 17: (a) The architecture of the 91-screws spacer. (b) The architecture of the 37-screws spacer.

2.3 The Rogowski coil of the pulsed-power system

Most of our experiments use the big current, ≈ 135 kA, provided by the pulsed-power system. We can't use the conventional ammeter to measure the current or the huge current will toast the conventional ammeter. Therefore, we built a Rogowski coil. Figure 18 shows the principle of the Rogowski coil[13]. When a current passes through the center of the coil, a voltage at the output of the Rogowski coil is induced. The induced voltage is then integrated by a R-C integrator. Finally, we measure the induced voltage with an integrator so that we can calculate the amount of the current.

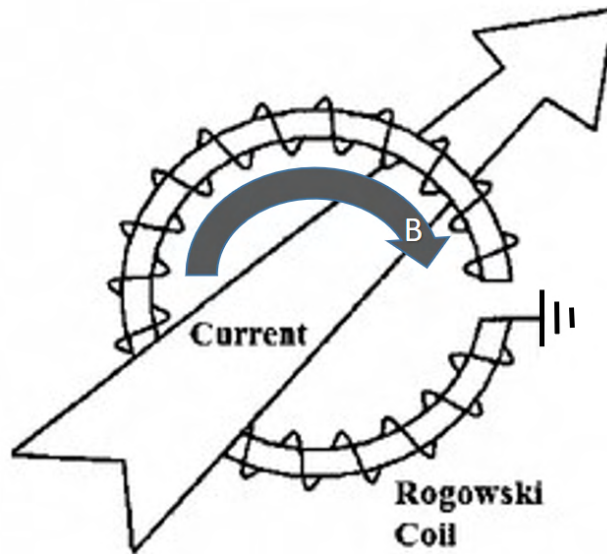


Figure 18: The principle of the Rogowski coil working.

2.3.1 The motivation of upgrading the Rogowski coil

Figure 19 is the cross section of the vacuum chamber. The red points indicate the location of the Rogowski coil if we use the old Rogowski coil made by Chieh-Jui[14]. The green points point out where the new Rogowski coil locates. The size of the Rogowski coil is now smaller than the old one. Figure 20(a) is the old version of the Rogowski coil. The inner radius of the old one is about 150 mm. The new version of the Rogowski coil is shown in figure 20(b). The inner radius of the new one is about 139 mm, i.e., 11 mm smaller than the old one.

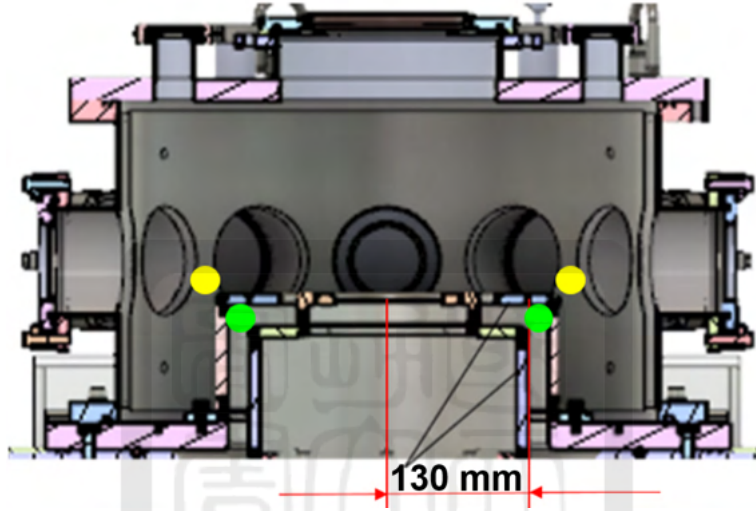


Figure 19: The cross-section drawing of the vacuum chamber.

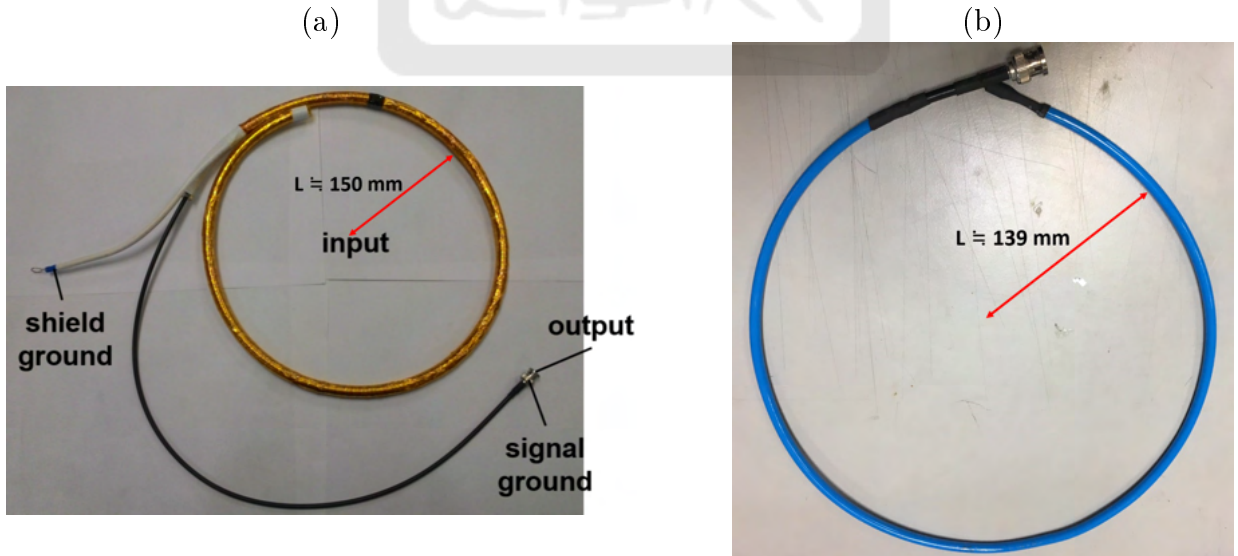


Figure 20: (a) The old version of the Rogowski coil. (b) The new version of the Rogowski coil.

2.3.2 The design of the new Rogowski coil

The new Rogowski coil was made from a RG-58 coaxial cable. Figure 21 is the cross section of the coaxial cable. It consists of the ground layer and the metal core. Both of them are protected by the inner insulation layer and the outer insulation layer. We use the inner insulation layer and the metal core as the structure for the Rogowski coil. The old version of the Rogowski coil used the wire to wrap around the coaxial cable forming a curved solenoid coil. In order to make the size smaller, we replace the wire with aluminum tape.

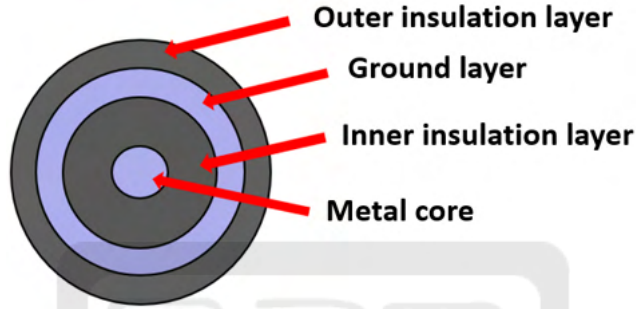


Figure 21: The cross-section of the coaxial cable.

Figure 22 is the drawing of the Rogowski coil[14]. I_{in} is the current we would like to measure, r is the radius of each loop of the curved solenoid coil and L is the radius of the Rogowski coil. We can calibrate the mutual inductance of the Rogowski coil ($M_{\text{Rogowski coil}}$) by measuring the output voltage (V_{out}) with a given I_{in} . When the current passes through the Rogowski coil, it produces the magnetic field in the curved solenoid coil:

$$B = \frac{\mu_0 I_{\text{in}}}{2\pi L} . \quad (11)$$

According to Faraday's law, the induced voltage of one turn of the curved solenoid aluminum tape is:

$$V_{\text{percoil}} = -\frac{d}{dt}(B \times \pi \times r^2) . \quad (12)$$

Because the Rogowski coil has N turns of coils, the total induced voltage is:

$$V_{\text{out}} = N \times \left[-\frac{d}{dt}(B \times \pi \times r^2) \right] . \quad (13)$$

Combining Eq. 11 and Eq. 13, we get:

$$V_{\text{out}} = -\frac{r^2 N \mu_0}{2L} \frac{dI_{\text{in}}}{dt} \equiv M_{\text{Rogowski coil}} \times \frac{dI_{\text{in}}}{dt} \quad (14)$$

where $M_{\text{Rogowski coil}} = -\frac{r^2 N \mu_0}{2L}$ is the mutual inductance of the Rogowski coil.

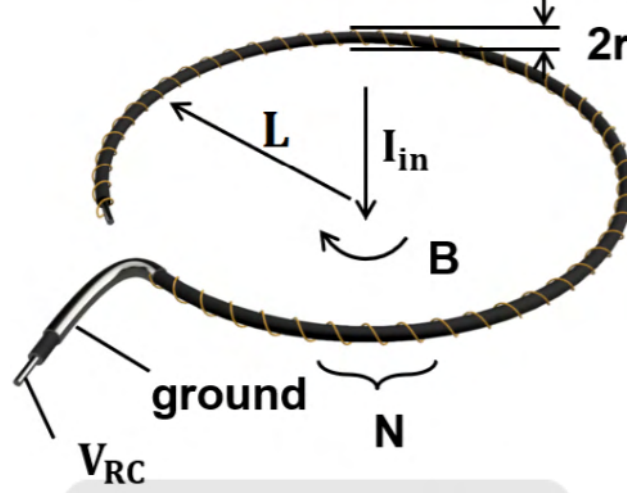


Figure 22: The drawing of the Rogowski coil working.

In our pulsed-power system, the peak current is 135 kA with a rise time of $1.6 \mu\text{s}$, i.e., $\frac{dI_{\text{in}}}{dt} \sim \frac{135 \text{ kA}}{1.6 \mu\text{s}} = 8.4375 \times 10^{10} \text{ A/s}$. After calculating, we came out with two versions of the Rogowski coil. The first version is 138.75 mm in L and the second version is 137.8 mm in L . Both Rogowski coil designs fit into the coaxial transmission line. Both designs use plastic tubes to prevent the arcing between the Rogowski coil and the coaxial transmission line. As shown in Figure 22, the number of turns and the radius of each turn of wire are affected by how coils are made. They are determined using Eq. 14. Details of the two designs are the following:

(1) Use the aluminum tape for the curved solenoid coil. A Polyurethane (PU) tube is used to protect the curved solenoid coil from the arcing between the coil and the coaxial transmission line. This version is called 138.75-mm L . The parameter L is 138.75 mm as shown in figures 23(a) and (b). It is the sum of the radius of the inner coaxial transmission line (130 mm), the distance between the wall of the inner coaxial transmission line and the PU tube (7 mm), the thickness of the PU tube (1 mm), and the distance between the solid conductors and the PU tube (0.75 mm). The radius of the inner core of the cable is considered as the radius of the solenoid coil (r) because the thickness of the aluminum tape is much less than 1 mm.

(2) Use wires for the curved solenoid coil. A Polypropylene (PP) tube is used to protect the curved solenoid coil from the arcing between the coil and the coaxial transmission line. This

version is called 137.8-mm L . The parameter L is 137.8 mm as shown in figures 23(c) and (d). It is the sum of the radius of the inner coaxial transmission line (130 mm), the distance between the wall of the inner coaxial transmission line and the PU tube (5.85 mm), the thickness of the PU tube (1.6 mm), and the distance between the solid conductors and the PU tube (0.35 mm).

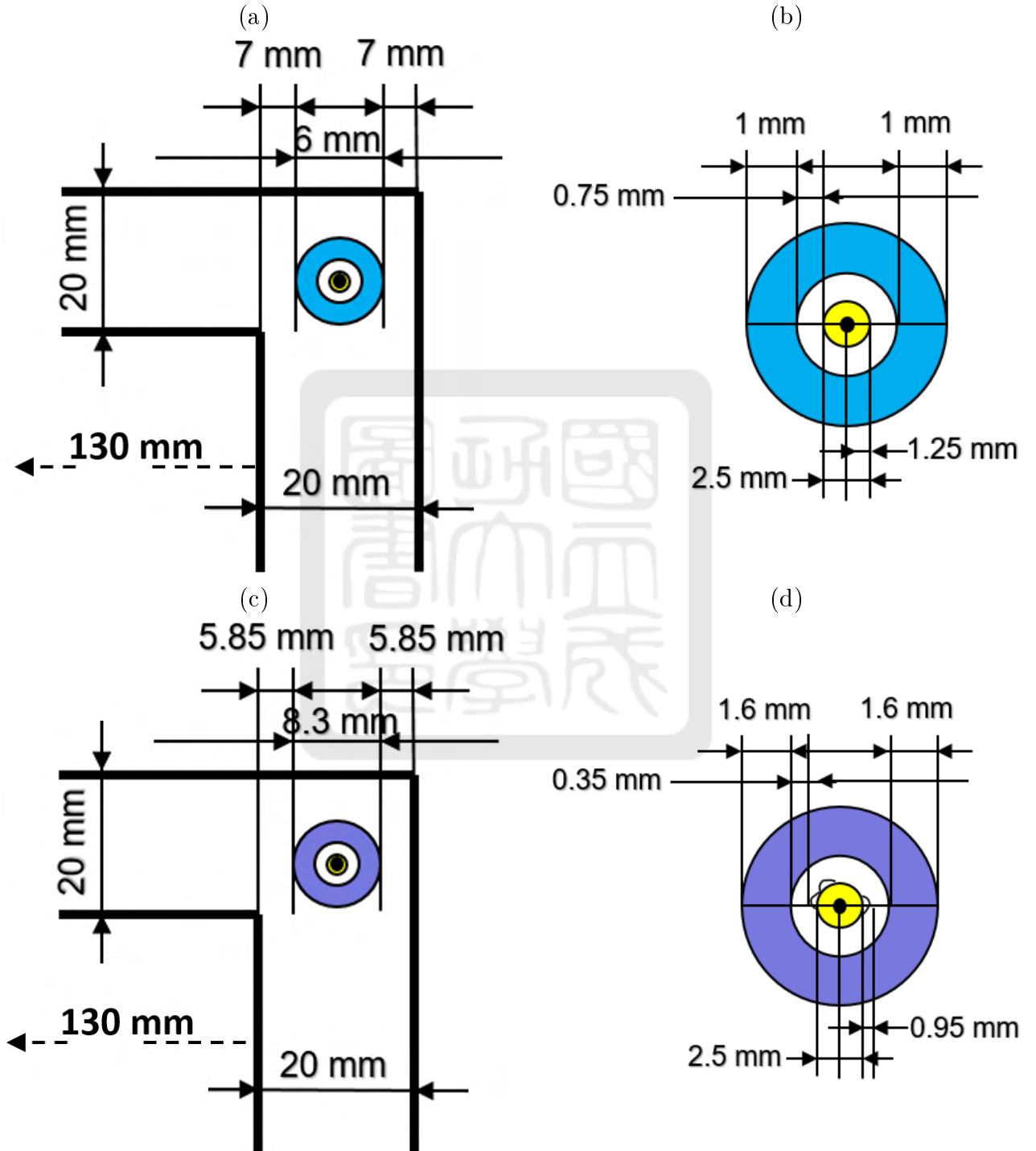


Figure 23: The cross-section drawing of the Rogowski coil in the coaxial transmission line.

Finally, we chose the first version (aluminum tape with PU tube) to build the Rogowski coil. The first reason is that the first version of the Rogowski coil has more turns of the curved

solenoid coil than the second one as shown in table 2. The more turns of the curved solenoid coil the Rogowski coil has, the more uniform the Rogowski coil is. The second reason is that we have a PU tube which has a soft texture and high formability. The PU tube is better for us to protect the curved solenoid coil. The only disadvantage of the first version is that there are many turns of the coils. It is more difficult to build the first version of the Rogowski coil than to build the second version.

Table 2: The comparison between the first version and second version of the Rogowski coils.

	Tape with PU tube	Wire with PP tube
The radius of the Rogowski coil (L)	138.75 mm	137.8 mm
The radius of the solenoid conductive layer (r)	1.25 mm	2.2 mm
The turns of the solenoid conductive layer (N)	130 turns	41 turns

We use a coaxial cable with a BNC connector to build the Rogowski coil as shown in Figure 24. The cross section of the Rogowski coil is shown in figure 21. It consists of the outer insulation layer, the grounded layer, the inner insulation layer, and the metal core. The procedure of building the Rogowski coil has four steps:

- (1) Cut off the BNC connector at one end of the coaxial cable and remove a bit of the outer insulation layer.
- (2) Remove the grounded layer with a length of $2\pi L$ where $L= 138.75$ mm is the inner radius of the Rogowski coil.
- (3) Remove a bit of the inner insulation layer so that the metal core appears.
- (4) Use the aluminum tape with 3 mm in width as the curved solenoid coil to wrap around the inner insulation layer with 130 turns. The distance between each turn of the curved solenoid coil is 6.7 mm ($\frac{2\pi L}{\text{Number of turns}} = \frac{2\pi \times 138.75}{130}$). One end of the curved solenoid coil uses the metal ring to connect with the metal core. The other end of the curved solenoid coil is connected to the grounded layer.

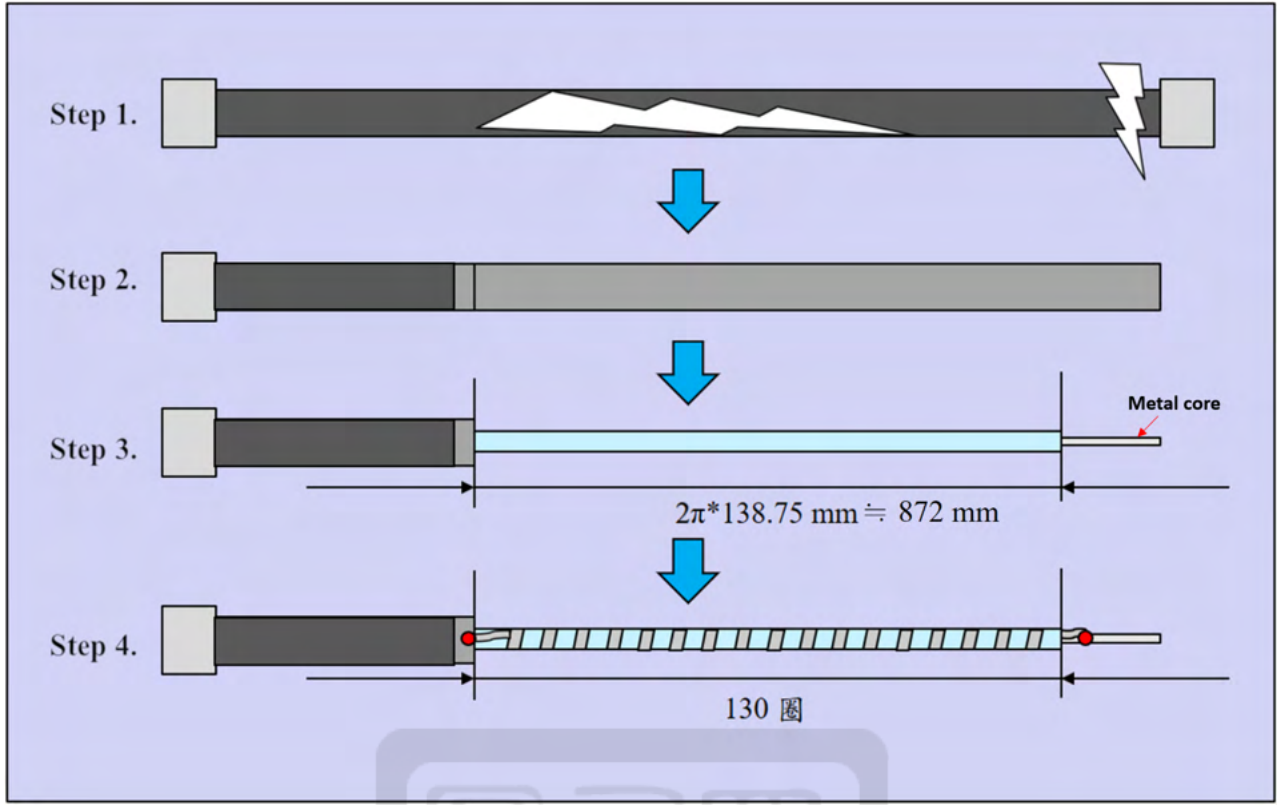


Figure 24: The production of the Rogowski coil.

2.3.3 The mount of the new Rogowski coil

We place the Rogowski coil in the vacuum chamber of our pulse-power system located between two cylinders of the cylindrical coaxial transmission line (CTL), shown as the green points in figure 19. The Rogowski coil is fixed under the top plate of the CTL as shown in figure 25. To fix the Rogowski coil at the location, we proposed two ways:

(1) Use four Rogowski coil holders to hold the Rogowski coil under the top plate of the CTL. Figure 26 (a) is the holder made of Polyethylene (PE). First, the Rogowski coil passes through four holders. Then, each holder is fixed under the top plate of the CTL using M2 screws.

(2) Use four cable ties to hold the Rogowski coil under the top plate of the CTL. Figure 26 (b) is the cable ties made of Polyethylene (PE). We only need to make several holes through the top plate of the CTL and use cable ties to hold the Rogowski coil under the top plate of the CTL.



Figure 25: The sectional drawing of the coaxial outer and Rogowski coil.

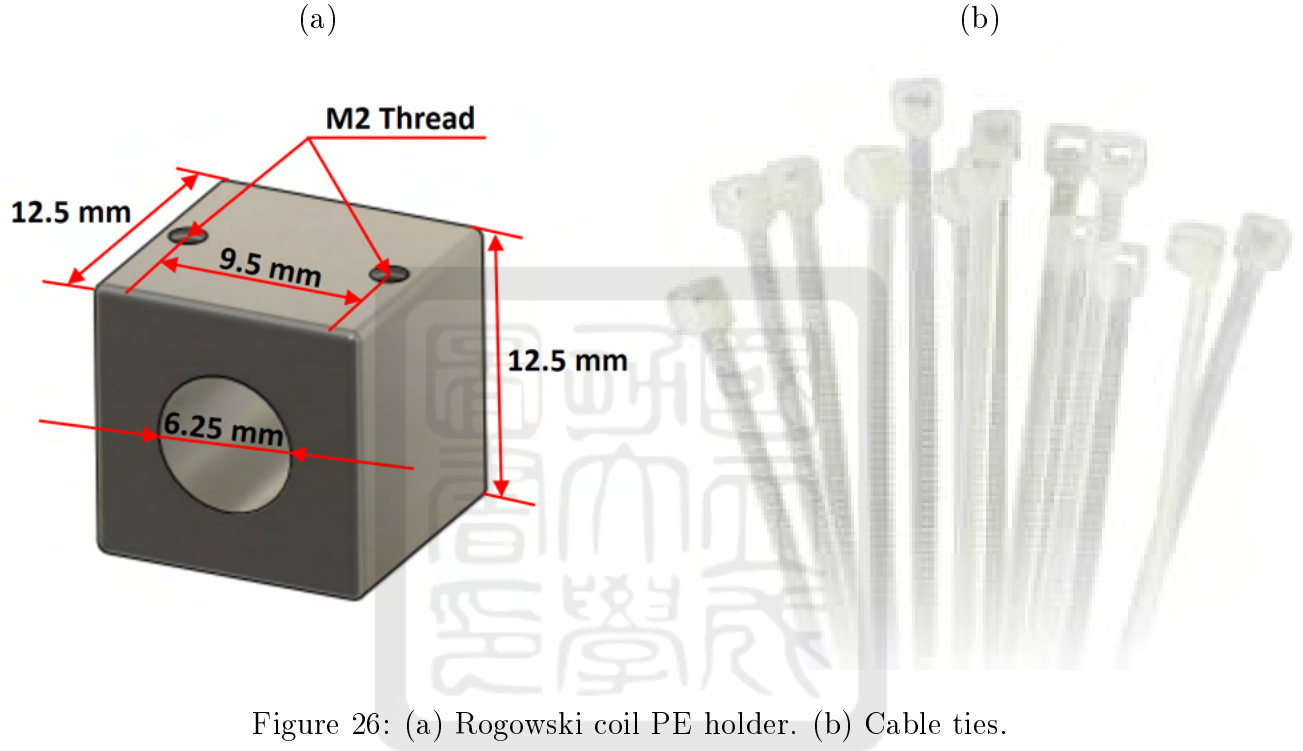


Figure 26: (a) Rogowski coil PE holder. (b) Cable ties.

To determine which way to use, we compare the workability, stability, and cost between two designs and show them in table 3. The cable tie has a lower cost and a easier workability than the PE holder. Therefore, we use the cable ties.

Table 3: The comparison of the Rogowski coil fixing methods.

	PE holder	Cable tie
Workability	Difficult	Easy
Stability	Good	Bad
Cost	High	Low

2.3.4 The calibration of the new Rogowski coil

After the Rogowski coil was fixed in the pulsed-power system, we needed to calibrate the Rogowski coil *in situ*. As shown in figure 27, we used four wires as the dummy load

passing through the Pearson current monitor (model 301x) and connected between the anode (the outer cylinder of the CTL) and the cathode (the inner cylinder of the CTL). A PE plate was placed between the Pearson current monitor and the top plate of the CTL as the insulator. The 1-kJ pulsed-power system can provide a peak current of ≈ 135 kA. However, the maximum peak current that can be measured by the Pearson current monitor was ≈ 50 kA. Therefore, we disconnected the south wing of the pulsed-power system to reduce the current by half, i.e. ~ 50 kA. Then, we measured the outputs of both the Pearson current monitor and the Rogowski coil when the pulsed current passed through both of them at the same time. Finally, we calculated the ratio between the current measured by the Pearson current monitor and the induced voltage of the Rogowski coil for calibration.

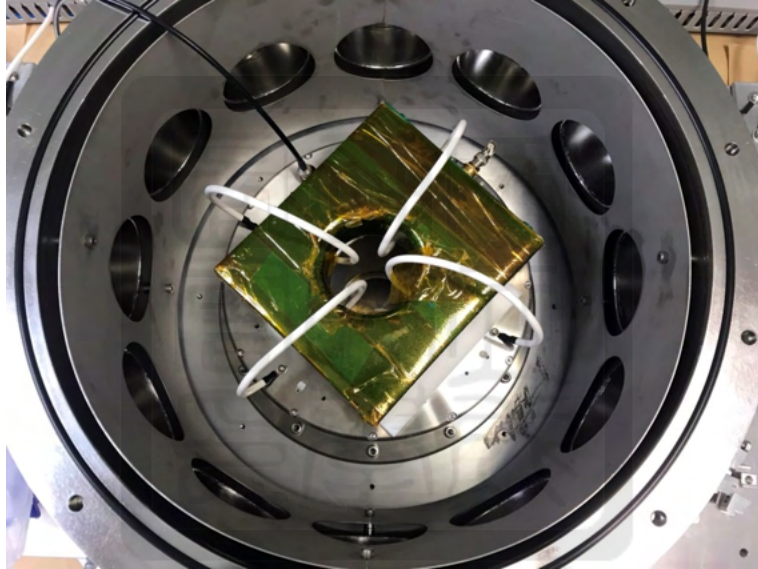


Figure 27: The Rogowski coil was calibrated with the Pearson current monitor.

2.3.5 Calibration results

Figure 28 is the raw data from the Pearson current monitor and the Rogowski coil. The red dash line was the current measured by the Pearson current monitor while the blue solid line was the output from the Rogowski coil with the integrator. To calibrate, we used Eq. 15 and Eq. 16 to fit to curves in figure 28 where I_0 , α , ω and V_0 were fitting parameters.

$$I_{\text{input}}(t) = I_0 e^{-\alpha(t-\Delta t)} \sin[\omega(t - \Delta t)] , \quad (15)$$

$$V_{\text{measure}}(t) = V_0 e^{-\alpha(t-\Delta t)} \sin[\omega(t - \Delta t)] . \quad (16)$$

After curve fittings, we got the parameters I_0 , t , w , α and V_0 for both the Pearson current monitor and the Rogowski coil. We then plotted the relation between the $V_{\text{measured}}(t)$ in x axis and $I_{\text{input}}(t)$ in y axis at different time as shown in figure 29. Each point in figure 29 represents the point of $(V_{\text{measured}}(t_i), I_{\text{input}}(t_i))$ at t_i . Then, we got the slope of figure 29 which was the calibration ratio. As a result, the calibration ratio was 188000 ± 300 (A / V).

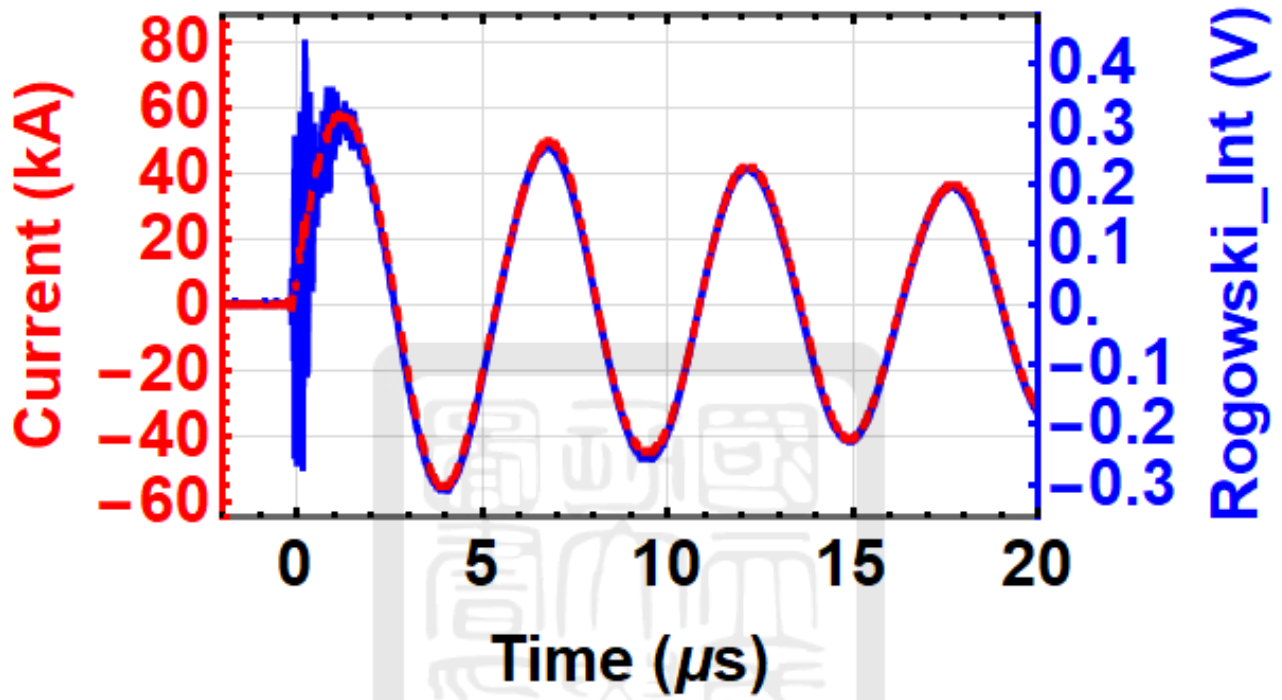


Figure 28: The result of the Rogowski coil curve fitting.

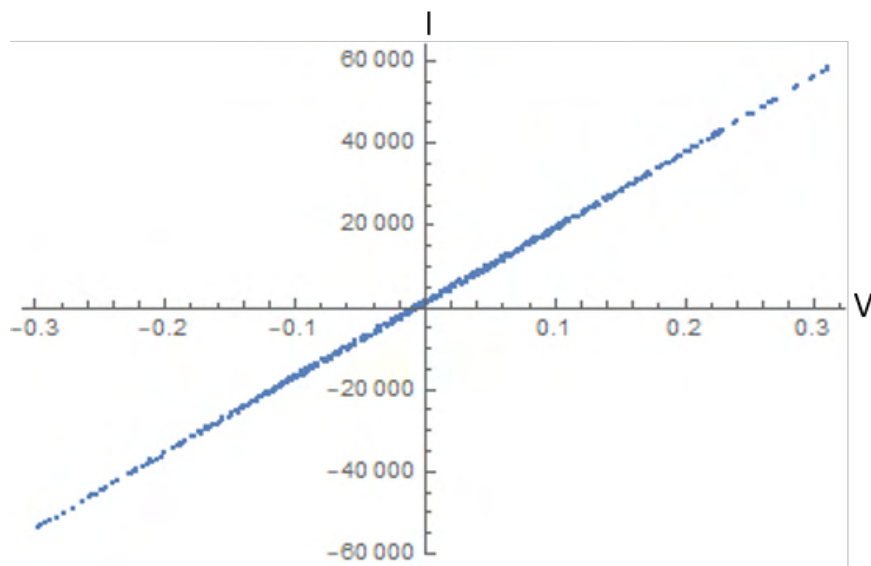


Figure 29: The relationship between input current and output voltage.

2.3.6 Output of the pulsed-power system

After getting the calibration ratio, the measured current I_{input} can be directly obtained from the Rogowski coil using Eq. 17.

$$I_{\text{measured}} = V_{\text{measurement}} \times (188000 \pm 300) . \quad (17)$$

Then, we used the Rogowski coil to measure the current provided by the full 1-kJ pulse-power system. First, we removed the Pearson current monitor and kept the dummy load as shown in figure 30. Figure 31 shows one of the measurements obtained from ten shots. The peak current was 135 ± 1 kA with a rise time of 1592 ± 3 ns.

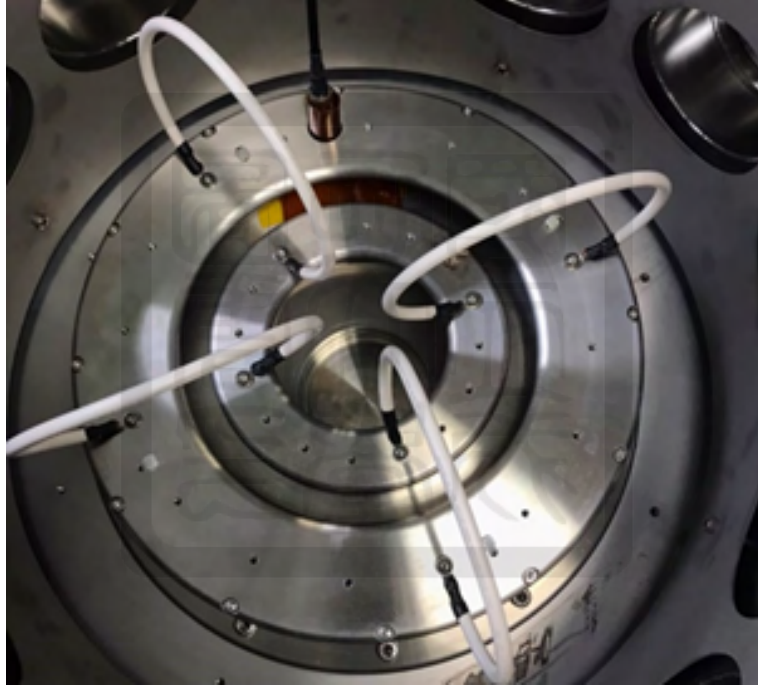


Figure 30: The Rogowski coil measured the current from the 1-kJ pulse-power system.

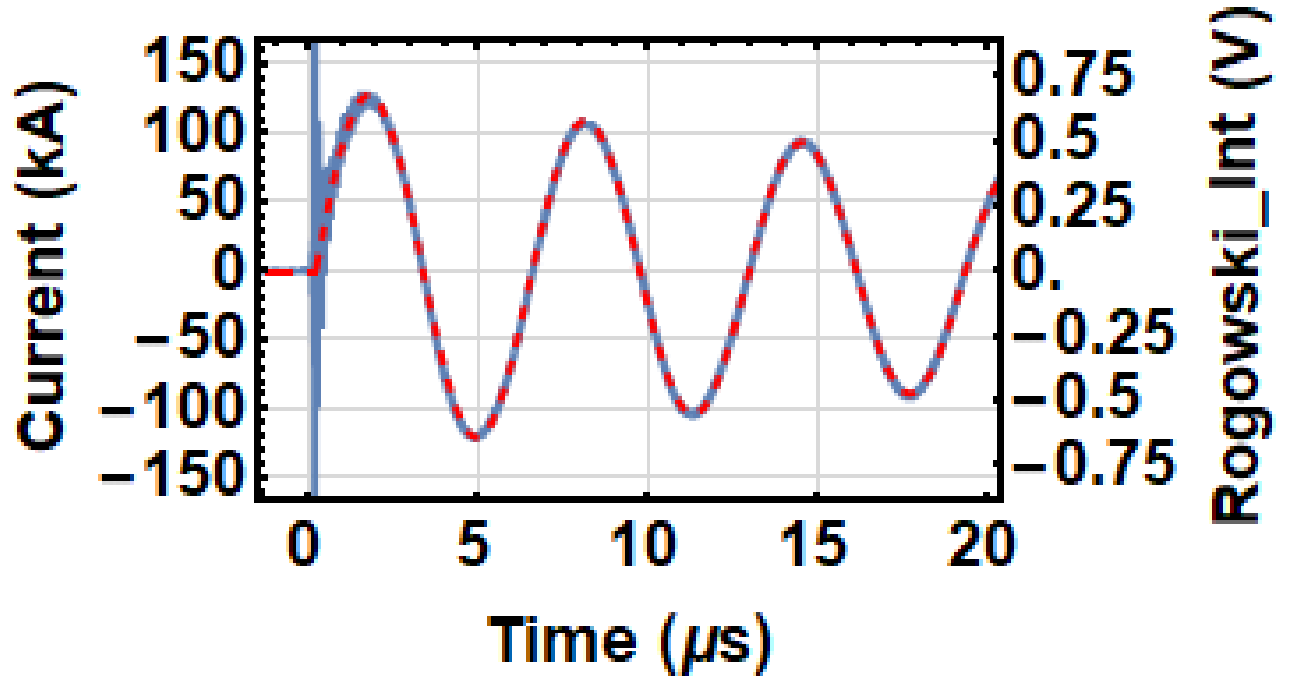


Figure 31: The current measurement from both of south and north wings triggered.

2.4 Summary

We have built the spacer and the new Rogowski coil for the pulsed-power system. The spacer of the rail-gap switch was built to control the gap distance between the HV electrode and the grounded electrode. On the other hand, the new Rogowski coil made of coaxial cable, the aluminum tape, and the PU tube was built. The Rogowski coil is placed within the coaxial transmission line. Finally, we used the Pearson current monitor to calibrate the Rogowski coil with the integrator. The calibration ratio of the Rogowski coil is 188000 ± 300 (A / V). Finally, the pulse-power system can provide a current output of 135 ± 1 kA with a rise time of 1592 ± 3 ns.

3 The gas puff

In order to generate the plasma plume, a gas puff as the precursor is ionized by the arc discharge between a pair of electrodes. In this chapter, a gas gun as the generator of the gas puff is introduced. The construction of the gas-gun system will be introduced in Section 3.1. Then, the pulse-valve system combined with the control box will be introduced in Section 3.2. Since we need the gas input with a stable pressure, a reservoir system will be used and introduced in Section 3.3. We used the convergent-divergent nozzles which will be introduced in Section 3.4. Finally, the procedure of operating the gas-puff generator will be introduced in Section 3.5. A summary is given in Section 3.6.

3.1 The construction of the gas-gun system

The gas-gun system provides the high-pressure gas puff in my experiments. Figure 32 is the schematic of the pulse-valve system. The system consists of a function generator, an electrical-to-optical converter, a pulse-valve control box, a 24-V battery, a pulse valve, and a convergent-divergent nozzle. The function generator is used to provide a square pulse. The width of the square pulse controls the opening time of the pulse valve. The signal is then delivered to the electrical-to-optical converter via the coaxial cable. The electrical-to-optical converter is connected with the receiver in the pulse-valve control box via a fiber. The optical signal coupling can protect the function generator being damaged by electromagnetic pulses (EMP) and the reversed current generated by the discharge of the pulsed-power system when the gas-gun system is integrated into the pulsed-power system in the future. The pulse-valve control box is powered by a 24-V battery. The convergent-divergent nozzles are attached to the pulse valve for increasing the flow speed.

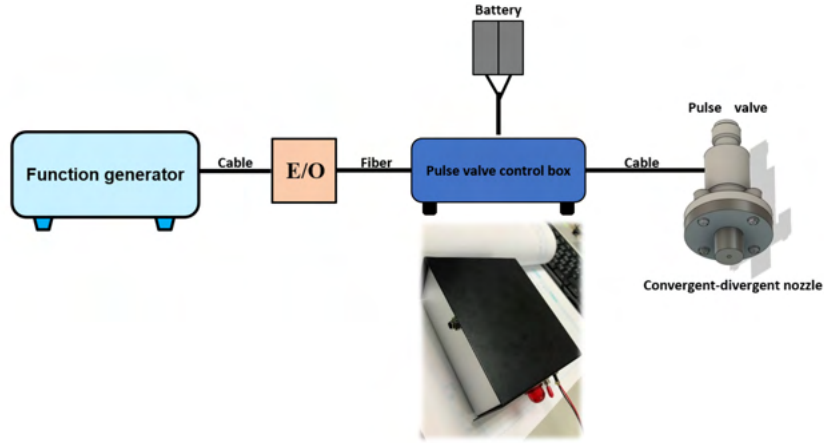


Figure 32: The CAD drawing of the pulsed-valve system.

3.2 The pulse-valve system

In order to generate the gas puff, a pulse valve system plays an important role. It is used to control the gas output for a short period of time. A pulse-valve system consists of the pulse valve and the control box. Figure 33(a) is the 24-V pulse valve made by Parker Hannifin Corporation, part number 009-1668-900. The 24-V pulse valve is a 2-way normally-closed valve and it can work at 4 to 105°C. Figure 33(b) is the 12-V pulse valve made by Le-Jing Corporation. The 12-V pulse valve is also a 2-way normally-closed valve and it can work at 0 to 55°C. Both of the 24-V pulse valve and the 12-V pulse valve are suitable for my experiments.

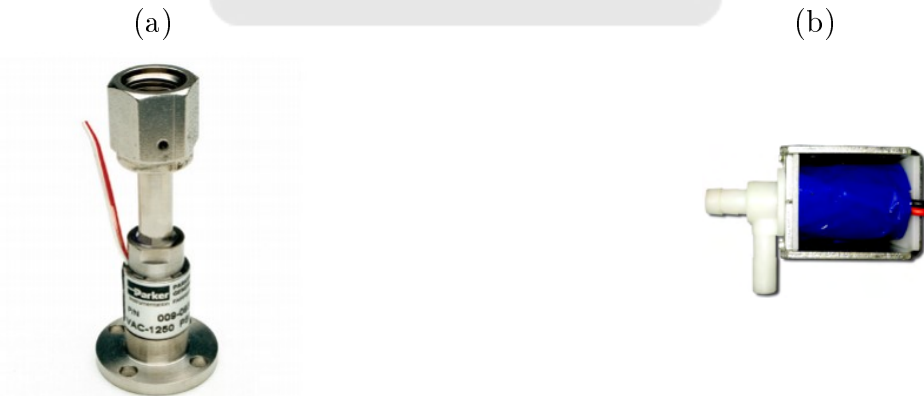


Figure 33: (a) The figure of the 24-V pulse valve. (b) The figure of the 12-V pulse valve.

3.2.1 The 24-V pulse-valve system

Figure 34 is the cross-section drawing of the 24-V pulse valve. The diameter of port 1, i.e., the gas outlet, is 0.1 mm. The top of the pulse valve is port 2 for gas input and the middle

part is the coil assembly used to induce electromagnetic forces. The electromagnetic force can attract the poppet up to open the pulse valve. The body of the pulse valve is made of stainless steel and the pulse valve has the main spring to push the poppet against port 1 preventing the gas from leaking out. On the other side, the pulse valve also has a buffer spring to protect port 1. When a 24-V electrical pulse drives the 24-V pulse valve, it can open with a response time less than 2 ms. Because of the short response time of the 24-V pulse valve, a gas puff can be generated.

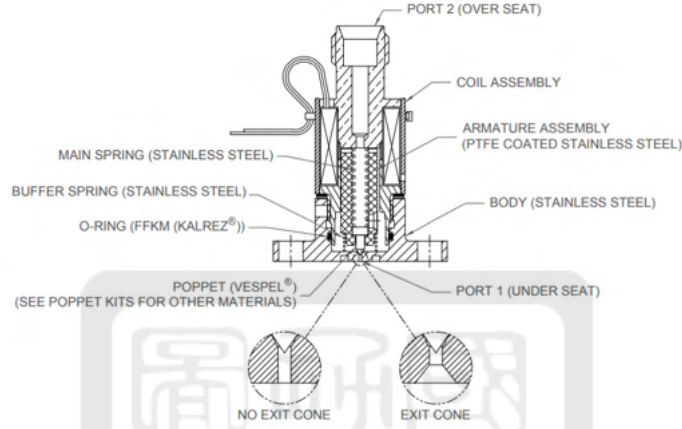


Figure 34: The cross-section drawing of the 24-V pulse valve.

Figure 35(a) is the circuit of the 24-V pulse-valve control box. The opening time of the 24-V pulse valve is important. It can affect the pressure of the gas puff since the pressure in the reservoir reduces as the gas exhausts from the reservoir. To control the opening time of the pulse valve, we use a relay (FOD3184) as the signal controller. It can convert a transistor-transistor logic (TTL, 5 V) signal to a signal with a higher voltage using a photocoupler in the relay. When the TTL signal is provided to the input of the FOD3184, the output voltage of the relay V_{01} and V_{02} will be connected to V_{DD} , i.e. at 24 V in our design. Otherwise, the output voltage of the relay V_{01} and V_{02} is connected to V_{SS} at the ground. As shown in figure 35(b), to provide a stable 24 V, we use a DC-DC Converter (SKE10B-24) and a 24-V battery as the power supply. The DC-DC Converter provides a stable 24-V output even when the battery voltage drops below 24V. Then, the fiber is used to protect the function generator from the discharge of our 1-kJ pulsed-power system in the future. The optical signal is converted back to the electrical signal via a receiver. The receiver is stably powered by the same DC-DC Converter combining a voltage divider with a 5-V Zener diode. Figure 36(a) is the photo of the 24-V pulse-valve control box. The aluminum box is used to protect our circuit from the

potential EMP in the future. Figure 36(b) is the layout drawing of the 24-V pulse-valve control circuit.

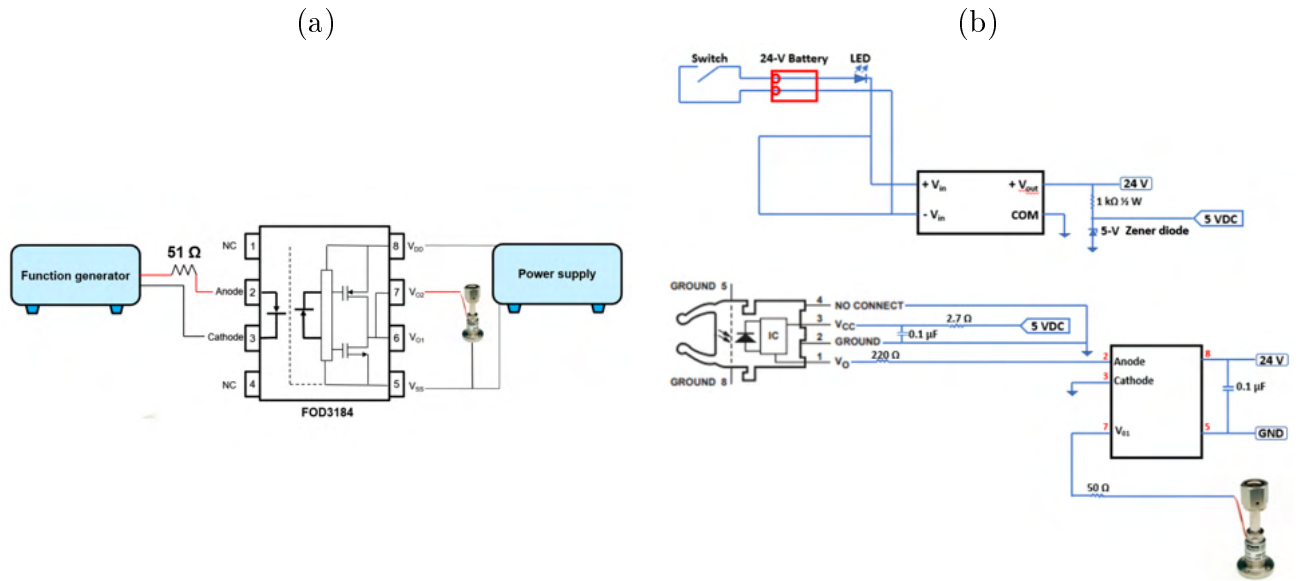


Figure 35: (a) The circuit of the relay (FOD3184). (b) The circuit of the 24-V pulse-valve control box.

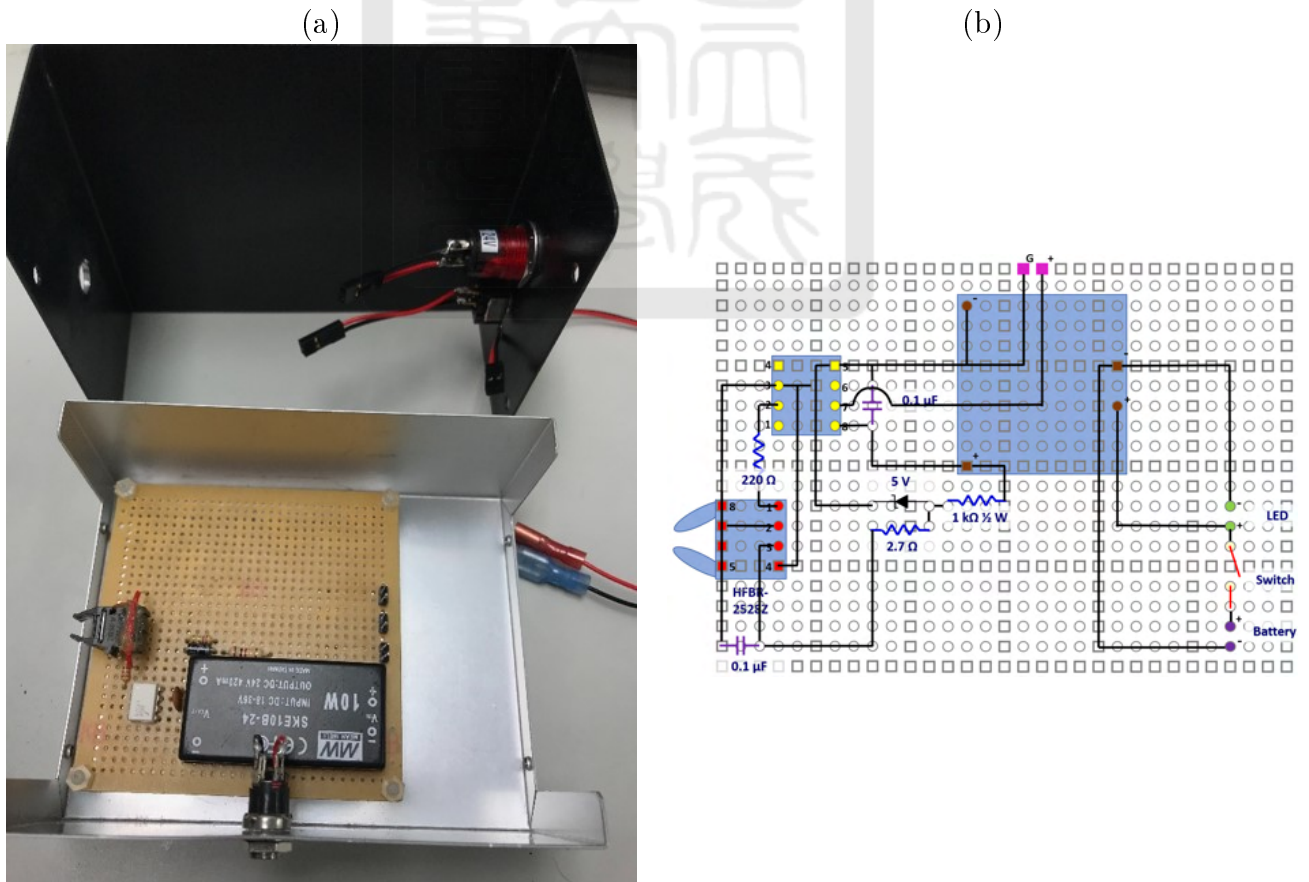


Figure 36: (a) The 24-V pulse-valve control box. (b) The layout drawing of the 24-V pulse-valve control circuit.

3.2.2 The 12-V pulse-valve system

Figure 37 is the cross-section drawing of the 12-V pulse valve. The diameter of the output is 5.5 mm. The coil assembly is used to induce electromagnetic force to attract the core. The spring pushes the core down to close the valve. The o-ring can avoid the gas from leaking out. The 12-V pulse valve is made of stainless steel and can work with an 88-mA current and an 1.06-W power.

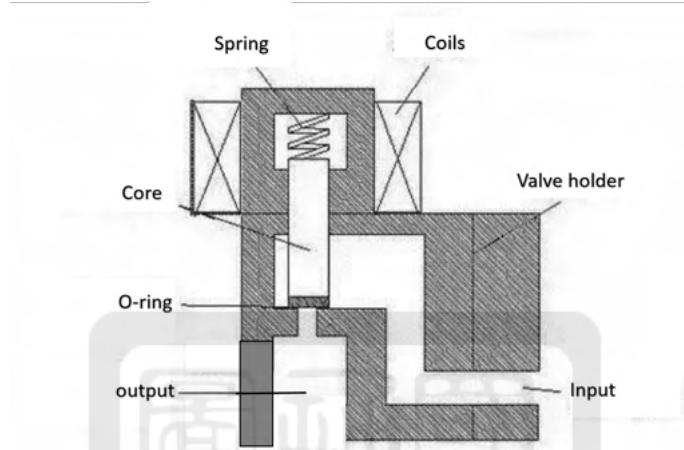


Figure 37: The cross-section drawing of the 12-V pulse valve.

Figure 38(a) is the circuit of the 12-V pulse-valve control box. We also use a relay (FOD3180) as the signal controller to control the opening time of the pulse valve. The function of the relay (FOD3180) is the same as the one (FOD3184) used in the 24-V pulse-valve control box. The difference is that the power of the 24-V pulse-valve control box is 11.2 W and the 12-V one is 1.2 W. As shown in Figure 38(b), to keep the input voltage stable, we use a DC-DC Converter (SKE10B-12) and a 24-V battery. The DC-DC Converter converts the 24-V input to a stable 12-V output.

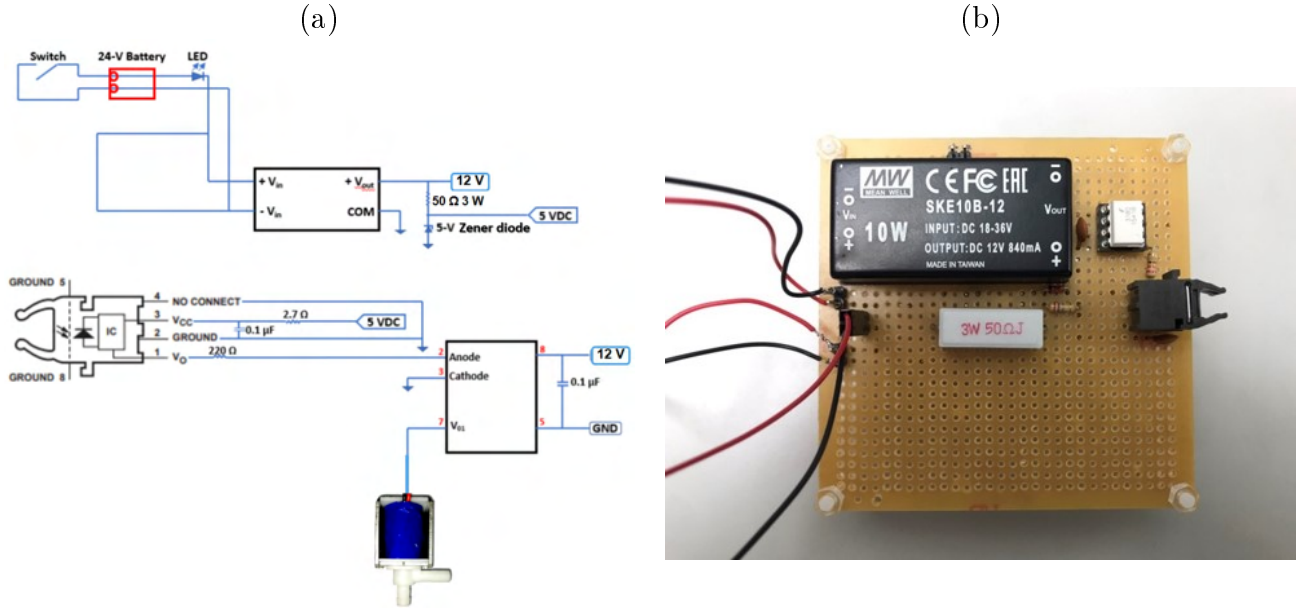


Figure 38: (a) The circuit of the 12-V pulsed-valve control box. (b) The 12-V pulsed-valve control box.

The airtight capability of the 12-V and 24-V pulse valves is very important. As shown in table 4, both the 12-V and the 24-V pulse valves have a limit of the pressure difference between the gas inlet and outlet. The 12-V pulse valve can handle a pressure difference about 450-torr and the export size is 5.5 mm. The 24-V pulse valve can load about 64655-torr pressure difference and the export size is 0.001 mm. Our designs of all experiments are in the range of the limit.

Table 4: The information of the pulse valves.

	12-V DC pulse valve	24-V DC pulse valve
Pressure difference	450 torr	64655 torr
Export size	5.5 mm	0.1 mm

3.2.3 The pulse-valve opening-time measurements

The sound of the pulse valve's movement was used to determine the time that the valve moved. Figure 39 is the experimental setup of the 24-V pulse-valve opening-time measurement. We used a cellphone to record the moving sound of the pulse valve. In figure 40, we used the software Audacity to convert the audio file to the intensity data file. The opening and closing peaks were obtained by analyzing the recorded sound. In order to make sure whether the width of the square pulse from the function generator was the actual opening time of the pulse valve, we test the width set at 0.004, 0.005, 0.01, 0.05, 0.1, 0.5, and 1 sec. Data of 1 sec is shown as

an example in this subsection and the total results are given in section A.2.2.

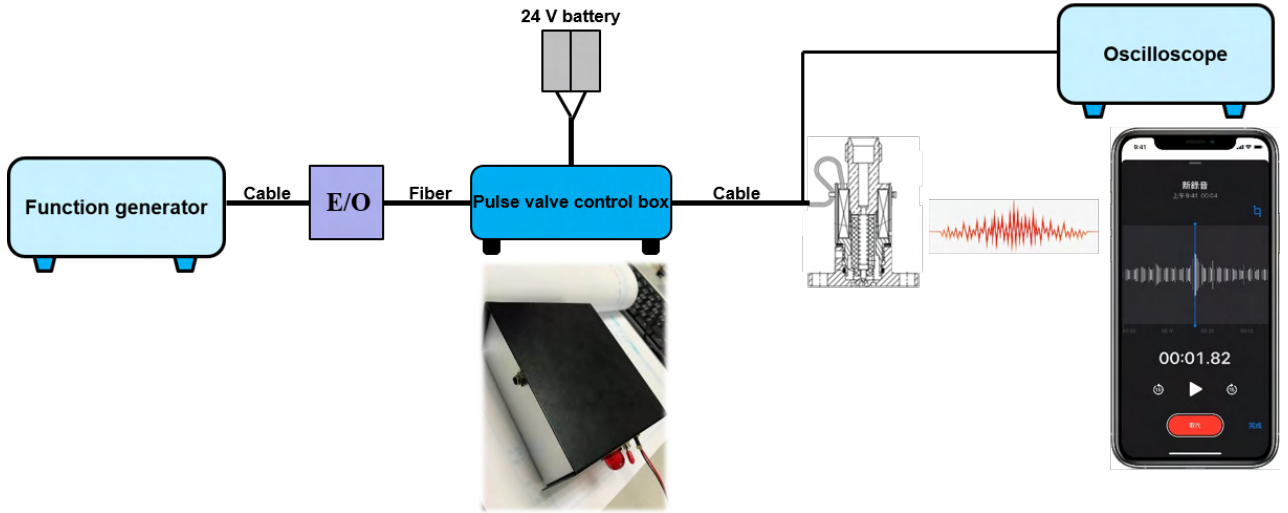


Figure 39: The experimental setup of the 24-V pulse valve sound measurement.

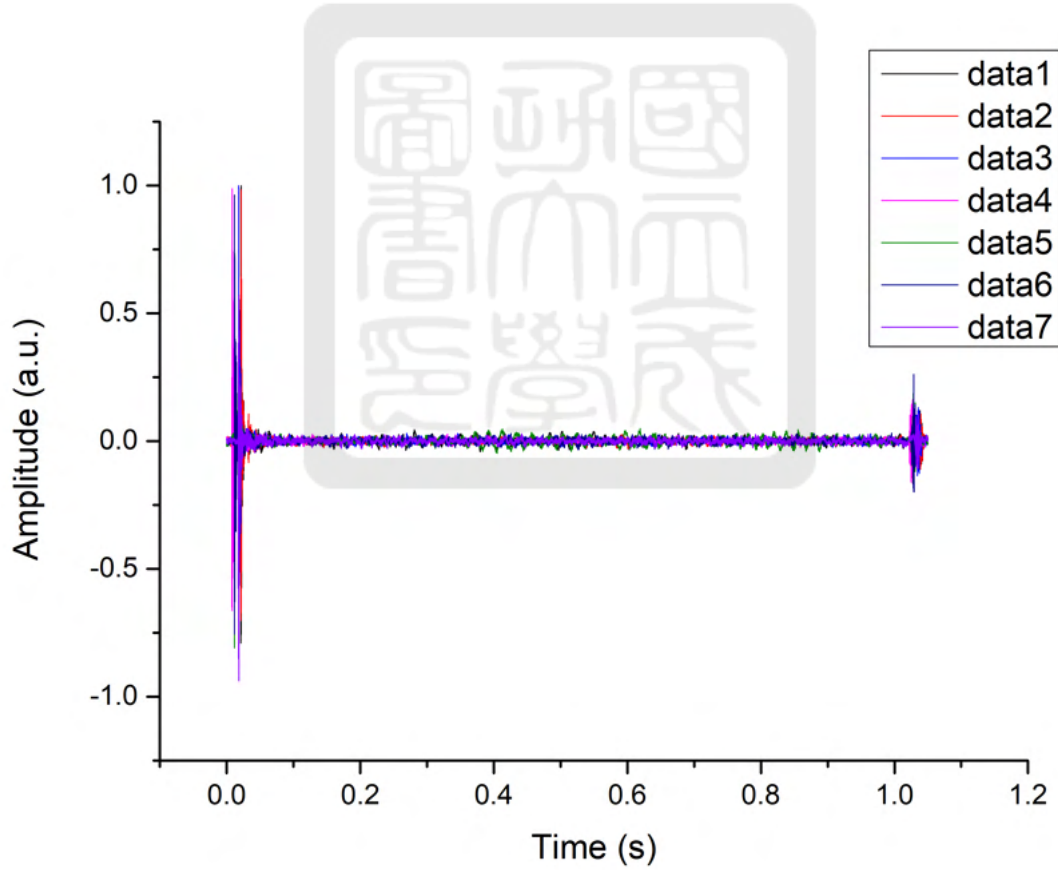


Figure 40: The sound recording of the time delay setting at 1 s.

In figure 41, we considered the time where the max number occurred in the first target wave as the valve opening time. On the other hand, the valve closing time is defined as the time where the max number occurred in the second target wave. Then, we obtained the time

difference between the pulse valve's opening and the closing time. Finally, we showed the results and the deviations from the settings in table 5. The actual time delay is 1.74 % longer than the width of the square pulse from the function generator.

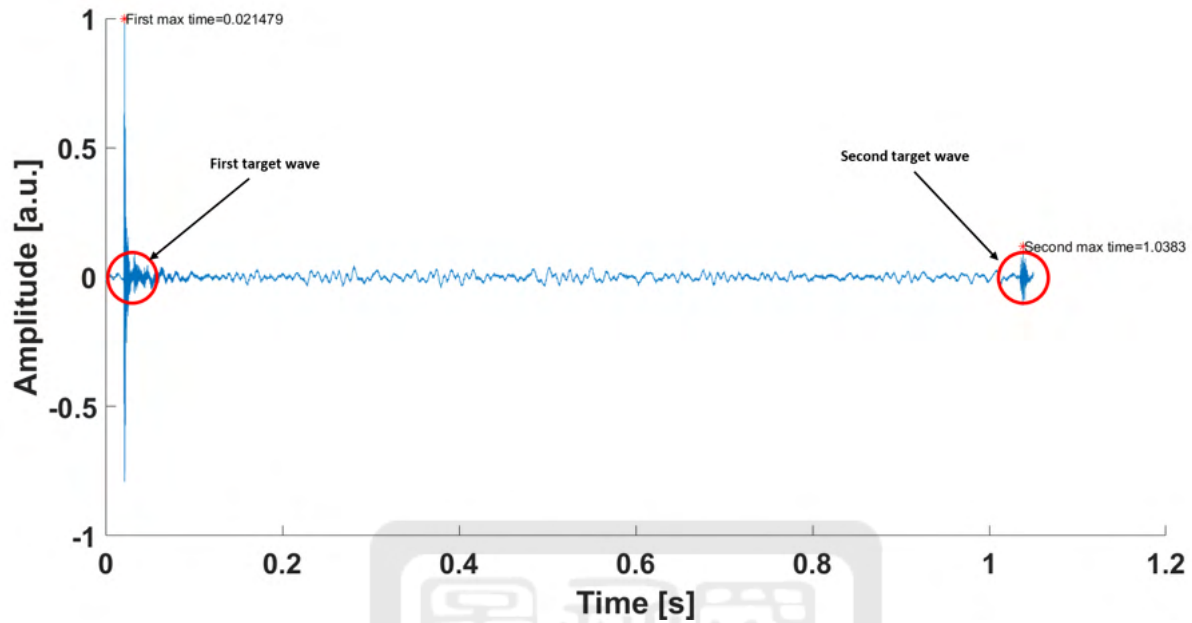


Figure 41: The 1-s time delay result of cutting data with Matlab.

Table 5: The deviation of the time delay setting at 1 s.

	Data 1	Data 2	Data 3	Data 4	Data 5	Data 6	Data 7	Average	Standard Deviation
The amplitude of the opening voice (a.u.)	0.99997	0.98352	0.99997	0.98807	0.927	0.96255	0.57190	-	-
The amplitude of the closing voice (a.u.)	0.11887	0.10593	0.13068	0.16257	0.18622	0.26062	0.10599	-	-
Opening time (s)	0.02148	0.02154	0.01804	0.00810	0.01177	0.01183	0.01825	-	-
Closing time (s)	1.03831	1.03948	1.03571	1.02683	1.02833	1.02852	1.03554	-	-
Time difference (s)	1.01683	1.01794	1.01767	1.01873	1.01656	1.01669	1.01729	1.01739	0.00078
Deviation (%)	1.6%	1.8%	1.8%	1.9%	1.7%	1.7%	1.7%	1.74%	0.001%

Figure 42 is the relation of the time differences between function generator settings and sound measurements. We found that the smaller time difference of the function generator is set, the larger deviation becomes. In order to find the accurate time differences between function generator settings and sound measurements, we removed the inaccurate data with setting below 0.01 sec as shown in figure 43. When the function generator gives a signal with a width larger than 0.05 sec, the pulse valve remains open with the same period of time with a deviation lower than 0.022 % shown in table 6.

Table 6: The deviation of the time delay setting.

Time delay setting (s)	1	0.5	0.1	0.05	0.01	0.005	0.004
Deviation (%)	0.001	0.003	0.008	0.022	-	-	-

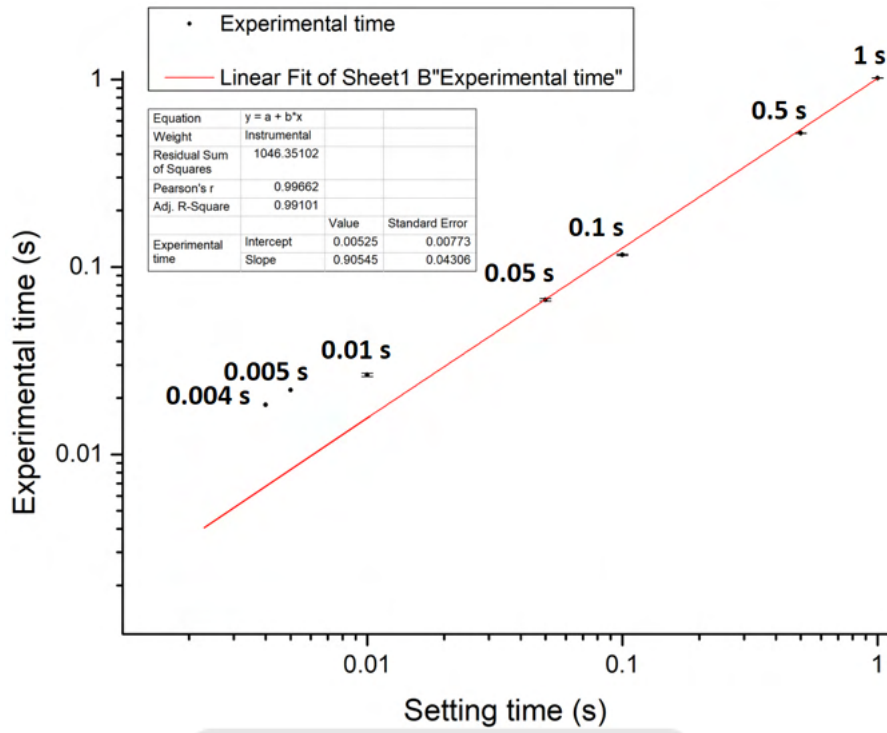


Figure 42: The relation of the time delay between function generator setting and pulsed-valve opening.

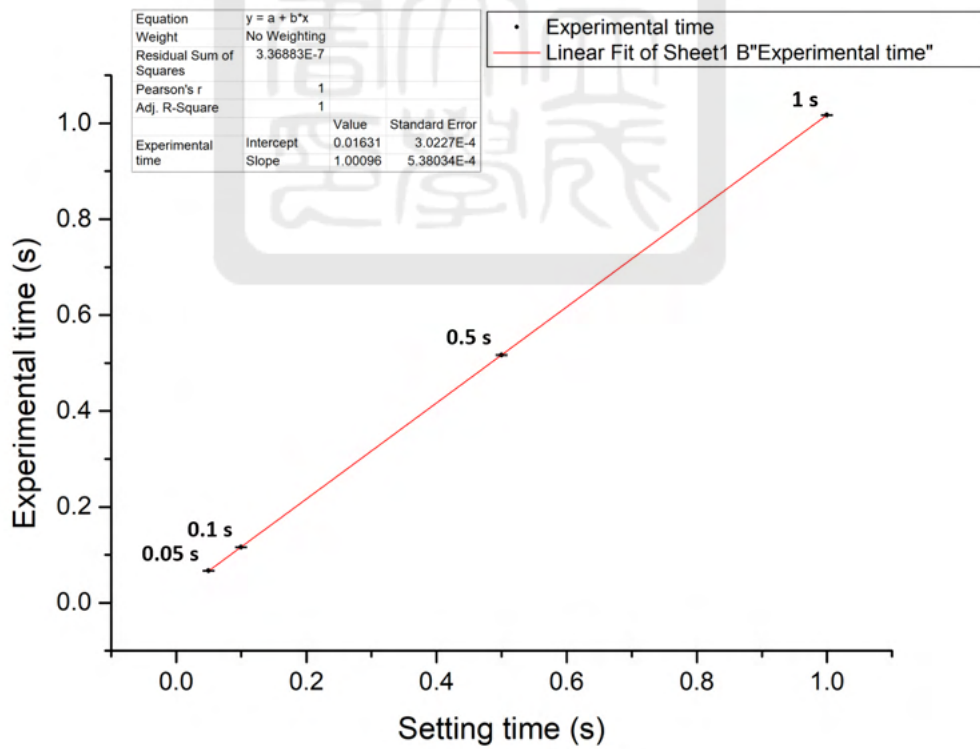


Figure 43: The curve fitting result of the time delay.

3.3 The reservoir system

Figure 44 is the schematic of the reservoir system. The gas (Air or Argon) is provided by the gas cylinder. We use a polyurethane (PU) tube to connect all the devices in this system. The blue ball valve is used to control the gas input. The needle valve behind the ball valve is used to accurately control the flow rates of fluids. To measure the pressure between the pulse valve and the gas cylinder, the gauge is located in the gas line. The safety relief valve is designed to open at a set pressure and depressurizes until the pressure drops below the setting. The black ball valve near the safety relief valve is to release the pressure when we finish our experiments.

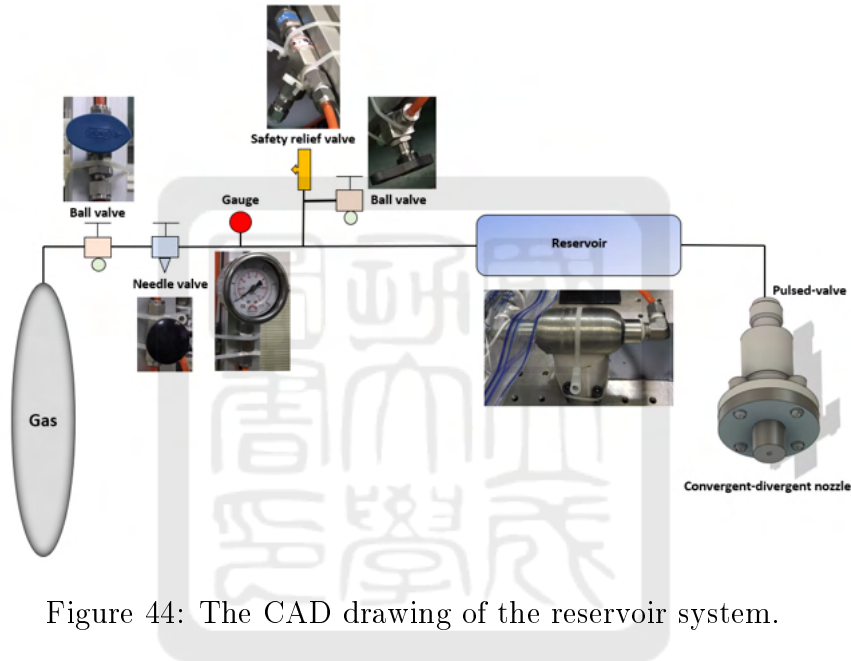


Figure 44: The CAD drawing of the reservoir system.

Figure 45(a) is the reservoir made by Swagelok Corporation and the model is 304L-HDF4-50. It is a double-ended cylinder which is made of 304 stainless steel with an 1800 psig pressure rating. Figure 45(b) is the cross-section drawing of the reservoir with the 1/4 FNPT porting. We use the reservoir to provide the stable pressure for our pulse valve.

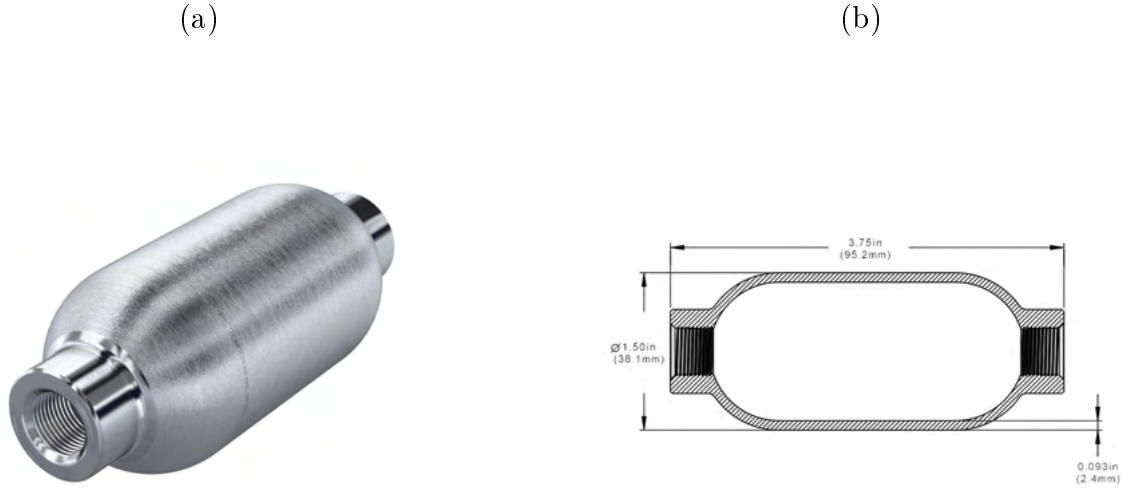


Figure 45: (a) The figure of the reservoir. (b) The cross-section drawing of the reservoir.

In order to know how much gas remained in the reservoir after the pulse valve opens once, we measured the gas exhausting at different pressure setting. We open the 24-V pulse valve for 50 ms and 100 ms. The pressure difference setting was 2, 3, 4, and 5 atm between the reservoir and the atmospheric pressure. We let the gas purge from the reservoir until the pressure went down 0.2 atm. Then, we calculated the number of openings during the process. Therefore, we knew the amount of the gas remained in the reservoir after the pulse valve opened once. Figure 46 is the relation between the amount of remaining gas substance and pressure difference setting. The black dash line was measured when the pulse valve opened at 50 ms for each time. The red solid line was measured when the pulse valve opened at 100 ms each time. When the pressure difference setting becomes larger, the gas remains less in the reservoir. The slope of their curve fitting line in the 50-ms case is almost identical to the 100-ms case. Therefore, we know the gas stably exhausts from the reservoir after the pulse valve opens once.

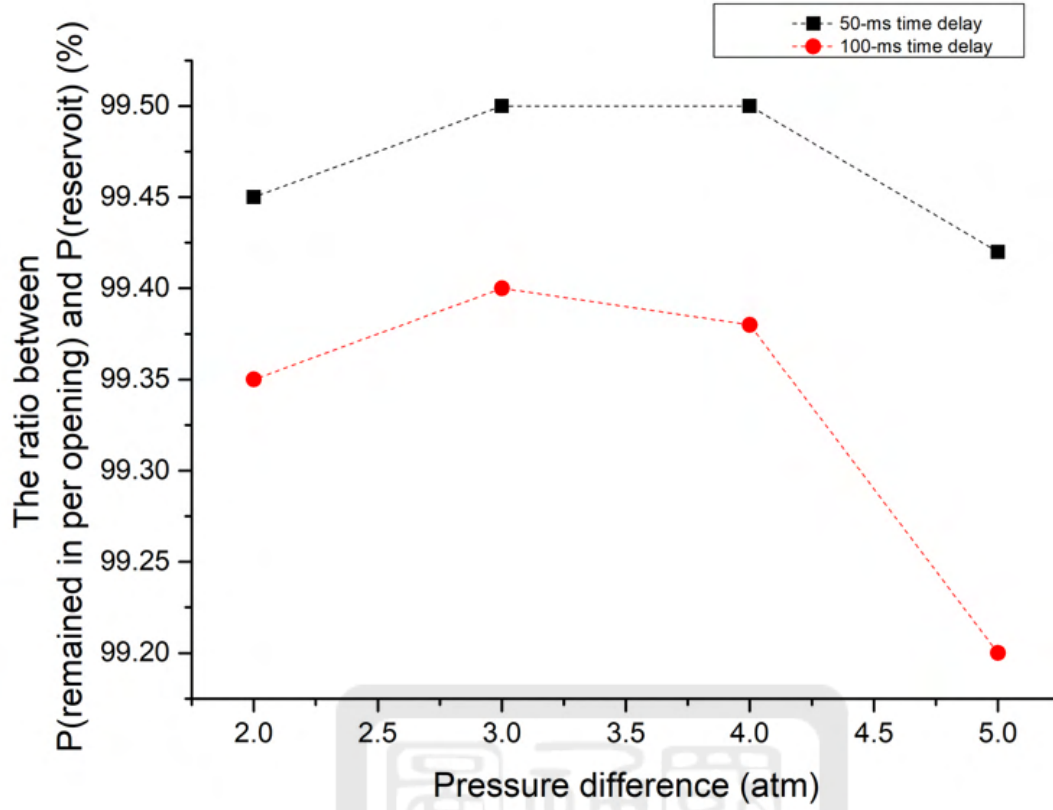
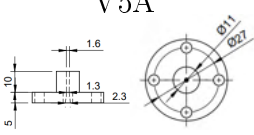
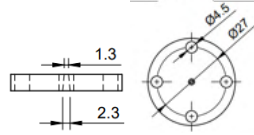
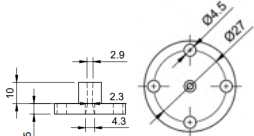
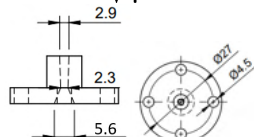
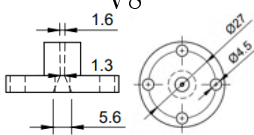


Figure 46: The relation of the air in the reservoir at 50-ms and 100-ms time delay between the amount of gas substance remaining and pressure difference setting.

3.4 The convergent-divergent nozzles(CDN)

In the gas-gun system, we used the convergent-divergent nozzles to generate a supersonic flow. In table 7, there are five versions of the convergent-divergent nozzles. All of them are made of PLA using a 3D printer. Since the 3D printer has about 0.3-mm systematic error between the CAD drawing and the final product, we add 0.3 mm in the CAD drawing. The V5A, V5B, and V6 CDN were used for the 24-V pulse valve. The V7 and the V8 CDNs were used for the 12-V pulse valve. The V6 CDN is 2 times larger than V5A CDN. The V7 CDN is 2 times more than the V8 CDN. The velocity of the gas puff is controlled by the different versions of CDNs.

Table 7: The size of the different convergent-divergent nozzles.

The version of convergent-divergent nozzles	Intake size (unit: mm)	Waist size (unit: mm)	Output size (unit: mm)	Velocity (unit: mach)
V5A 	2	1	1.3	$\Delta P = 5 \text{ atm: } 2.2$ $\Delta P = 10\text{-atm: } 2.2$
V5B 	2	1	none	$\Delta P = 5 \text{ atm: } 1.3$ $\Delta P = 10\text{-atm: } 1.3$
V6 	4	2	2.6	$\Delta P = 5 \text{ atm: } 2.2$ $\Delta P = 10\text{-atm: } 2.2$
V7 	5.3	2	2.6	$\Delta P = 0.5 \text{ atm: } 0.5$ $\Delta P = 1\text{-atm: } 2.2$
V8 	5.3	1	1.3	$\Delta P = 0.5 \text{ atm: } 0.5$ $\Delta P = 1\text{-atm: } 2.2$

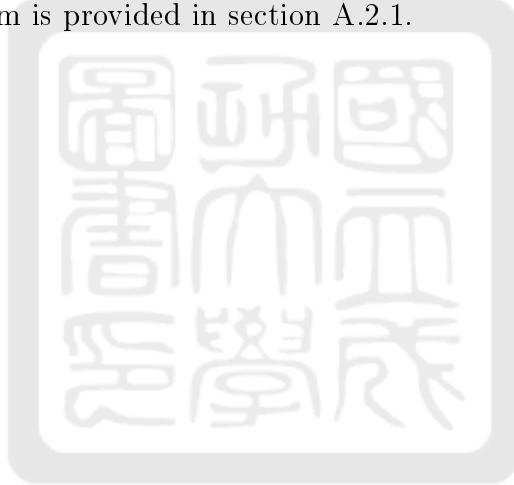
3.5 The procedure of operating the gas-gun system

In order to generate the gas puff, we have developed an operation procedure for it. The procedure is:

- (1) Turn on the function generator, pulse-valve control box, and electrical-to-optical transmitter.
- (2) Set the time width of the square-pulse signal of the function generator.
- (3) Adjust the gas pressure with the reservoir system.
- (4) Deliver the pulse signal to the pulse valve.
- (5) After finishing the experiment, we need to purge the gas in the reservoir system using the ball valve. The detailed procedure of operating the gas-gun system is given in section A.2.1.

3.6 Summary

The gas-gun system includes the pulse-valve system, the reservoir system, and the convergent-divergent nozzles(CDN). The pulse-valve system powered by the 24-V battery has two versions: (1) the 24-V pulse-valve system, and (2) the 12-V pulse-valve system. The 24-V pulse-valve system works with a response time less than 2 ms. The time difference between the opening and the closing is more than 0.05 s and the limit of the pressure difference is 64655 torr. The 12-V pulse-valve system works with an 88-mA current and a 1.06-W power. The limit of the pressure difference of the 12-V pulse-valve system is 450 torr. The reservoir system is used to control the pressure in the gas line and make the outputting pressure stable. Then, we made five versions of the CDN for different experiments. We control the velocity of the gas puff by changing the intake, waist, and output size of the CDNs. Finally, the procedure of operating the gas-gun system is provided in section A.2.1.



4 Schlieren system

In the thesis, we are studying gas puff in the EUV light source using a theta pinch. In order to study the gas puff, we built a Schlieren system. The design of the Schlieren system is shown in section 4.1. We adjusted the light path of the Schlieren system to improve the quality of the Schlieren images. Therefore, the improvement of the Schlieren system will be introduced in section 4.2. A summary is given in Section 4.3.

4.1 The design of the Schlieren system

In the first goal, we would like to synchronize the time of the plasma-plume generation and the time of the theta pinch. Therefore, the propagating speed of the gas puff needs to be measured. The price of the high-speed camera is so expensive that we use the 10-kHz optical chopper to build the high-speed Schlieren system as shown in Figure 47. A continuous-wave (CW) He-Ne laser is used as the light source. Then, the 10-kHz optical chopper converts the CW light source to pulses for the Schlieren system. The convex lenses are used to control the beam size of the light source. The knife-edge is set at the con-focal point of the second sets of a convex lens. It is used to block parts of the light which is refracted by the gas puff and enhance the image of the edge of the gas puff. Figure 48(a) is the schematic of the signal of the gas puff without the knife edge and Figure 48(b) is the schematic of the signal of the gas puff with the knife edge. The edge of either the plasma plume or the gas puff becomes obvious due to the higher density gradient. As long as edges from two snapshots do not overlap with each other, they can be distinguished from each other even if two snapshots are recorded on the same image. Finally, a series of the Schlieren images with a $100\text{-}\mu\text{s}$ time difference between each image overlap on the screen. We can measure the distance between two edges and adjust the motor's rotation speed to get the propagating speed of the plasma plume or gas puff. The formula of the propagating speed V is:

$$V = \frac{\Delta S}{\Delta t} = \Delta S \cdot f \quad (18)$$

where ΔS is the distance between two edges and f is the frequency of the optical chopper.

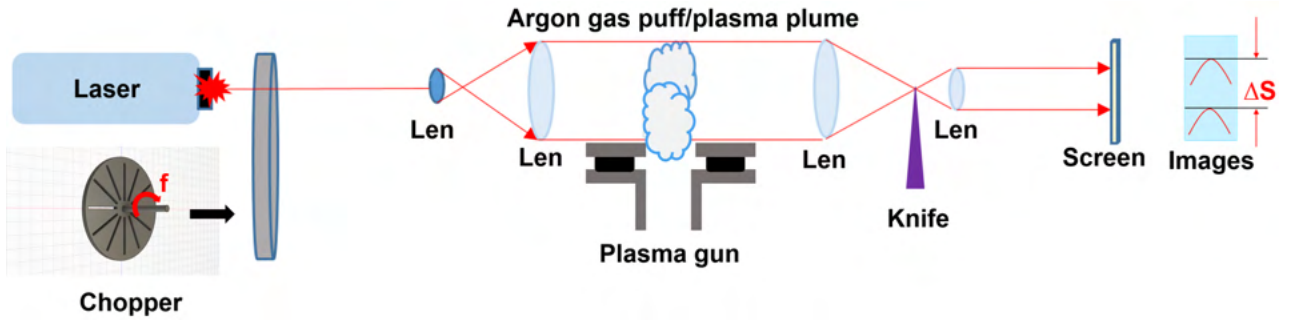


Figure 47: The optical pathway diagram of the Schlieren system.

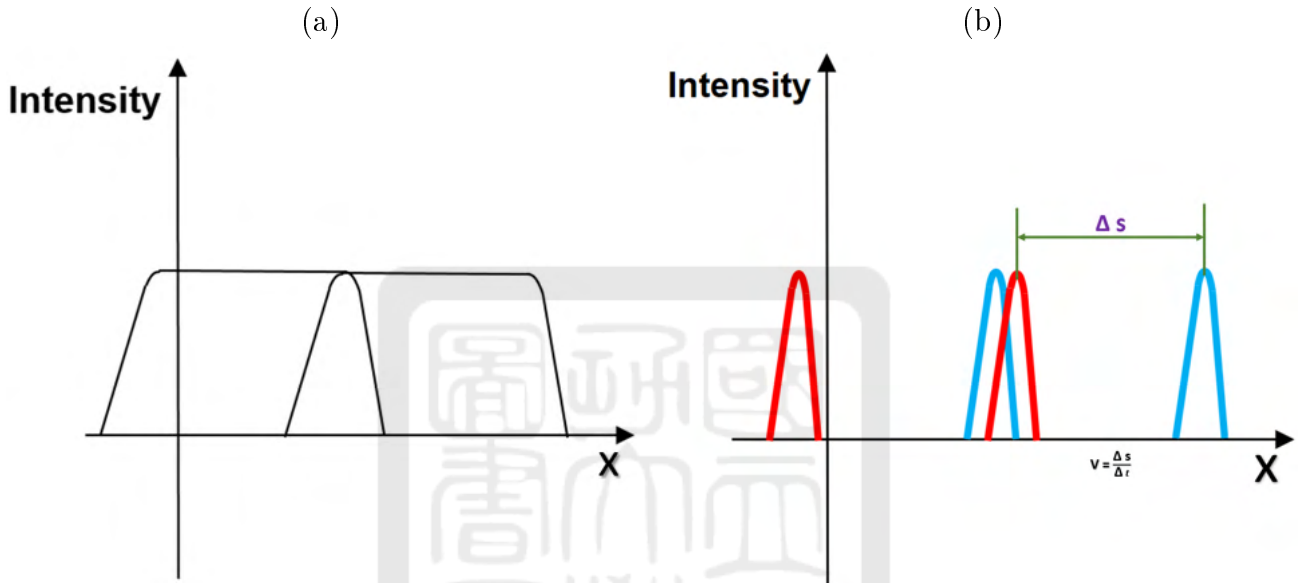


Figure 48: (a) The schematic of the signal of the gas puff without the knife edge. (b) The schematic of the signal of the gas puff with the knife edge.

4.2 The improvement of the Schlieren system

When we started our experiments, we encountered two problems of our pulse valves:

- (1) The output size of the 24-V pulse valve was so small that the structure of the gas puff was too small and was hard to be observed.
- (2) The pressure difference between the reservoir and the outlet of the 12-V pulse valve was so low that the density gradient of the gas puff was too small so that the Schlieren image was not clear.

According to both of the problems we met, we focused on studying the change of the gas puff which was from the pulse valve in different conditions. The 24-V pulse valve was used for the gas puff generator here. In order to focus on improving the quality of the Schlieren image, the optical chopper was not used. In addition, convergent-divergent nozzles were attached to

the outlet of the pulse valve to accelerate the gas puff. The convergent-divergent nozzles are introduced in Chapter 3.

Nine versions of the Schlieren system are introduced as follows:

(1) Figure 49(a) is the 1st schlieren setup using the continuous wave He-Ne laser. Figure 49(b) is the image of the 1st setup. The white arrows show the propagating way of the gas puff. The image was not well focused and spherical diffraction patterns are shown in the background. The spherical patterns interfere with the target signal.

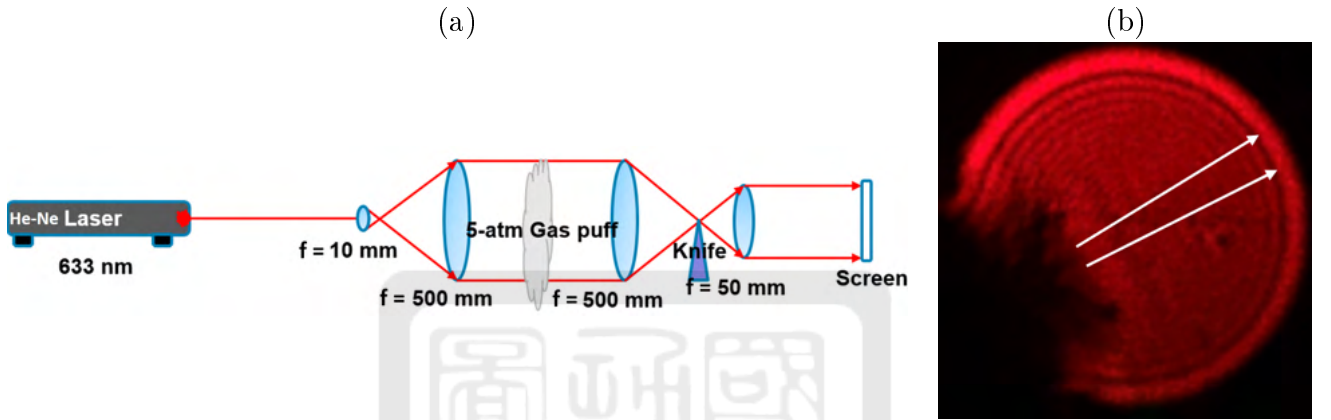


Figure 49: (a) Schematic of the first version of the experimental setup. (b) The first version of the Schlieren image of the gas puff.

(2) In order to enhance the contrast and make the size of the light beam larger, we replaced the He-Ne laser with a flashlight. The flashlight was a broadband light source and used the white light-emitting diode (LED). We added a mirror so that the optical path was not constrained by the length of the optical table as shown in Figure 50(a). Figure 50(b) is the second version of the Schlieren image of the gas puff. We can find the shadow of the gas puff in the red area but the image is blurry. The white LED emitted lights in different wavelengths. Figure 51 is the schematic of chromatic aberration. Different colors have different focal lengths so that images of different wavelengths are at different locations. We also observed the chromatic aberration in the background.

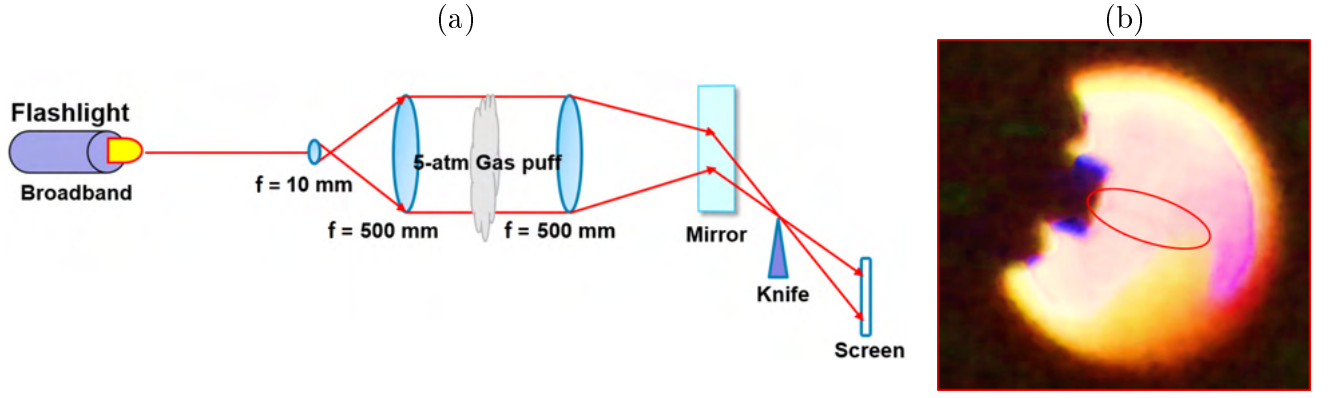


Figure 50: (a) Schematic of the second version of the experimental setup. (b) The second version of the Schlieren image of the gas puff.

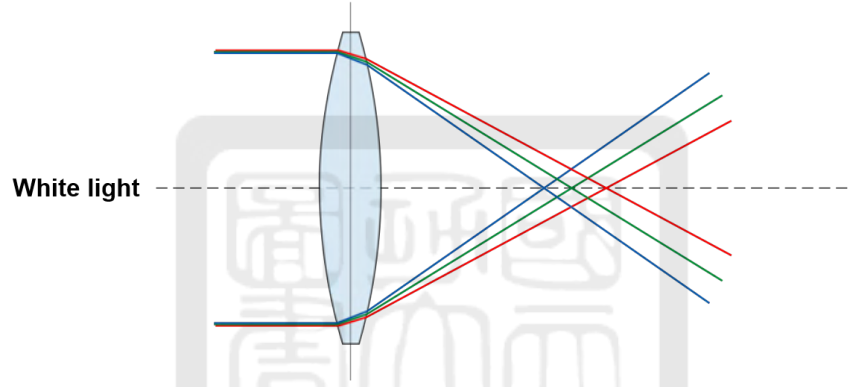


Figure 51: Schematic of chromatic aberration.

(3) Figure 52(a) is the schematic of the third version of the experimental setup. We used a blue LED instead of the flashlight to solve the chromatic aberration issue. In order to make the optical path simpler, the plano-convex lens with a 10-mm focal length and the mirror were removed. Unfortunately, the blue LED light was too weak. In Figure 52(b), we couldn't see the image of the gas puff near the output of the 24-V pulse valve.

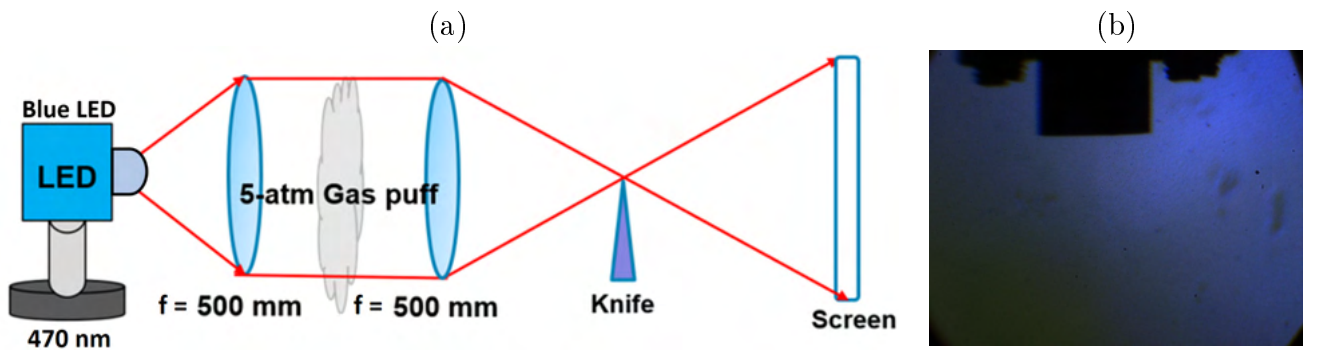


Figure 52: (a) Schematic of the third version of the experimental setup. (b) The third version of the Schlieren image of the gas puff.

(4) In the third version experimental setup, the blue LED light was so weak that the schlieren image was difficult to be observed. Therefore, the white LED was used as the light source again. An iris right in front of the LED was used to control the size of the light source as shown in Figure 53(a). In the past versions, the schlieren images were observed on the screen. In order to take the schlieren images easier and clearer, we replaced the screen with a CMOS Camera with a 50-mm plano-convex lens. In Figure 53(b), chromatic aberration still occurred in the background. Nevertheless, the fourth version of the Schlieren image of the gas puff in this version was brighter than that in the third version.

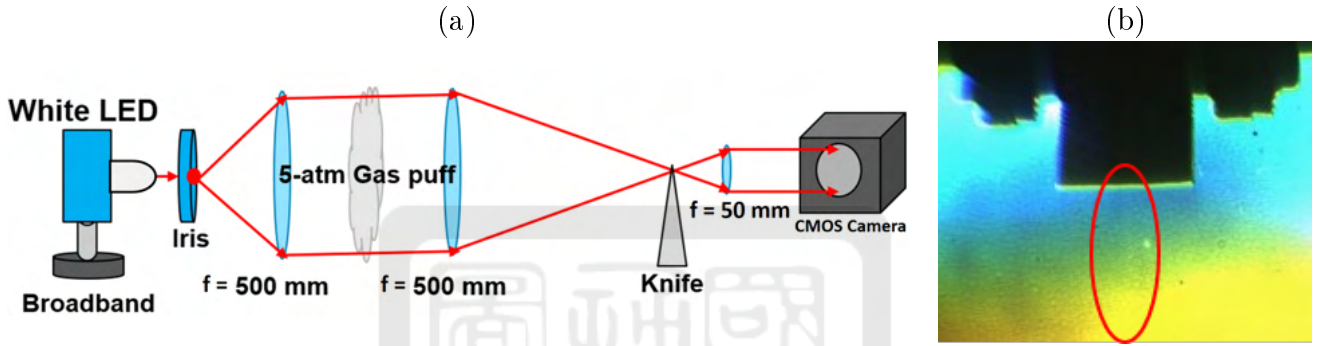


Figure 53: (a) Schematic of the fourth version of the experimental setup. (b) The fourth version of the Schlieren image of the gas puff.

(5) Figure 54(a) is the schematic of the fifth version of the experimental setup. We replaced the 50-mm lens with the f-50-mm camera lens to focus the object more conveniently. We also flipped the plano-convex lens from Figure 55(a) to Figure 55(b). The shadow of the 24-V pulse valve was clearer than the previous version. However, the background had color variation due to the chromatic aberration. The schlieren image of the gas puff within the red solid line range was blurry as shown in Figure 54(b).

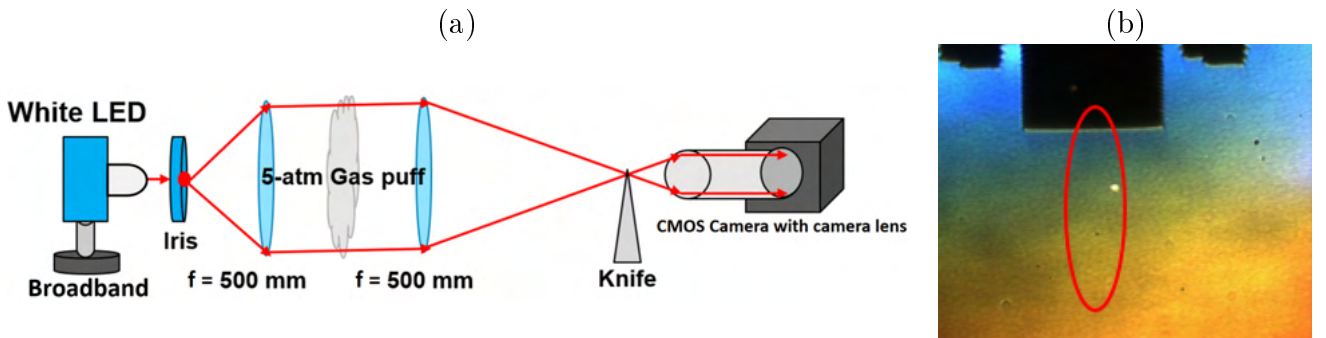


Figure 54: (a) Schematic of the fifth version of the experimental setup. (b) The fifth version of the Schlieren image of the gas puff.

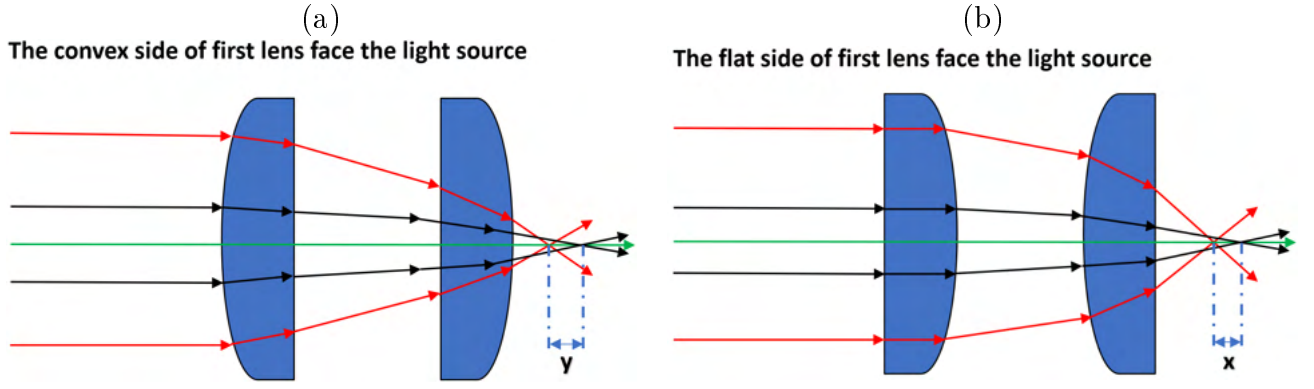


Figure 55: (a) The convex side of first lens face the light source. (b) The flat side of first lens face the light source.

(6) Figure 56 is the schematic of the sixth version of the experimental setup. In order to remove chromatic aberration, we replaced the white LED with the green LED. The wavelength of the green LED was 527 nm. Because our plano-convex lenses don't have anti-reflective coatings, Newton's rings occurred in the background as shown in Figure 57(a). We had the knife oriented horizontally try to observe the schlieren images with vertical density jump, i.e., the front edge of the gas puff. However, the propagating speed of the gas puff was so fast in our experiment that we couldn't catch the front edge of the gas puff. Therefore, we try to analyze the horizontal line profile of the image as shown in Figure 57(b). We couldn't see the (side) edge of the gas puff.

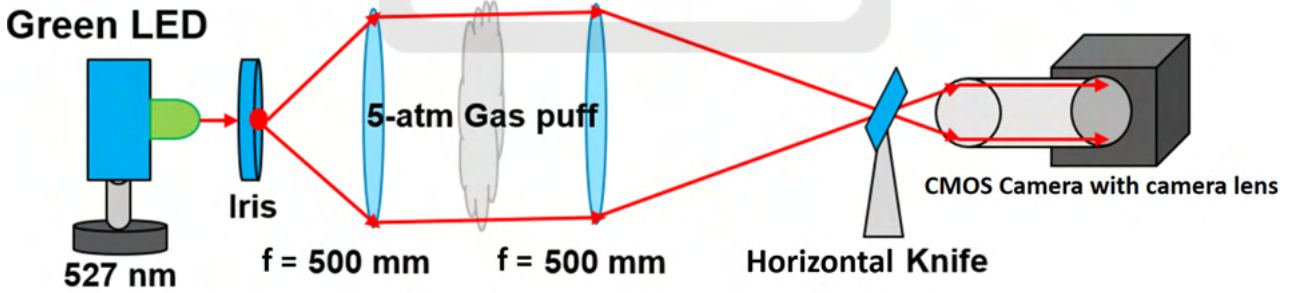


Figure 56: Schematic of the sixth version of the experimental setup.

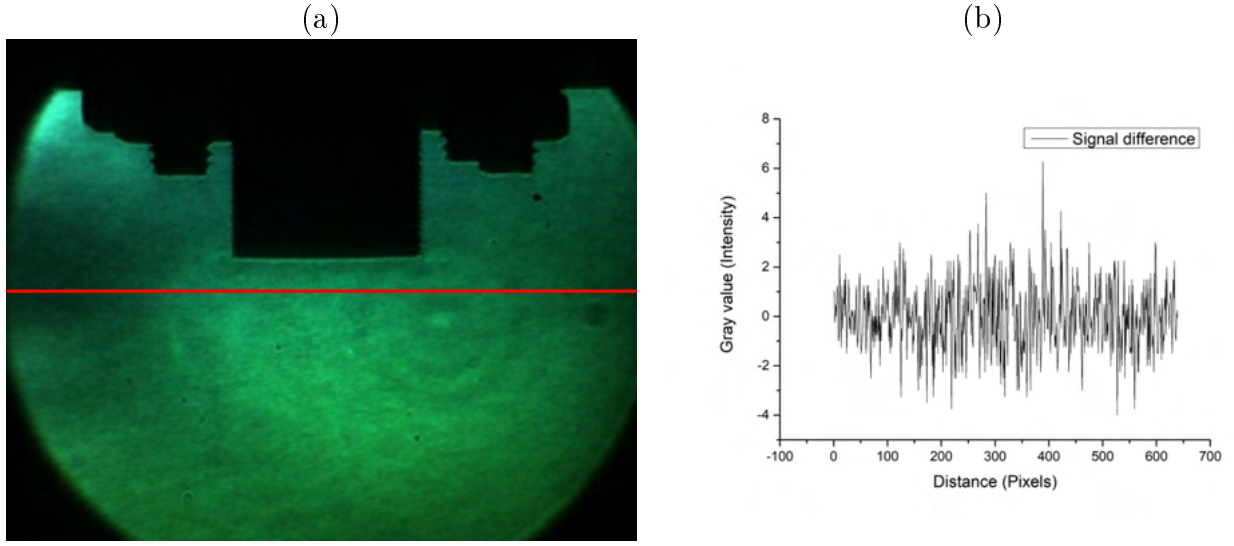


Figure 57: (a) The sixth version of the Schlieren image of the gas puff. (b) The horizontal line profile of the seventh version of the image.

(7) Figure 58 is the schematic of the seventh version of the experimental setup. The signal intensity of the previous data was weak. In order to enhance the sensitivity of the schlieren system, we removed the Iris and the first 500-mm plano-convex lens to let the light beam larger. The blocking area of the knife can become larger due to the large light beam. Since our schlieren system couldn't catch the front edge of the gas puff, we switched back to observing the horizontal density variation by having the knife oriented vertically. In Figure 59(a), the horizontal variation of the gas puff was clearer. We also fine-tuned an angle of the plano-convex lens to move Newton's ring away from our view. Finally, the gas-puff structure showed up on the horizontal profile. The amplitude of the gas-puff signal was much higher than the background noise as shown in Figure 59(b).

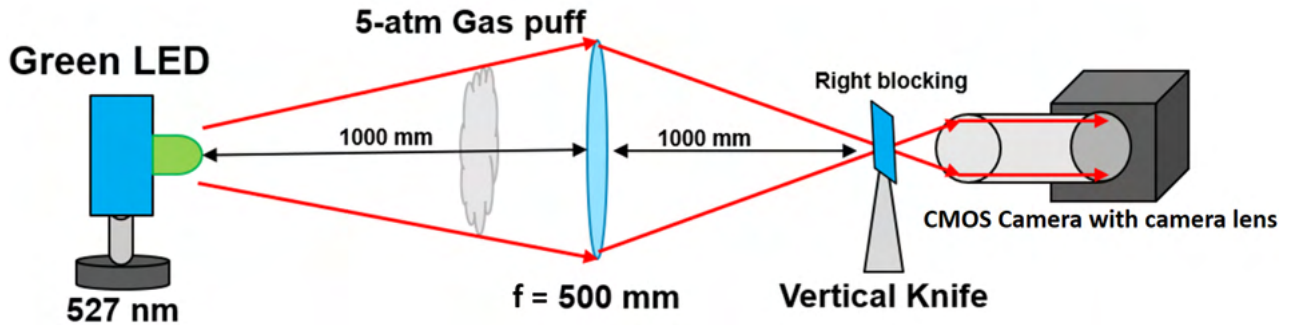


Figure 58: Schematic of the seventh version of the experimental setup.

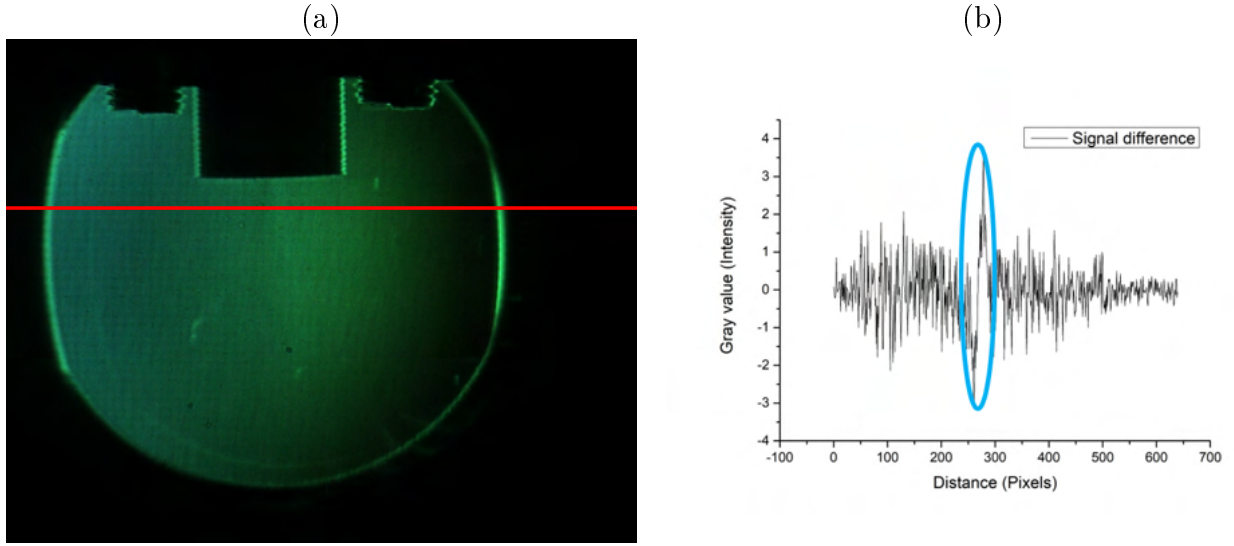


Figure 59: (a) The seventh version of the Schlieren image of the gas puff. (b) The horizontal line profile of the seventh version of the image.

(8) Figure 60 is the schematic of the eighth version of the experimental setup. In this version, we tried to make the schlieren images larger so that the signal of the schlieren images can be observed easier. Therefore, the 24-V pulse valve was moved to 420 mm from the plano-convex lens. In Figure 61(a), the size of the 24-V pulse valve and the gas puff in the schlieren image are significantly larger than those in Figure 59(a). The vertical knife was set on the left side of the image of the Green LED. In Figure 61(b), the peak of the signal appears at the inversed side compared with Figure 59(b).

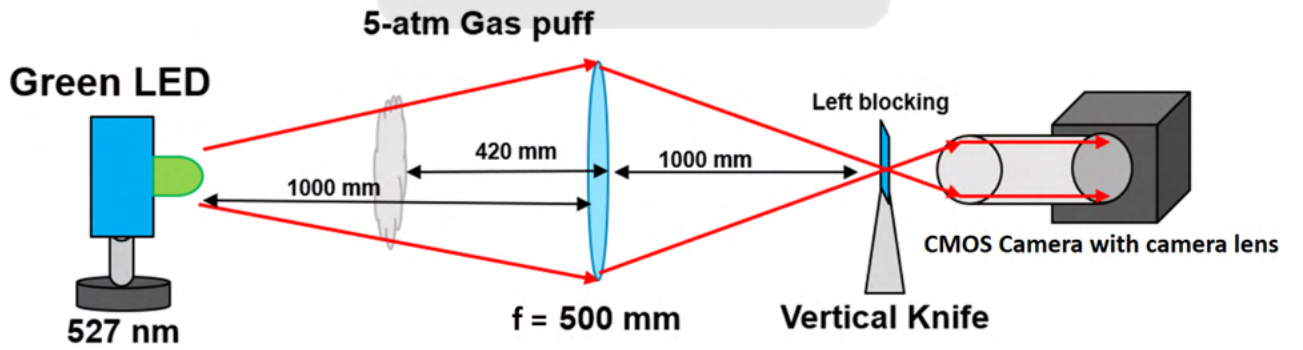


Figure 60: Schematic of the eighth version of the experimental setup.

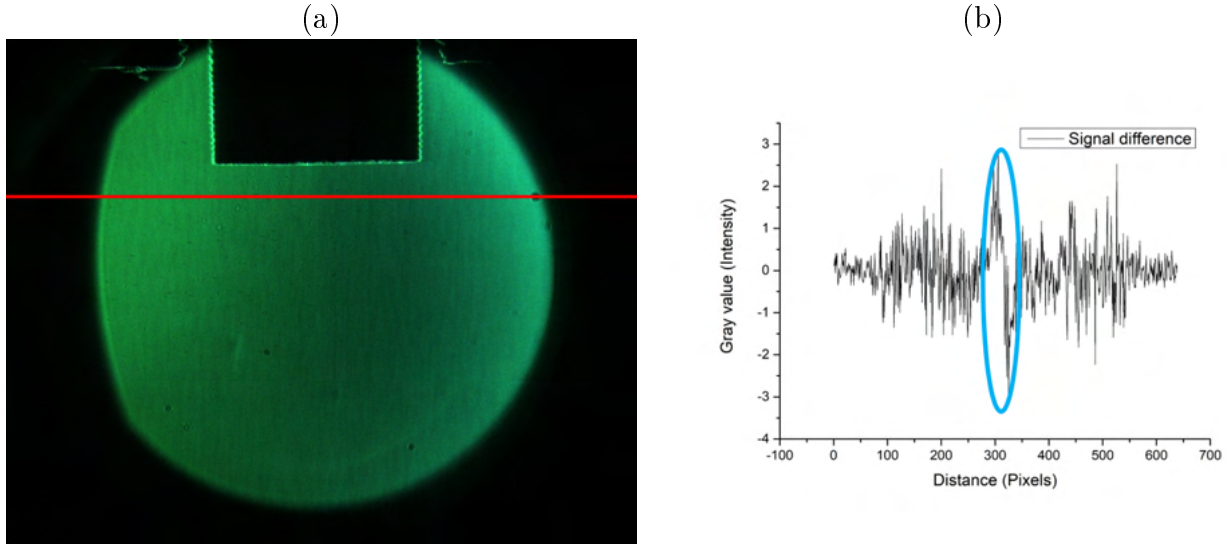


Figure 61: (a) The eighth version of the Schlieren image of the gas puff. (b) The horizontal line profile of the eighth version of the image.

(9) The results of the eighth version experimental setup did not enhance the intensity of the signal. Therefore, the 24-V pulse valve was moved to 200 mm from the plano-convex lens as shown in Figure 62. Figure 63 (a) is the ninth version of the schlieren image of the gas puff. The schlieren image of the gas puff became clear. Moreover, the amplitude of the gas-puff signal was two times larger than the previous version in Figure 61 (b). This was the final Schlieren system setup we used for the result of the work.

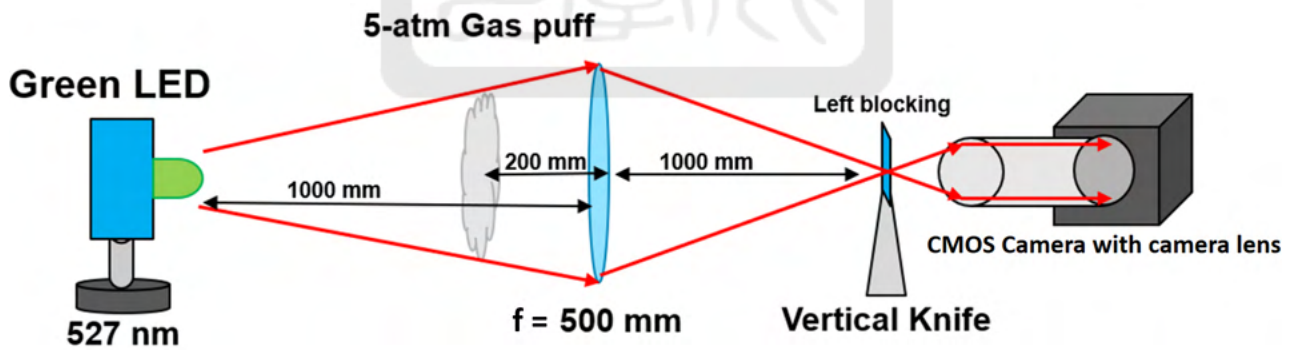


Figure 62: Schematic of the ninth version of the experimental setup.

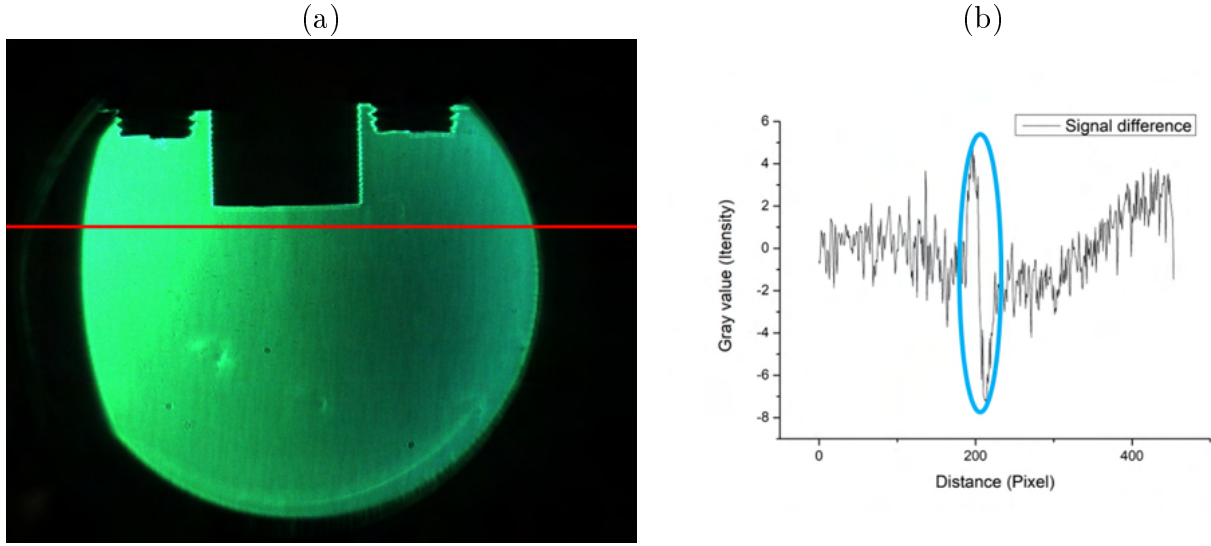


Figure 63: (a) The ninth version of the Schlieren image of the gas puff. (b) The horizontal line profile of the ninth version of the image.

4.3 Summary

Schlieren system was used in our experiments. We used this system to observe the gas puff. We solved many problems such as chromatic aberration and Newton's ring. The chromatic aberration was removed by using monochromatic light. Newton's rings were removed by tilting the lens with a small angle. In order to make the sensitivity of the Schlieren system higher, we used a green LED with finite size. Furthermore, we found that the signal of the 24-V pulse valve at 200 mm from the plano-convex lens was two times stronger than the signal of the 24-V pulse valve at 420 mm from the plano-convex lens. Therefore, we have the pulse valve at 200 mm from the plano-convex lens, green LED as the light source for the rest of experiments.

5 Experimental results

In order to study the gas puff, we analyzed the schlieren image to obtain the opening angle of the gas puff. Then, we made comparisons between different conditions. In subsection 5.1, the analyzing procedure is given. In subsection 5.2, the experimental results using a 24-V pulse valve are given. In subsection 5.3, the experimental results using a 12-V pulse valve are given. Finally, the summary is given in section 5.4.

5.1 Analyzing procedure

From all images we got, we obtained the width of the gas puff, the opening angle of the gas puff, the tilted angle of the Convergent-divergent nozzle (CDN), and the contrast of the differential image. We use the experimental setup with a 12-V pulse valve, V8 convergent-divergent nozzle, vertical schlieren knife, and 1-atm pressure difference as an example to explain the analysis procedure.

5.1.1 Width of the gas puff

We follow the following steps to obtain the width of the gas puff.

(1) From the video we take, we extract one frame of the video before the pulse valve is opened as shown in figure 64(a). It is used as the background. Then, we extract one frame of the video after the pulse valve is open as shown in figure 64(b). In figure 64(b), we can observe the gas puff near the output of the CDN.

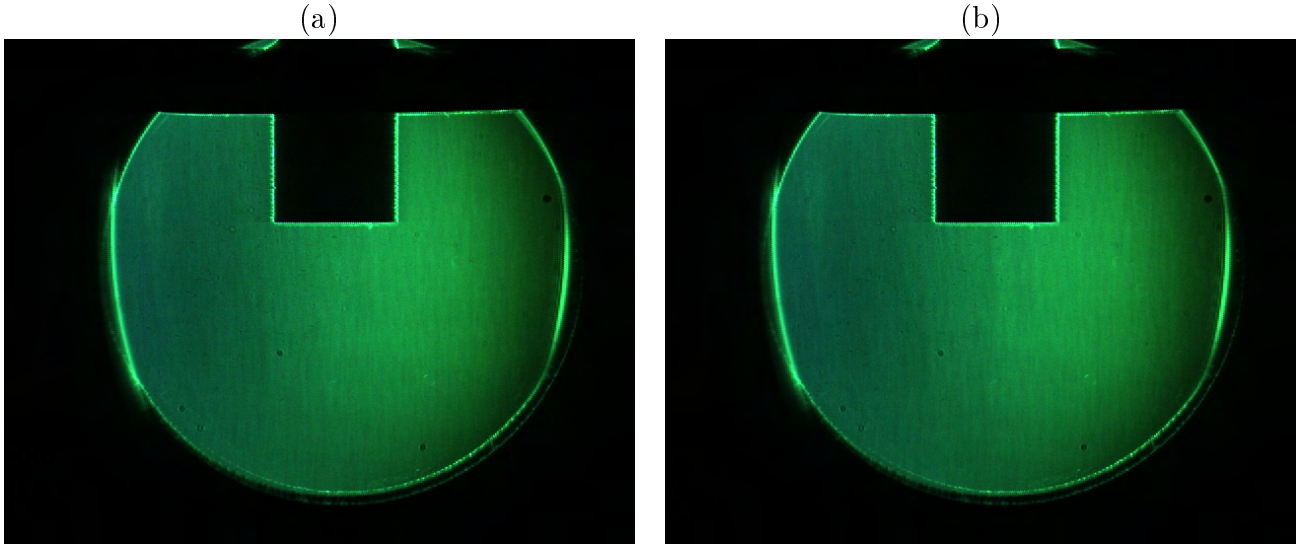


Figure 64: (a) The RGB-scale of the schlieren image without gas puff. (b) The RGB-scale of the schlieren image with gas puff.

(2) We convert the schlieren images from RGB-scale to grayscale as shown in figure 65(a) and figure 65(b).

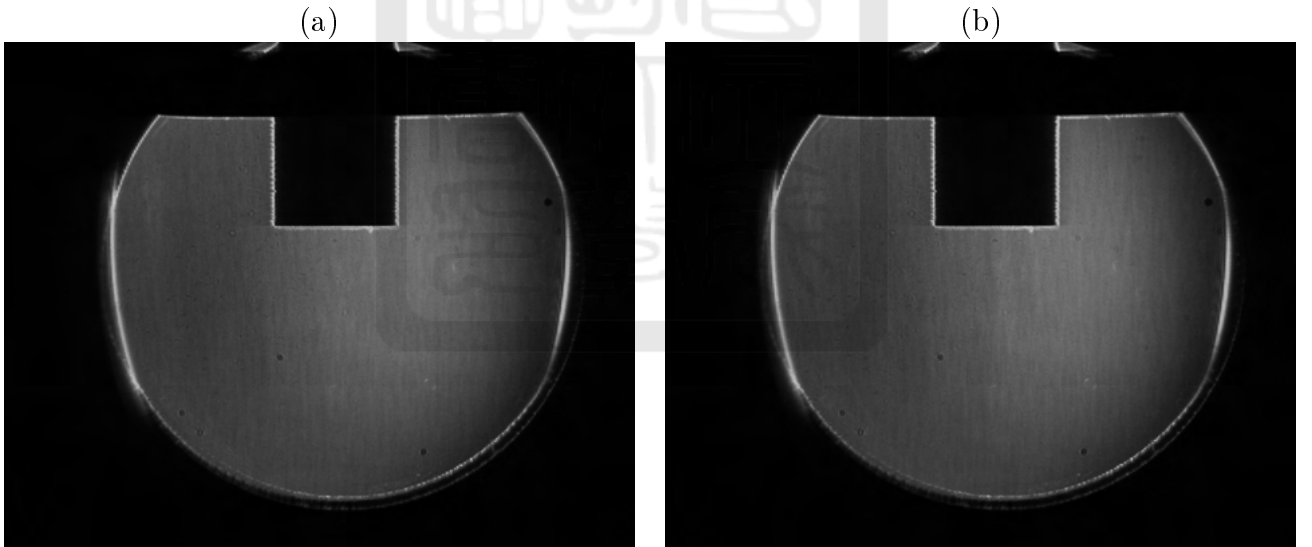


Figure 65: (a) The grayscale of the schlieren image without gas puff. (b) The grayscale of the schlieren image with gas puff.

(3) We use Matlab to generate the differential image in the double-precision value from substrating figure 65(a) from figure 65(b) as shown in figure 66. The gas puff is clear. Since the knife-edge blocked parts of the light refracted by the gas puff from the side, the image of the gas puff has a dark side and a bright side.

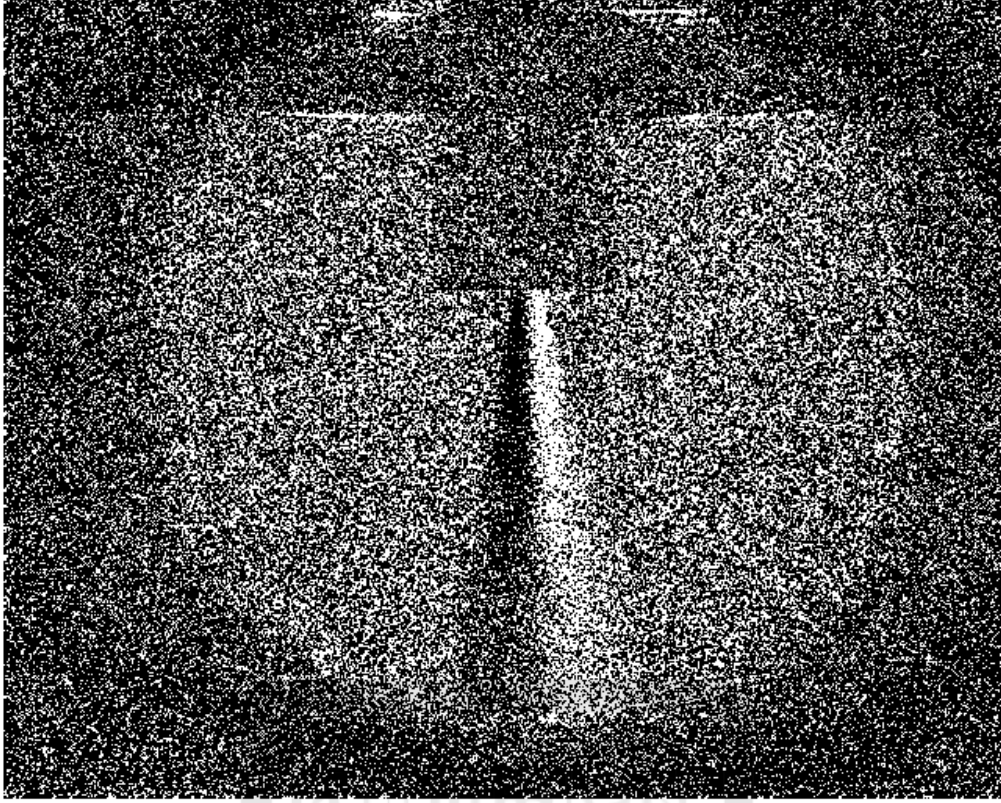


Figure 66: The double-precision value of the differential image.

(4) We get horizontal profiles along red lines at different heights in figure 67(a). For example, the profile along the red solid line at 190 pixels is shown in figure 67(b). All profiles along different red lines are analyzed.

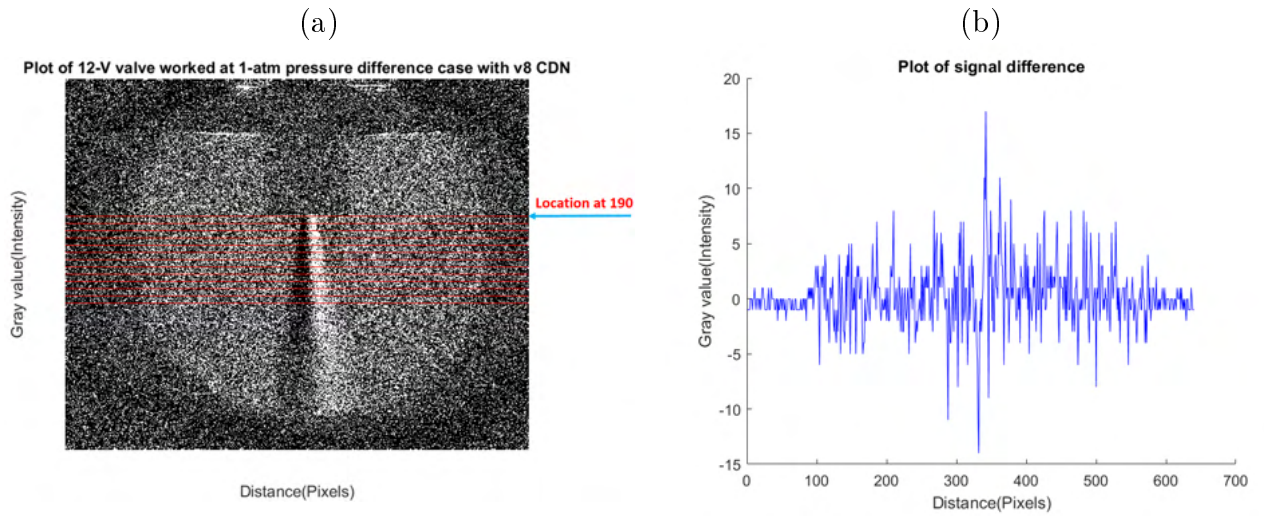


Figure 67: (a) The horizontal line profiles of the image. (b) The intensity signal difference of the image at 190 pixels.

After getting the profiles, we would like to determine the characteristic of the gas puff. Therefore, we mark the gas puff region in orange in figure 68 by eyes.

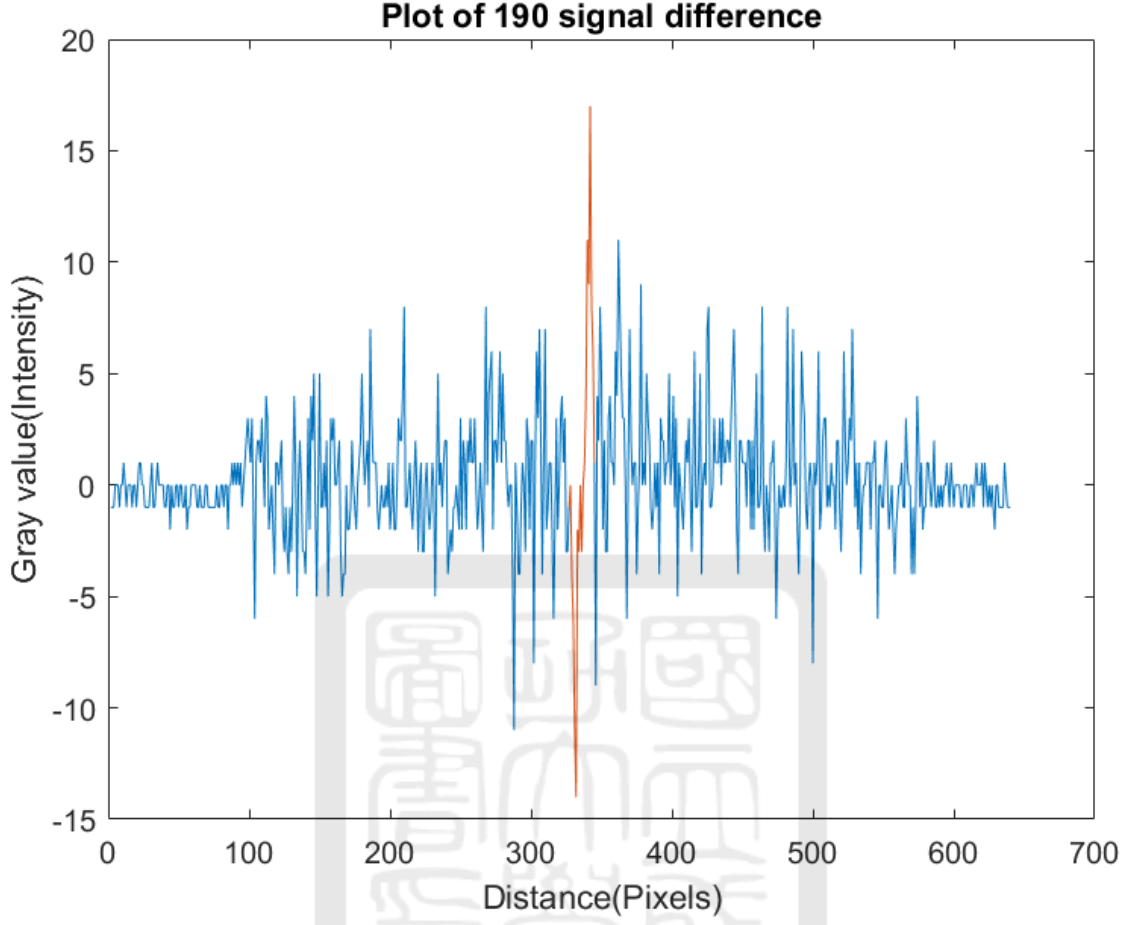


Figure 68: The target wave of the intensity signal difference.

(5) In order to find the minimum of the orange profile in figure 68, we mark the valley of the profile and use a Gaussian function to fit the valley as shown in figure 69(a). The Gaussian function is as follow:

$$y = y_0 + Ae^{-\frac{(x-x_c)^2}{2\sigma^2}} \quad (19)$$

where y_0 is the background intensity, A is the amplitude of the Gaussian function, σ is the width of the Gaussian function and x_c is the center of the Gaussian function. The peak is defined as y_0+A . The fitting result of the Gaussian function is shown as the red solid line in figure 69(b) while the black solid line is the raw data. The minimum appears at 331.5 ± 0.1 pixels and the corresponding intensity is -13 ± 2 (a.u.).

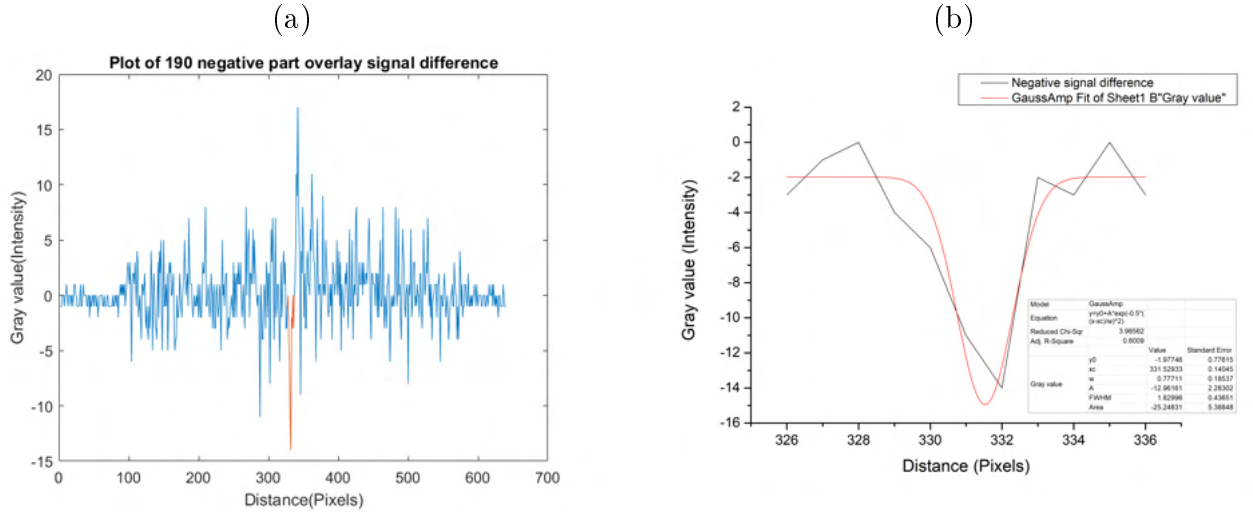


Figure 69: (a) The valley of the target wave. (b) The curve fitting result of the valley.

(6) We use the same way to find the maximum. Figure 70(a) is the peak region of the orange profile. The peak of the profile is marked and fit by using the Gaussian function as shown in figure 70(b). The maximum appears at 341.6 ± 0.3 pixels and the corresponding intensity is 16 ± 3 (a.u.).

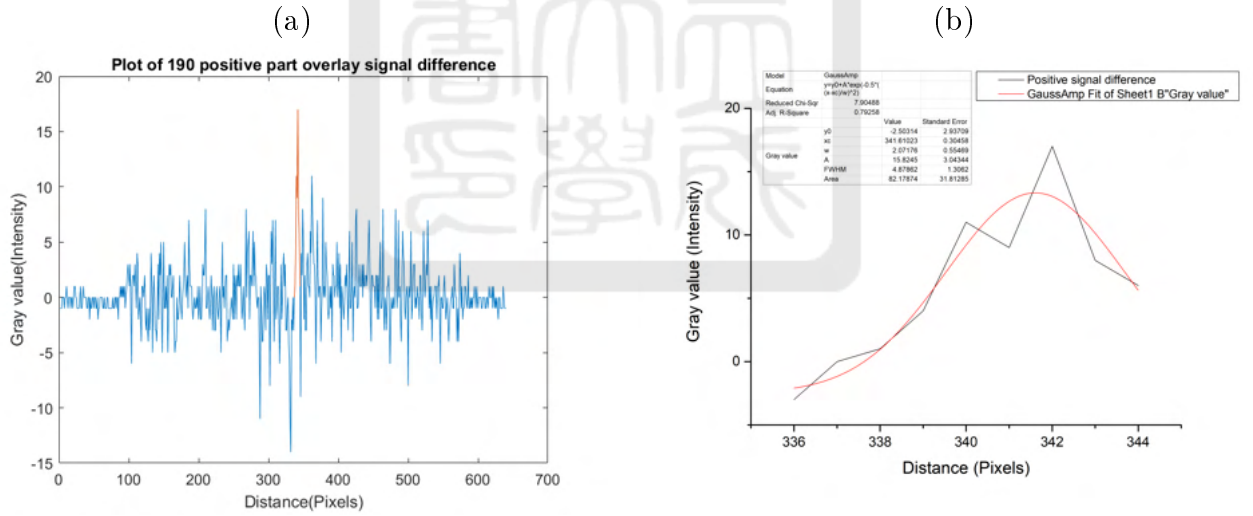


Figure 70: (a) The peak of the target wave. (b) The curve fitting result of the peak.

(7) We combine the fitting result of the valley with the peak region as the blue line in figure 71(a). The raw data is shown as the orange curve in figure 71(a). Figure 71(b) is the curve fitting result. The distance between the peak and the valley is 10.1 ± 0.4 pixels. It is the width of the gas puff at that specific height represented in pixels.

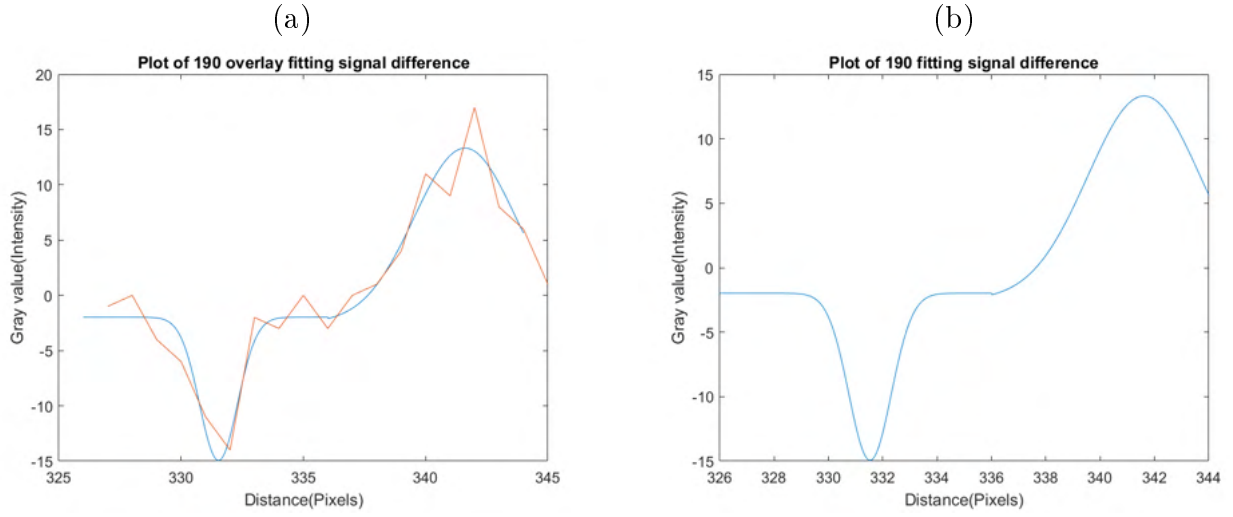


Figure 71: (a) The curve fitting result overlay with the original wave. (b) The curve fitting result of the target wave.

(8) In order to convert pixels into minimeters, the size between two side edges of the CDN in pixels is measured by the original grayscale schlieren image in step (2)(Figure 65(a)). The red horizontal line in figure 72(a) indicates the line of profile we use to obtain the conversion ratio between the physical size and the pixel numbers. The profile along the red line is shown in figure 72(b). The boundaries of the CDN have higher intensity signal as shown in figure 72(b). The first peak of the boundary of the CDN appears at 274 pixels and the intensity signal is 199 a.u.. Furthermore, the second peak of the boundary of the CDN appears at 400 pixels and the intensity signal is 205 a.u.. The distance between two peaks is 126 pixels while the physical size between two side edges of the CDN is 11 mm. Therefore, the conversion ratio of pixels to minimeters is 0.087 mm/pixels.

(9) The width of the gas puff at the specific height is 0.88 ± 0.03 mm using the conversion ratio obtained in step (8).

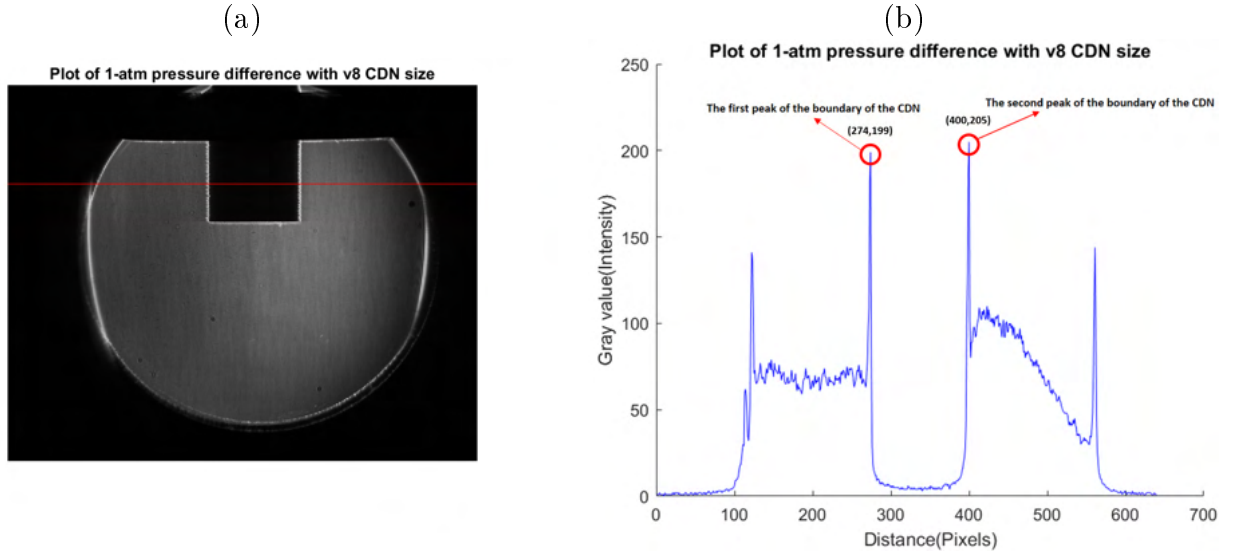


Figure 72: (a) The horizontal line profile of the Convergent divergent nozzles (CDN). (b) The intensity signal difference of the Convergent divergent nozzles (CDN).

5.1.2 Opening angle of the gas puff

In order to measure the opening angle of the gas puff, the half width of the gas puff in each horizontal line profile needs to be calculated using Eq. 20,

$$\text{Half-width} \equiv \frac{\Delta X}{2} \equiv \frac{|X_{\min} - X_{\max}|}{2} \quad (20)$$

where X_{\min} is the position of the minimum obtained in step (5) in section 1.1.1 and X_{\max} is the position of the maximum obtained in step (6) in section 1.1.1. After we get the half width of the gas puff in each horizontal line profile, the opening angle can be measured by the slope of the gas-puff path using Eq. 21.

$$\theta = \arctan\left(\frac{\frac{\Delta X}{2}}{z_{\text{axis}}}\right). \quad (21)$$

The red solid line in Figure 73 is the fitted slope of the propagating path of the gas puff. Each data point corresponds to the half width of each horizontal line profile with the standard deviation as the error bar. The slope of the propagating path of the gas puff is 0.05 ± 0.02 . The opening angle of the gas puff is $2.86^\circ \pm 1.15^\circ$.

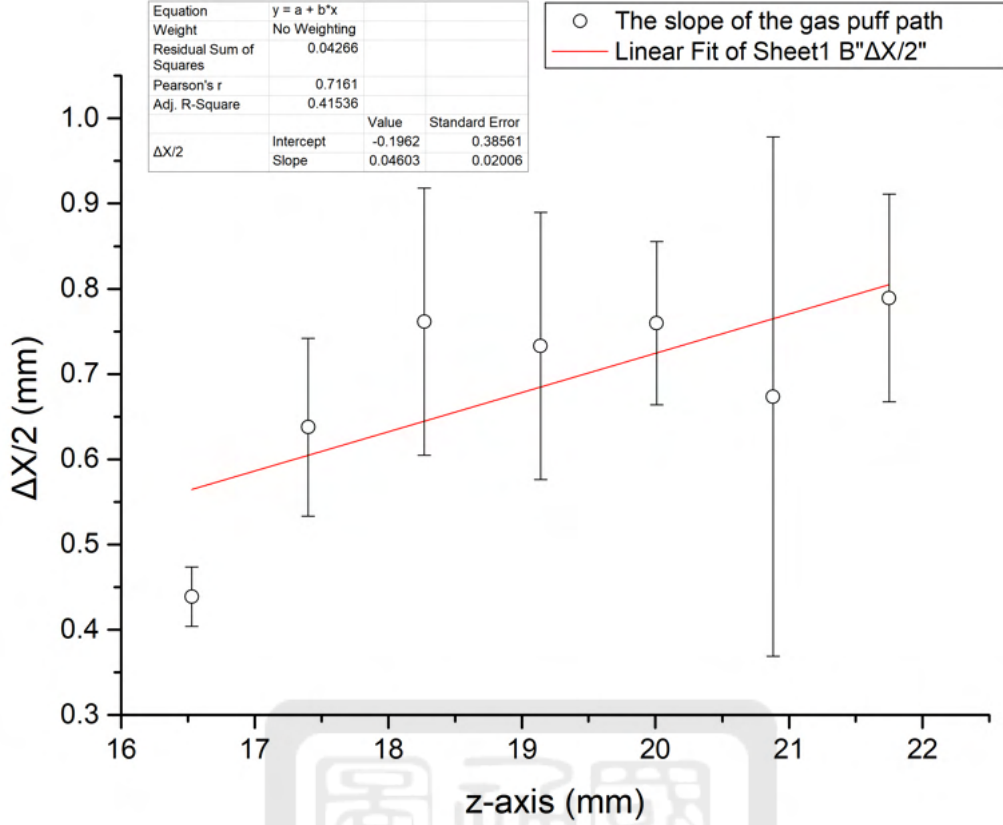


Figure 73: The slope of the propagating path of the gas puff.

5.1.3 Tilted angle of the Convergent-divergent nozzle (CDN)

Besides the opening angle of the gas puff, we consider the tilted angle of the CDN as the angle of the center of the gas puff. Before we measure the angle of the center of the gas puff, the center of the horizontal line profile needs to be calculated by using Eq. 22,

$$\text{Center} \equiv X_C \equiv \frac{X_{\min} + X_{\max}}{2} \quad (22)$$

where X_{\min} is the position of the minimum obtained in step (5) in section 1.1.1 and X_{\max} is the position of the maximum obtained in step (6) in section 1.1.1. After we get the center of each horizontal line profile, the tilted angle of the CDN can be calculated by the slope of the gas-puff center using Eq. 23,

$$\theta = \arctan\left(\frac{X_C}{z_{\text{axis}}}\right). \quad (23)$$

Figure 74 is the slope of the propagating center of the gas puff. Each data point corresponds to the center of each horizontal-line profile with the standard deviation as the error bar. The slope of the propagating center of the gas puff is -0.01 ± 0.03 . The calculated tilted angle of the CDN is $-0.57^\circ \pm 1.72^\circ$.

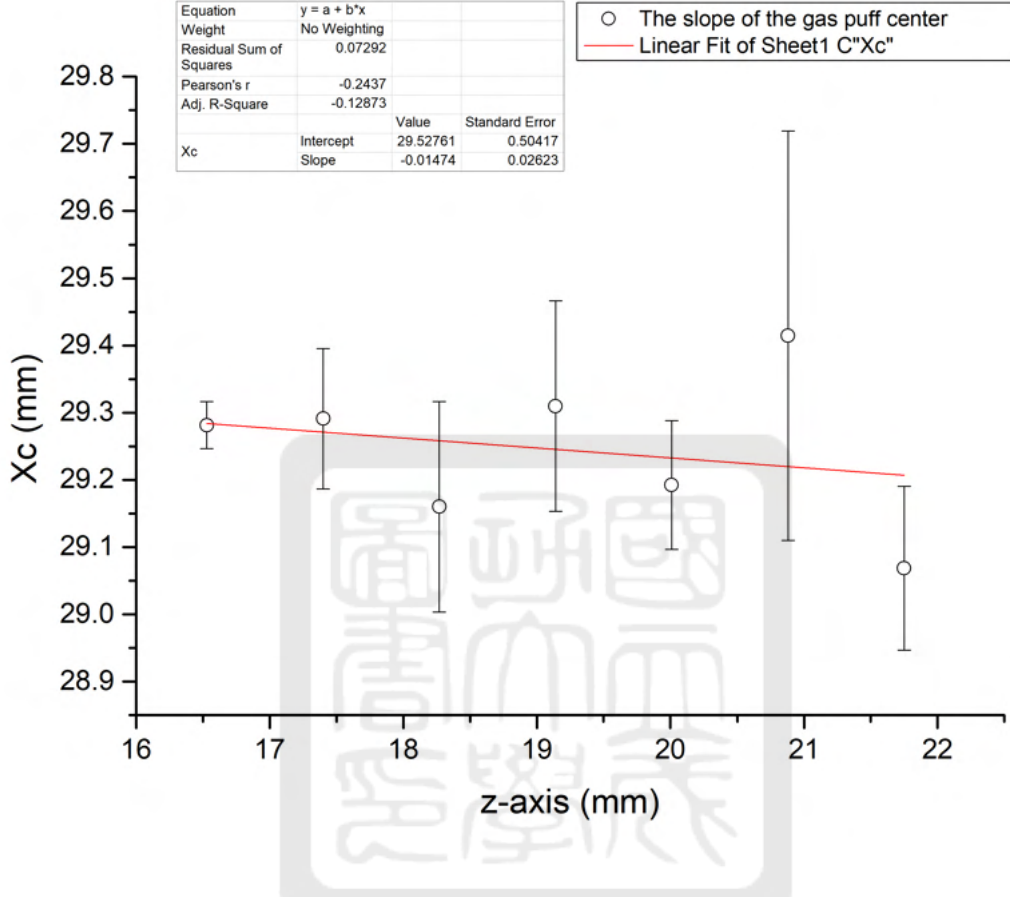


Figure 74: The slope of the propagating center of the gas puff.

5.1.4 Contrast of the differential image

In order to measure the contrast, the position of the horizontal line profile needs to be defined. Figure 75(a) is the vertical line profile of the image. The profile of the intensity along the yellow vertical line is shown in figure 75(b). The boundary of the CDN output appears at 181 pixels. Figure 76(a) is the differential image in figure 66. The red solid line in figure 76(a), which is 199 pixels below the nozzle, i.e., 1.1 mm below the nozzle. Figure 76(b) is the profile of the differential image along the red line in figure 76(a). The maximum of the profile is 4 ± 3 a.u. and the minimum is -8 ± 2 a.u.. The contrast is 12 ± 5 a.u..

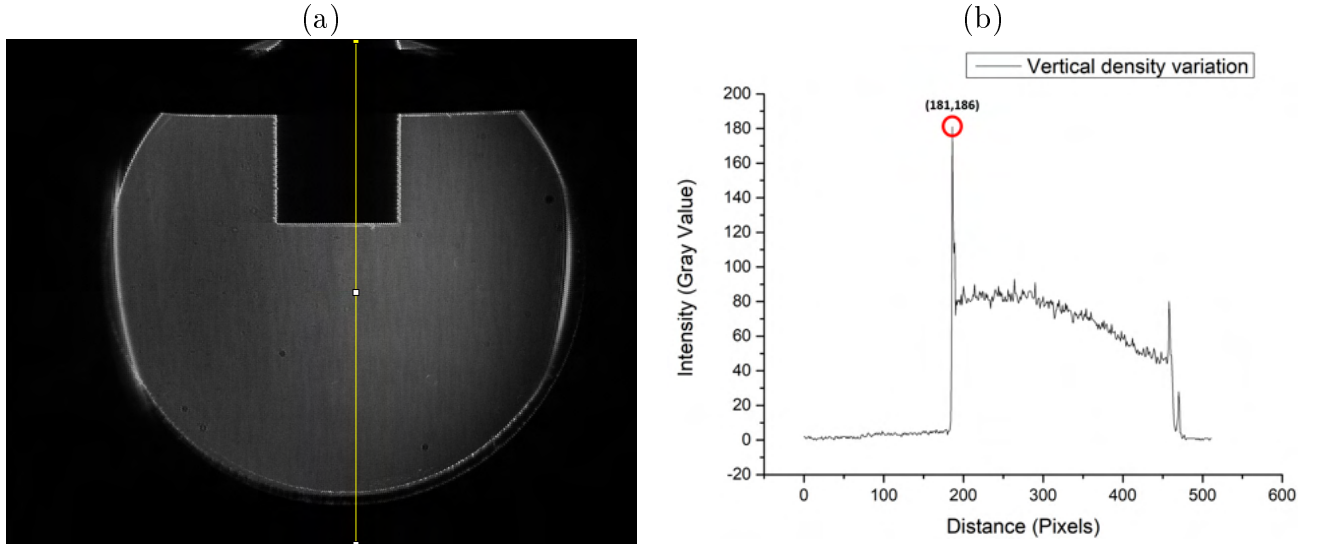


Figure 75: (a) The vertical line profile of the image. (b) The signal intensity difference of the location of the vertical line profile.

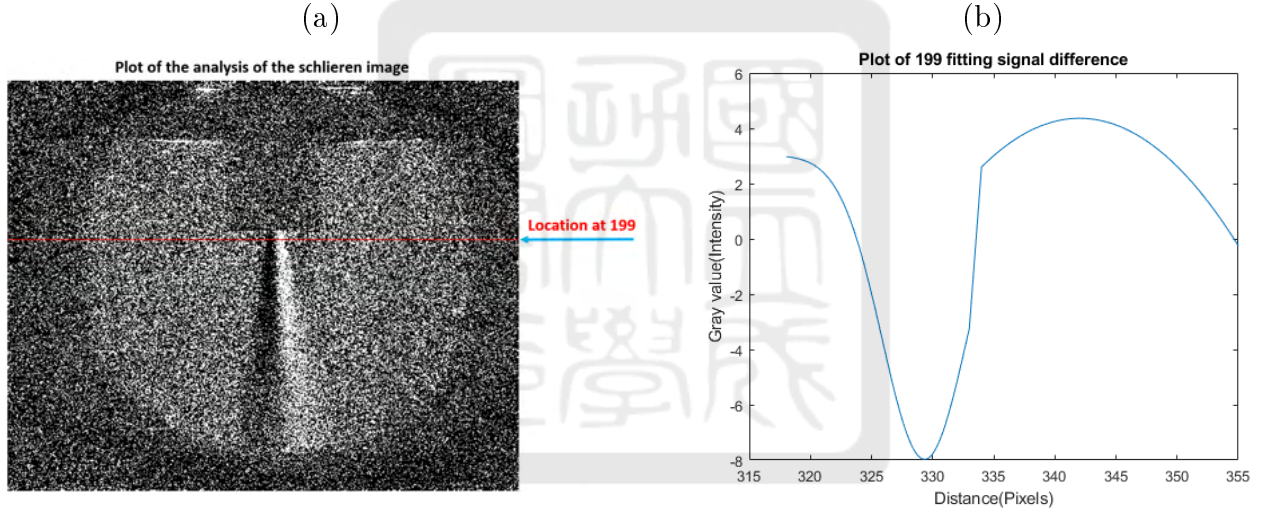


Figure 76: (a) The horizontal line profile of the image. (b) The signal intensity difference of the location of the horizontal line at 199 pixels.

5.2 The 24-V pulse valve

In this section, we will present the experimental results using the 24-V pulse valve with different experimental conditions listed in table 8. Figure 77(a) is the V5A CDN. The V5A CDN has an intake with 2 mm in diameter, a waist with 1 mm in diameter, and an output with 1.3 mm in diameter. The structure of the CDN has a 0.3-mm systematic error between the CAD drawing and the final product made by using the 3D printer. The V5A CDN is used in section 5.2.1, 5.2.2, 5.2.3, 5.2.4, and 5.2.5. Figure 77(b) is the V5B CDN. The V5B CDN is a pure convergent nozzle. It has an intake with 2 mm in diameter and an output with 1 mm in

diameter. The V5B CDN is used in section 5.2.4. Figure 77(c) is the V6 CDN. The V6 CDN has an intake with 4 mm in diameter, a waist with 2 mm in diameter, and an output with 2.6 mm in diameter. The V6 CDN is used in section 5.2.4 to compare with the V5A and the V5B CDN. Notice that a short summary with a table is given at the end of each section.

Table 8: The 24-V pulse valve experimental setup with Convergent-divergent nozzle (CDN) in different conditions.

	The experimental setup with Convergent-divergent nozzle (CDN)	Section
Different locations of the pulse valve (20 cm case v.s. 42 cm from the convex lens)	V5A CDN	1.2.1
Different Schlieren knife-edge setting (Tilted v.s. horizontal v.s. vertical schlieren knife)	V5A CDN	1.2.2
Different temperature of the gas puff (15°C v.s. 25°C)	V5A CDN	1.2.3
Different convergent-divergent nozzles (V5A v.s. V5B v.s. V6 CDN)	V5A, V5B and V6 CDN	1.2.4
Different pressure of the argon gas (5 ~ 9 atm pressure difference)	V5A CDN	1.2.5

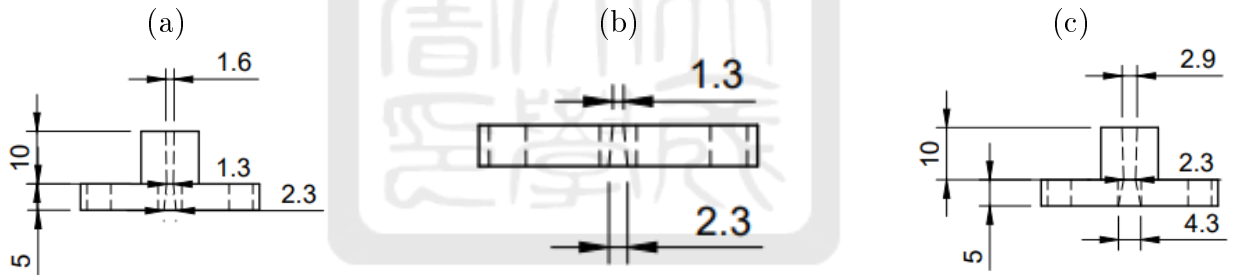


Figure 77: (a) V5A CDN. (b) V5B CDN. (c) V6 CDN.

5.2.1 Different locations of the pulse valve setting

In this experiment, the location of the 24-V pulse valve was adjusted to optimize the contrast of the differential image. We designed two versions of the 24-V pulse valve set at different locations as shown in figures 78(a) and (b). Figure 78(a) is the 24-V pulse valve set at 20 cm from the convex lens. Figure 78(b) is the 24-V pulse valve set at 42 cm from the convex lens. The experimental setups with V5A CDN, vertical knife-edge, and the temperature of 25°C were used. We made three comparisons between both of them. (1) The contrast of the differential image. (2) The opening angle of the gas puff. (3) The tilted angle of the CDN.

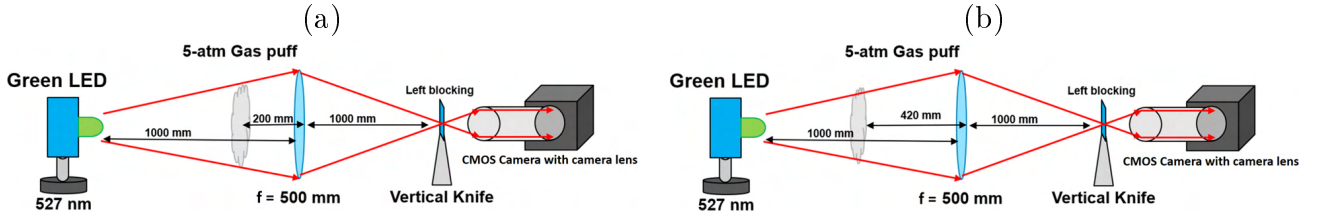


Figure 78: (a) Schematic of the location set at 20 cm from the convex lens of the experimental setup. (b) Schematic of the location set at 42 cm from the convex lens of the experimental setup.

Following the steps in section 1.1.4, the horizontal profiles of the differential images 1.1 mm below the nozzles were obtained. Figure 79(a) is the differential image in the case where the pulse valve is 20 cm from the convex lens. Figure 79(b) is the profile of the differential image along the red line in the figure 79(a). The maximum of the profile is 10 ± 2 a.u. and the minimum is -12 ± 2 a.u. The contrast is 22 ± 4 a.u..

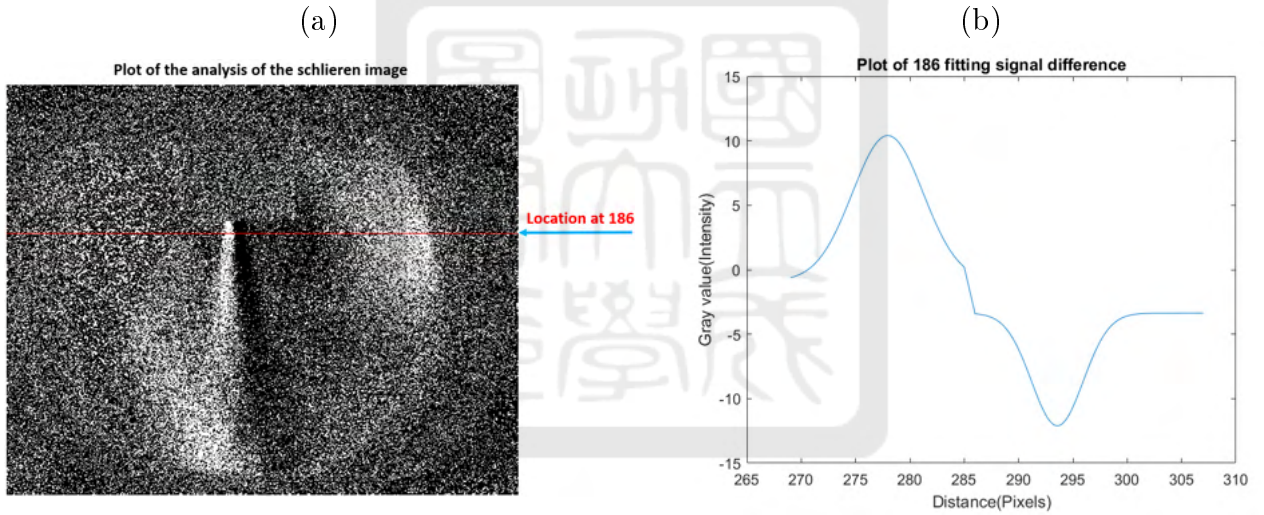


Figure 79: (a) The horizontal line profile of the image in the pulse valve 20 cm from the convex lens case. (b) The signal intensity difference of the location of the horizontal line at 186 pixels.

Following the steps in section 1.1.4, the horizontal profiles of the differential images 1.1 mm below the nozzles for two cases were obtained. Figure 80(a) is the differential image in the case where the pulse valve is 42 cm from the convex lens. Figure 80(b) is the profile of the differential image along the red line in the figure 80(a). The maximum of the profile is 2 ± 2 a.u. and the minimum is -4 ± 1 a.u.. The contrast is 6 ± 3 a.u..

The contrast of the differential image is higher in the 20-cm case than in the 42-cm case.

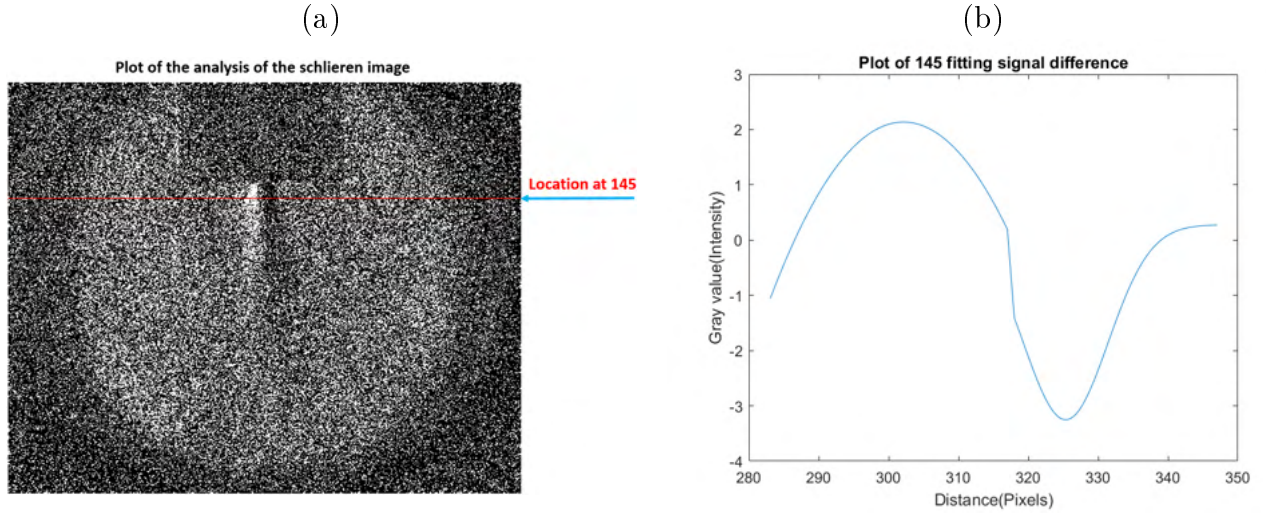


Figure 80: (a) The horizontal line profile of the image in the pulse valve 42 cm from the convex lens case. (b) The signal intensity difference of the location of the horizontal line at 145 pixels.

Following the steps in section 1.1.2, the slope of the propagating path of the gas puff in the pulse valve set at 20 cm from the convex lens case is 0.13 ± 0.01 as shown in figure 81. Therefore, the opening angle of the gas puff is $7.4^\circ \pm 0.6^\circ$. On the other hand, following the step in section 1.1.3, the slope of the propagating center of the gas puff in the pulse valve set at 20 cm from the convex lens case is 0.004 ± 0.016 as shown in figure 82. The tilted angle of the CDN is $0.23^\circ \pm 0.92^\circ$.

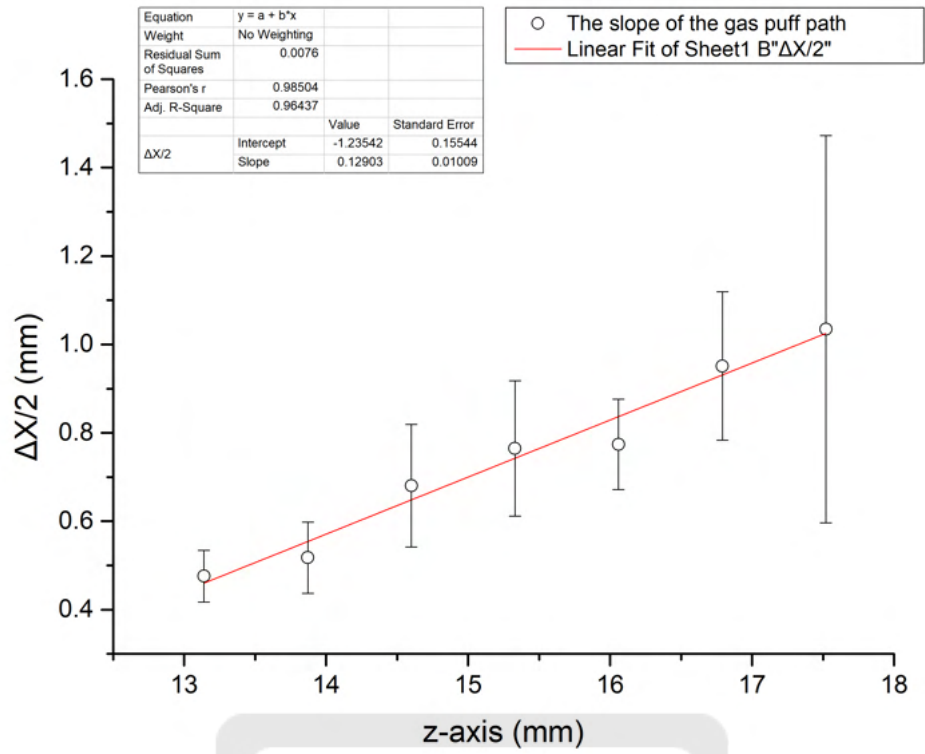


Figure 81: The slope of the propagating path of the gas puff in the pulse valve 20 cm from the convex lens case.

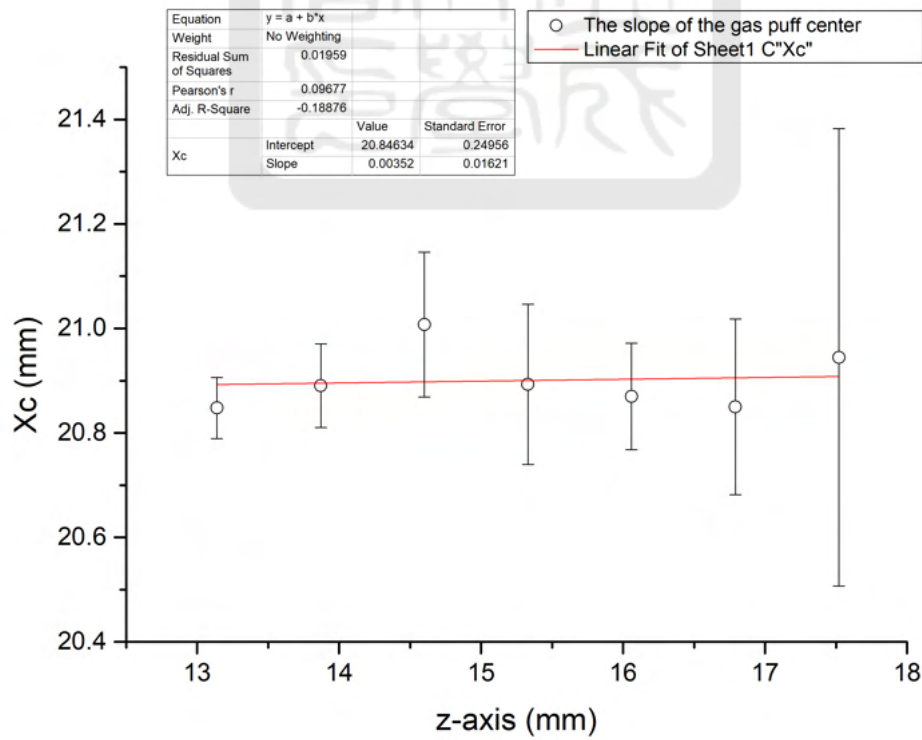


Figure 82: The slope of the propagating center of the gas puff in the pulse valve 20 cm from the convex lens case.

Similarly, the slope of the propagating path of the gas puff in the pulse valve set at 42 cm from the convex lens case is 0.01 ± 0.02 as shown in figure 83. Thus, the opening angle of the gas puff is $0.57^\circ \pm 1.15^\circ$. The slope of the propagating center of the gas puff is -0.09 ± 0.08 as shown in figure 84. The tilted angle of the CDN is $-5.14^\circ \pm 4.57^\circ$.

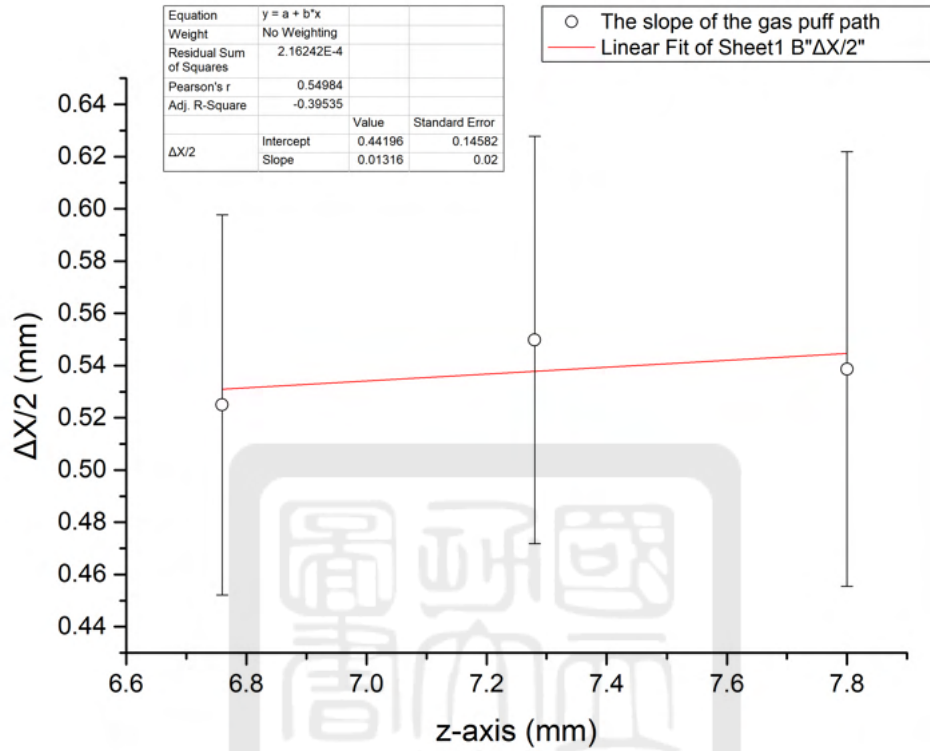


Figure 83: The slope of the propagating path of the gas puff in the pulse valve 42 cm from the convex lens case.

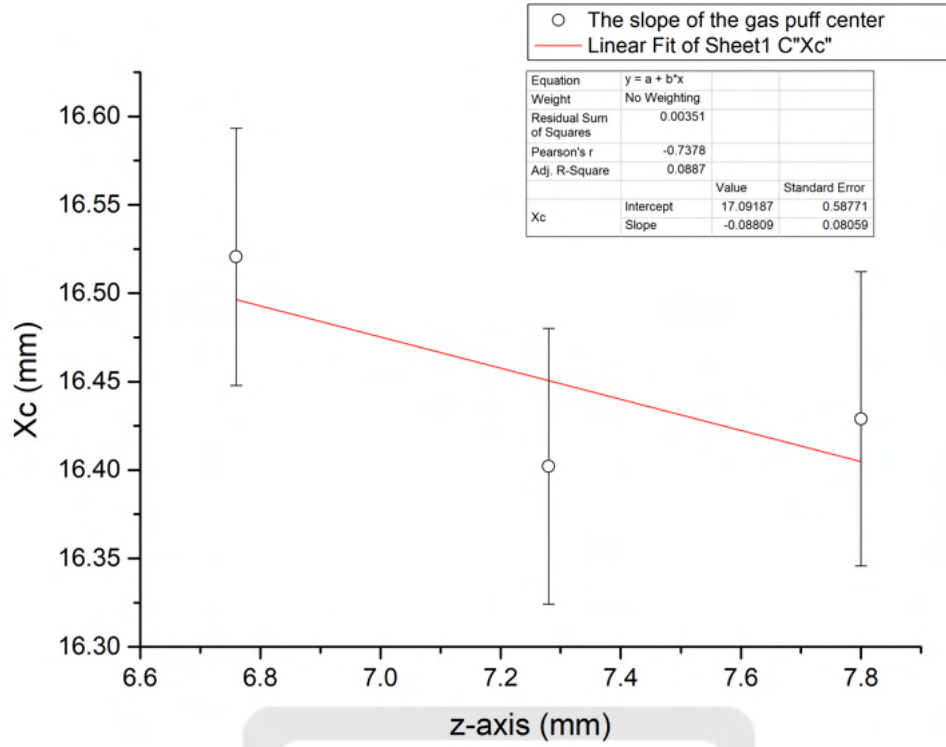


Figure 84: The slope of the propagating center of the gas puff in the pulse valve 42 cm from the convex lens case.

Table 9 is the comparison results of the 24-V pulse valve set at different positions. The opening angle in the pulse valve set at 20 cm from the convex lens case was obviously larger than that of the pulse valve set at 42 cm from the convex lens. But the tilted angle of the CDN in the pulse valve 20 cm from the convex lens case was smaller than that in the pulse valve 42 cm from the convex lens. The number of data points of the 42-cm case was less than that of the 20-cm case because the background noise of the 42-cm case was higher than that in the 20-cm case. The contrast of the differential image of the 20-cm case was higher than that in the 42-cm case. Therefore, we set the pulse valve at 20 cm from the convex lens case for the rest of experiments.

Table 9: The comparisons of the 24-V pulse valve set at different position.

	20 cm from the convex lens (★)	42 cm from the convex lens
The contrast (a.u.)	22 ± 4	6 ± 3
The opening angle of the gas puff	$7.4^\circ \pm 0.6^\circ$	$0.57^\circ \pm 1.15^\circ$
The tilted angle of the CDN	$0.23^\circ \pm 0.92^\circ$	$-5.14^\circ \pm 4.57^\circ$

5.2.2 Different Schlieren knife-edge settings

In this section, we are focusing on the clearness of the schlieren image in different schlieren knife settings. The experimental setups with the pulse valve set at 20 cm from the convex lens, V5A CDN, and the temperature of 25°C were used. Three versions of the schlieren knife including tilted, horizontal, and vertical to the optical table were used. The clearness of the schlieren image was dependent on the background noise. When the background noise was high, the schlieren image was not clear.

Figure 85 is the grayscale of the schlieren image with a tilted knife-edge. The left one is the image without the gas puff and the right one is the image with the gas puff. Figure 86 is the profile along with the yellow blocks in figure 85. The background noise was so large that the profile of the gas puff was not clear.

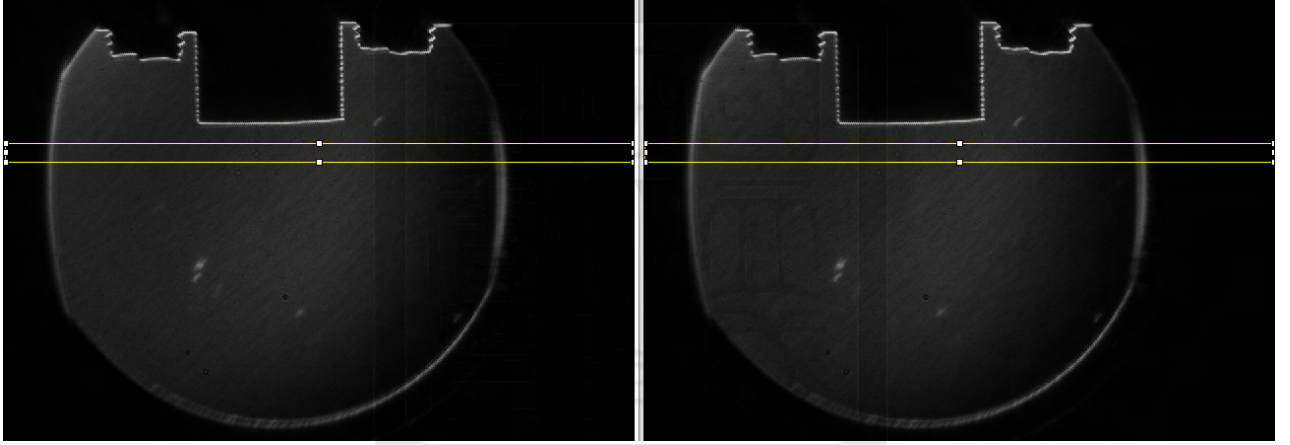


Figure 85: The grayscale of the schlieren image with tilted knife-edge. Left one is the image without gas puff and right one is the image with gas puff.

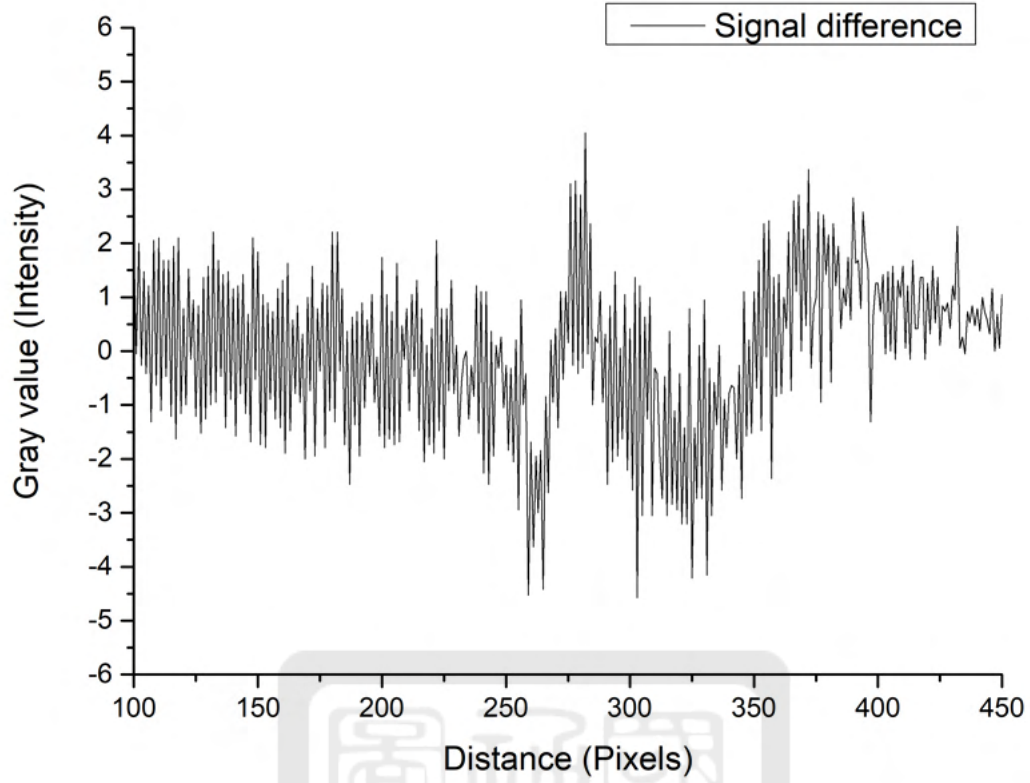


Figure 86: The signal difference of the schlieren image in knife-edge set oblique to the optical table case.

Figure 87 is the grayscale of the schlieren image with a horizontal knife-edge. Figure 88 is the profile along with the yellow blocks in figure 87. The profile of the gas puff didn't appear because the horizontal knife case was used to observe the horizontal density variation.

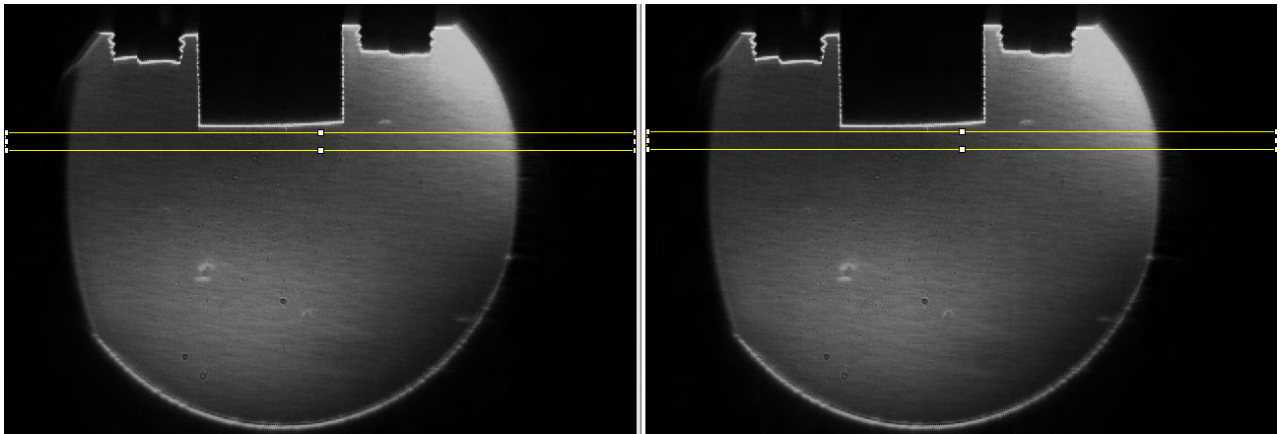


Figure 87: The grayscale of the schlieren image with horizontal knife-edge. Left one is the image without gas puff and right one is the image with gas puff.

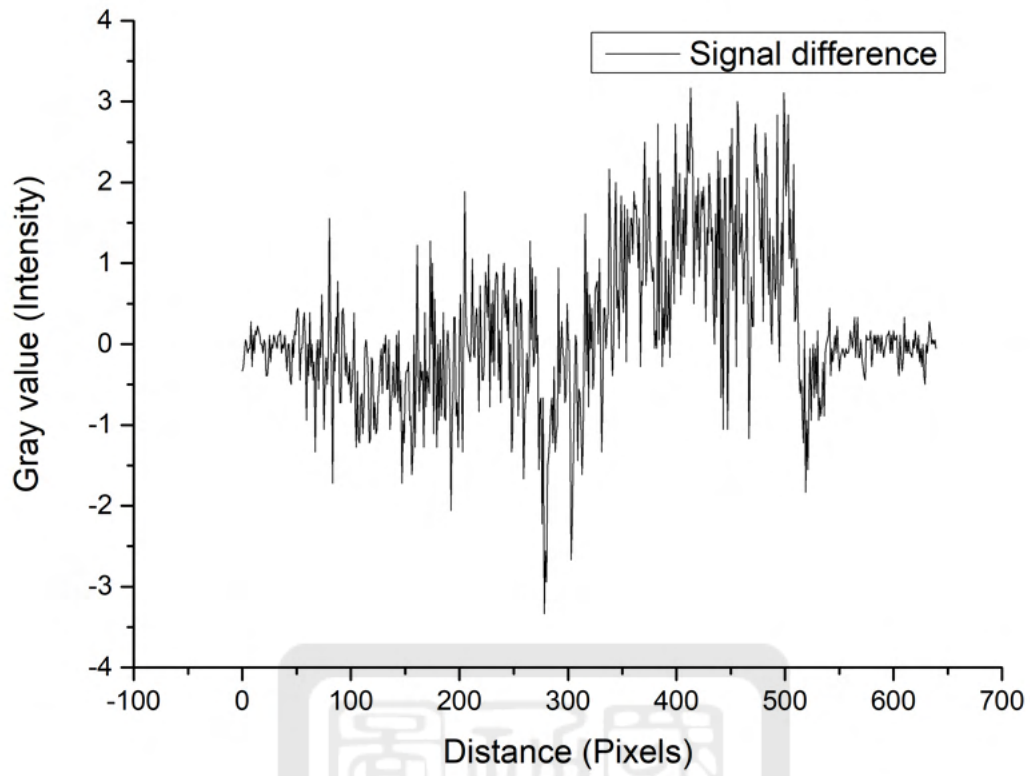


Figure 88: The signal difference of the schlieren image in knife-edge set horizontal to the optical table case.

Figure 89 is the grayscale of the schlieren image with a vertical knife-edge. Figure 90 is the profile along with the yellow blocks in figure 89. The profile of the gas puff was obvious and the background noise is weaker than those in the previous two cases.

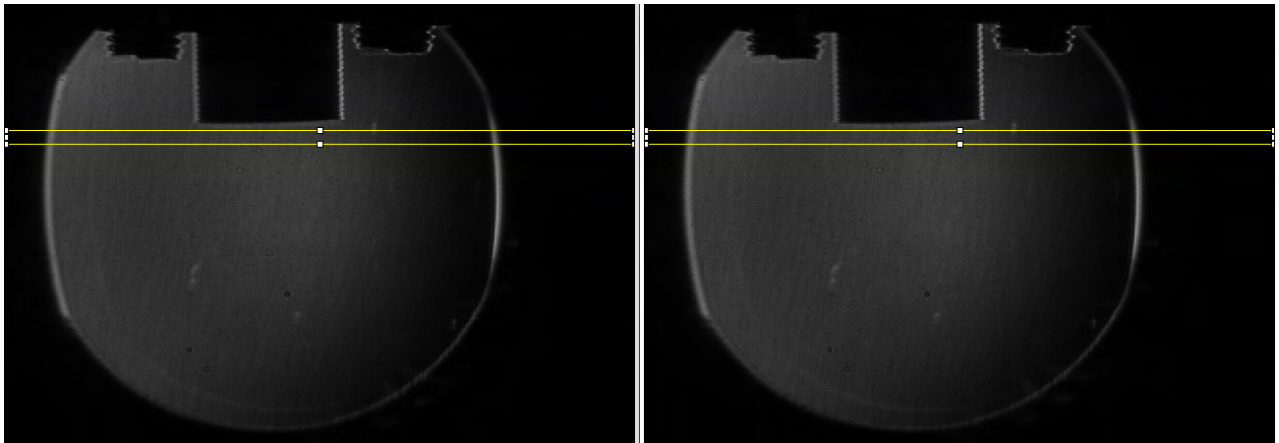


Figure 89: The grayscale of the schlieren image with a vertical knife-edge. Left one is the image without gas puff and right one is the image with gas puff.

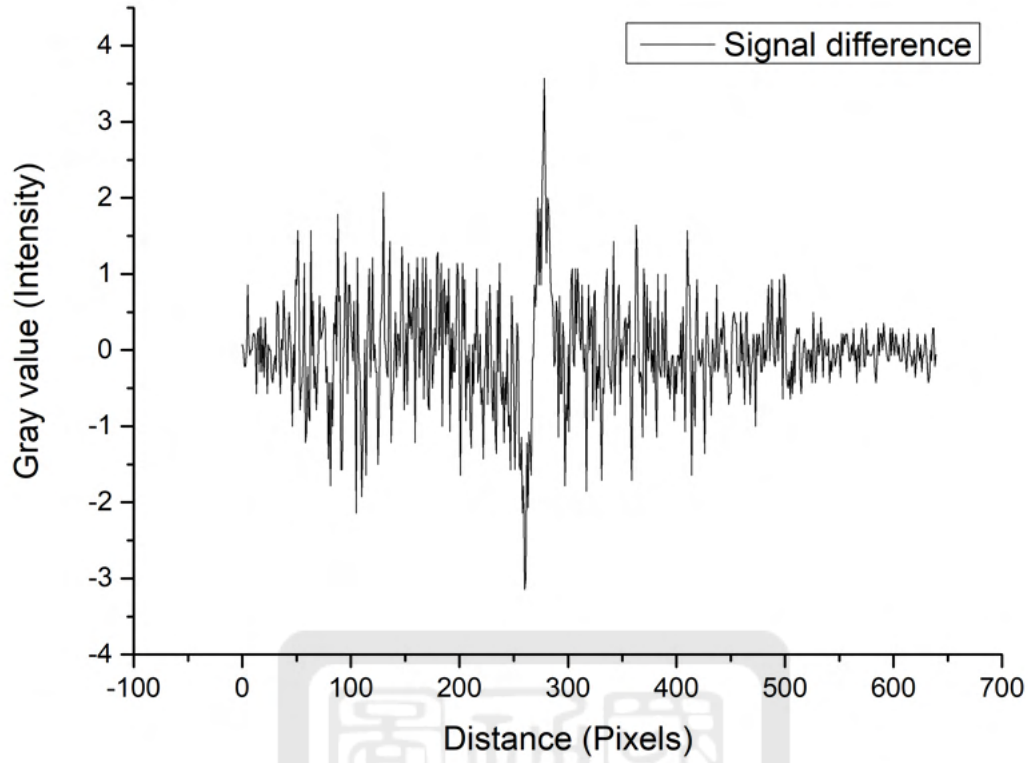


Figure 90: The signal difference of the schlieren image in knife-edge set vertical to the optical table case.

Table 10 is the comparison between different schlieren knife settings. The horizontal knife-edge was used to observe the vertical density gradient. However, we couldn't observe the profile of the gas puff in this case. Therefore, this knife-edge setting was no longer used in the rest of experiments. Furthermore, the background noise in the tilted knife-edge setting was larger than that in the vertical knife-edge setting. Therefore, we chose the vertical knife-edge setting for the rest of experiments.

Table 10: The comparisons of the different schlieren knife set.

	knife set oblique to the optical table case	knife set horizontal to the optical table case	knife set vertical to the optical table case (★)
Gas-puff profile	Not clear	Not clear	Clear

5.2.3 Different temperature of the gas puff

In this section, we focused on the temperature of the gas puff. We wanted to see if a colder gas can be denser so that the signal could be stronger. We had two different temperature

setting, 25°C and 15°C . The ice was used to lower the temperature of the gas puff. The experimental setups with the pulse valve set at 20 cm from the convex lens, vertical knife-edge, and V5A CDN were used. We used the infra-red thermography (Sunche, DT8380H) to measure the temperature of the reservoir that was used to store the gas. The 24-V pulse valve was set at 20 cm from the convex lens with a vertical schlieren knife-edge.

Following the steps in section 1.1.4, the horizontal profiles of the differential images 1 mm below the nozzle was obtained. Figure 91(a) is the differential image in the case where the temperature of the gas puff is 15°C. Figure 91(b) is the profile of the differential image along the red line in figure 91(a). The maximum of the profile is 6.2 ± 1.5 a.u. and the minimum is -5.1 ± 1.9 a.u. The contrast is 11.3 ± 3.4 a.u..

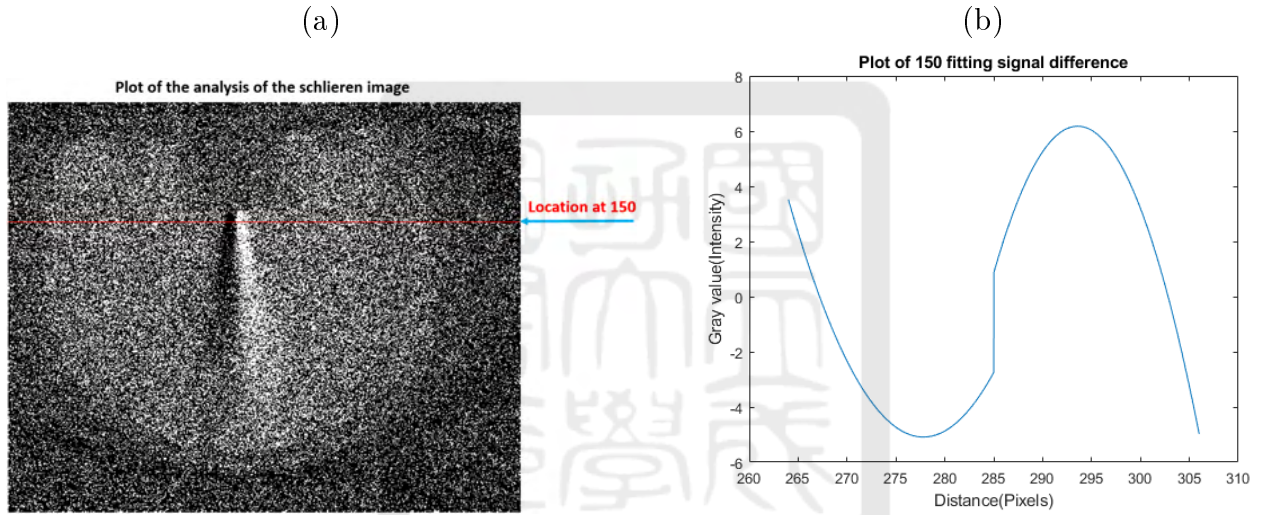


Figure 91: (a) The horizontal line profile of the image in 15°C–gas puff case. (b) The signal intensity difference of the location of the horizontal line at 150 pixels.

Following the steps in section 1.1.4, the horizontal profiles of the differential images 1 mm below the nozzles for two cases was obtained. Figure 92(a) is the differential image in the case where the temperature of the gas puff is 25°C. Figure 92(b) is the profile of the differential image along the red line in figure 92(a). The maximum of the profile is 12.5 ± 1.4 a.u. and the minimum is -4.1 ± 1.9 a.u.. The contrast is 16.6 ± 3.3 a.u..

The contrast of the differential image was higher in the 25°C–gas puff case than in the 15°C–gas puff case.

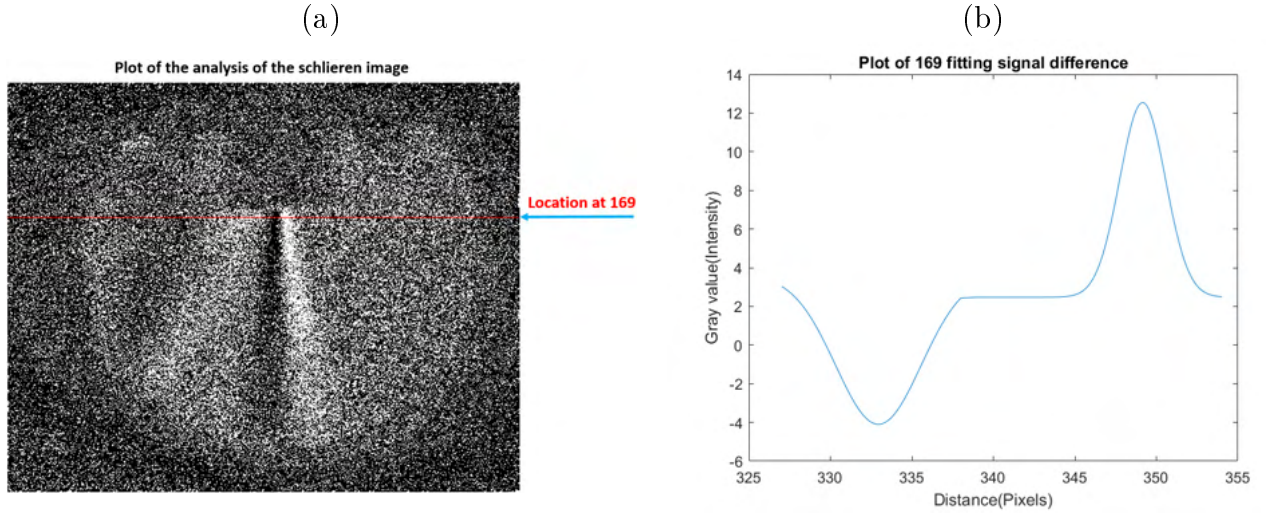


Figure 92: (a) The horizontal line profile of the image in 25°C –gas puff case. (b) The signal intensity difference of the location of the horizontal line at 169 pixels.

Following the step in section 1.1.2, the slope of the propagating path of the 15°C –gas puff case is 0.08 ± 0.05 as shown in figure 93. Therefore, the opening angle of the gas puff is $4.57^{\circ} \pm 2.86^{\circ}$. On the other hand, following the step in section 1.1.3, the slope of the propagating center of the 15°C –gas puff case is -0.009 ± 0.063 as shown in figure 94. The tilted angle of the CDN is $-0.52^{\circ} \pm 3.60^{\circ}$.

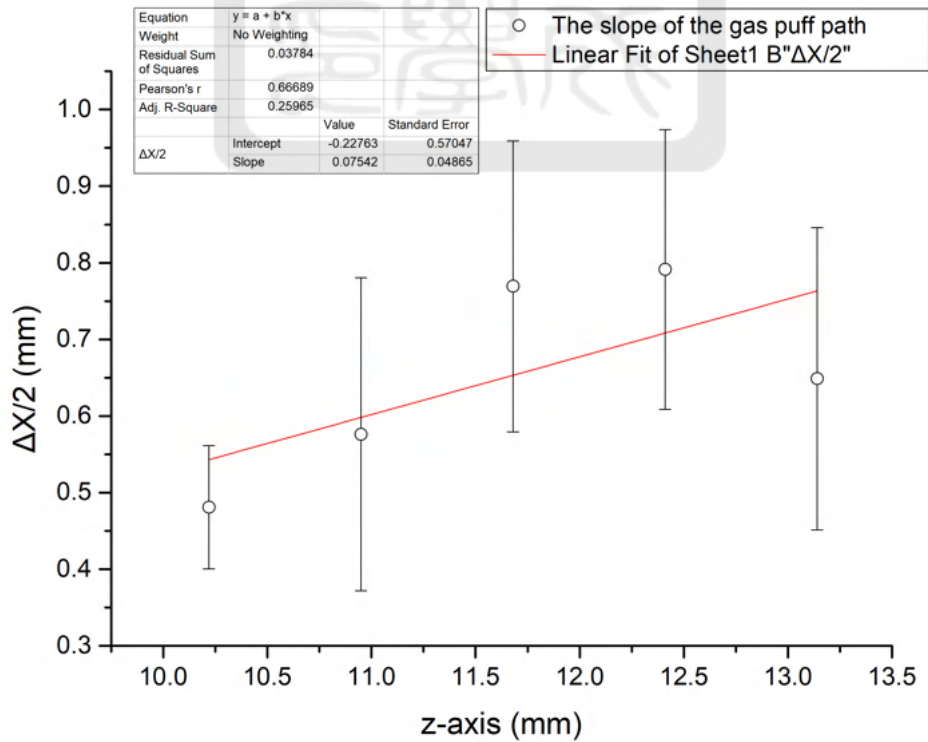


Figure 93: The slope of the propagating path of the gas puff in 15° –gas puff case.

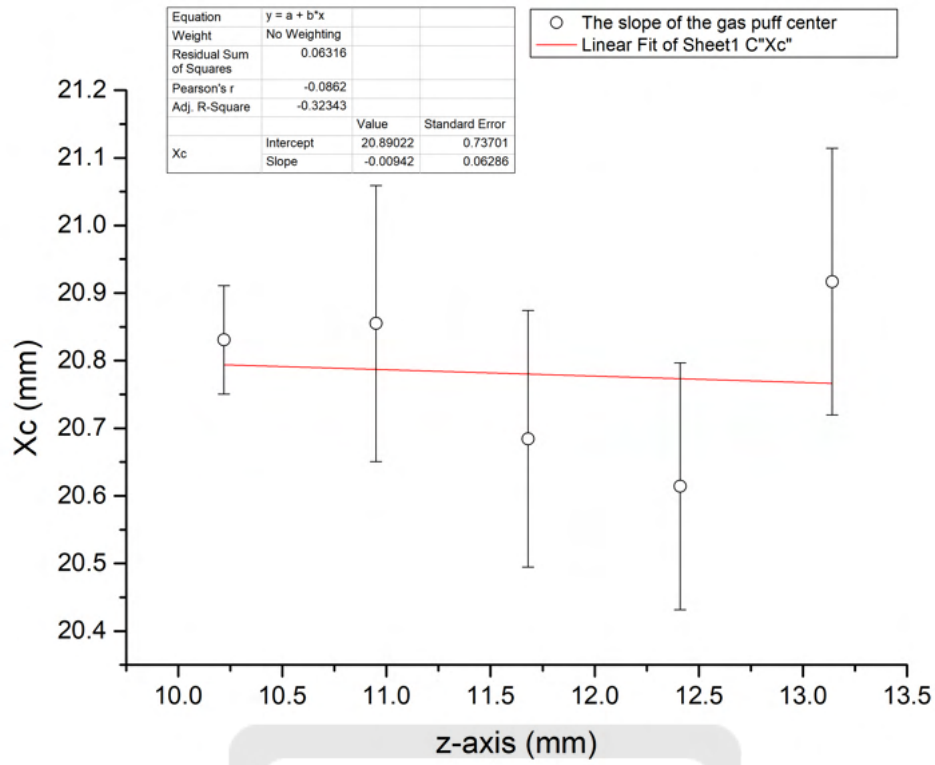


Figure 94: The slope of the propagating center of the gas puff in 15°–gass puff case.

Similarly, the slope of the propagating path of the gas puff in 25°C–gass puff case is 0.05 ± 0.06 as shown in figure 95. The opening angle of the gas puff is $2.86^\circ \pm 3.43^\circ$. The slope of the propagating center of the gas puff is 0.14 ± 0.07 as shown in figure 96. The tilted angle of the CDN is $7.97^\circ \pm 4^\circ$.

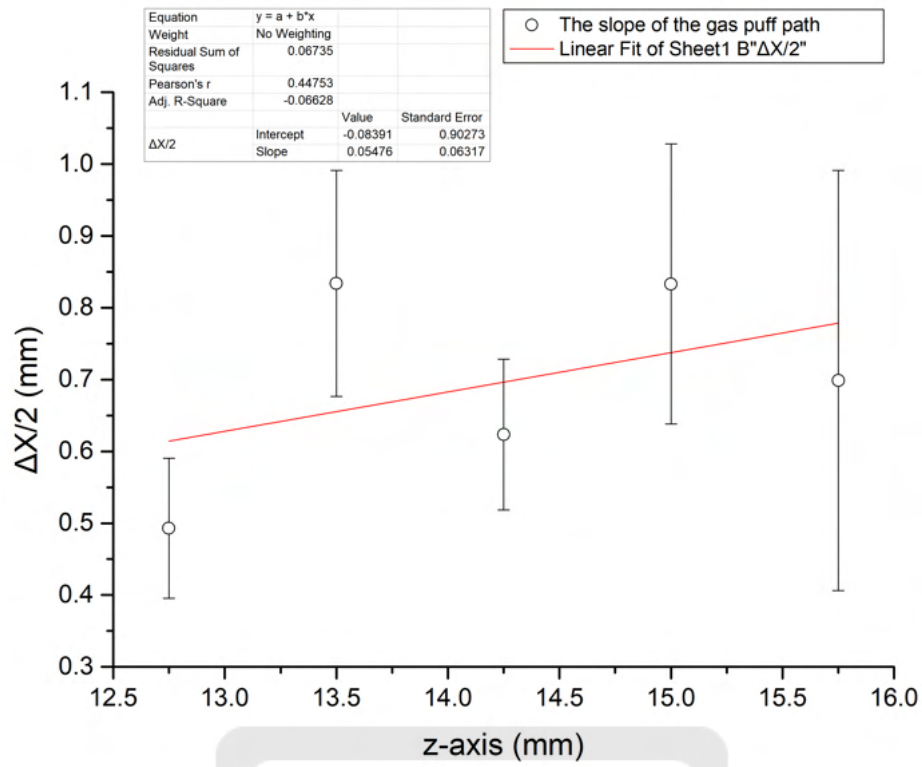


Figure 95: The slope of the propagating path of the gas puff in 25°-gass puff case.

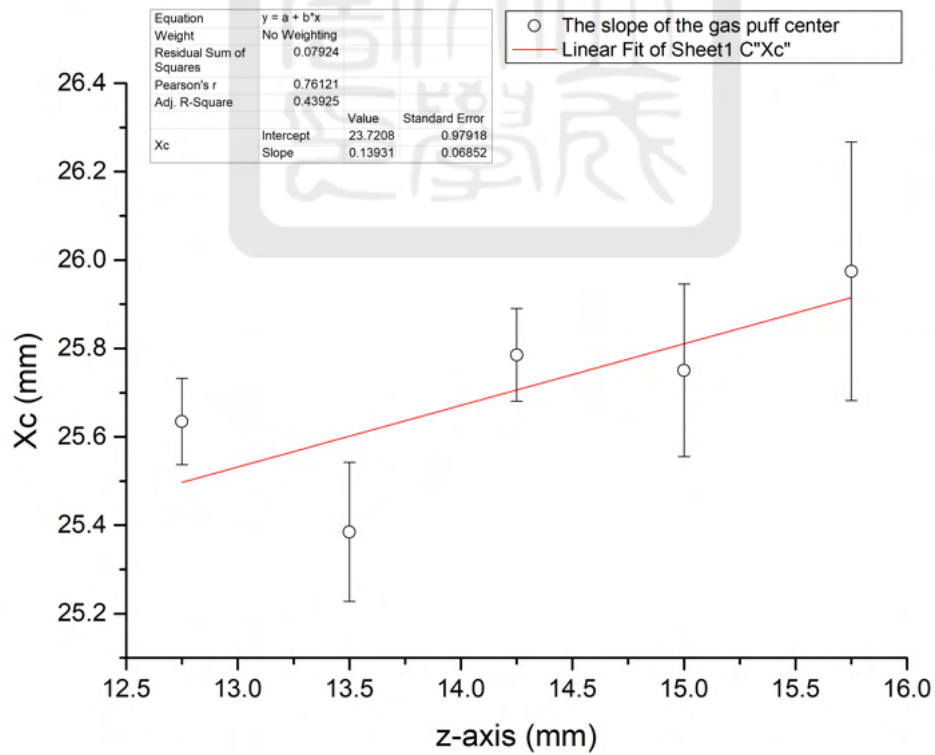


Figure 96: The slope of the propagating center of the gas puff in 25°-gass puff case.

Table 11 is the comparison result of the 24-V pulse valve with different gas-puff temper-

atures. The opening angle in 15°C–gas puff case was not significantly different from that in 25°C–gas puff case. However, it was difficult to keep the temperature of the gas puff at 15°C. On the other hand, the tilted angle of the CDN in 25°C–gas puff case was larger than that in 15°C–gas puff case. Nevertheless, the contrast of the differential image of 25°C–gas puff case was higher than that of 15°C–gas puff case. Therefore, we chose 25°C–gas puff for the rest of experiments.

Table 11: The comparisons of the 24-V pulse valve set at different temperatures.

	15°–gas puff	25°–gas puff (★)
The contrast (a.u.)	11.3 ± 3.4	16.6 ± 3.3
The opening angle of the gas puff	$4.57^\circ \pm 2.86^\circ$	$2.86^\circ \pm 3.43^\circ$
The tilted angle of the CDN	$-0.52^\circ \pm 3.60^\circ$	$7.97^\circ \pm 4^\circ$

5.2.4 Different convergent-divergent nozzles (CDN)

In Chapter 3, we introduced five versions of convergent-divergent nozzles (CDN) which are used to generate a supersonic flow. We focused on observing the differences of the gas puff generated with V5A, V5B, and V6 CDN as shown in figure 77. The experimental setups with the pulse valve set at 20 cm from the convex lens, vertical knife-edge, and the temperature of 25°C were used.

Following the steps in section 1.1.4, the horizontal profiles of the differential images 1.1 mm below the nozzle was obtained. Figure 97(a) is the differential image in the case where V5A CDN was used. Figure 97(b) is the profile of the differential image along the red line in figure 97(a). The maximum of the profile is 5.5 ± 2.5 a.u. and the minimum is -4 ± 1 a.u.. The contrast is 9.5 ± 3.5 a.u..

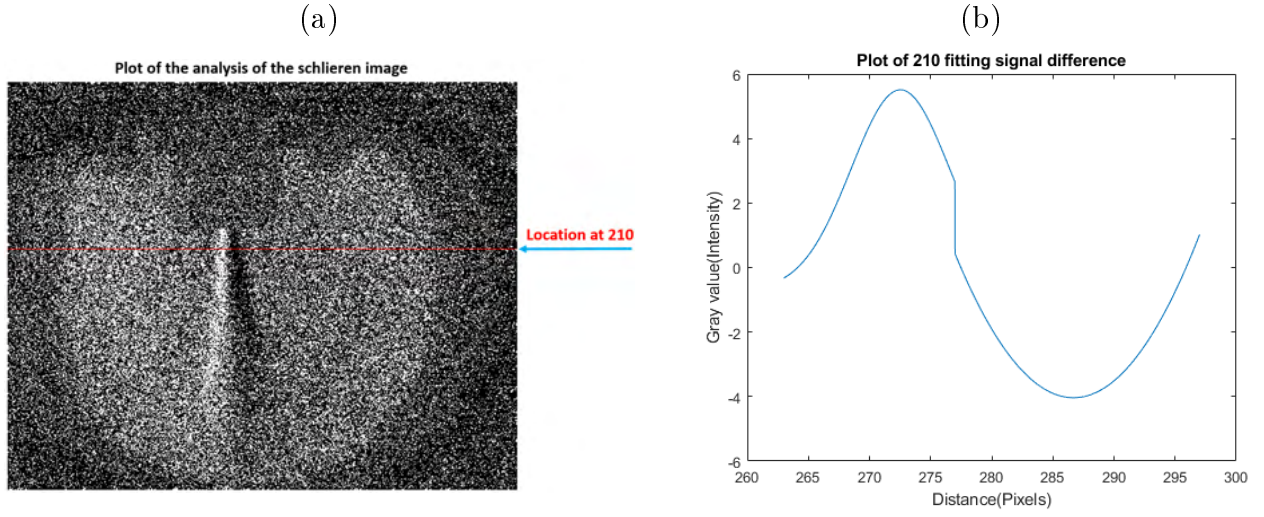


Figure 97: (a) The horizontal line profile of the experimental setup with V5A CDN case. (b) The signal intensity difference of the location of the horizontal line at 210 pixels.

Following the steps in section 1.1.4, the horizontal profiles of the differential images 1.1 mm below the nozzle was obtained. Figure 98(a) is the differential image in the case where V5B CDN was used. Figure 98(b) is the profile of the differential image along the red line in figure 98(a). The maximum of the profile is 5.9 ± 1.6 a.u. and the minimum is -1.4 ± 1.9 a.u.. The contrast is 7.3 ± 3.5 a.u..

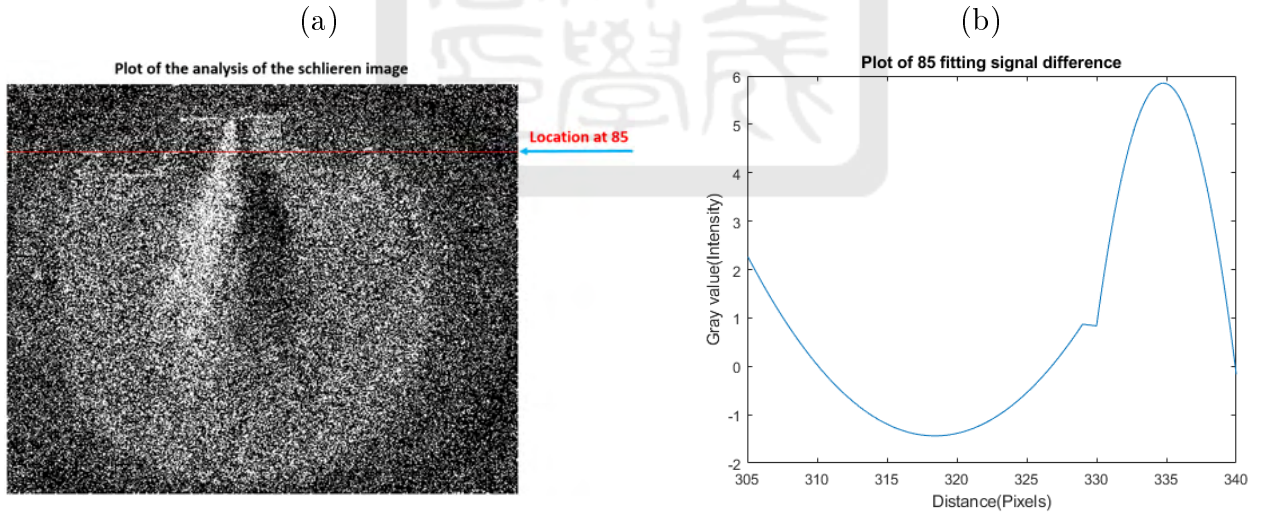


Figure 98: (a) The horizontal line profile of the experimental setup with V5B CDN case. (b) The signal intensity difference of the location of the horizontal line at 85 pixels.

Following the steps in section 1.1.4, the horizontal profiles of the differential images 1.1 mm below the nozzle was obtained. Figure 99(a) is the differential image in the case where V6 CDN was used. Figure 99(b) is the profile of the differential image along the red line in figure 99(a). The maximum of the profile is 2 ± 1.4 a.u. and the minimum is -5.3 ± 1.4 a.u.. The contrast

is 7.3 ± 2.8 a.u..

The contrast of the differential image is the highest in the V5A CDN case.

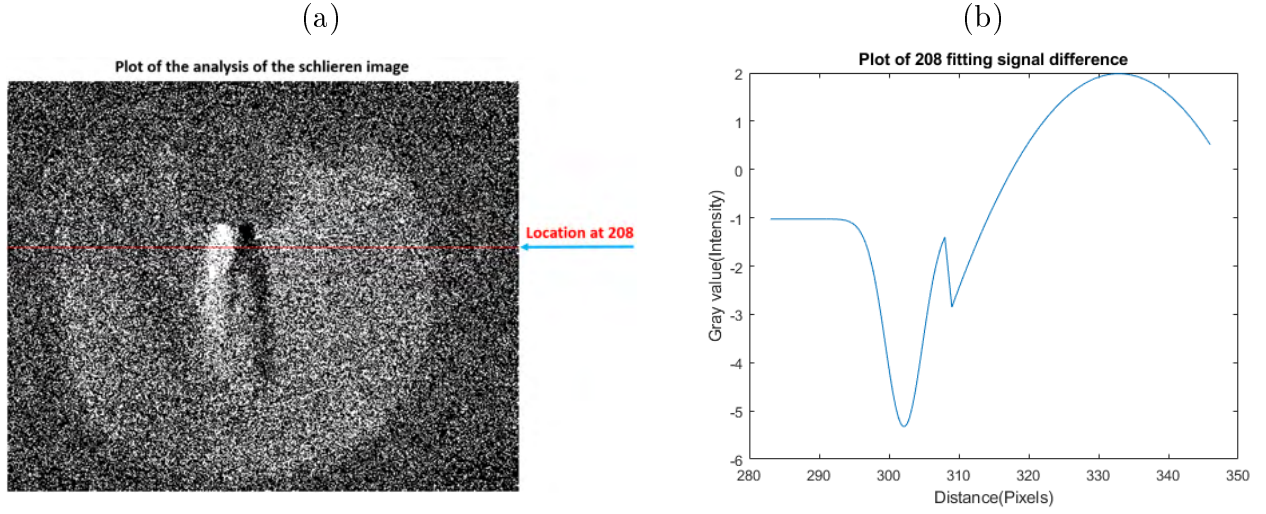


Figure 99: (a) The horizontal line profile of the experimental setup with V6 CDN case. (b) The signal intensity difference of the location of the horizontal line at 208 pixels.

Following the step in section 1.1.2, the slope of the propagating path of the V5A CDN case is 0.11 ± 0.05 as shown in figure 100. Therefore, the opening angle of the gas puff is $6.28^\circ \pm 2.86^\circ$. On the other hand, following the step in section 1.1.3, the slope of the propagating center of the V5A CDN case is 0.007 ± 0.07 as shown in figure 101. The tilted angle of the CDN is $0.4^\circ \pm 4^\circ$.

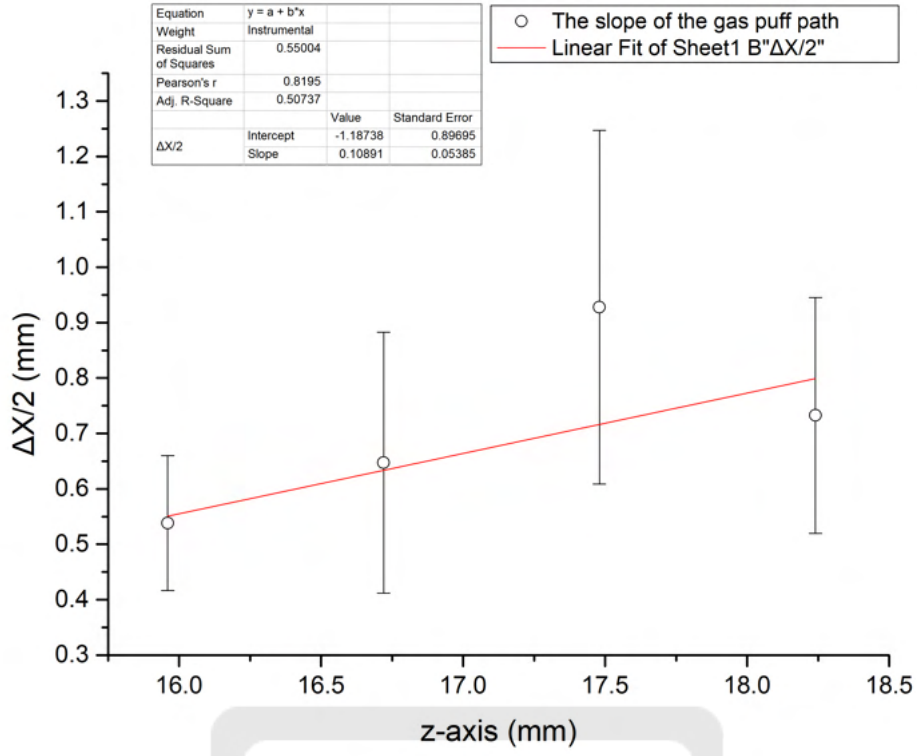


Figure 100: The slope of the propagating path of the experimental setup with V5A CDN case.

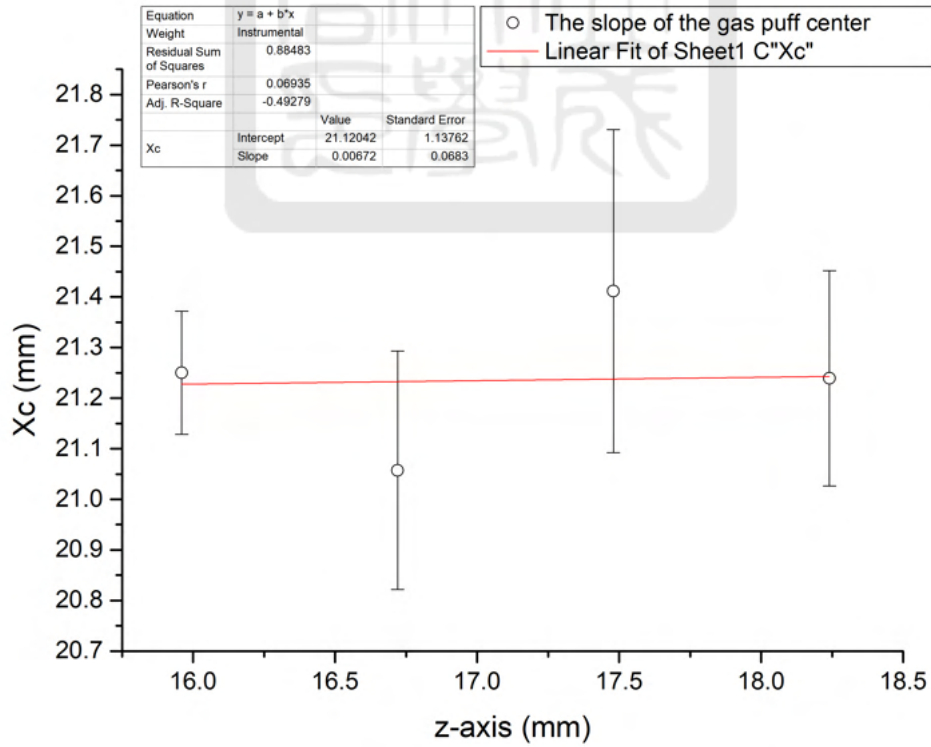


Figure 101: The slope of the propagating center of the experimental setup with V5A CDN case.

Similarly, the slope of the propagating path of the V5B CDN case is 0.15 ± 0.03 as shown

in figure 102. Therefore, the opening angle of the gas puff is $8.53^\circ \pm 1.72^\circ$. On the other hand, following the step in section 1.1.3, the slope of the propagating center of the V5B CDN case is -0.49 ± 0.33 as shown in figure 103. The tilted angle of the CDN is $-26.1^\circ \pm 18.26^\circ$. The number of data points in this case is less than those in other cases because the background noise is higher.

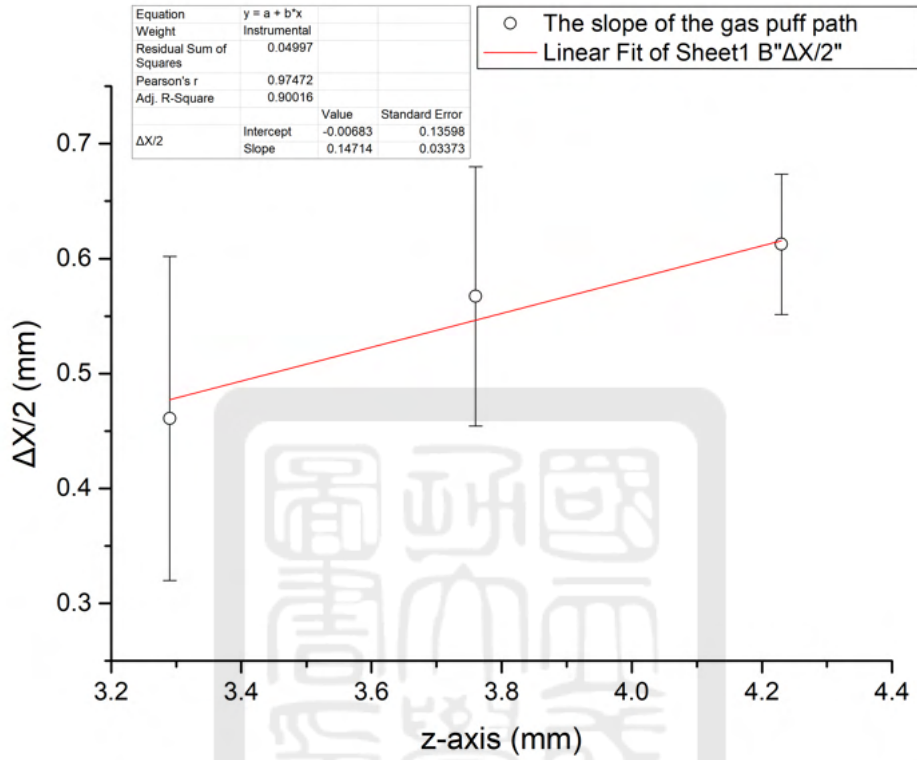


Figure 102: The slope of the propagating path of the experimental setup with V5B CDN case.

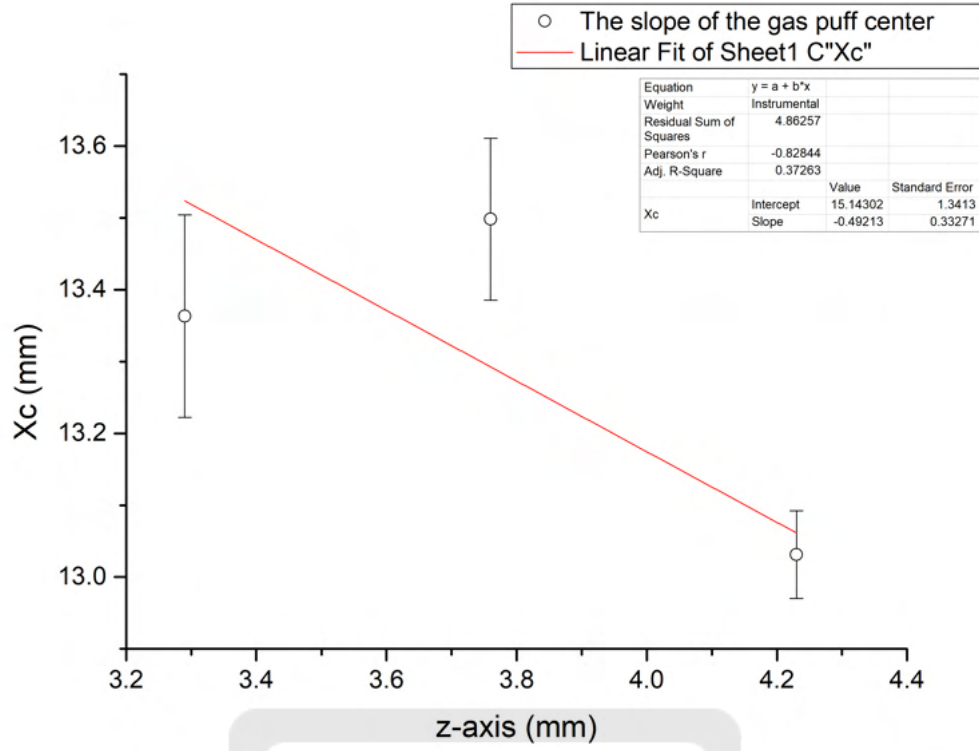


Figure 103: The slope of the propagating center of the experimental setup with V5B CDN case.

Similarly, the slope of the propagating path of the V6 CDN case is 0.16 ± 0.06 as shown in figure 104. Therefore, the opening angle of the gas puff is $9.09^\circ \pm 3.43^\circ$. On the other hand, following the step in section 1.1.3, the slope of the propagating center of the V6 CDN case is -0.1 ± 0.2 as shown in figure 105. The tilted angle of the CDN is $-5.7^\circ \pm 11.3^\circ$.

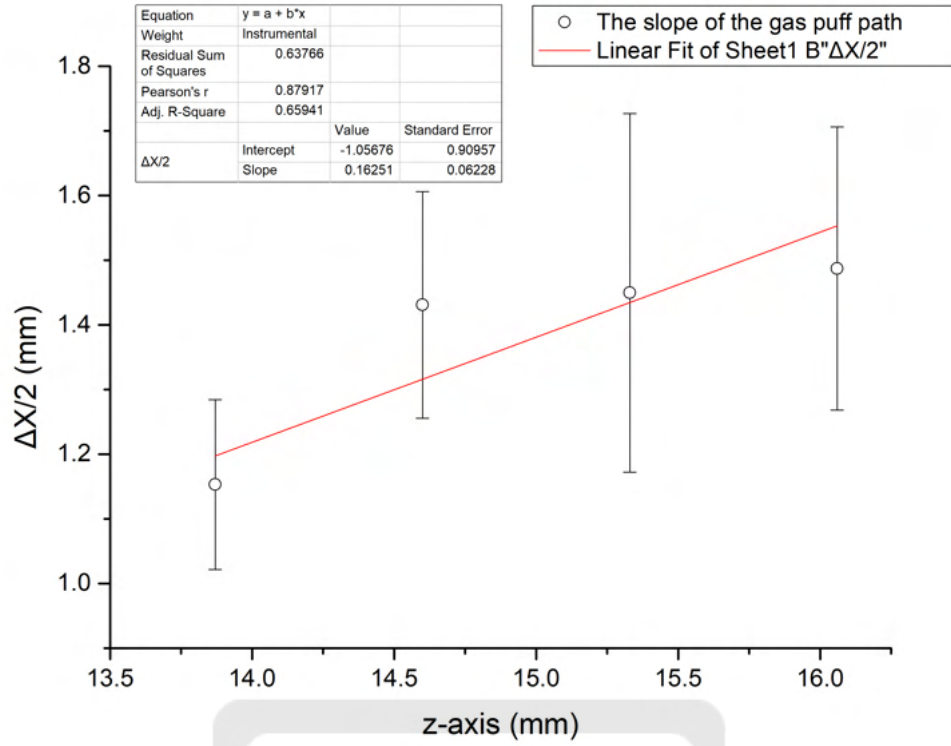


Figure 104: The slope of the propagating path of the experimental setup with V6 CDN case.

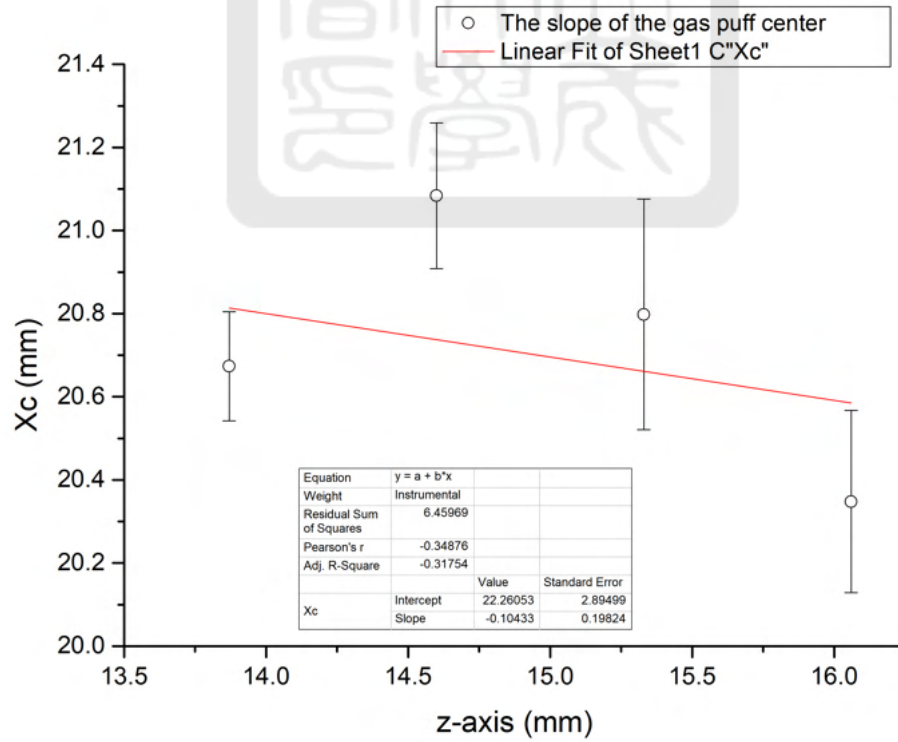


Figure 105: The slope of the propagating center of the experimental setup with V6 CDN case.

Table 12 is the comparison result of the experimental setups with different CDNs. The

opening angles in all cases were not significantly different. Finally, we used the V5A CDN in the rest of section 5.2 since the tilted angle of the CDN in the experimental setup with V5A CDN was the smallest.

Table 12: The comparisons of the experimental setup with different CDN.

	V5A CDN (★)	V5B CDN	V6 CDN
The contrast (a.u.)	9.5 ± 3.5	7.3 ± 3.5	7.3 ± 2.8
The opening angle of the gas puff	$6.28^\circ \pm 2.86^\circ$	$8.53^\circ \pm 1.72^\circ$	$9.09^\circ \pm 3.43^\circ$
The tilted angle of the CDN	$0.4^\circ \pm 4^\circ$	$-26.1^\circ \pm 18.26^\circ$	$-5.7^\circ \pm 11.3^\circ$

5.2.5 Different pressure of the argon gas

We want to study if the gas pressure will influence the gas puff. Therefore, we conducted experiments with Ar gas pressure of 6 ~ 10 atm, i.e., pressure difference of 5 ~ 9 atm. The experimental setups with the pulse valve set at 20 cm from the convex lens, vertical knife-edge, the V5A CDN, and the temperature of 25°C were used.

Following the steps in section 1.1.4, the horizontal profiles of the differential images 1.1 mm below the nozzles was obtained. Figure 106(a) is the differential image in the case where 5-atm pressure difference was used. Figure 106(b) is the profile of the differential image along the red line in figure 106(a). The maximum of the profile is 6.7 ± 0.9 a.u. and the minimum is -4.5 ± 1.4 a.u.. The contrast is 11.2 ± 2.3 a.u..

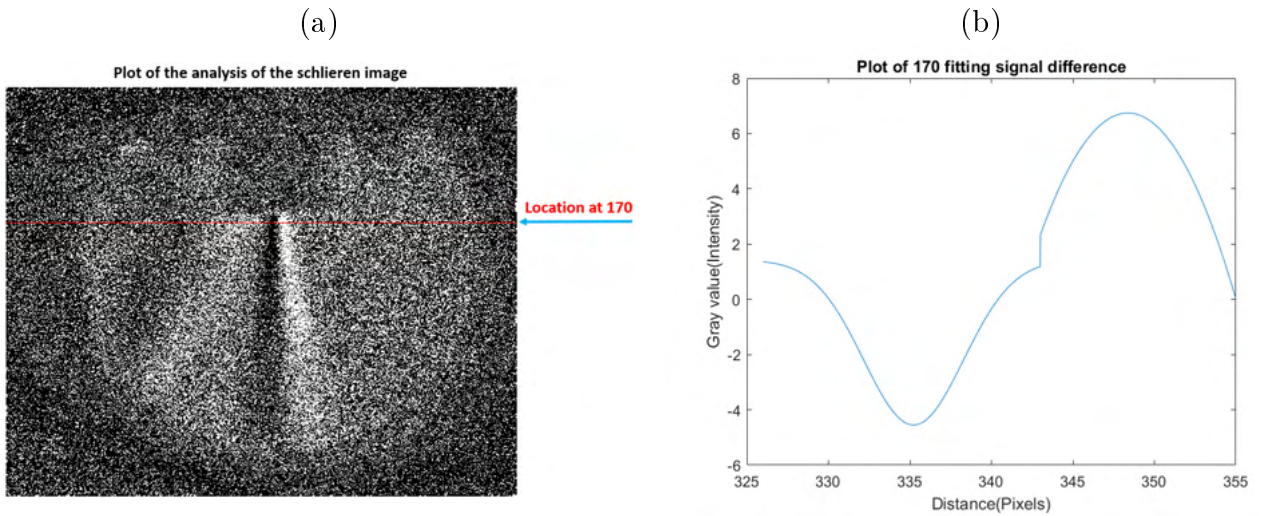


Figure 106: (a) The horizontal line profile of the experimental setup at 5-atm pressure difference case. (b) The signal intensity difference of the location of the horizontal line at 170 pixels.

Following the steps in section 1.1.4, the horizontal profiles of the differential images 1.1 mm below the nozzles was obtained. Figure 107(a) is the differential image in the case where 6-atm pressure difference was used. Figure 107(b) is the profile of the differential image along the red line in figure 107(a). The maximum of the profile is 5.2 ± 3.2 a.u. and the minimum is -4.5 ± 1.9 a.u.. The contrast is 9.7 ± 5.1 a.u..

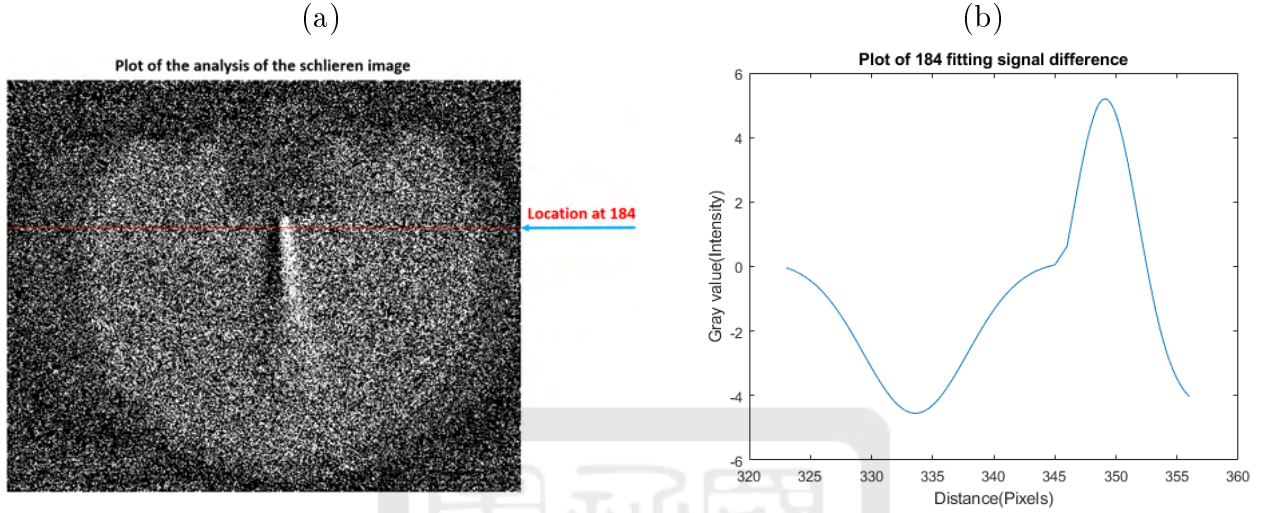


Figure 107: (a) The horizontal line profile of the experimental setup at 6-atm pressure difference case. (b) The signal intensity difference of the location of the horizontal line at 184 pixels.

Following the steps in section 1.1.4, the horizontal profiles of the differential images 1.1 mm below the nozzles was obtained. Figure 108(a) is the differential image in the case where 7-atm pressure difference was used. Figure 108(b) is the profile of the differential image along the red line in figure 108(a). The maximum of the profile is 7.3 ± 1.8 a.u. and the minimum is -4.4 ± 2 a.u.. The contrast is 11.7 ± 3.8 a.u..

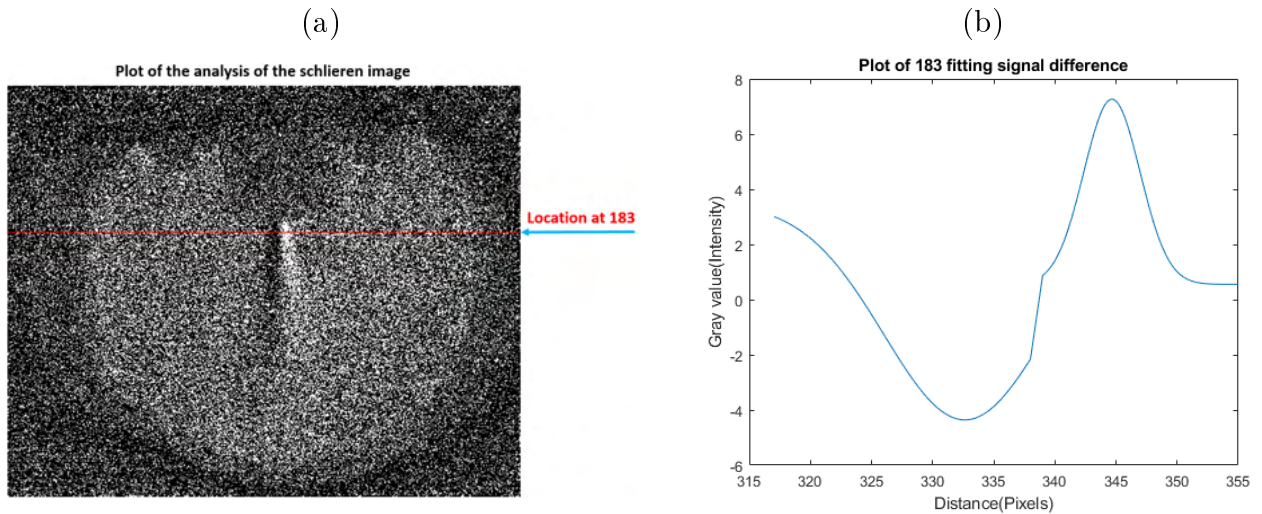


Figure 108: (a) The horizontal line profile of the experimental setup at 7-atm pressure difference case. (b) The signal intensity difference of the location of the horizontal line at 183 pixels.

Following the steps in section 1.1.4, the horizontal profiles of the differential images 1.1 mm below the nozzle was obtained. Figure 109(a) is the differential image in the case where 8-atm pressure difference was used. Figure 109(b) is the profile of the differential image along the red line in figure 109(a). The maximum of the profile is 4.1 ± 1.1 a.u. and the minimum is -2.6 ± 2 a.u.. The contrast is 6.7 ± 3.1 a.u..

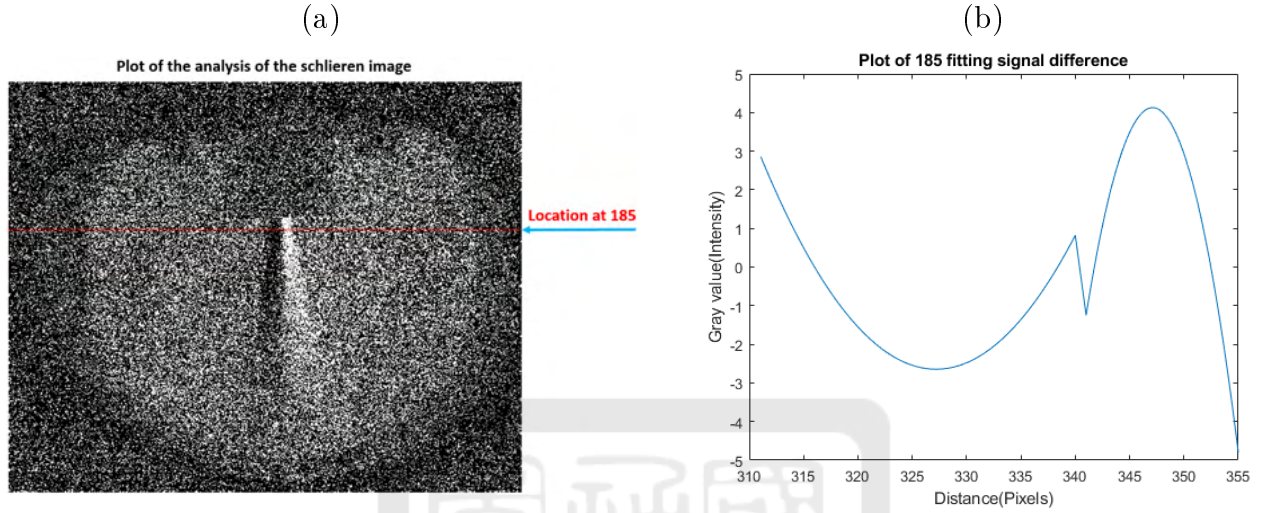


Figure 109: (a) The horizontal line profile of the experimental setup at 8-atm pressure difference case. (b) The signal intensity difference of the location of the horizontal line at 185 pixels.

Following the steps in section 1.1.4, the horizontal profiles of the differential images 1.1 mm below the nozzle was obtained. Figure 110(a) is the differential image in the case where 9-atm pressure difference was used. Figure 110(b) is the profile of the differential image along the red line in figure 110(a). The maximum of the profile is 3.3 ± 4 a.u. and the minimum is -2.7 ± 4.1 a.u.. The contrast is 6 ± 8.1 a.u..

The contrast of the differential images was no difference in all cases.

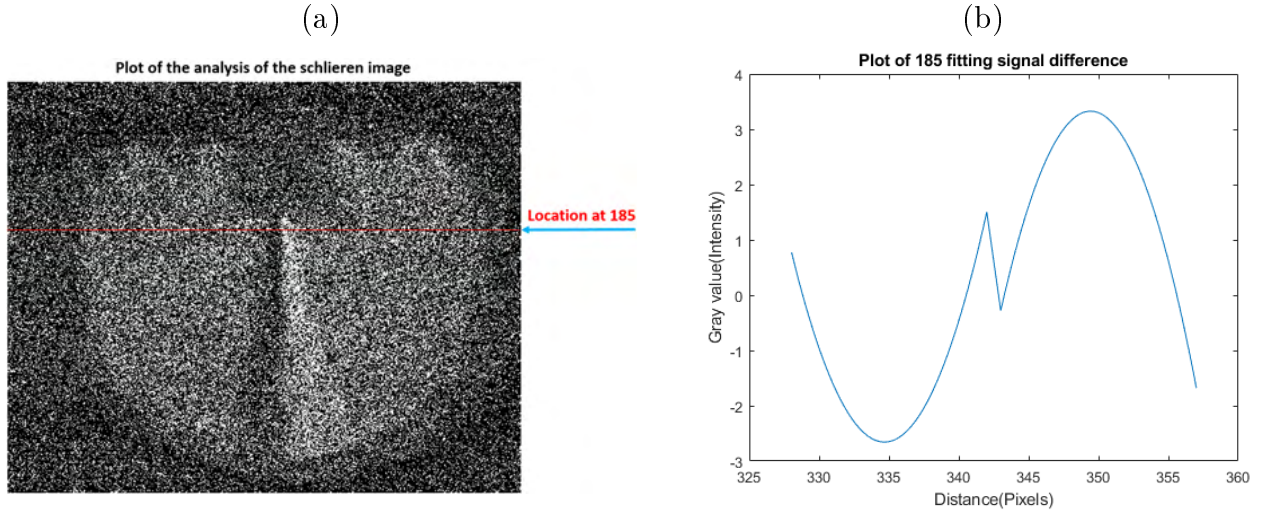


Figure 110: (a) The horizontal line profile of the experimental setup at 9-atm pressure difference case. (b) The signal intensity difference of the location of the horizontal line at 185 pixels.

Following the step in section 1.1.2, the slope of the propagating path of the 5-atm pressure difference case is 0.05 ± 0.06 as shown in figure 111. Therefore, the opening angle of the gas puff is $2.86^\circ \pm 3.43^\circ$. On the other hand, following the step in section 1.1.3, the slope of the propagating center of the 5-atm pressure difference case is 0.14 ± 0.07 as shown in figure 112. The tilted angle of the CDN is $7.97^\circ \pm 4^\circ$.

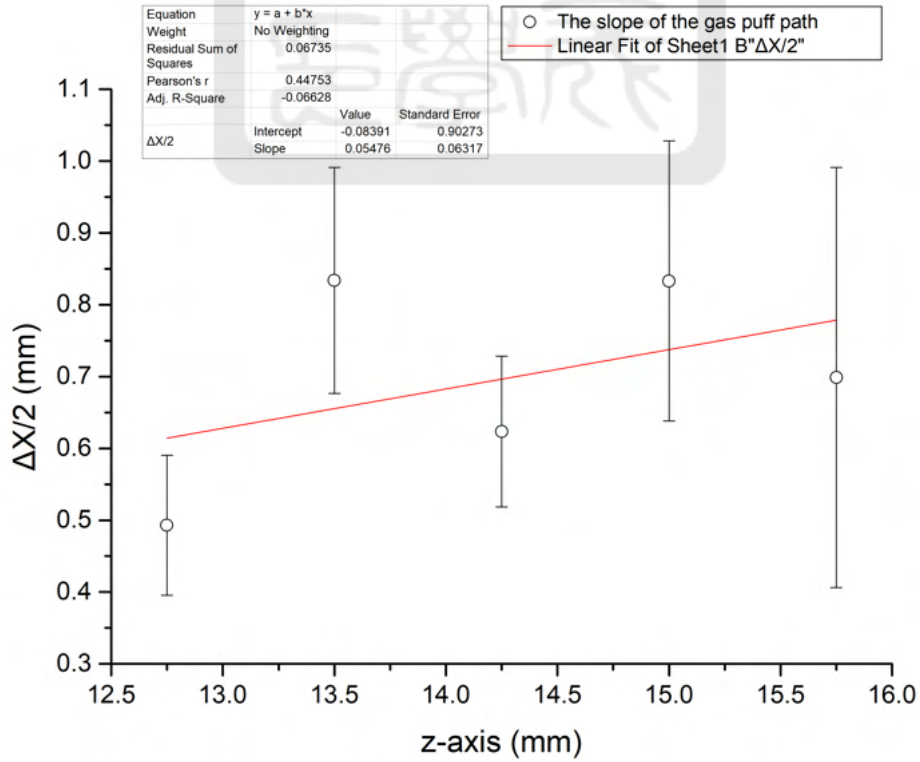


Figure 111: The slope of the propagating path of the experimental setup at 5-atm pressure difference case.

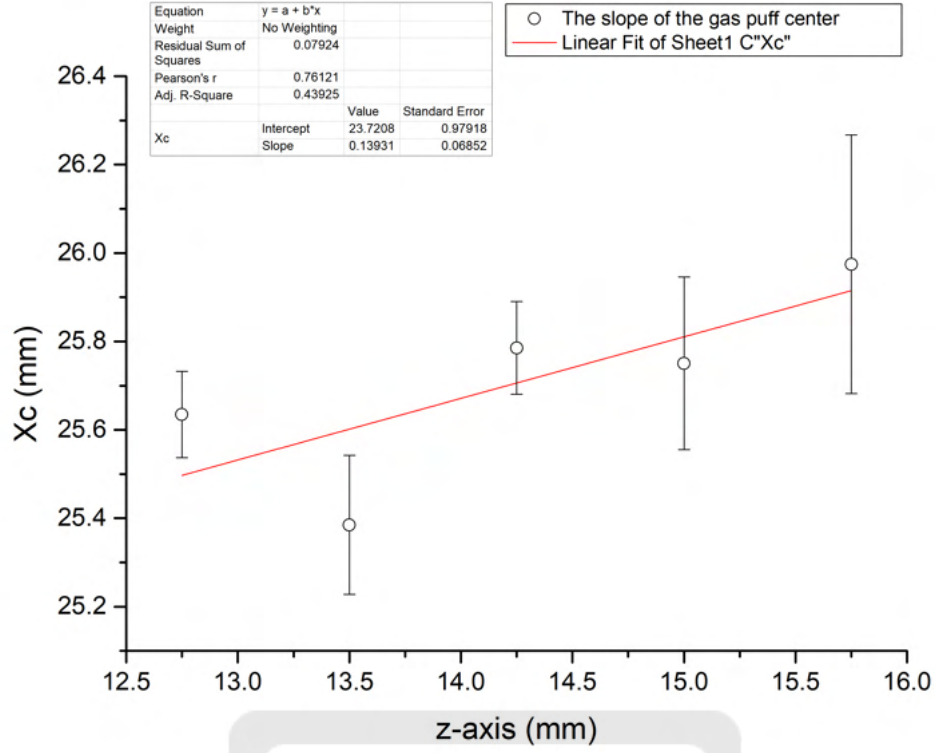


Figure 112: The slope of the propagating center of the experimental setup at 5-atm pressure difference case.

Following the step in section 1.1.2, the slope of the propagating path of the 6-atm pressure difference case is -0.01 ± 0.03 as shown in figure 113. Therefore, the opening angle of the gas puff is $-0.57^\circ \pm 1.72^\circ$. On the other hand, following the step in section 1.1.3, the slope of the propagating center of the 6-atm pressure difference case is 0.07 ± 0.07 as shown in figure 114. The tilted angle of the CDN is $4^\circ \pm 4^\circ$.

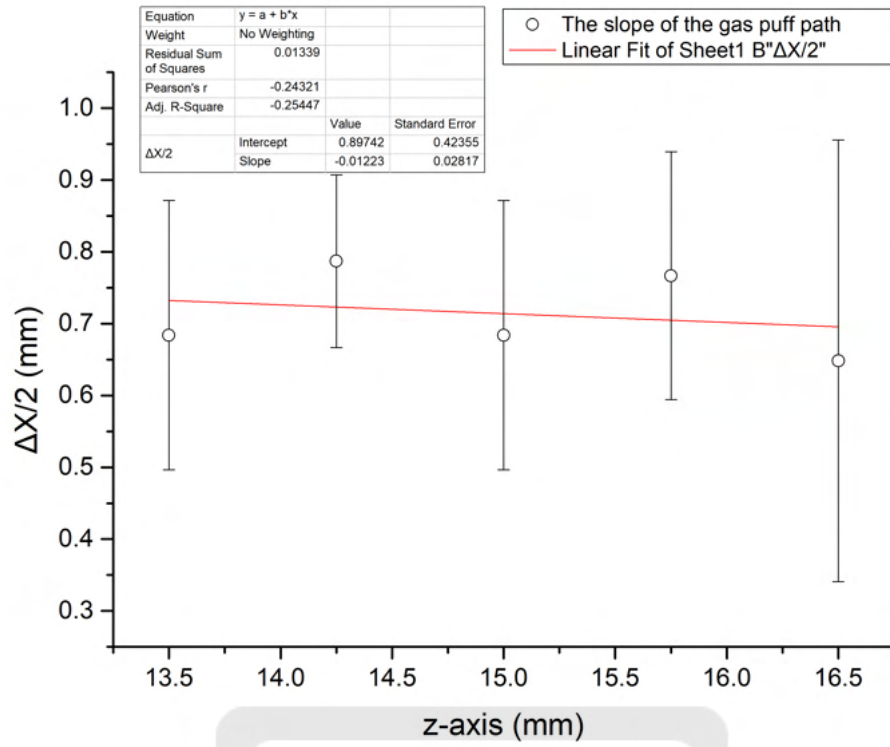


Figure 113: The slope of the propagating path of the experimental setup at 6-atm pressure difference case.

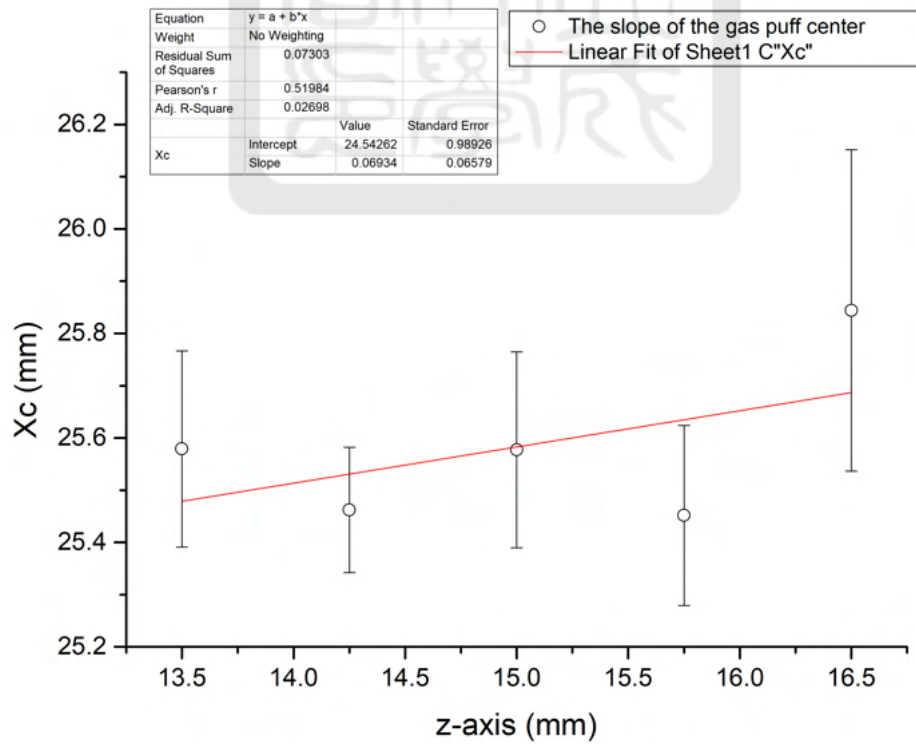


Figure 114: The slope of the propagating center of the experimental setup at 6-atm pressure difference case.

Following the step in section 1.1.2, the slope of the propagating path of the 7-atm pressure difference case is 0.06 ± 0.05 as shown in figure 115. Therefore, the opening angle of the gas puff is $3.43^\circ \pm 2.86^\circ$. On the other hand, following the step in section 1.1.3, the slope of the propagating center of the 7-atm pressure difference case is 0.04 ± 0.05 as shown in figure 116. The tilted angle of the CDN is $2.29^\circ \pm 2.86^\circ$.

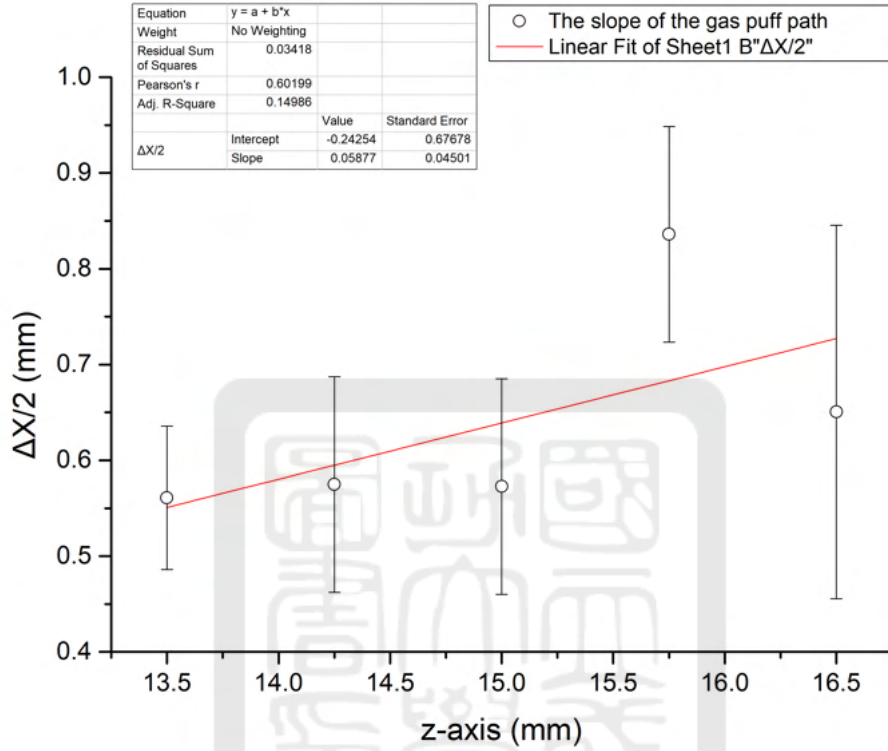


Figure 115: The slope of the propagating path of the experimental setup at 7-atm pressure difference case.

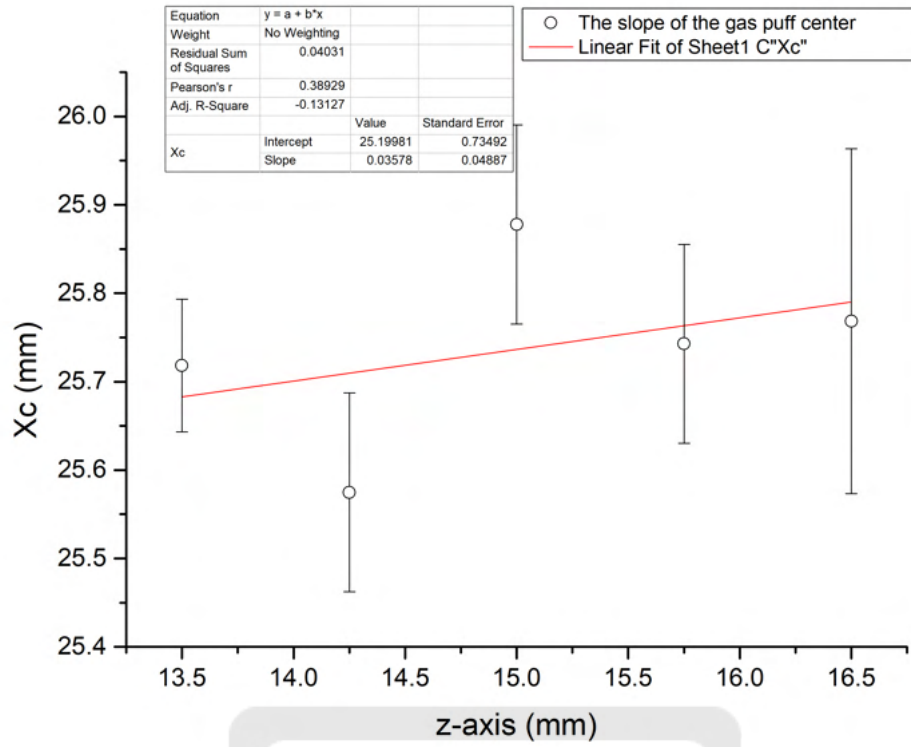


Figure 116: The slope of the propagating center of the experimental setup at 7-atm pressure difference case.

Following the step in section 1.1.2, the slope of the propagating path of the 8-atm pressure difference case is 0.12 ± 0.06 as shown in figure 117. Therefore, the opening angle of the gas puff is $6.84^\circ \pm 3.43^\circ$. On the other hand, following the step in section 1.1.3, the slope of the propagating center of the 8-atm pressure difference case is -0.04 ± 0.1 as shown in figure 118. The tilted angle of the CDN is $-2.29^\circ \pm 5.71^\circ$.

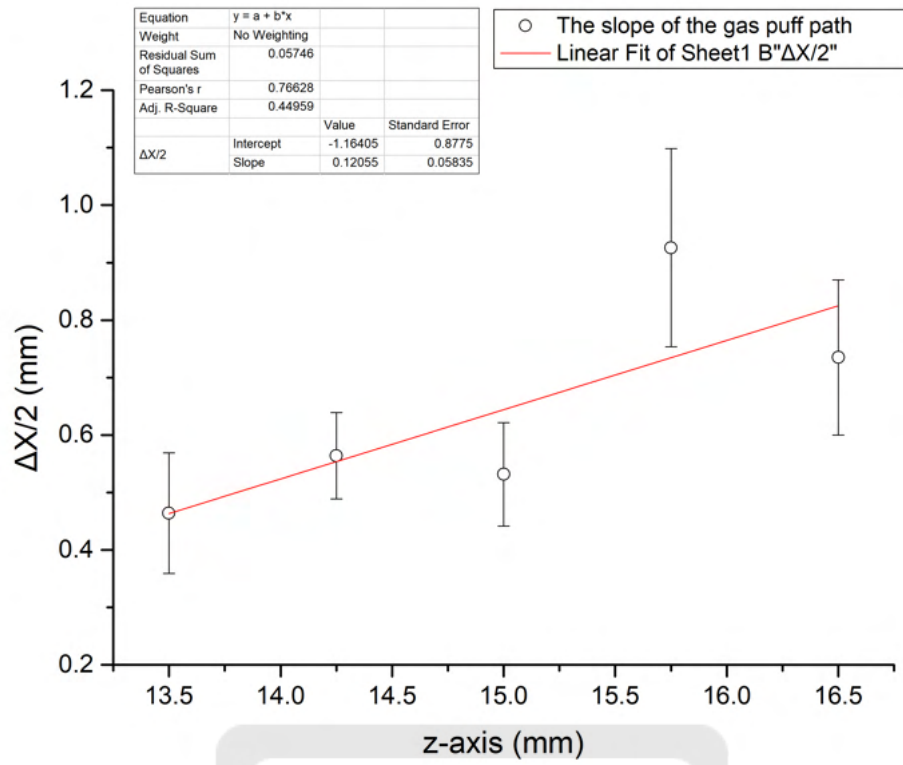


Figure 117: The slope of the propagating path of the experimental setup at 8-atm pressure difference case.

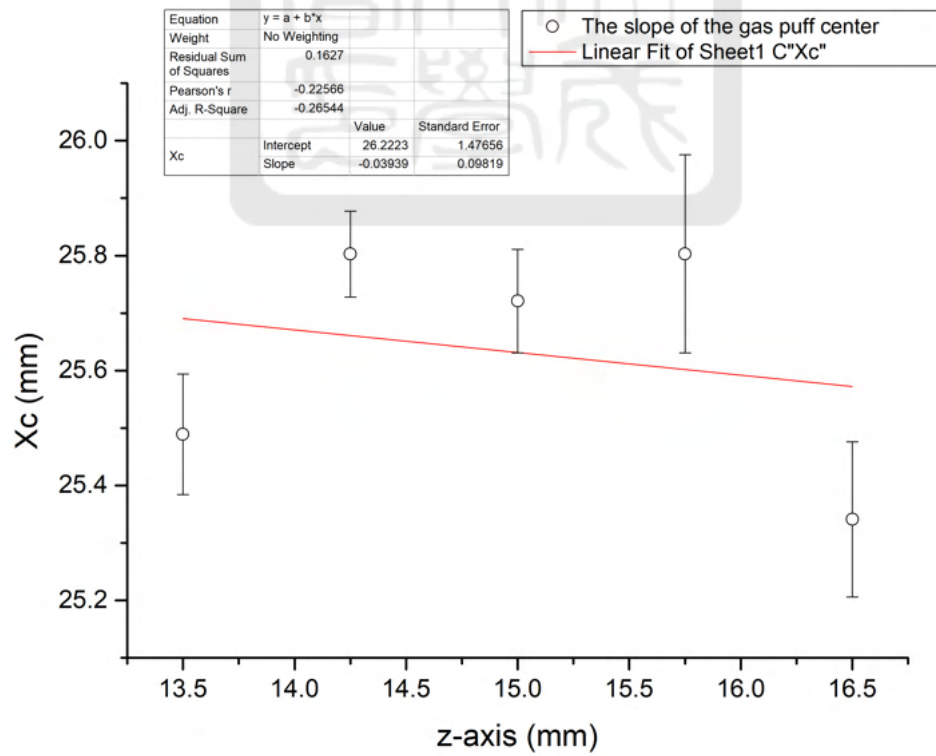


Figure 118: The slope of the propagating center of the experimental setup at 8-atm pressure difference case.

Following the step in section 1.1.2, the slope of the propagating path of the 9-atm pressure difference case is 0.04 ± 0.05 as shown in figure 119. Therefore, the opening angle of the gas puff is $2.29^\circ \pm 2.86^\circ$. On the other hand, following the step in section 1.1.3, the slope of the propagating center of the 9-atm pressure difference case is 0.27 ± 0.13 as shown in figure 120. The tilted angle of the CDN is $15.11^\circ \pm 7.41^\circ$.

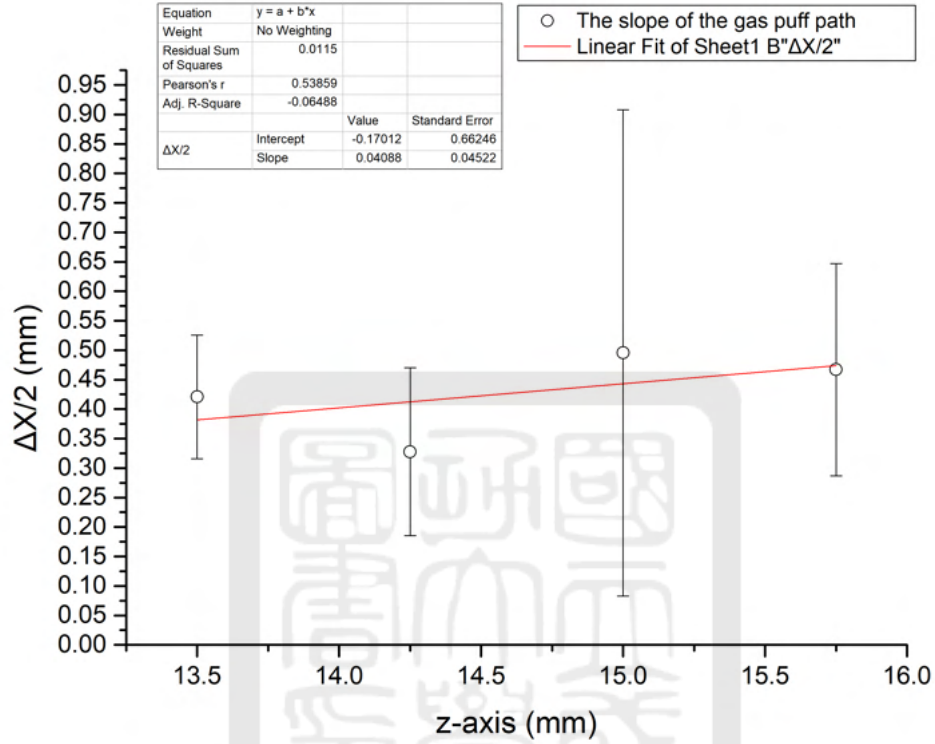


Figure 119: The slope of the propagating path of the experimental setup at 9-atm pressure difference case.

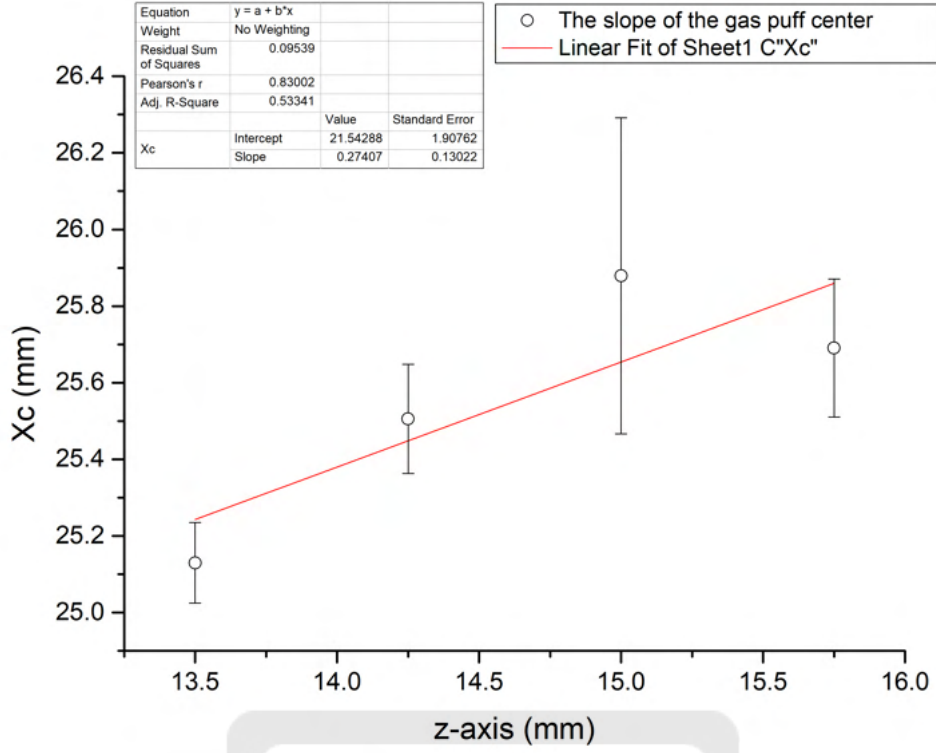


Figure 120: The slope of the propagating center of the experimental setup at 9-atm pressure difference case.

Table 13 is the comparison result of the experimental setups with different gas pressure. The opening angles of the gas puffs were not significantly different in all cases. The tilted angle of the CDN with gas pressure of 9 atm was the largest. Because of the largest tilted angle, the 9-atm pressure difference case was out of our choices. In order to do the experiment more safely, we chose the 5-atm pressure difference case in the rest of experiments.

Table 13: The comparisons of the experimental setup at different pressure.

	5 atm (★)	6 atm	7 atm	8 atm	9 atm
The contrast (a.u.)	11.2 ± 2.3	9.7 ± 5.1	11.7 ± 3.8	6.7 ± 3.1	6 ± 8.1
The opening angle of the gas puff	$2.86^\circ \pm 3.43^\circ$	$-0.57^\circ \pm 1.72^\circ$	$3.43^\circ \pm 2.86^\circ$	$6.84^\circ \pm 3.43^\circ$	$2.29^\circ \pm 2.86^\circ$
The tilt angle of the CDN	$7.97^\circ \pm 4^\circ$	$4^\circ \pm 4^\circ$	$2.29^\circ \pm 2.86^\circ$	$-2.29^\circ \pm 5.71^\circ$	$15.11^\circ \pm 7.41^\circ$

5.2.6 Summary

We have tested many experimental setups with a 24-V pulse valve. They are:

- (1) Different locations of the pulse valve (20 cm case v.s. 42 cm from the convex lens).

- (2) Different Schlieren knife-edge setting (Tilted v.s. horizontal v.s. vertical schlieren knife).
- (3) Different temperature of the gas puff (15°C v.s. 25°C).
- (4) Different convergent-divergent nozzles (V5A v.s. V5B v.s. V6 CDN).
- (5) Different pressure of the argon gas (5 ~ 9 atm pressure difference).

From the first two experiments, we found that the pulse valve set at 20 cm from the convex lens and the vertical knife-edge provided the clearest schlieren images. On the other hand, the contrast of the differential image was higher in the 25°C–gas puff case than in the 15°C–gas puff case in the third experiment. Further for different CDNs, the results were that the contrast of the differential image was higher in the V5A CDN case than those in other cases, and the tilted angle of the V5A CDN was the smallest. Furthermore, the results with different gas pressure were no significantly different in all cases. However, the 5-atm pressure difference case was safer than those choices when we did experiments. Finally, conditions with the pulse valve set at 20 cm from the convex lens, the vertical knife-edge, the 25°C–gas puff, the V5A CDN, and the 5-atm pressure difference was the best.

5.3 12-V pulse valve

The 12-V pulse valve with a larger output diameter was used to provide a larger gas puff compared to the 24-V pulse valve. Because of the large output diameter, we used V7 and V8 CDN for the 12-V pulse valve as shown in figure 121(a) and figure 121(b). The V7 CDN has an intake with 5.3 mm in diameter, a waist with 2 mm in diameter, and an output with 2.6 mm in diameter. The V8 CDN has an intake with 5.3 mm in diameter, a waist with 1 mm in diameter, and an output with 1.3 mm in diameter. Notice that the structure of the CDN has a 0.3-mm systematic difference between the CAD drawing and the final product made by the 3D printer so the diameters in figure 121 are 0.3 mm larger than the final product. The experimental setups with the pulse valve 20 cm from the convex lens, the vertical knife-edge, and 25° - gas puff were used. Shown in table 14 are all different conditions we tested. A short summary is provided at the end of each section. A summary is provided at the end of the section.

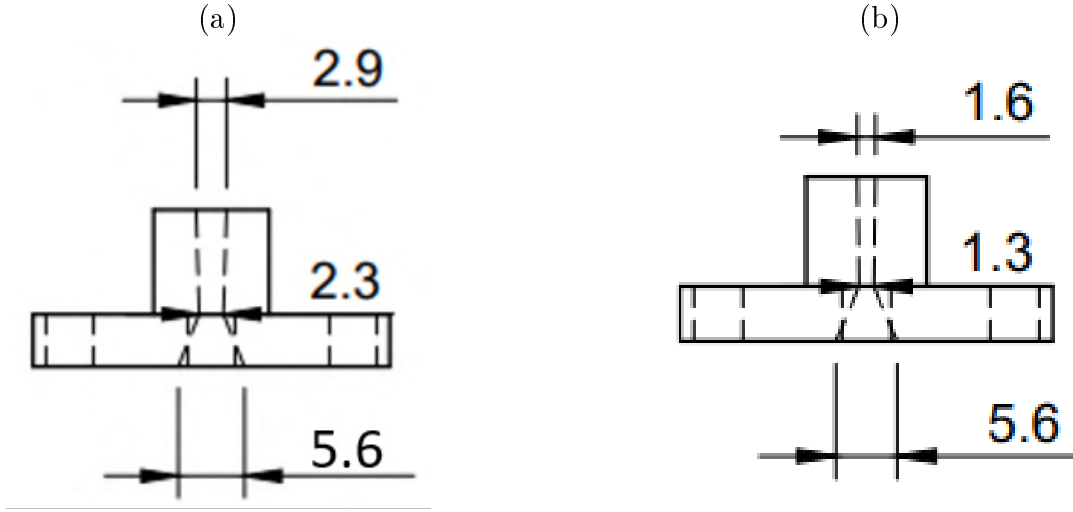


Figure 121: (a) V7 CDN. (b) V8 CDN.

Table 14: The 12-V pulse valve experimental setup in different conditions.

	The choice of Convergent-divergent nozzle (CDN)	The choice of Convergent-divergent nozzle (CDN)	The choice of Convergent-divergent nozzle (CDN)
0.5-atm pressure difference	None	V7	V8
1-atm pressure difference	None	V7	V8

5.3.1 No convergent-divergent nozzle (CDN), 0.5-atm pressure difference

In this section, we focus on observing the collimation of the gas puff generated by the 12-V pulse valve directly. Therefore, we conducted experiments without CDNs.

Following the steps in section 1.1.4, the horizontal profiles of the differential images 1.1 mm below the nozzle was obtained. Figure 122(a) is the differential image in the case without CDN at 0.5-atm pressure difference. Figure 122(b) is the profile of the differential image along the red line in figure 122(a). The maximum of the profile is $16.9 \pm 1.5 \text{ a.u.}$ and the minimum is $-4 \pm 1 \text{ a.u.}$. The contrast is $20.9 \pm 2.5 \text{ a.u.}$.

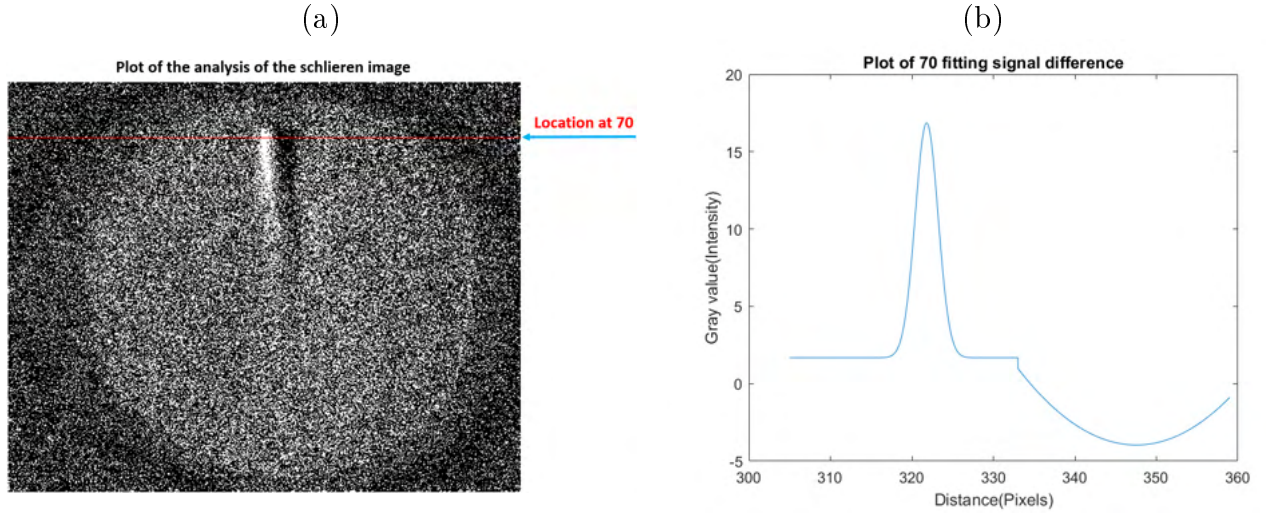


Figure 122: (a) The horizontal line profile of the experimental setup without CDN at 0.5-atm pressure difference case. (b) The signal intensity difference of the location of the horizontal line at 70 pixels.

Following the step in section 1.1.2, the slope of the propagating path in the case without CDN at 0.5-atm pressure difference is 0.04 ± 0.08 as shown in figure 123. Because the most of data points with the standard deviation were out of the fitting line, the signal intensity was not stable. Therefore, the opening angle of the gas puff is $2.29^\circ \pm 4.57^\circ$. On the other hand, following the step in section 1.1.3, the slope of the propagating center of the case without CDN at 0.5-atm pressure difference is 0.1 ± 0.05 as shown in figure 124. The tilted angle of the 12-V pulse valve is $5.71^\circ \pm 2.86^\circ$.

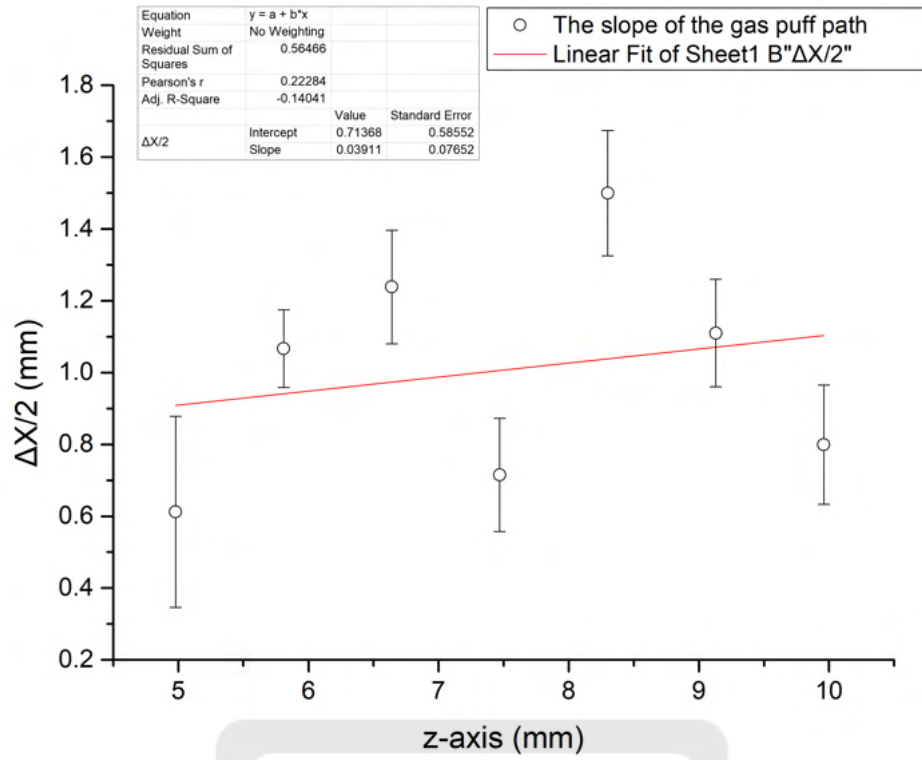


Figure 123: The slope of the propagating path of the experimental setup without CDN at 0.5-atm pressure difference case.

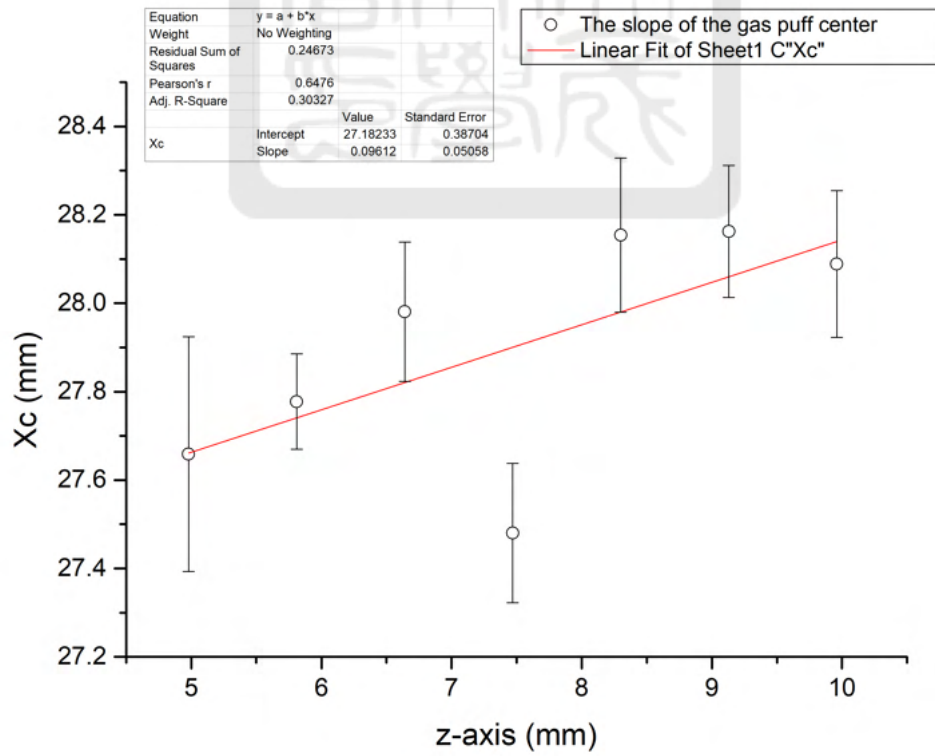


Figure 124: The slope of the propagating center of the experimental setup without CDN at 0.5-atm pressure difference case.

For no CDN at 0.5-atm pressure difference, the contrast is 20.9 ± 2.5 a.u., the opening angle of the gas puff is $2.29^\circ \pm 4.57^\circ$ and the tilted angle of the 12-V pulse valve is $5.71^\circ \pm 2.86^\circ$.

5.3.2 No convergent-divergent nozzle (CDN), 1-atm pressure difference

Following the steps in section 1.1.4, the horizontal profiles of the differential images 1.1 mm below the nozzle was obtained. Figure 125(a) is the differential image in the case where without CDN at 1-atm pressure difference. Figure 125(b) is the profile of the differential image along the red line in figure 125(a). The maximum of the profile is 46 ± 2.4 a.u. and the minimum is -17.2 ± 14.3 a.u.. The contrast is 63.2 ± 16.7 a.u..

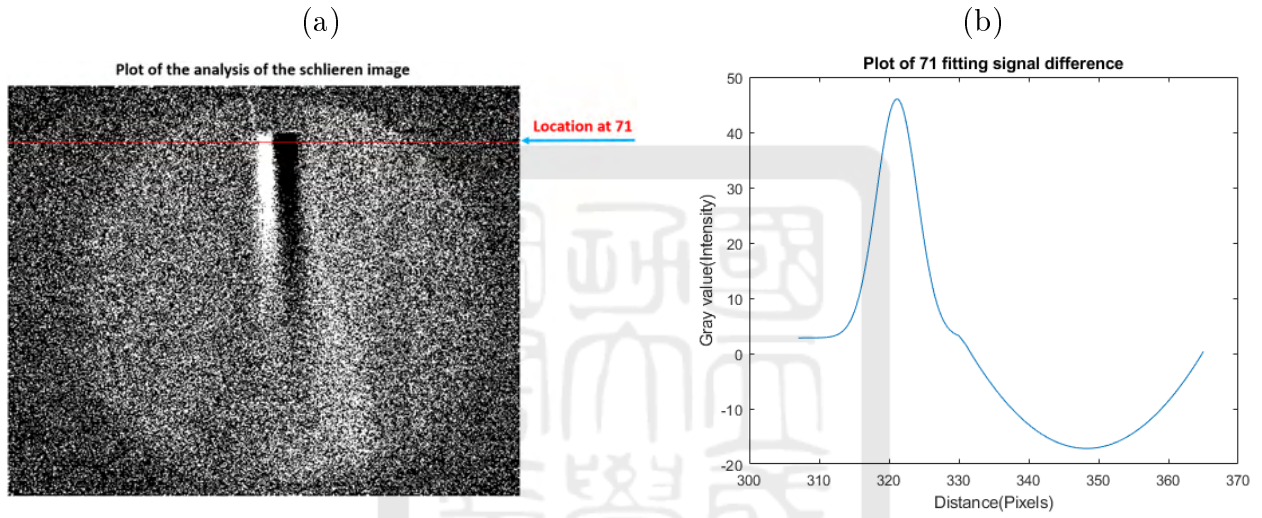


Figure 125: (a) The horizontal line profile of the experimental setup without CDN at 1-atm pressure difference case. (b) The signal intensity difference of the location of the horizontal line at 71 pixels.

Following the step in section 1.1.2, the slope of the propagating path in the case without CDN at 1-atm pressure difference is 0.002 ± 0.005 as shown in figure 126. Therefore, the opening angle of the gas puff is $0.115^\circ \pm 0.286^\circ$. On the other hand, following the step in section 1.1.3, the slope of the propagating center of the case without CDN at 0.5-atm pressure difference is 0.051 ± 0.012 as shown in figure 127. The tilted angle of the 12-V pulse valve is $2.92^\circ \pm 0.69^\circ$.

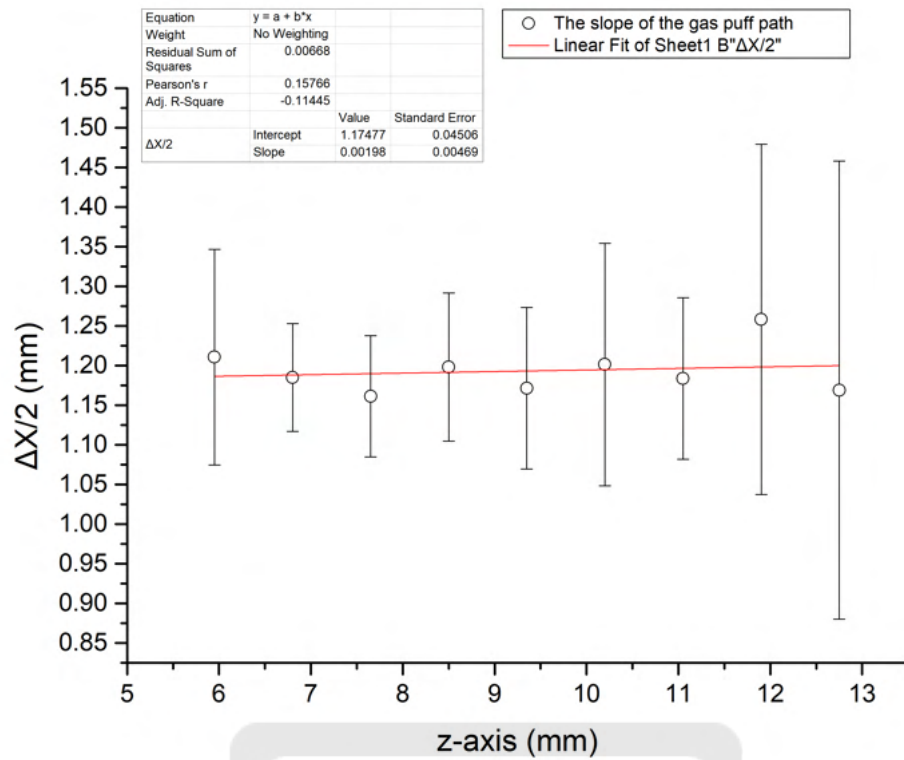


Figure 126: The slope of the propagating path of the experimental setup without CDN at 1-atm pressure difference case.

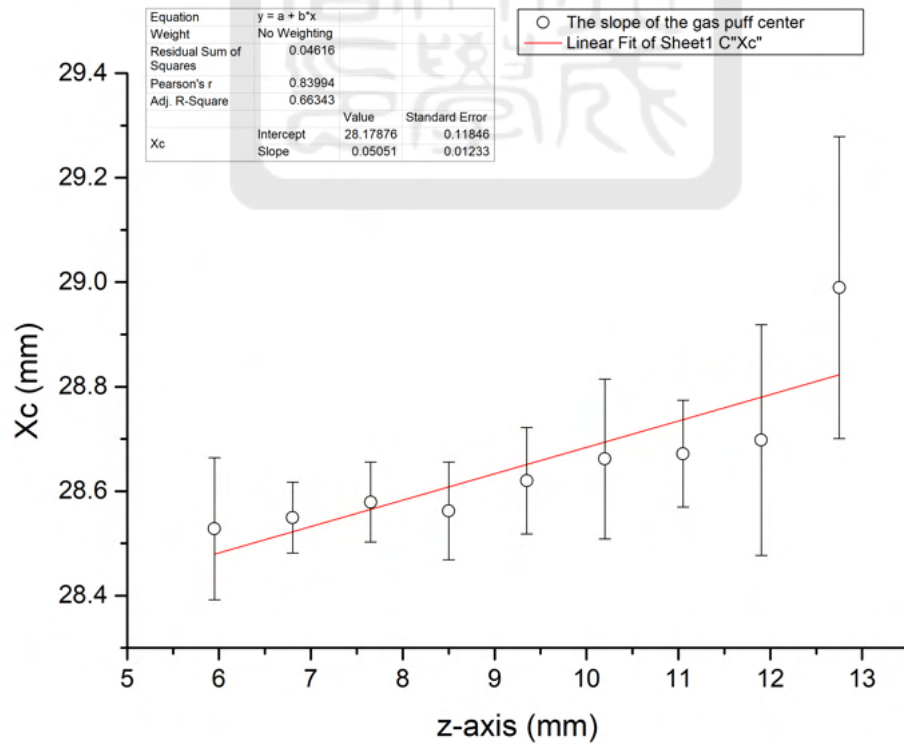


Figure 127: The slope of the propagating center of the experimental setup without CDN at 1-atm pressure difference case.

For no CDN at 1-atm pressure difference, the contrast is 63.2 ± 16.7 a.u., the opening angle of the gas puff is $2.29^\circ \pm 4.57^\circ$ and the tilted angle of the 12-V pulse valve is $5.71^\circ \pm 2.86^\circ$.

5.3.3 V7 convergent-divergent nozzle (CDN), 0.5-atm pressure difference

Following the steps in section 1.1.4, the horizontal profiles of the differential images 1.1 mm below the nozzle was obtained. Figure 128(a) is the differential image in the case with V7 CDN at 0.5-atm pressure difference. Figure 128(b) is the profile of the differential image along the red line in figure 128(a). The maximum of the profile is 27.7 ± 2 a.u. and the minimum is -13 ± 9.4 a.u.. The contrast is 40.7 ± 11.4 a.u..

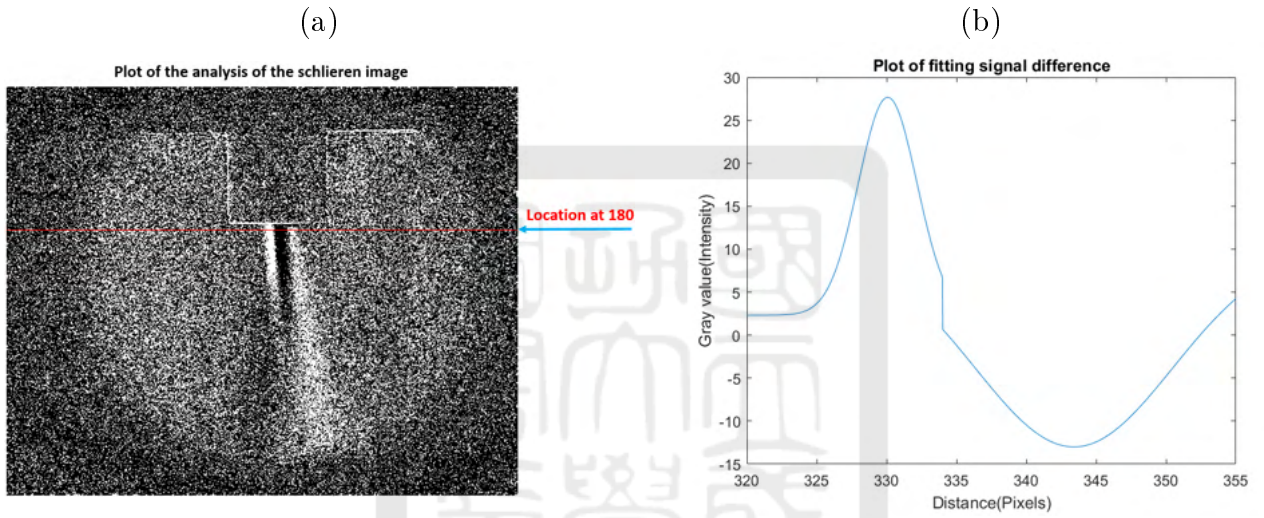


Figure 128: (a) The horizontal line profile of the experimental setup with V7 CDN at 0.5-atm pressure difference case. (b) The signal intensity difference of the location of the horizontal line at 180 pixels.

Following the step in section 1.1.2, the slope of the propagating path in the case with V7 CDN at 0.5-atm pressure difference case is -0.0001 ± 0.0112 as shown in figure 129. Therefore, the opening angle of the gas puff is $-0.006^\circ \pm 0.642^\circ$. On the other hand, following the step in section 1.1.3, the slope of the propagating center of the case with V7 CDN at 0.5-atm pressure difference is 0.067 ± 0.023 as shown in figure 130. The tilted angle of the V7 CDN is $3.83^\circ \pm 1.32^\circ$.

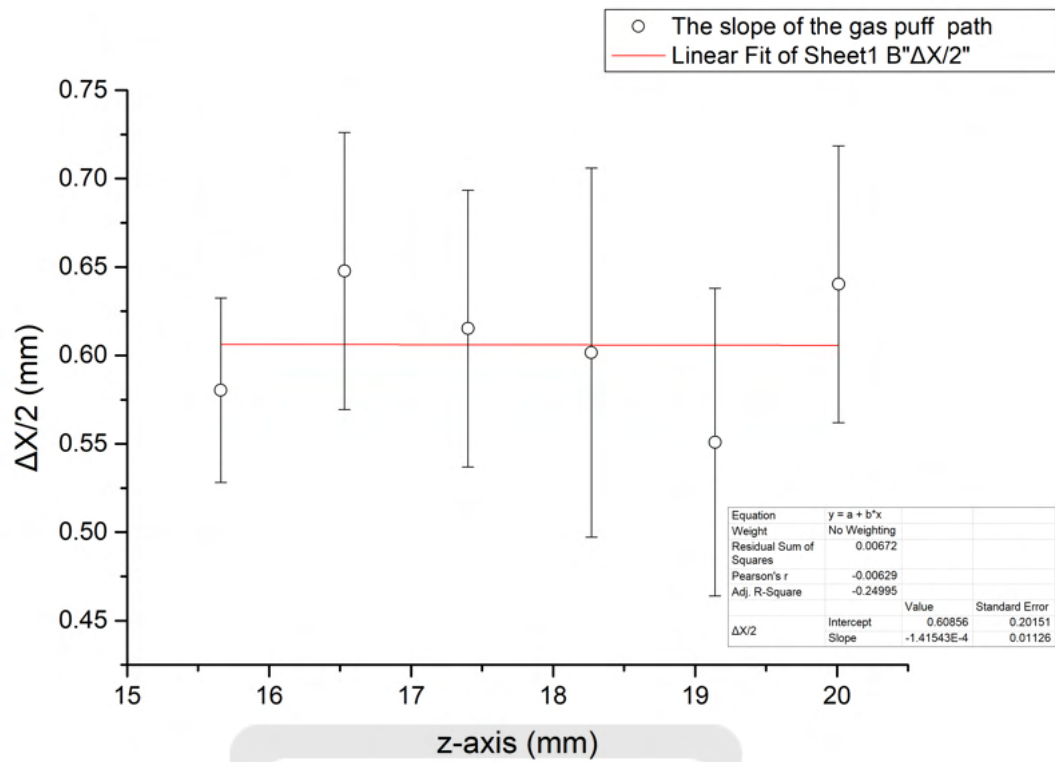


Figure 129: The slope of the propagating path of the experimental setup with V7 CDN at 0.5-atm pressure difference case.

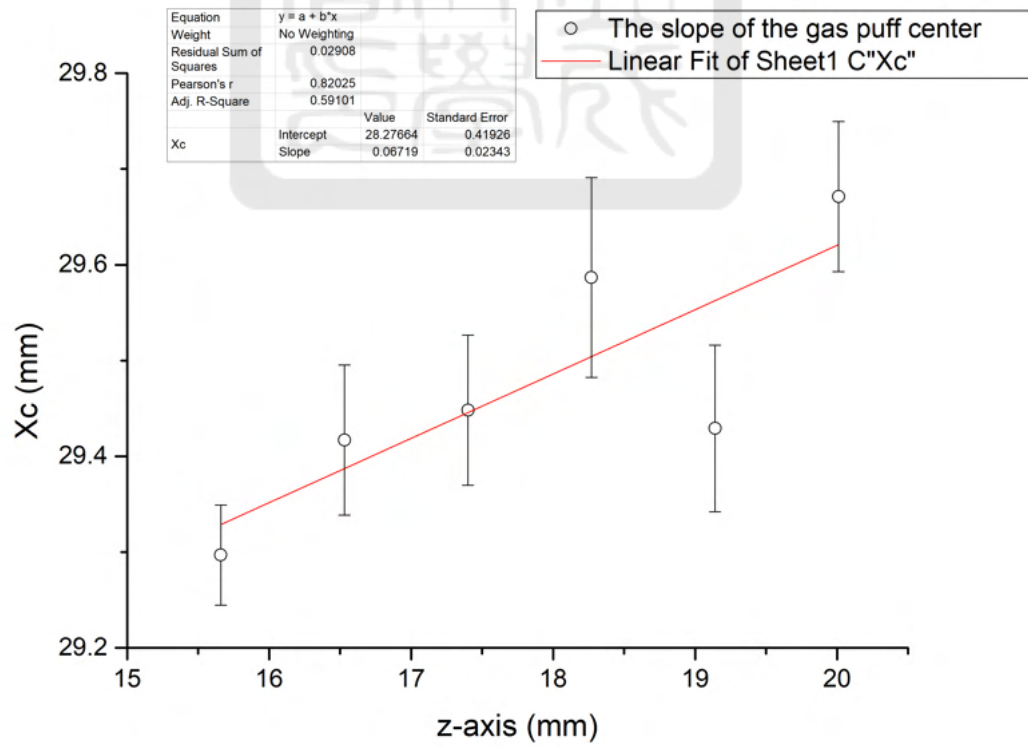


Figure 130: The slope of the propagating center of the experimental setup with V7 CDN at 0.5-atm pressure difference case.

For V7 CDN at 0.5-atm pressure difference, the result of the contrast is 40.7 ± 11.4 a.u., the opening angle of the gas puff is $-0.006^\circ \pm 0.642^\circ$ and the tilted angle of the V7 CDN is $3.83^\circ \pm 1.32^\circ$.

5.3.4 V7 convergent-divergent nozzle (CDN), 1-atm pressure difference

Following the steps in section 1.1.4, the horizontal profiles of the differential images 1.1 mm below the nozzle was obtained. Figure 131(a) is the differential image in the case with V7 CDN at 1-atm pressure difference. Figure 131(b) is the profile of the differential image along the red line in figure 131(a). The maximum of the profile is 40.2 ± 2.2 a.u. and the minimum is -19.6 ± 2.2 a.u.. The contrast is 59.8 ± 4.4 a.u..

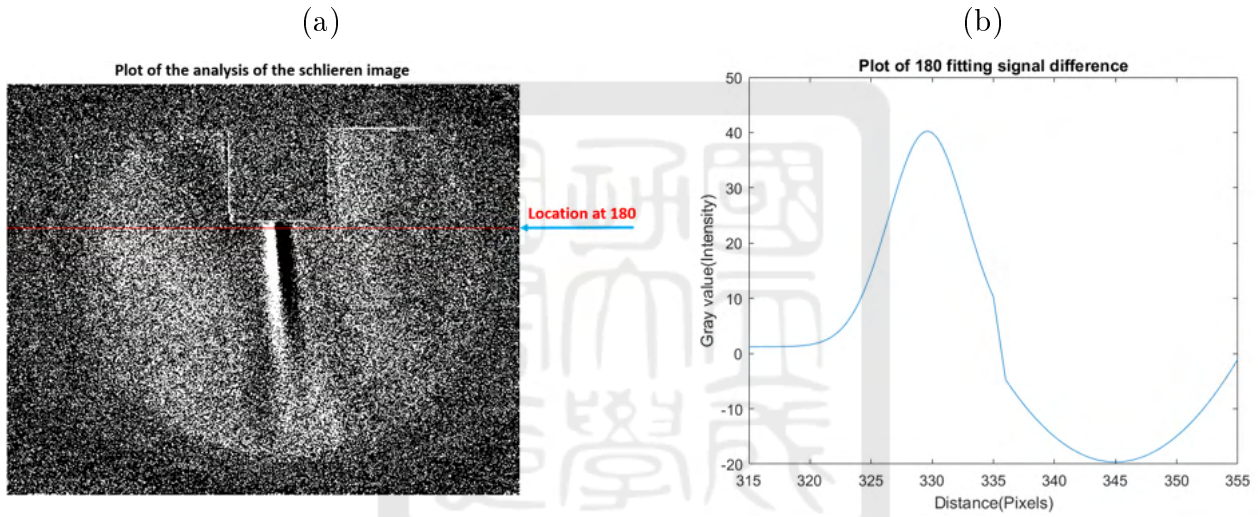


Figure 131: (a) The horizontal line profile of the experimental setup with V7 CDN at 1-atm pressure difference case. (b) The signal intensity difference of the location of the horizontal line at 180 pixels.

Following the step in section 1.1.2, the slope of the propagating path in the case with V7 CDN at 1-atm pressure difference is 0.023 ± 0.005 as shown in figure 132. Therefore, the opening angle of the gas puff is $1.32^\circ \pm 0.29^\circ$. On the other hand, following the step in section 1.1.3, the slope of the propagating center of the case with V7 CDN at 1-atm pressure difference is 0.083 ± 0.004 as shown in figure 133. The tilted angle of the CDN is $4.74^\circ \pm 0.23^\circ$.

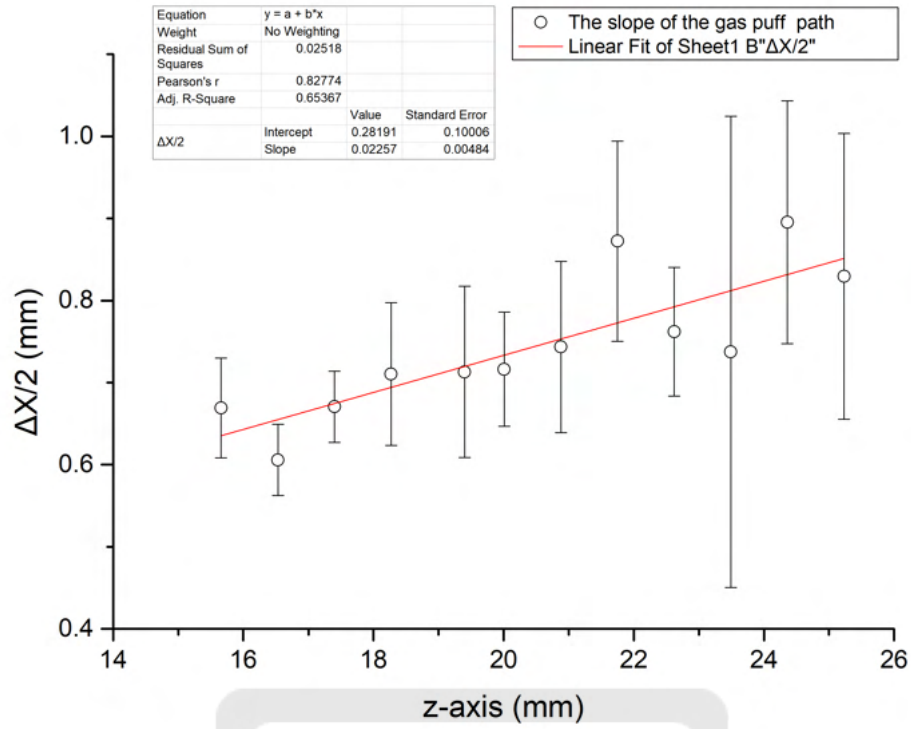


Figure 132: The slope of the propagating path of the experimental setup with V7 CDN at 1-atm pressure difference case.

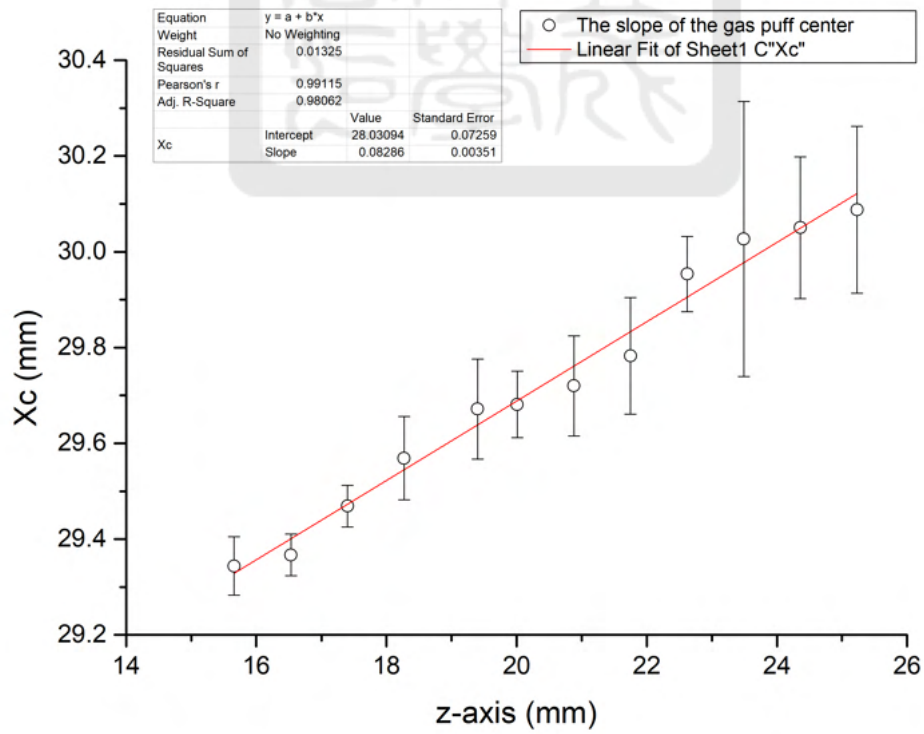


Figure 133: The slope of the propagating center of the experimental setup with V7 CDN at 1-atm pressure difference case.

For V7 CDN at 1-atm pressure difference, the contrast is 59.8 ± 4.4 a.u., the opening angle of the gas puff is $1.32^\circ \pm 0.29^\circ$ and the tilted angle of the V7 CDN is $4.74^\circ \pm 0.23^\circ$.

5.3.5 V8 convergent-divergent nozzle (CDN), 0.5-atm pressure difference

Following the steps in section 1.1.4, the horizontal profiles of the differential images 1.1 mm below the nozzle was obtained. Figure 134(a) is the differential image in the case where the experimental setup with V8 CDN at 0.5-atm pressure difference. Figure 134(b) is the profile of the differential image along the red line in figure 134(a). The maximum of the profile is 6.1 ± 1.8 a.u. and the minimum is -4.3 ± 1.5 a.u.. The contrast is 10.4 ± 3.3 a.u..

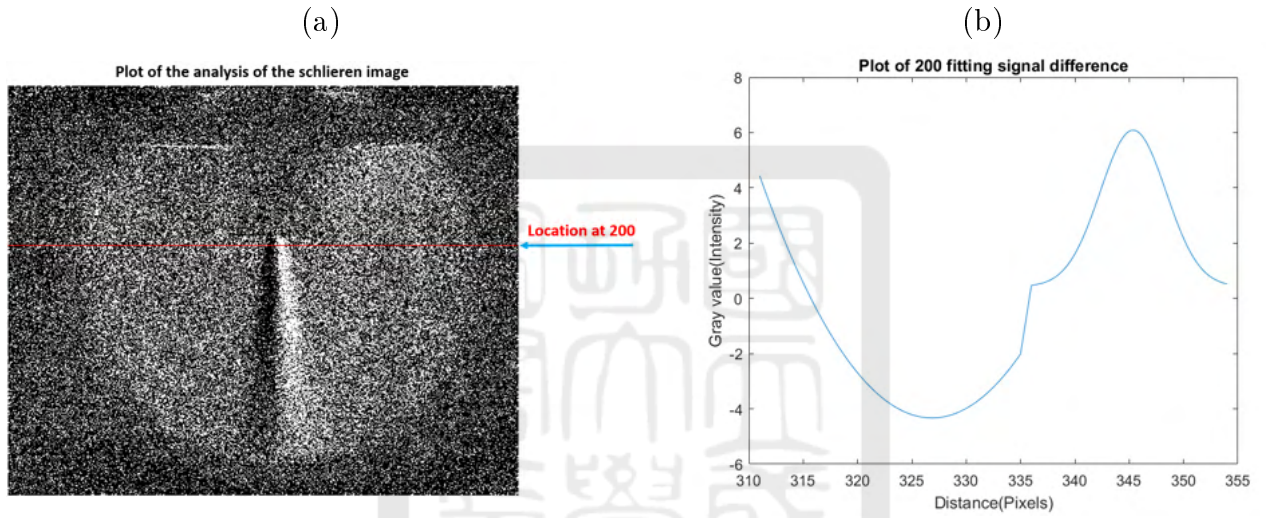


Figure 134: (a) The horizontal line profile of the experimental setup with V8 CDN at 0.5-atm pressure difference case. (b) The signal intensity difference of the location of the horizontal line at 200 pixels.

Following the step in section 1.1.2, the slope of the propagating path in the case with V8 CDN at 0.5-atm pressure difference is 0.09 ± 0.06 as shown in figure 135. Therefore, the opening angle of the gas puff is $5.14^\circ \pm 3.43^\circ$. On the other hand, following the step in section 1.1.3, the slope of the propagating center of the case with V8 CDN at 0.5-atm pressure difference is 0.06 ± 0.04 as shown in figure 136. The tilted angle of the CDN is $3.43^\circ \pm 2.29^\circ$.

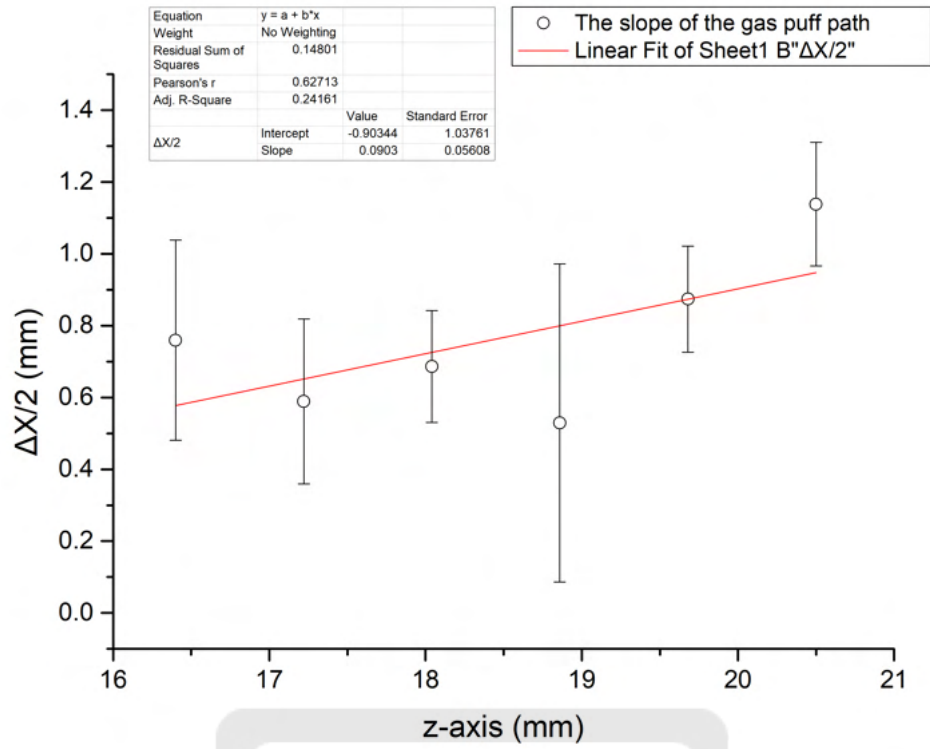


Figure 135: The slope of the propagating path of the experimental setup with V8 CDN at 0.5-atm pressure difference case.

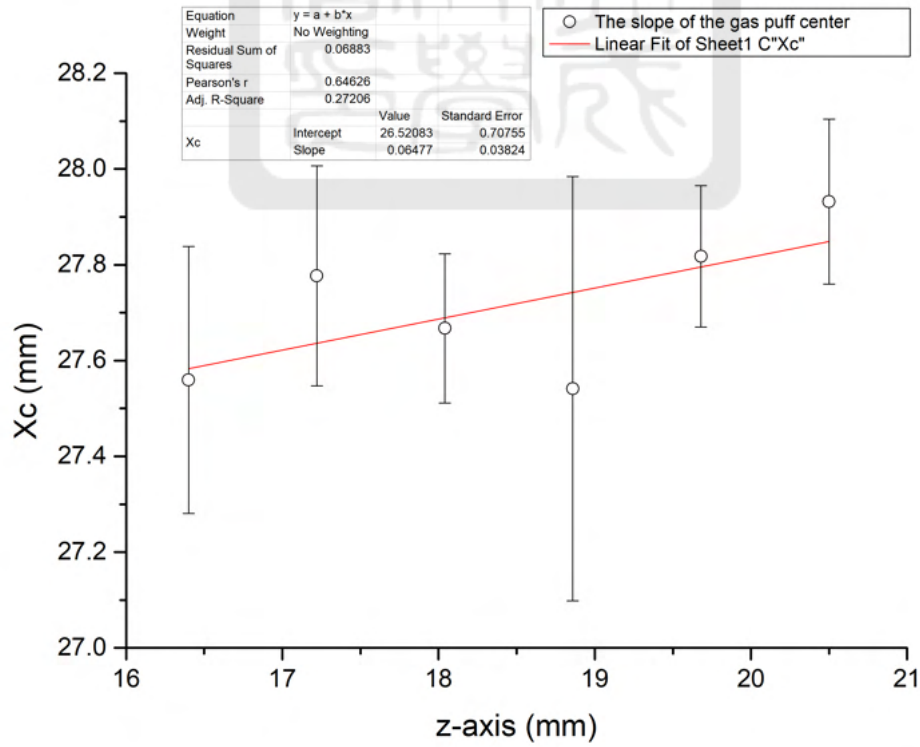


Figure 136: The slope of the propagating center of the experimental setup with V8 CDN at 0.5-atm pressure difference case.

For V8 CDN at 0.5-atm pressure difference, the contrast is 10.4 ± 3.3 a.u., the opening angle of the gas puff is $5.14^\circ \pm 3.43^\circ$ and the tilted angle of the V7 CDN is $3.43^\circ \pm 2.29^\circ$.

5.3.6 V8 convergent-divergent nozzle (CDN), 1-atm pressure difference

Following the steps in section 1.1.4, the horizontal profiles of the differential images 1.1 mm below the nozzle was obtained. Figure 137(a) is the differential image in the case where the experimental setup with V8 CDN at 1-atm pressure difference. Figure 137(b) is the profile of the differential image along the red line in figure 137(a). The maximum of the profile is 4.4 ± 3 a.u. and the minimum is -8 ± 1.8 a.u.. The contrast is 12.4 ± 4.8 a.u..

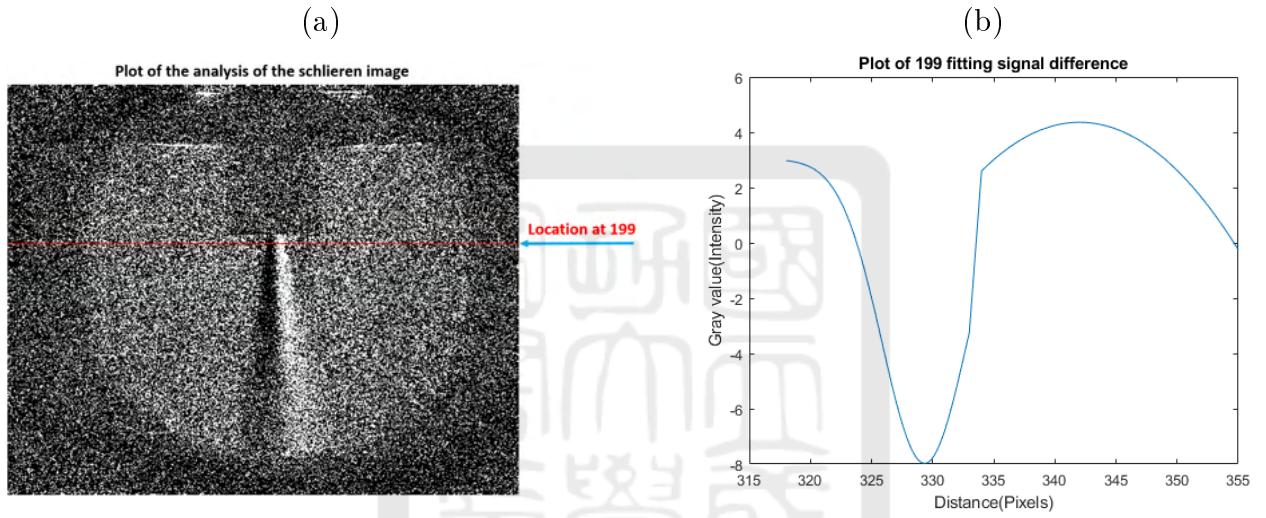


Figure 137: (a) The horizontal line profile of the experimental setup with V8 CDN at 1-atm pressure difference case. (b) The signal intensity difference of the location of the horizontal line at 199 pixels.

Following the step in section 1.1.2, the slope of the propagating path in the case with V8 CDN at 1-atm pressure difference case is 0.05 ± 0.02 as shown in figure 138. Therefore, the opening angle of the gas puff is $2.86^\circ \pm 1.15^\circ$. On the other hand, following the step in section 1.1.3, the slope of the propagating center of the case with V8 CDN CDN at 1-atm pressure difference is -0.01 ± 0.03 as shown in figure 139. The tilted angle of the CDN is $-0.57^\circ \pm 1.72^\circ$.

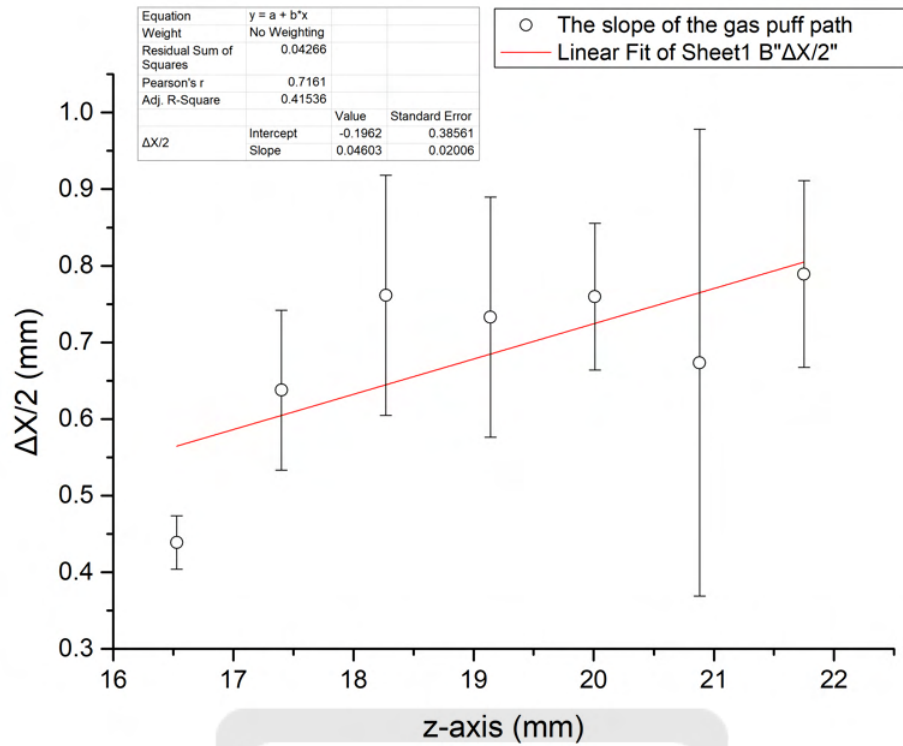


Figure 138: The slope of the propagating path of the experimental setup with V8 CDN at 1-atm pressure difference case.

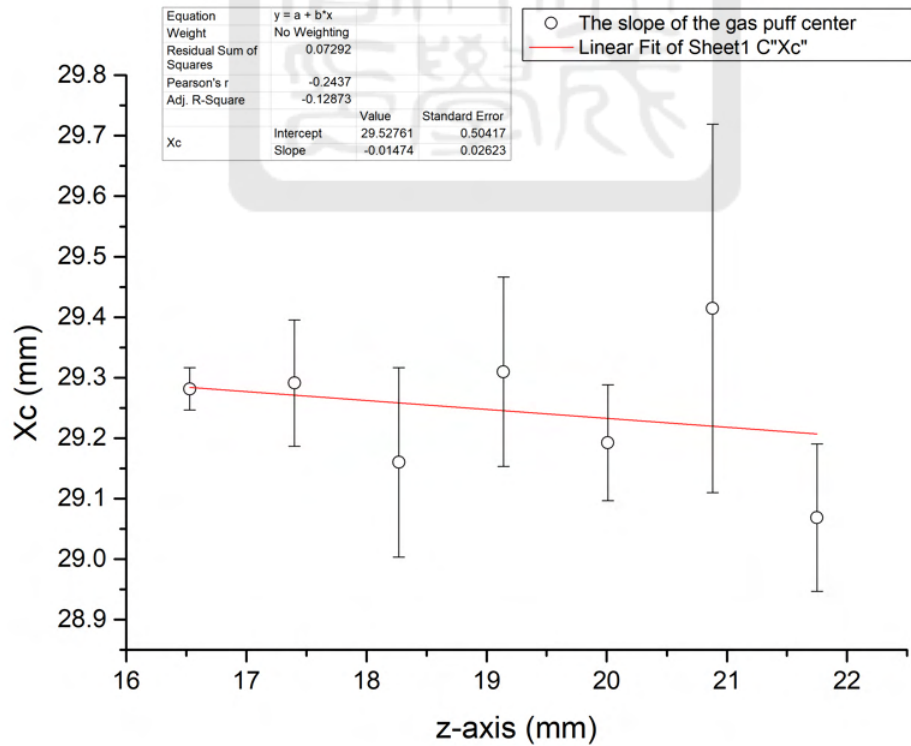


Figure 139: The slope of the propagating center of the experimental setup with V8 CDN at 1-atm pressure difference case.

For V8 CDN at 1-atm pressure difference, the contrast is $12.4 \pm 4.8 \text{ a.u.}$, the opening angle of the gas puff is $2.86^\circ \pm 1.15^\circ$ and the tilted angle of the V7 CDN is $-0.57^\circ \pm 1.72^\circ$.

5.3.7 Summary

We have tested many experimental setups with the 12-V pulse valve. They are:

- (1) No CDN, 0.5-atm pressure difference.
- (2) No CDN, 1-atm pressure difference.
- (3) V7 CDN, 0.5-atm pressure difference.
- (4) V7 CDN, 1-atm pressure difference.
- (5) V8 CDN, 0.5-atm pressure difference.
- (6) V8 CDN, 1-atm pressure difference.

Table 15 is the comparison results of the 12-V pulse valve experimental setups in different conditions. The comparison results are shown as the following:

(1) The contrast: in both of the results without CDN and with V7 CDN, the pressure difference set at 1 atm was larger than 0.5 atm. However, in the result with V8 CDN, there was no significantly different between the results with the pressure difference set at 1 atm and 0.5 atm.

(2) The opening angle of the gas puff: in both of the results without CDN and with V8 CDN, the pressure difference set at 0.5 atm was larger than 1 atm except for the results with V7 CDN.

(3) The tilted angle: it was independent on the CDNs and the pressure difference. Thus, the tilted angle showed only how well the pulse valves or the CDNs were installed.

Table 15: The comparison results of the 12-V pulse valve experimental setups in different conditions.

	No CDN at 0.5 atm	No CDN at 1 atm (★)	V7 CDN at 0.5 atm	V7 CDN at 1 atm	V8 CDN at 0.5 atm	V8 CDN at 1 atm
The contrast (a.u.)	20.9 ± 2.5	63.2 ± 16.7	40.7 ± 11.4	59.8 ± 4.4	10.4 ± 3.3	12.4 ± 4.8
The opening angle of the gas puff	$2.29^\circ \pm 4.57^\circ$	$0.115^\circ \pm 0.286^\circ$	$-0.006^\circ \pm 0.642^\circ$	$1.32^\circ \pm 0.29^\circ$	$5.14^\circ \pm 3.43^\circ$	$2.86^\circ \pm 1.15^\circ$
The tilted angle	$5.71^\circ \pm 2.86^\circ$	$2.92^\circ \pm 0.69^\circ$	$3.83^\circ \pm 1.32^\circ$	$4.74^\circ \pm 0.23^\circ$	$3.43^\circ \pm 2.29^\circ$	$-0.57^\circ \pm 1.72^\circ$

5.4 Summary

In this section, we would like to compare all experiments and determine which one is more suitable for experiments in the future. We have tested many experimental setups with a 24-V pulse valve. They are:

- (1) Different locations of the pulse valve (20 cm case v.s. 42 cm from the convex lens).
- (2) Different Schlieren knife-edge setting (tilted v.s. horizontal v.s. vertical schlieren knife).
- (3) Different temperature of the gas puff (15°C v.s. 25°C).
- (4) Different convergent-divergent nozzles (V5A v.s. V5B v.s. V6 CDN).
- (5) Different pressure of the argon gas (5 ~ 9 atm pressure difference).

The results of the condition with the pulse valve set at 20 cm from the convex lens, the vertical knife-edge, the 25°C–gas puff, the V5A CDN, and the 5-atm pressure difference were the best in the 24-V pulse valve experiments. Furthermore, We have tested many experimental setups with the 12-V pulse valve. They are:

- (1) No CDN, 0.5-atm pressure difference.
- (2) No CDN, 1-atm pressure difference.
- (3) V7 CDN, 0.5-atm pressure difference.
- (4) V7 CDN, 1-atm pressure difference.
- (5) V8 CDN, 0.5-atm pressure difference.
- (6) V8 CDN, 1-atm pressure difference.

The results of the condition without CDN and the 1-atm pressure difference was the best in the 12-V pulse valve experiments. All of the contrast results in the 12-V pulse valve were larger than that in the 24-V pulse valve. Moreover, the output diameter of the 12-V pulse valve was larger than the 24-V pulse valve as shown in table 16. Finally, the 12-V pulse valve is considered as the more suitable choice for the rest of experiments in the future.

Table 16: The output diameter of the pulse valves.

	24-V pulse valve	12-V pulse valve
Output diameter (mm)	0.1	5.5

6 Future works

The following is the list of future works:

1. The output diameter of the pulse valves was so small that the size of the gas puff was too small. We have to build a pulse valve with an output diameter larger than 5.5 mm and combine the new pulse valve with a quartz tube.
2. The plasma-plume generator will be built as shown in figure 140. It consists of a pair of brass-ring electrodes parallel to each other, a ring insulator between two brass rings and a small pulsed-power system with a capacitor (C). The self-breakdown voltage will be determined in experiments with different reservoir pressures and different distances between two electrodes. In order to synchronize the generation of the plasma plume and the response time of the theta pinch, we will test different charging voltage (V_A), the different gap distance between two electrodes (d), and different reservoir pressures (P_R). Finally, the propagating speed of the plasma plume needs to be measured. The relation between the propagating speed and (V_A , P_R , and d) needs to be studied.

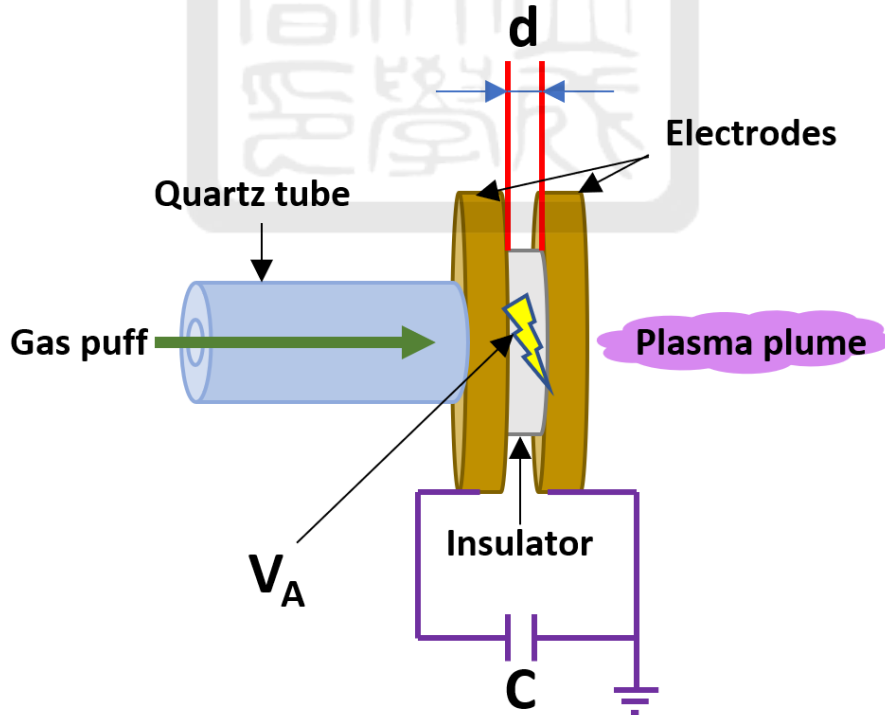


Figure 140: The schematic of the plasma plume generator.

3. In order to compress the plasma, a Helmholtz coil will be built as shown in figure 141(a). It consists of a pair of parallel-plate coils (PPC) made of stainless steel. It can provide

a spatially uniform magnetic field at the center of the PPC for the theta pinch. We also have to measure the strength of the magnetic field because it is important for the theta pinch. To measure the magnetic field, a B-dot probe will be built as shown in figure 141(b). When the time-varying magnetic field passes through the B-dot probe, a voltage (V_{Bdot}) will be induced:

$$V_{\text{Bdot}} = -\frac{d\phi}{dt} = -\pi r_{\text{Bdot}}^2 \frac{dB}{dt} \quad (24)$$

where ϕ is the magnetic flux, r_{Bdot} is the radius of the B-dot probe and B is the measured magnetic field.

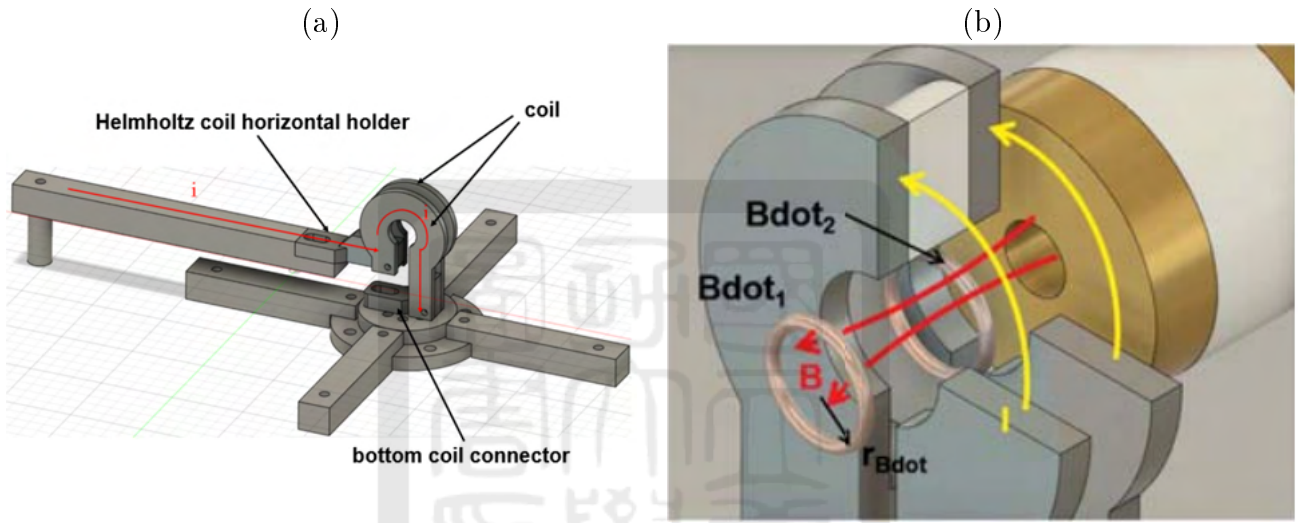


Figure 141: (a) The design of the Helmholtz coil. (b) The side view of the Helmholtz coil.

4. After all components are built, we need to study how the plasma plume is compressed in the theta pinch. Most importantly, we need to measure the radiation from the compressed plasma plume and see if the EUV light is generated.
5. Schlieren system will be improved by a white light source, a convex lens with 100 or 150-mm focal length, and an apochromatic lens.

7 Summary

The goal of this work was to study the gas puff in the EUV light source using a theta pinch. In order to drive the theta pinch in the future, a pulsed-power system was built. However, the old version of the Rogowski coil for measuring the current was too large. Therefore, we built a new Rogowski coil. The Rogowski coil was made of a coaxial cable, the aluminum tape, and the PU tube. We placed it within the coaxial transmission line of the pulsed-power system and used the Pearson current monitor to calibrate the Rogowski coil with an integrator. The result of the calibration ratio was 188 ± 0.3 (kA / V). Finally, the pulsed-power system can provide a current output of 135 ± 1 kA with a rise time of 1592 ± 3 ns. On the other hand, we also built a spacer for the rail-gap switch of the pulsed-power system to control the gap distance between electrodes in the switch. Finally, the procedure of building the Rogowski coil and the spacer was written and provided in sections A.1.1 and A.1.6.

Our design of the EUV light source is by compressing the discharge-produced plasma (DPP). In order to generate the plasma plume, a gas puff as the precursor is ionized by an arc discharge. The gas puff was provided by a gas-gun system which included the pulse-valve, the reservoir, and the convergent-divergent nozzle (CDN). There were two pulse-valve versions: (1) the 24-V pulse valve, (2) the 12-V pulse valve. The 24-V pulse valve worked with a response time less than 2 ms. The time difference between the opening and the closing was more than 0.05 s. The limit of the pressure difference between the inlet and the output was 64655 torr. The 12-V pulse valve worked with 88-mA current with 1.06-W power. The upper limit of the pressure difference between the inlet and the output of the 12-V pulse valve was 450 torr. The reservoir was used to control the pressure in the gas line and make the output pressure stable. Then, we made five versions of the CDNs for different experiments. We control the velocity of the gas puff by changing the intake, waist, and output size of the CDNs. Finally, the procedure of operating the gas-gun system was written and provided in section A.2.1.

After generating a gas puff, the Schlieren system was built for capturing the schlieren images of the gas puff. The Schlieren system consists of a green LED with a finite size, a 500-mm plano-convex lens, a schlieren knife-edge, and a CMOS camera. We solved many problems such as chromatic aberration and Newton's ring during our experiments. The chromatic aberration was removed by using monochromatic light. Newton's rings were removed by tilting the lens

with a small angle. Furthermore, we found that the image contrast of the 24-V pulse valve set at 20 cm from the plano-convex lens was two times higher than that of the 24-V pulse valve at 42 cm from the plano-convex lens. Therefore, we have the pulse valve at 20 cm from the plano-convex lens, green LED as the light source for the rest of experiments.

The Schlieren system captured a series of images of the gas puff under different conditions. To determine which condition is the best for experiments in the future, we compared all experiments and tested many experimental setups with a 24-V pulse valve. They were:

- (1) Different locations of the pulse valve (20 cm case v.s. 42 cm from the convex lens).
- (2) Different Schlieren knife-edge setting (tilted v.s. horizontal v.s. vertical schlieren knife).
- (3) Different temperature of the gas puff (15°C v.s. 25°C).
- (4) Different convergent-divergent nozzles (V5A v.s. V5B v.s. V6 CDN).
- (5) Different pressure of the argon gas (5 ~ 9 atm pressure difference).

In our experiments, we focus on the contrast of the differential images, the opening angle of the gas puff, and the tilted angle of the CDN. The results with a larger contrast, a smaller opening angle, and a smaller tilted angle are the best choice for us. The results of the condition with the pulse valve set at 20 cm from the convex lens, the vertical knife-edge, the 25°C—gas puff, the V5A CDN, and the 5-atm pressure difference were the best in the 24-V pulse valve experiments. The diameter of the inlet, the waist, and the output of the V5A CDN were 2 mm, 1 mm, and 1.3 mm, respectively.

Furthermore, We tested many experimental setups with a 12-V pulse valve. They were:

- (1) No CDN, 0.5-atm pressure difference.
- (2) No CDN, 1-atm pressure difference.
- (3) V7 CDN, 0.5-atm pressure difference.
- (4) V7 CDN, 1-atm pressure difference.
- (5) V8 CDN, 0.5-atm pressure difference.
- (6) V8 CDN, 1-atm pressure difference.

The results without CDN and the 1-atm pressure difference were the best in the 12-V pulse valve experiments. All contrasts of 12-V pulse valve experiments were larger than those in 24-V pulse valve experiments. It was because the output diameter of the 12-V pulse valve was larger than that of the 24-V pulse valve. Therefore, the 12-V pulse valve is considered as a better

choice for experiments in the future. Alternatively, a pulse valve with a larger output diameter needs to be built for future experiments.



References

- [1] <https://case.ntu.edu.tw/blog/?p=33519>.
- [2] Po-Yu Chang. Proposal aec most euv.
- [3] <https://www.engapplets.vt.edu/fluids/cdnozzle/cdinfo.html>.
- [4] <https://zh.wikipedia.org/zh-tw/>
- [5] Wen-long Yang Wen-yue Wang, Dong Ruige. Sensitivity investigation of schlieren imaging system. *Laser Optoelectronics Progress*, 2018.
- [6] Vivek Bakshi. Euv sources for lithography. *SPIE*, 2006.
- [7] Gordon E. Moore. Cramming more components onto integrated circuits. *reprinted from electronics*, 1965.
- [8] <https://www.tsmc.com/english/dedicatedfoundry/technology>.
- [9] Martyn Leenders Vadim Banine, Jos P. Benschop and Roel Moors. Relationship between an euv source and the performance of an euv lithographic system. *Emerging Lithographic Technologies IV*, 2000.
- [10] Igor V. Fomenkov William N. Partlo and Daniel L. Birx. Euv (13.5-nm) light generation using a dense plasma focus device. *Emerging Lithographic Technologies III*, 1999.
- [11] G. S. Settles. *Schlieren And Shadowgraph Techniques*. Springer, 2001.
- [12] Ming-Cheng Jheng. Development of a 400 mw pulsed-power system. *National Cheng Kung University Institute of Space and Plasma Sciences*, 2019.
- [13] R.S. Rawat Paul Lee Sing Lee, Sor Heoh Saw. Measurement and processing of fast pulsed discharge current in plasma focus machines. *Journal of Fusion Energy*, 2011.
- [14] Chieh-Jui Hsieh. Generation of plasma jets using a conical-wire array driven by a pulsed-power system. *National Cheng Kung University Institute of Space and Plasma Sciences*, 2020.

A Appendix

A.1 The pulsed-power system

A.1.1 The reports of the Rogowski coil calibration

New version Rogowski coil (Blue one)

data analysis report



Format:

$L = 138.75 \text{ mm}$, $r = 1.25 \text{ mm}$, $N = 130 \text{ turns}$

The procedure of calibrating Rogowski coil:

1. We will get the data from Pearson Current monitor and Blue one with the pulsed-power system using 50 kA (50 kA is the load voltage for Pearson current monitor).
2. Using Mathematica or other programs to do the curve fitting:
 - (a) In the Current measurement case, we should know the wave function about under damping:

$$I_{\text{input}} e^{-\alpha t} \sin(\omega t) \quad (1)$$

$$I_{\text{input}}(\text{Including the mutual inductance of Rogowski coil}) = V_{\text{Rogowski coil}} + \text{integrator} \quad (2)$$

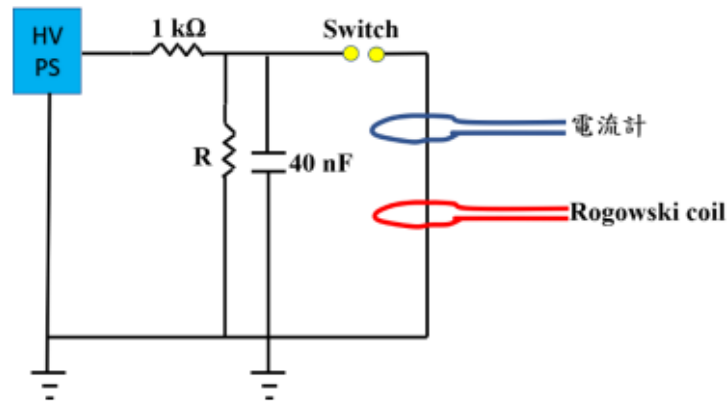
- (b) Use the (1) equation to do the curve fitting with the $V_{\text{Rogowski coil}}$ Pearson current monitor measured.
- (c) Use the (1) equation to do the curve fitting with the $V_{\text{Rogowski coil}} + \text{integrator}$ Rogowski coil measured.
- (d) We will get the parameter about I_{input} 、 t 、 ω 、 α from each (b) and (c).

- (e) Draw a chart with the $V_{\text{Rogowski coil + integrator}}$ (x-axis) and the I_{input} (y-axis).
- (f) We could use the Slope to know the calibration ratio between the I_{input} Pearson monitor measured and $V_{\text{Rogowski coil + integrator}}$.
- (g) $V_{\text{measurement}} \times \text{Calibration ration} = I_{\text{input}}$.



Rogowski coil calibration

電路圖如下



1. 計算 RC 暫態電路放電所需要的時間，並找取所對應的電阻以及電容大小。
2. 確認 gap switch 的觸發電壓。
3. 確定放電迴路的 power 要小於外加電阻(R)的 power。
4. 外加電阻(R)的電阻值要大於 1 kΩ。因為如果相等，充電的量等於放電的量，電容無法被充電。
5. 電源供應器功率要大於系統功率，如此在持續安全放電的情況下才足夠電容充電。

所需儀器

Spellman L130 電源供應器、1 kΩ 電阻、40 nF 電容、1 GΩ 電阻 x2(視放電時間需求計算而得)、Gap Switch、50kA 電流計、Rogowski coil。

使用公式

$$Vt = V_0 e^{-\frac{t}{RC}}$$

$$P = \frac{V^2}{R}$$

$$V = I \times R$$

Rogowski coil report by J.K Liu

Experiments:

1. 首先必須瞭解 RC circuit 原理，如下：

$$I = \frac{dQ}{dt} \rightarrow -C \frac{dV}{dt}$$

$$V_C - IR = 0$$

$$\rightarrow V_C + RC \frac{dV}{dt} = 0$$

$$\rightarrow V_C dt = -RC dV$$

$$\rightarrow \frac{-1}{RC} \int dt = \int \frac{dV}{V_C}$$

$$\int_{V_0}^{V_t} \frac{1}{V_C} dV = \frac{-1}{RC} \int_0^t dt$$

$$\rightarrow \ln V_t - \ln V_0 = \frac{-(t-0)}{RC}$$

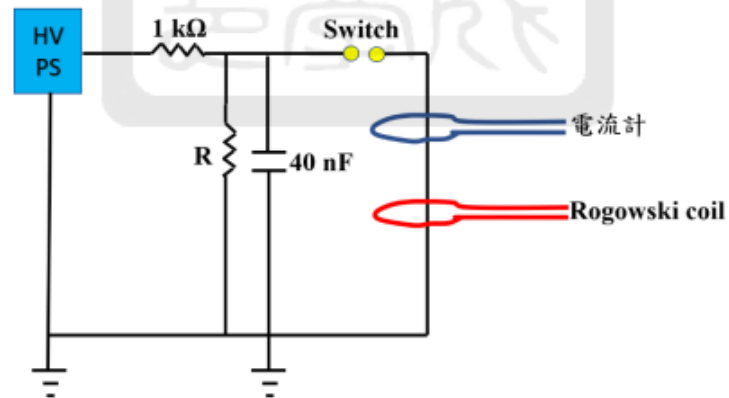
$$\rightarrow \ln \frac{V_t}{V_0} = \frac{-t}{RC}$$

$$\rightarrow e^{\ln \frac{V_t}{V_0}} = e^{\frac{-t}{RC}}$$

$$\rightarrow \frac{V_t}{V_0} = e^{\frac{-t}{RC}}$$

$$\rightarrow V_t = V_0 e^{\frac{-t}{RC}}$$

2. 電路圖如下：



電路元件選擇必須符合以下條件：

- (a) $RC \gg \mu s$
 $RC = \text{放電時間} = \tau$ 。
- (b) $V_B > 5 \text{ kV}$
 取決於 gap switch 的間距。
- (c) $P_{all} < P_{resistance}$
 外加電容(R)才不會因為 Gap switch 觸發放電而燒毀。
- (d) $R \gg 1 \text{ k}\Omega$
 此電阻主要用於持續放電保護實驗者，並且要大於前方 $1 \text{ k}\Omega$ ，如此電容才有辦法被充電，如果外加電阻(R) $\leq 1 \text{ k}\Omega$ ，會導致充電 \leq 放電。
- (e) $P_{power \text{ supply}} > P_{all}$
 $P_{power \text{ supply}}$ 夠大才足夠在外加電阻(R)對電容持續放電的情況下，對電容充電。



Through hole $\varnothing 20$
Through holes $\varnothing 4(x8)$

$\varnothing 20$ $\varnothing 270$ $\varnothing 258$

R132

Pre-exist

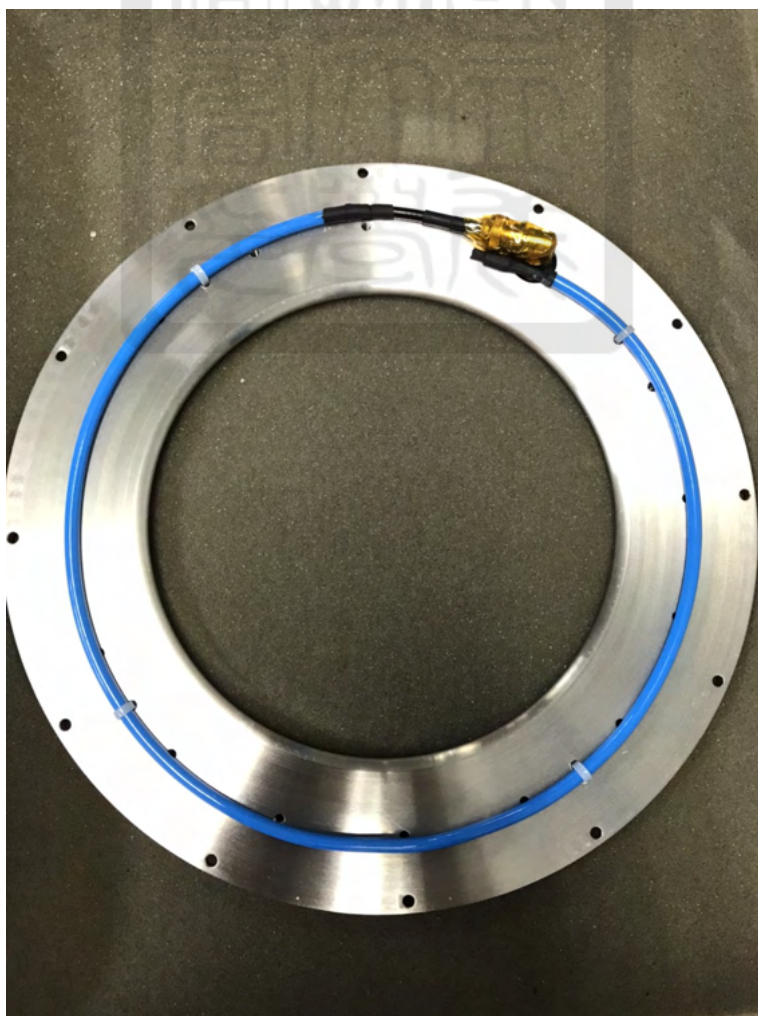
33.7° 33.8° 33.8° 36.25° 36.25°

Unit: mm

Note:
Unless other wise specified
• Tolerance: 2PL ± 0.005
• Edge: R2 Round Fillet
• Inside cor rad: 0.4

Dept. ISAPS	Technical reference	Created by JIA-KAI LIU	2020/9/14	Approved by
		Document type		Document status
		Title	DWG No.	
		Coaxial Outer Top		
		PGS202009001_JK		
		Rev.	Date of issue	Sheet
		A	2020/09/14	1/1

A.1.3 The photos of the Rogowski coil



A.1.4 The procedure of opening/closing the lid of the vacuum chamber

The procedure of opening/closing the lid of the vacuum chamber

工具:

1. 塑膠手套。
2. 19 號板手。

注意:全程配戴手套操作!!!

Opening procedure:

檢查主系統腔體:

1. 確認系統平行板傳輸線已淨空。
2. 將大海綿墊置於平行板傳輸線上。
3. 將連接主系統腔體上的所有訊號線移除。
4. 將有 BNC 之 KF40 法蘭移除。
5. 將 Rogowski coil 的 BNC 接線移除。
6. 將 Ion gauge 移除。
7. 將 pirani gauge 移除。
8. 使用 19 號板手移除上蓋螺絲、墊片並放置於藍色收納盒內。

使用天車(單節式移動式龍門吊架):

注意:此操作務必兩人以上!!!

1. 將天車兩端底座滾輪煞車調成 OFF，天車方能移動。
2. 將天車推至 PPCB 系統中央近主系統腔體處。
3. 將兩端底座滾輪煞車調成 ON 使其鎖死。
4. 確認天車是否已固定。
5. 將天車上方兩鐵鍊(銀&黑)與四個鉤頭卸下。

注意:不可敲擊主系統腔體，以及鉤頭側鋼索有鋼絲外露不要被刺傷!!!

6. 取銀鐵鍊並拉動其中一端，使鉤頭端下降至主系統腔體上方。
7. 將鉤頭缺口端朝外並鉤在主系統腔體上蓋的金色扣環處。
8. 拉動銀鐵鍊其中一端，使主系統上蓋上升約 5 公分。
9. 一人抓牢主系統上蓋，避免其搖晃。
10. 將天車兩端底座滾輪煞車調成 OFF。
11. 將天車推至放有大海綿墊平行板傳輸線的位置。
12. 將天車滾輪煞車調成 ON 使天車鎖死固定。
13. 拉動銀鐵鍊將上蓋放置於海綿墊上。

Closing procedure:

1. 將主系統上蓋調升至腔體高度再加約 5 公分的高度。
2. 一人抓牢主系統腔體上蓋，將天車兩端底座滾輪煞車調成 OFF。
3. 將天車推至主系統腔體上方。
4. 將滾輪煞車調至 ON 固定鎖死。
5. 將 Rogowski coil 內部 BNC 訊號線連接至主系統上蓋的 BNC 通孔。
6. 將 BNC 通孔裝回法蘭上。
7. 旋轉上蓋使對位膠帶互相對齊。
8. 將主系統腔體上蓋使用銀鐵鍊調降至所有螺絲都可以咬到牙。
9. 將上蓋放下。
10. 將鉤頭脫離金色扣環。
11. 用銀鐵鍊使鉤頭上升。
12. 將兩條鐵鍊(黑、銀)掛在天車上方固定。
13. 天車兩底座滾輪煞車調至 OFF。
14. 將天車推回原位。
15. 將主系統腔體螺絲、墊片鎖上固定。
16. 將外部 Rogowski coil 的 BNC 訊號線接上 BNC 通孔。
17. 使用三用電表確認 Rogowski coil 線路已成功連接。
18. 將 Ion gauge 裝回法蘭上。
19. 將 Pirani gauge 裝回法欄上。
20. 工具歸位。



A.1.5 The procedure of milling Electrodes

Milling the electrodes report by JK

Equipment:

Both north and south wings electrodes (*4) and knife edges(*2),
Sandpapers(250~400-Rough, 600~800-Thin),
Diamond Pastes(W3.5-Rough, W2.5-Thin, W1.5-The thinnest),
Polisher

Company:

Diamond Pastes: 永捷工具店(蝦皮購物)

Sandpapers: 開元五金行

Steps:

1. Spray water on the electrode surface using "wash bottle".
2. Using the Rough(250~400) sandpaper to mill the electrodes with some water.
3. Using the Thin(600~800) sandpaper to mill the electrodes with some water.
4. Stop milling until the burn marks are almost gone.
5. Using the Rough(W3.5) Diamond Pastes and Polisher to mill the electrodes with some water.
6. Using the Thin(W2.5) Diamond Pastes and Polisher to mill the electrodes with some water.
7. Using the Thinnest(W1.5) Diamond Pastes and Polisher to mill the electrodes with some water.
8. Stop polishing until the burn marks are gone.
9. After polishing the electrodes, we have to take all of electrodes to wash.
10. Dry all of them and finish.

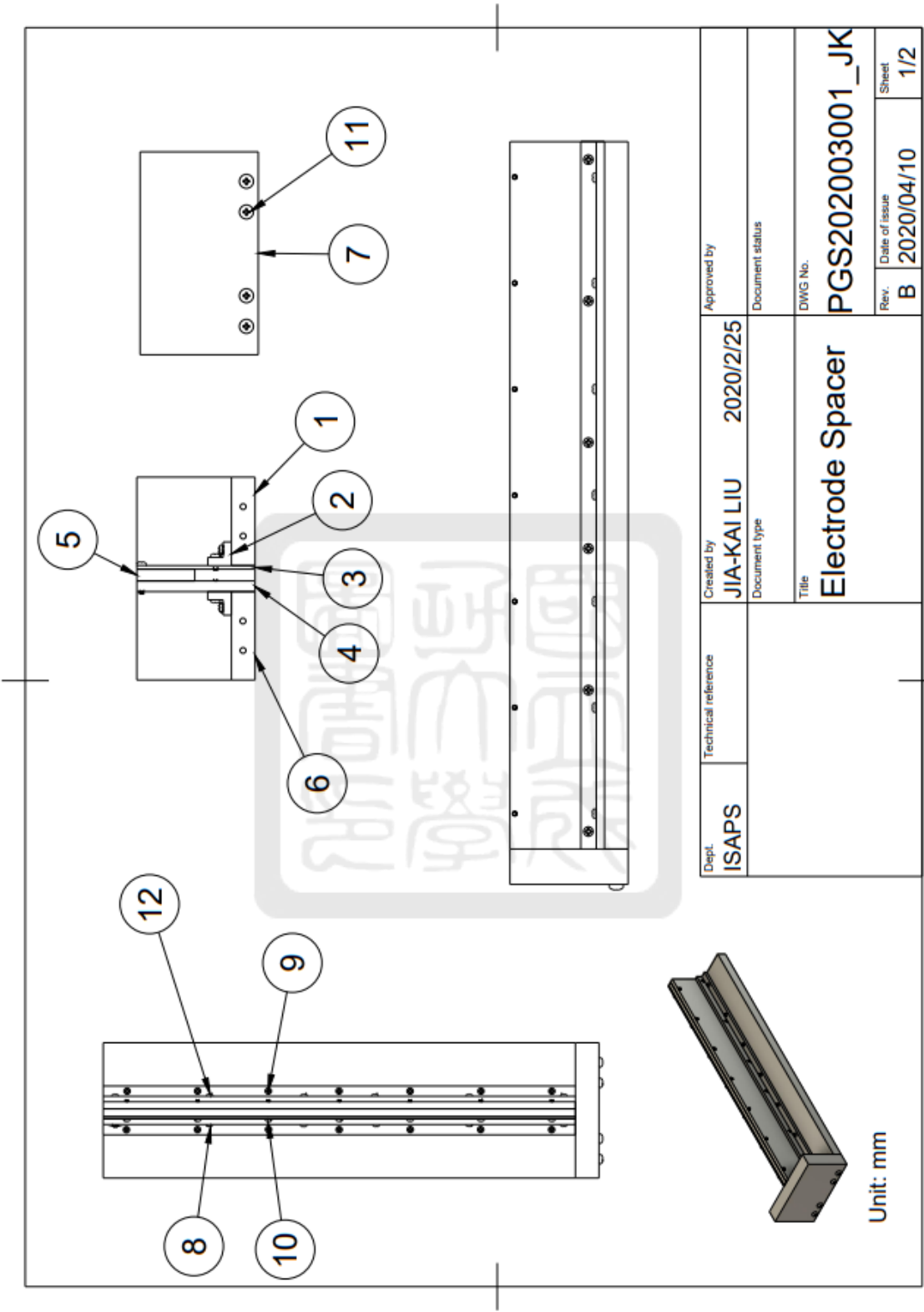
Ps.

If the surface of the electrode dries out, repeat step (1).

Step (2)~(3) milling with hands.

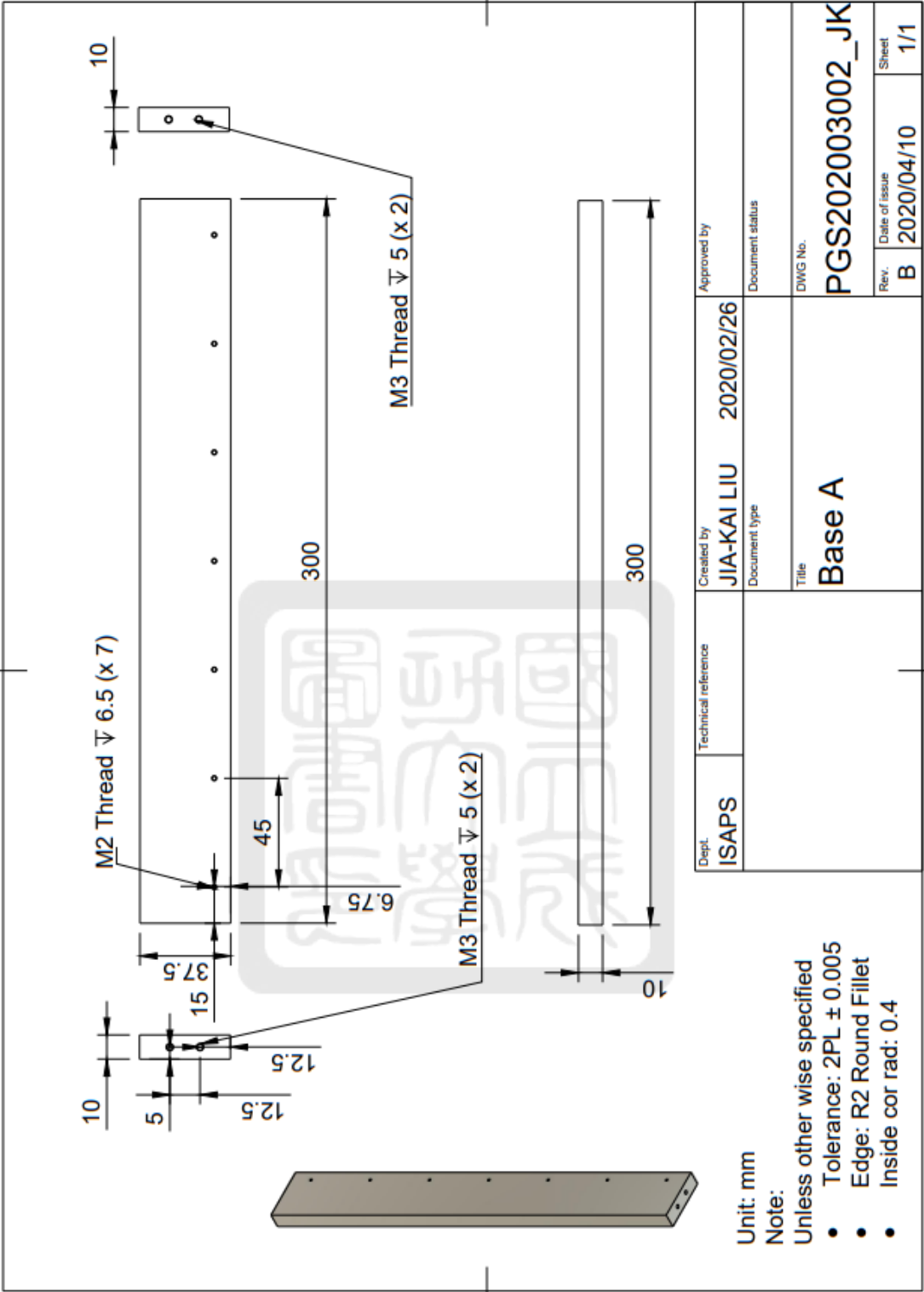
Step (5)~(7) polishing with polisher.

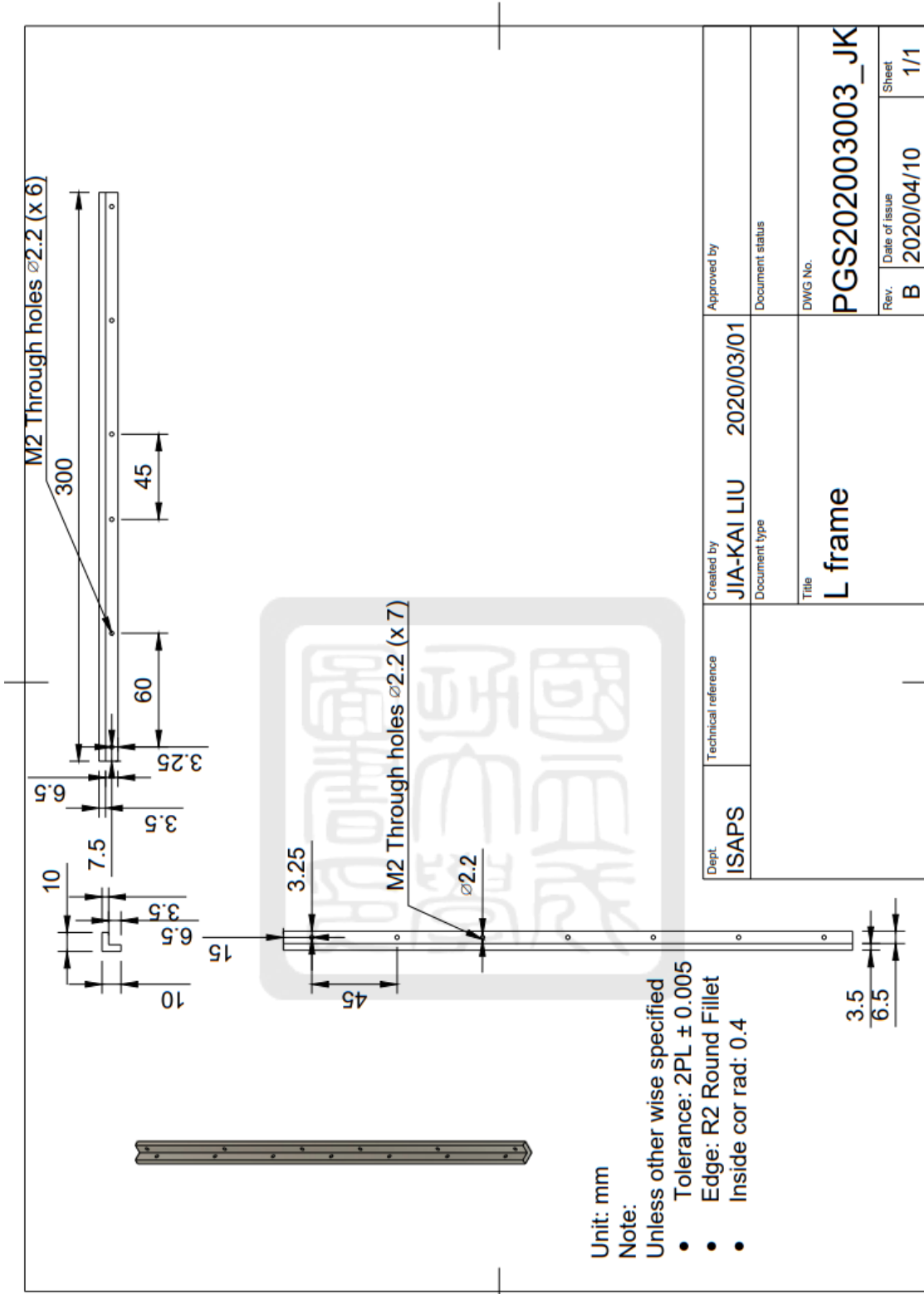
A.1.6 The drawing of the spacer of the rail-gap switch

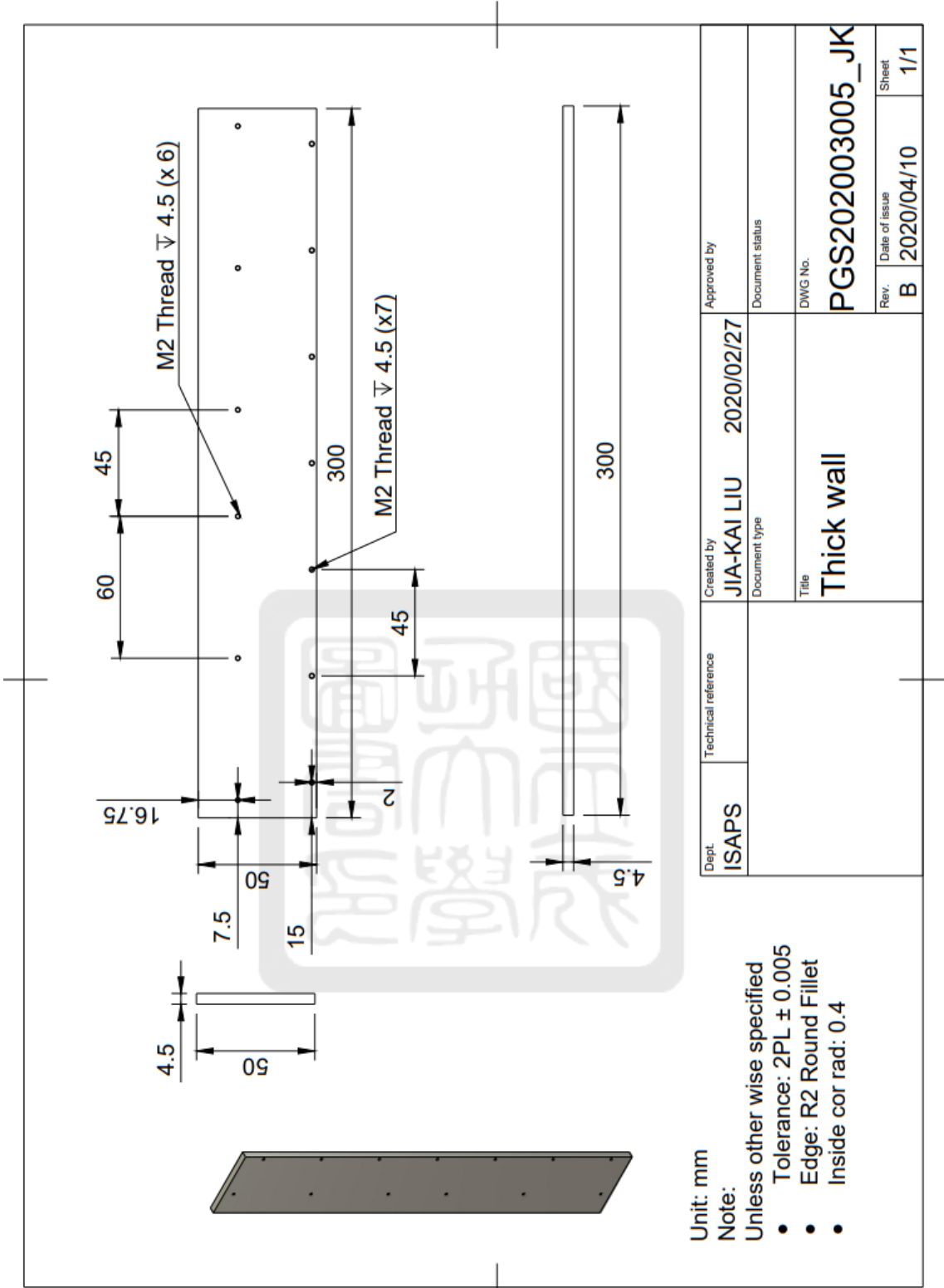


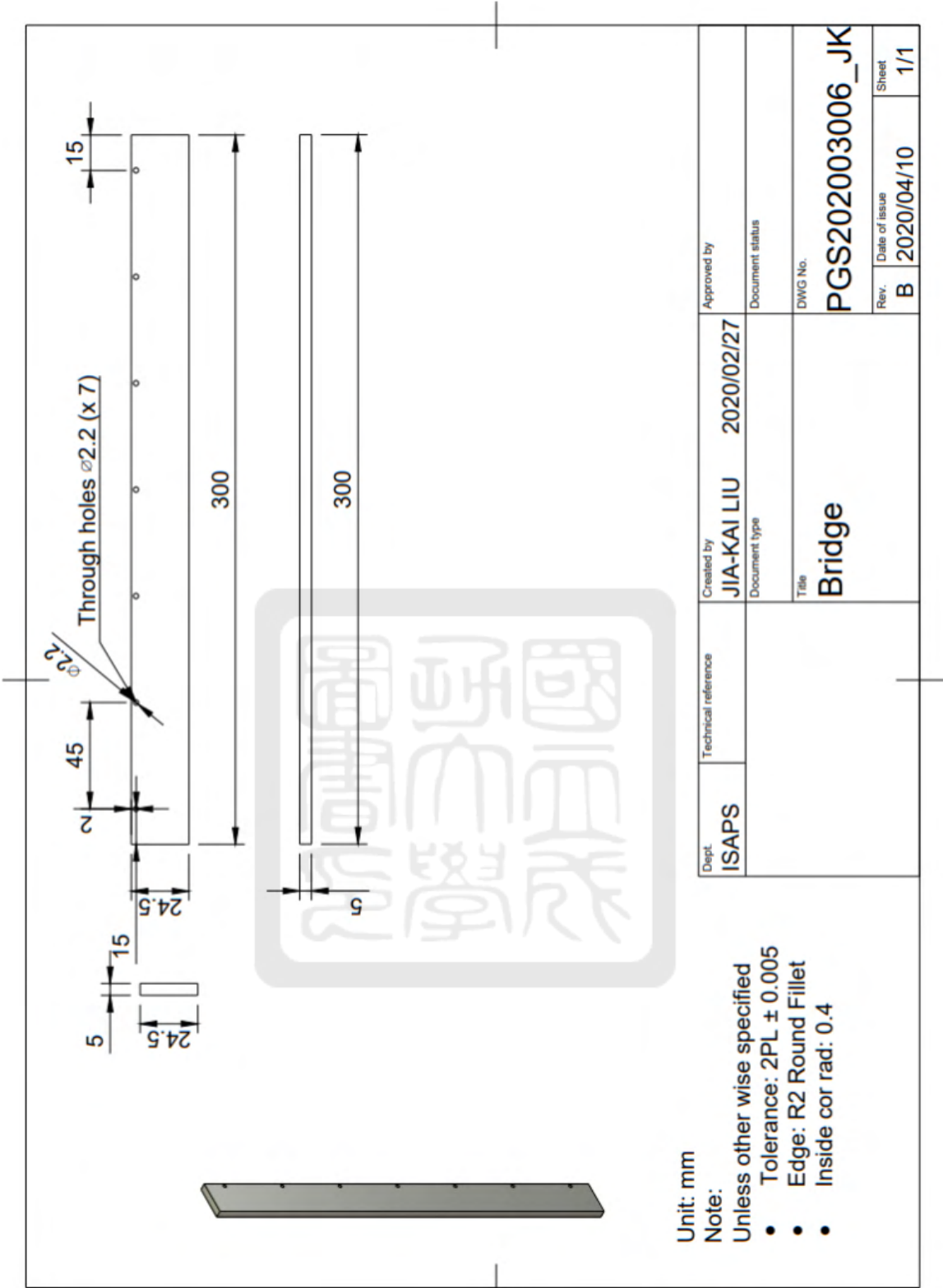
Parts List				
Item	Qty	Part Number	Description	Material
1	1	PGS202003002	Base A	Stainless Steel
2	2	PGS202003003	L frame	Stainless Steel
3	1	PGS202003004	Thin wall	Stainless Steel
4	1	PGS202003005	Thick wall	Stainless Steel
5	1	PGS202003006	Bridge	Stainless Steel
6	1	PGS202003007	Base B	Stainless Steel
7	1	PGS202003008	Back	Stainless Steel
8	6		M2 5 mm	Stainless Steel
9	14		M2 10 mm	Stainless Steel
10	7		M2 12 mm	Stainless Steel
11	4		M3 18 mm	Stainless Steel
12	6		M2 7 mm	Stainless Steel

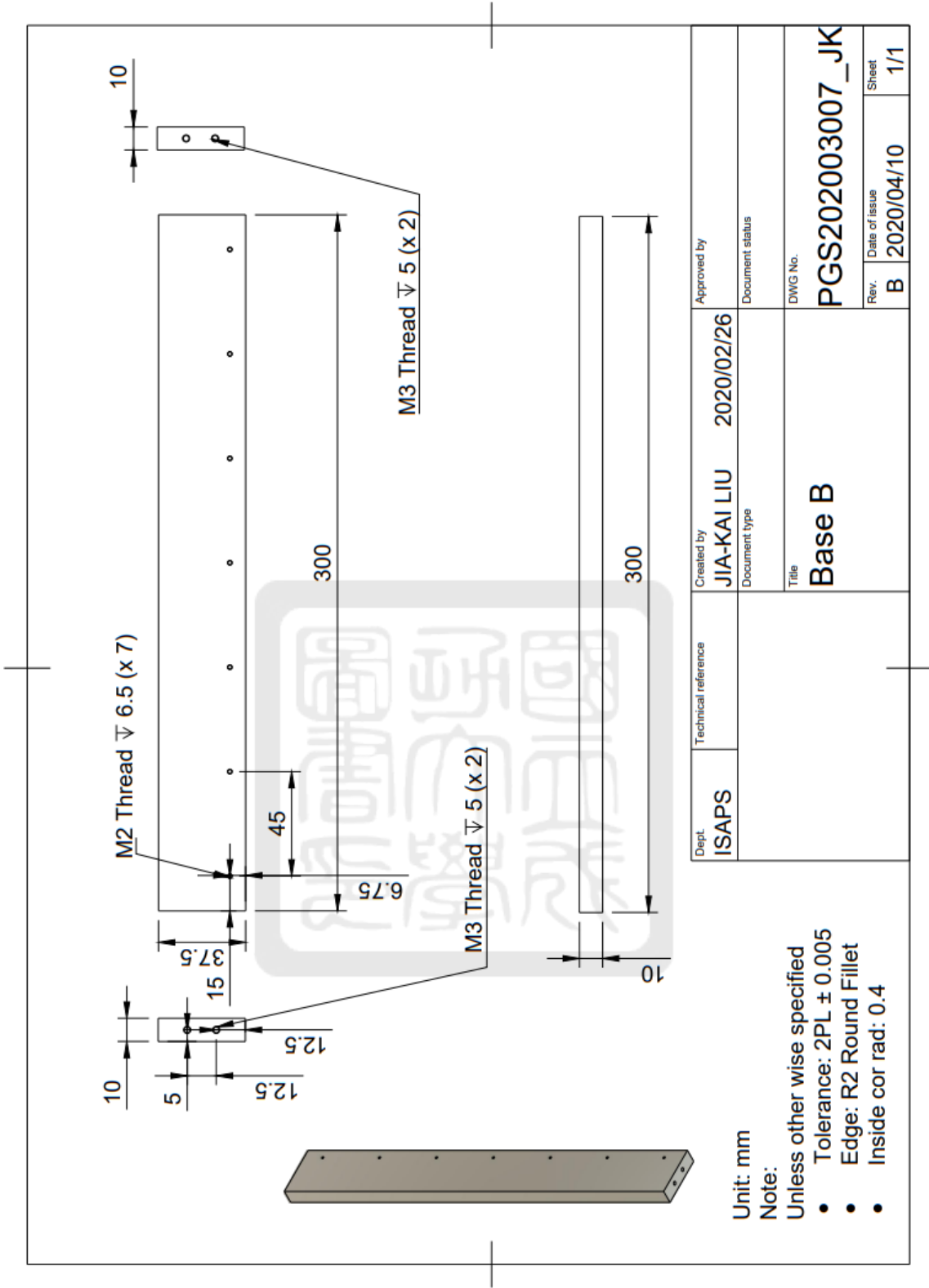
Dept. ISAPS	Technical reference	Created by JIA-KAI LIU	2020/2/25	Approved by
		Document type		Document status
		Title Electrode Spacer		DWG No. PGS202003001_JK
		Rev. B	Date of issue 2020/04/10	Sheet 2/2

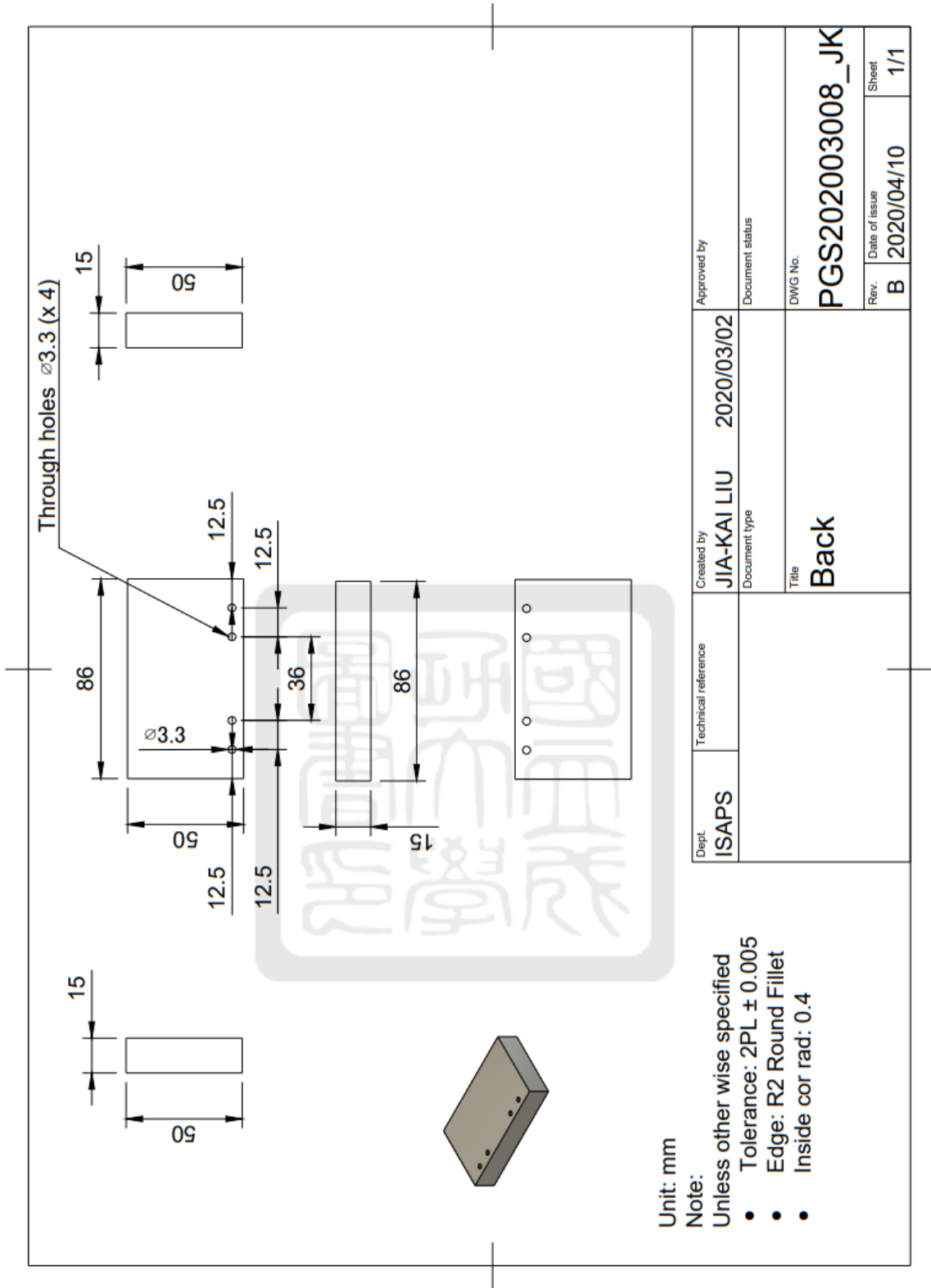






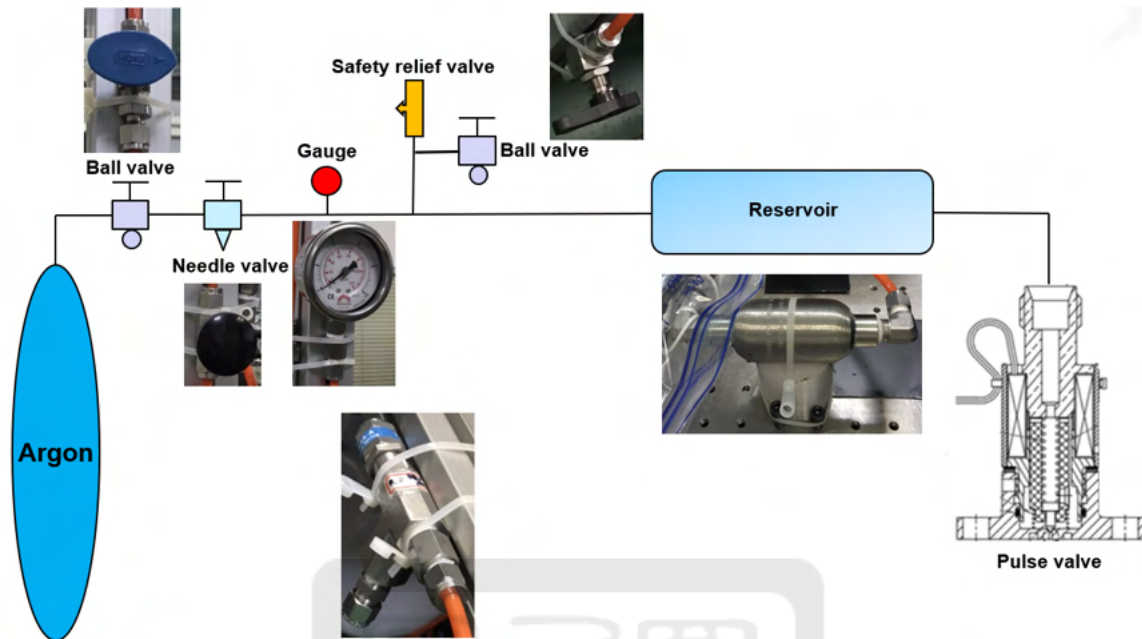






A.2 The gas puff

A.2.1 The procedure of operating the gas-gun system



The procedure of operating the gas-gun system

1. Open the Argon gas cylinder to inject the gas to the gas line.
2. Control the gas pressure in the gas line with the ball valve and the gauge, preliminarily.
3. Use the needle valve to control the gas pressure, precisely.
4. Connect the control box with the oscilloscope through the fiber.
5. Connect the control box with the battery.
6. Connect the control box with the pulse valve.
7. Turn on the control box for the pulse valve.
8. Use the oscilloscope to provide a pulse with a time delay.
9. Output a signal with a time delay from the oscilloscope to the fiber. Then, the receiver of the control box gets the signal and send it to the pulse valve.

A.2.2 The 24-V pulse valve opening-time measurements

4 ms Data analysis

	Wave width time delay 4 ms data analysis
	Data1
Open voice(a.u.)	0.9173
Close voice(a.u.)	0.17807
Open time(s)	0.0005
Close time(s)	0.018875
Time delay of pulse valve work(s)	0.018375
Time delay of function generator(s)	0.004
Deviation(%)	54%

5 ms Data analysis

	Wave width time delay 5 ms data analysis
	Data1
Open voice(a.u.)	0.8548
Close voice(a.u.)	0.06549
Open time(s)	0.001417
Close time(s)	0.023833
Time delay of pulse valve work(s)	0.022
Time delay of function generator(s)	0.005
Deviation(%)	100%

10 ms Data analysis

	Wave width time delay 10 ms data analysis							
	Data1	Data2	Data3	Data4	Data5	Data6	Data7	Data8
Open voice(a.u.)	0.99997	0.92557	0.94714	0.95200	0.86359	0.84164	0.82675	0.92889
Close voice(a.u.)	0.12726	0.14029	0.15979	0.15213	0.16229	0.16095	0.13385	0.08496
Open time(s)	0.00254	0.00360	0.00185	0.00192	0.00150	0.00154	0.00221	0.00106
Close time(s)	0.02944	0.03031	0.02783	0.02810	0.02765	0.02917	0.02860	0.02763
Time delay of pulse valve work(s)	0.0269	0.02671	0.02598	0.02618	0.02615	0.02763	0.02639	0.02657
Time delay of function generator(s)	0.01	0.01	0.01	0.01	0.01	0.01	0.01	0.01
Deviation(%)	100%	100%	100%	100%	100%	100%	100%	100%

50 ms Data analysis

	Wave width time delay 50 ms data analysis							
	Data1	Data2	Data3	Data4	Data5	Data6	Data7	Data8
Open voice(a.u.)	0.79922	0.97885	0.94000	0.92157	0.89484	0.85428	0.93610	0.99997
Close voice(a.u.)	0.23557	0.19275	0.14526	0.10880	0.12775	0.15442	0.08347	0.07391
Open time(s)	0.00694	0.00806	0.00821	0.00525	0.00519	0.00440	0.00456	0.00463
Close time(s)	0.07433	0.07444	0.07483	0.07183	0.07348	0.07213	0.06925	0.07110
Time delay of pulse valve work(s)	0.06739	0.06638	0.06662	0.06658	0.06829	0.06773	0.06469	0.06647
Time delay of function generator(s)	0.05	0.05	0.05	0.05	0.05	0.05	0.05	0.05
Deviation(%)	34%	32%	33%	33%	37%	35%	29%	33%

0.1 s Data analysis

	Wave width time delay 0.1 s data analysis						
	Data1	Data2	Data3	Data4	Data5	Data6	Data7
Open voice(a.u.)	0.95758	0.99997	0.93765	0.78677	0.99658	0.85892	0.78058
Close voice(a.u.)	0.10519	0.11703	0.12088	0.09641	0.13266	0.10516	0.09326
Open time(s)	0.02035	0.02044	0.01571	0.01208	0.02121	0.01129	0.01356
Close time(s)	0.13835	0.13721	0.13179	0.12683	0.13815	0.12825	0.12892
Time delay of pulse valve work(s)	0.118	0.11677	0.11608	0.11475	0.11694	0.11696	0.11536
Time delay of function generator(s)	0.1	0.1	0.1	0.1	0.1	0.1	0.1
Deviation(%)	16%	17%	16%	15%	17%	17%	15%

0.5 s Data analysis

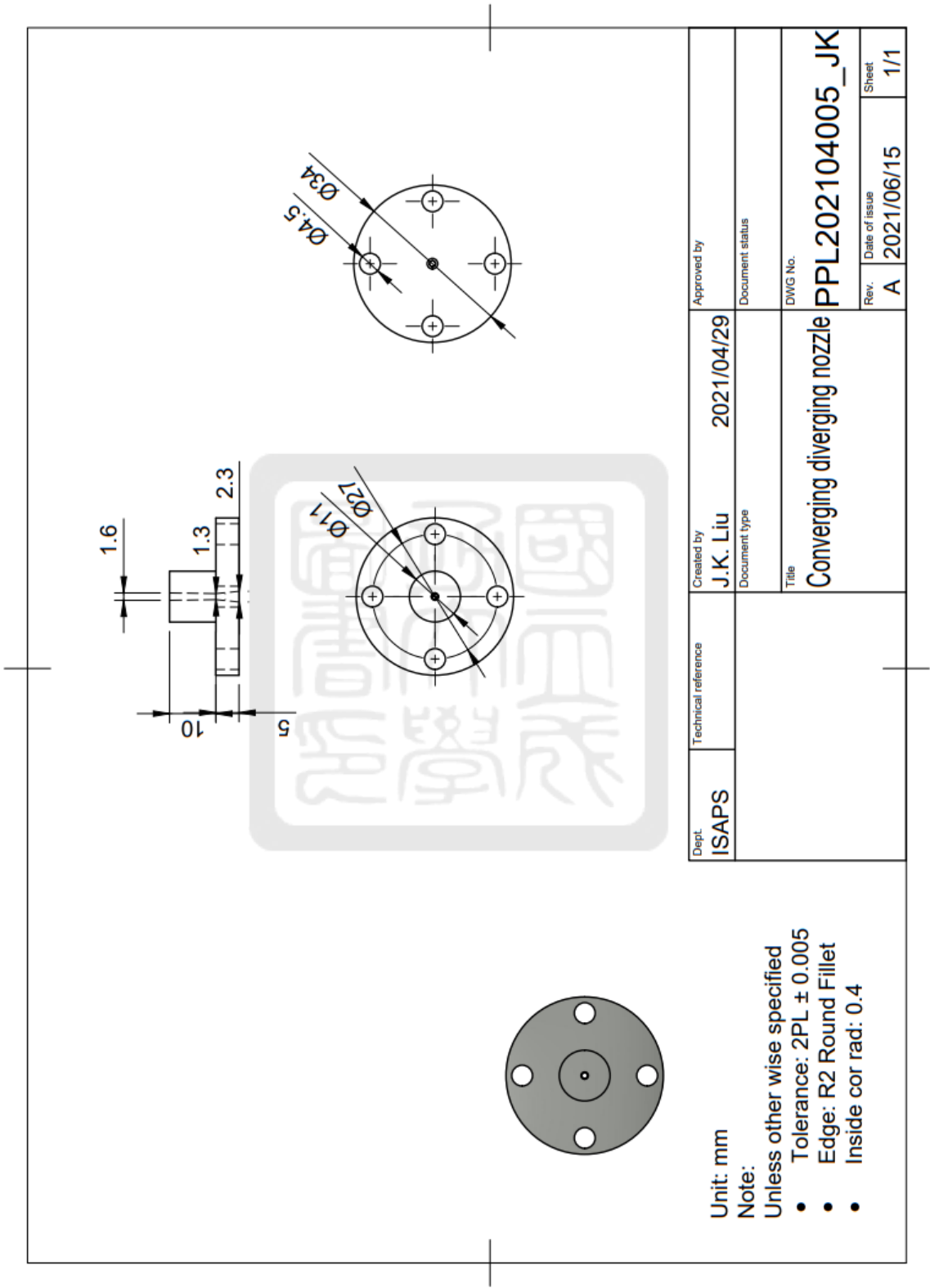
	Wave width time delay 0.5 s data analysis					
	Data1	Data2	Data3	Data4	Data5	Data6
Open voice(a.u.)	0.88556	0.91592	0.85754	0.78748	0.94543	0.85626
Close voice(a.u.)	0.15256	0.14264	0.16174	0.11465	0.10529	0.08966
Open time(s)	0.01715	0.02208	0.01744	0.01750	0.01900	0.01577
Close time(s)	0.53567	0.54055	0.53410	0.53465	0.53692	0.53090
Time delay of pulse valve work(s)	0.51852	0.51847	0.51666	0.51715	0.51792	0.51513
Time delay of function generator(s)	0.5	0.5	0.5	0.5	0.5	0.5
Deviation(%)	3.7%	3.7%	3.3%	3.4%	3.6%	3%

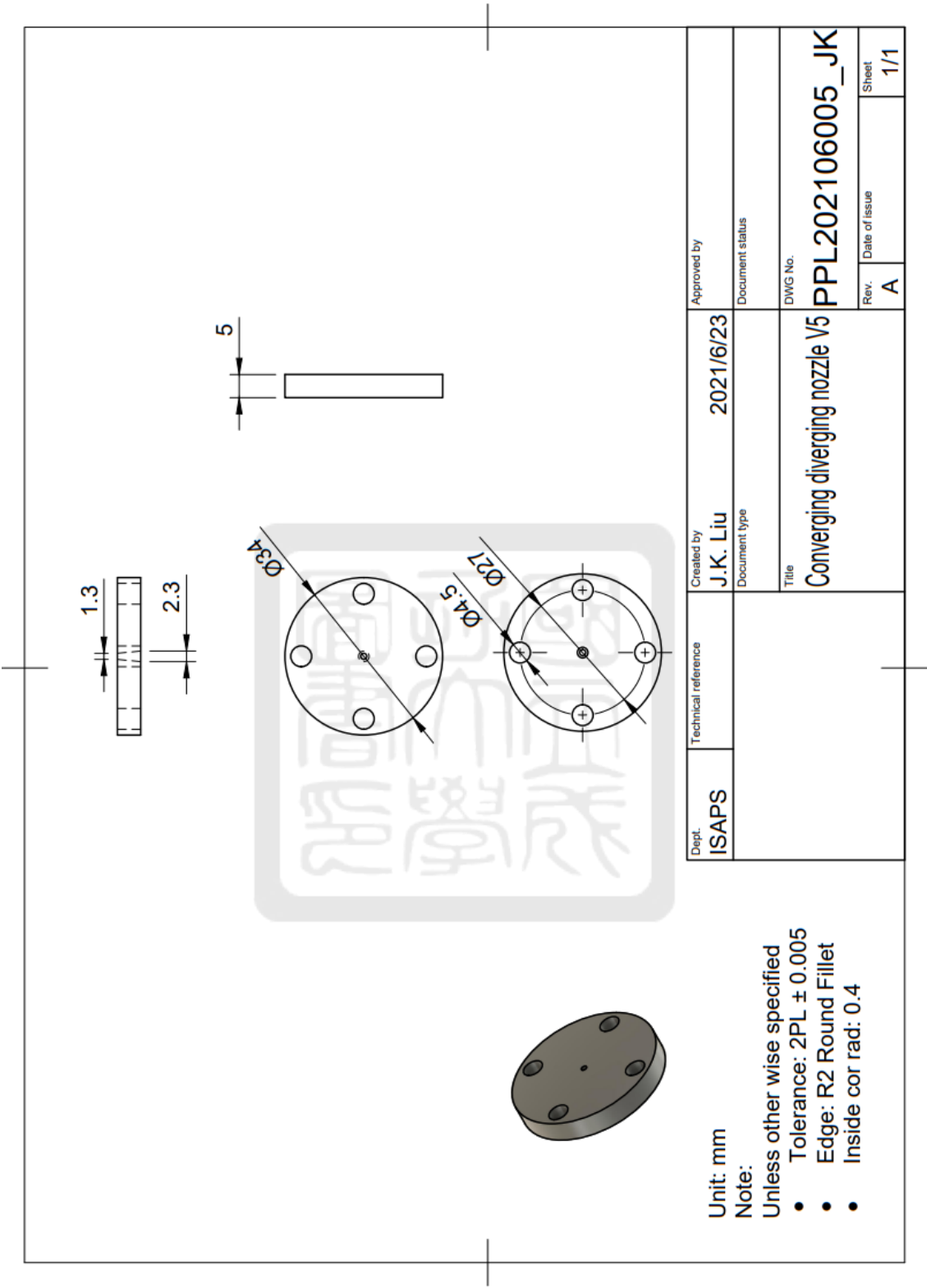
1 s Data analysis

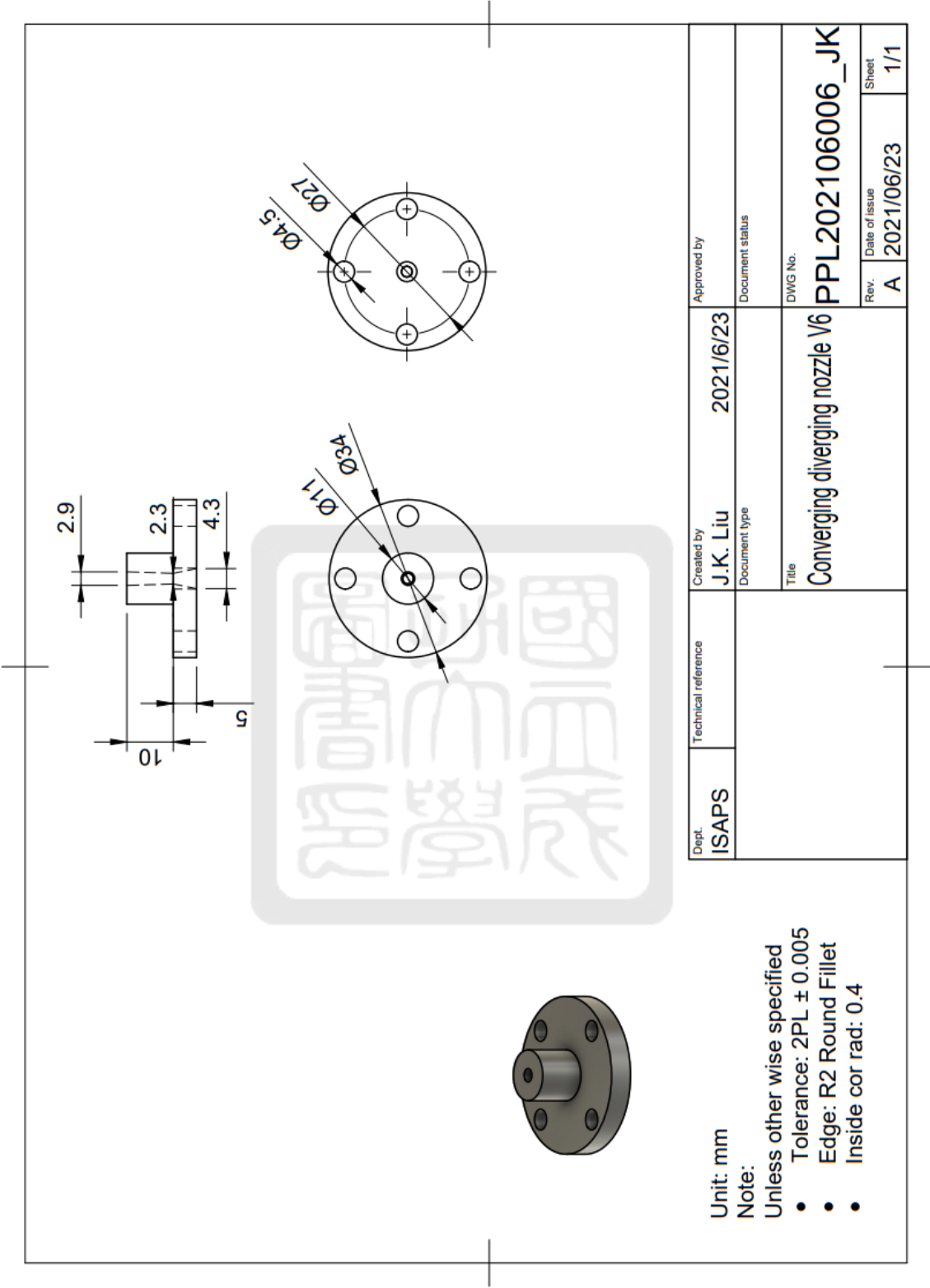
	Wave width time delay 1 s data analysis						
	Data1	Data2	Data3	Data4	Data5	Data6	Data7
Open voice(a.u.)	0.99997	0.98352	0.99997	0.98807	0.927	0.96255	0.57190
Close voice(a.u.)	0.11887	0.10593	0.13068	0.16257	0.18622	0.26062	0.10599
Open time(s)	0.02148	0.02154	0.01804	0.00810	0.01177	0.01183	0.01825
Close time(s)	1.03831	1.03948	1.03571	1.02683	1.02833	1.02852	1.03554
Time delay of pulse valve work(s)	1.01683	1.01794	1.01767	1.01873	1.01656	1.01669	1.01729
Time delay of function generator(s)	1	1	1	1	1	1	1
Deviation(%)	1.6%	1.8%	1.8%	1.9%	1.7%	1.7%	1.7%

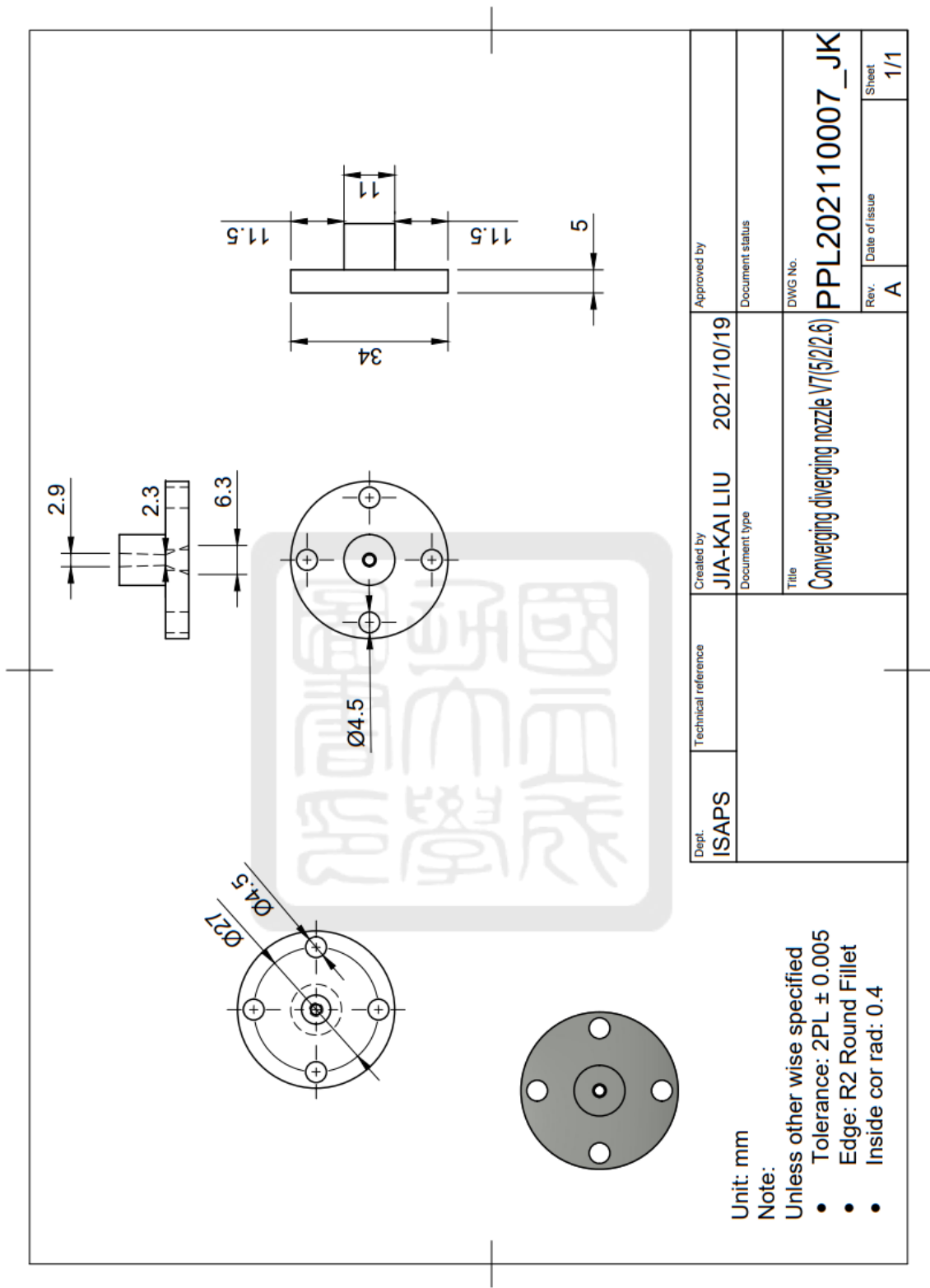
A.2.3 The drawing of the Convergent-divergent nozzles (CDNs)

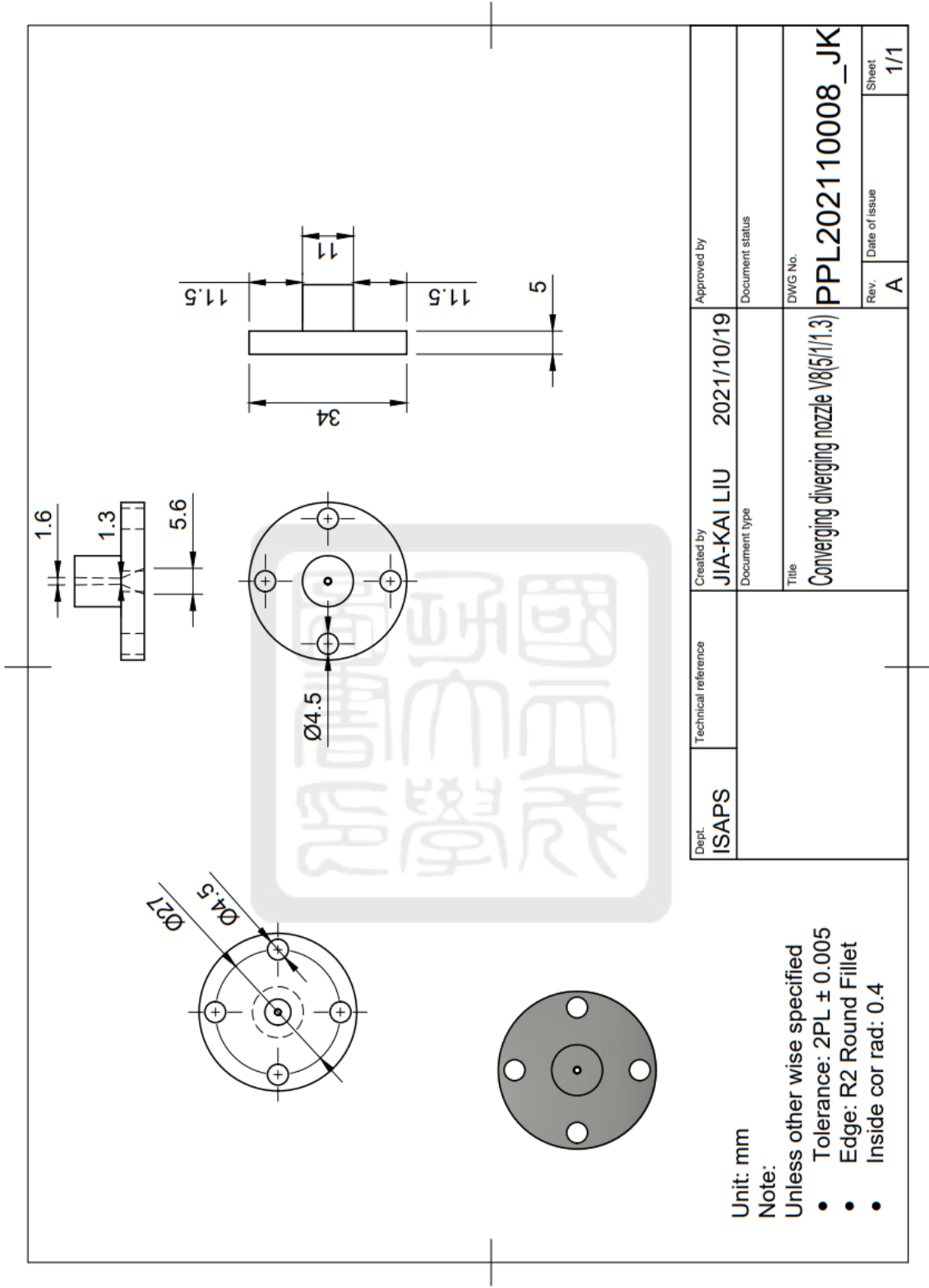
V5A CDN







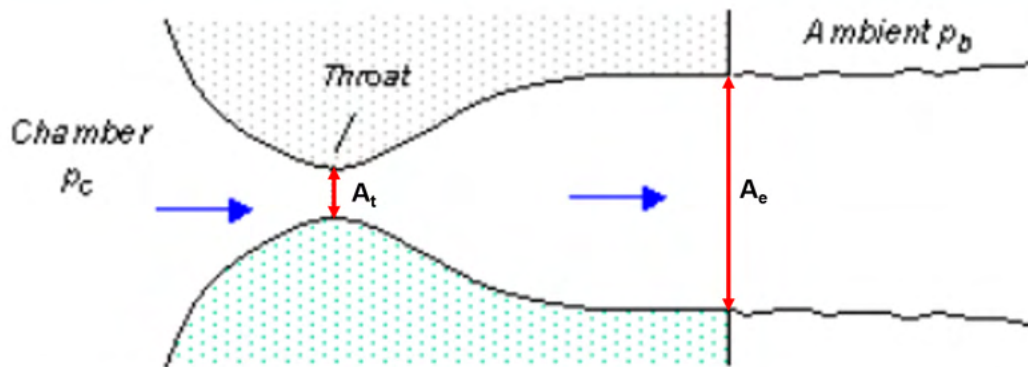




A.2.4 The simulation of CDNs

The information of the simulation

The simulation for 12-V pulse valve, condition of no CDN, and 1-atm pressure difference provided the best result

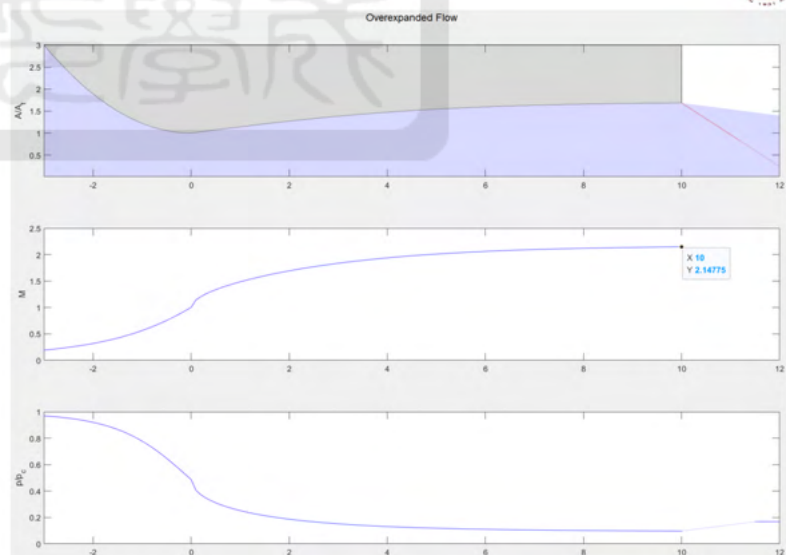
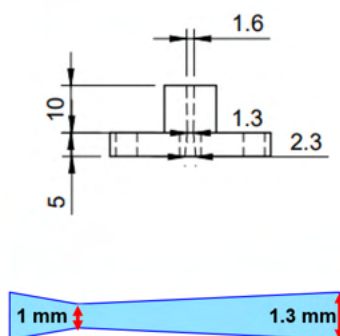


- P_c is the pressure of the reservoir
- P_b is the pressure of the environment
- C_p / C_v is the specific heat capacity of the gas puff



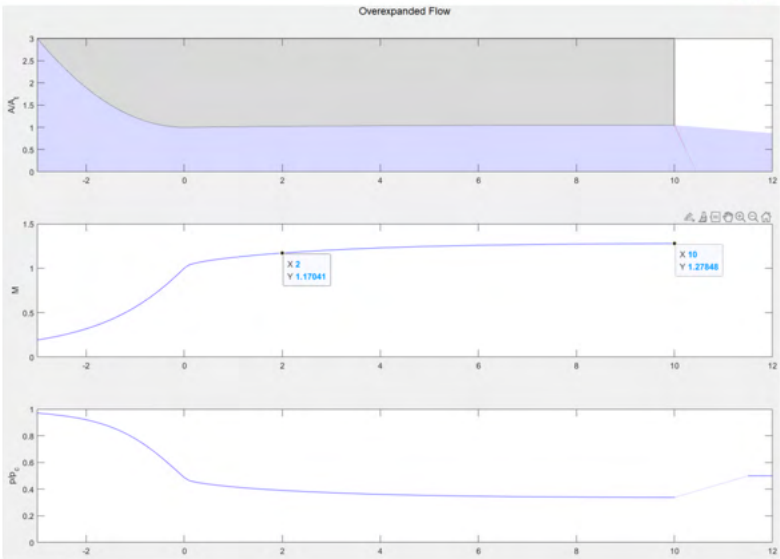
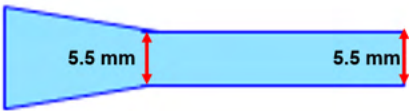
<https://www.engapplets.vt.edu/fluids/CDnozzle/cdinfo.html> (CDN simulation)

The simulation for 24-V pulse valve in the best conditions



<https://www.engapplets.vt.edu/fluids/CDnozzle/cdinfo.html> (CDN simulation)

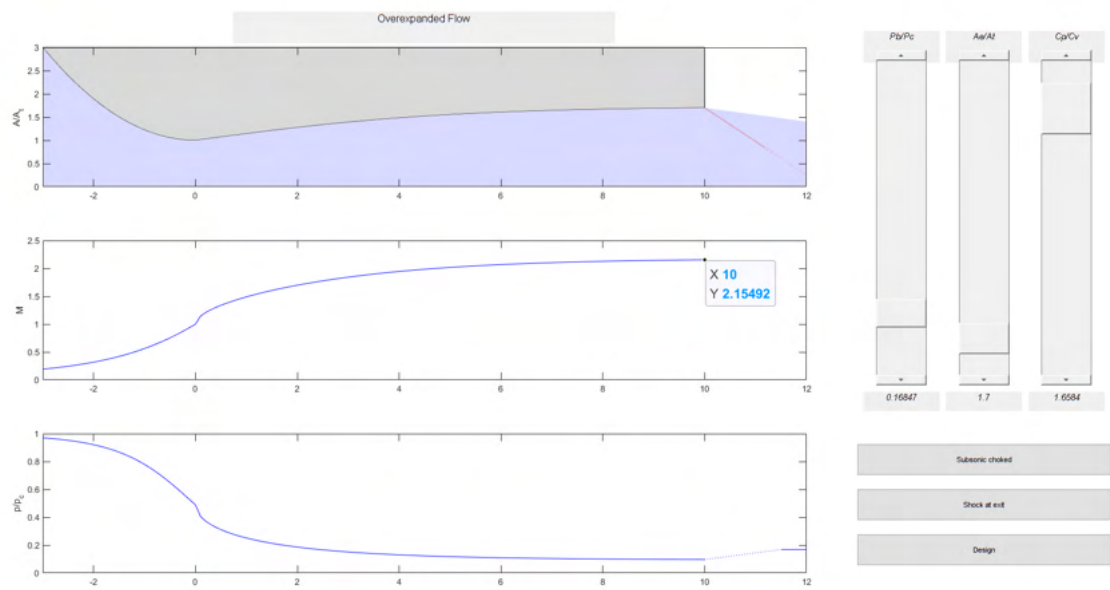
The simulation for 12-V pulse valve in the best conditions



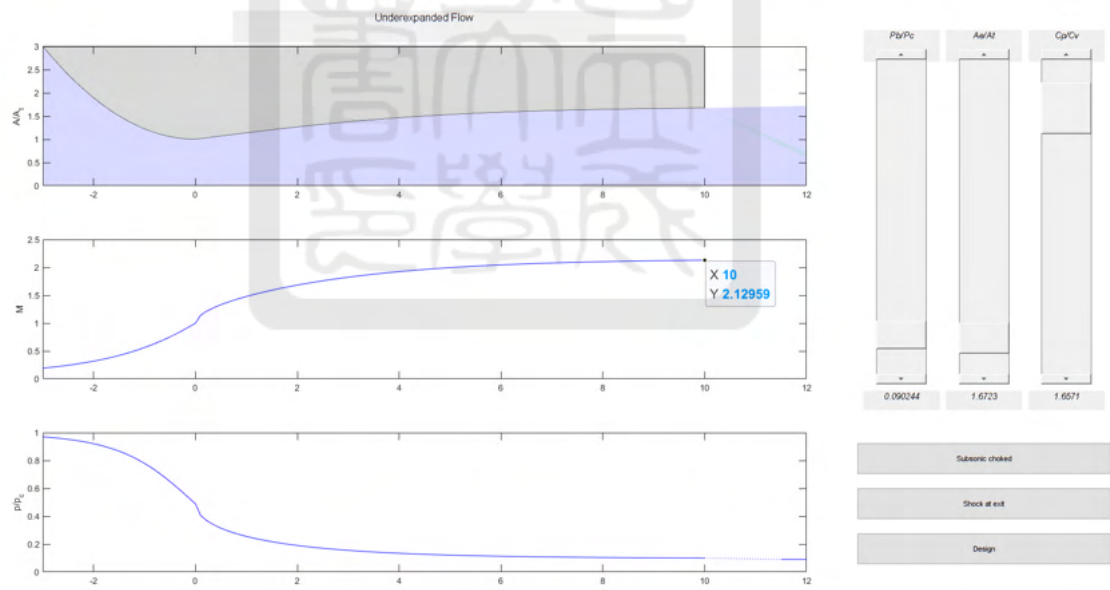
<https://www.engapplets.vt.edu/fluids/CDnozzle/cdinfo.html> (CDN simulation)



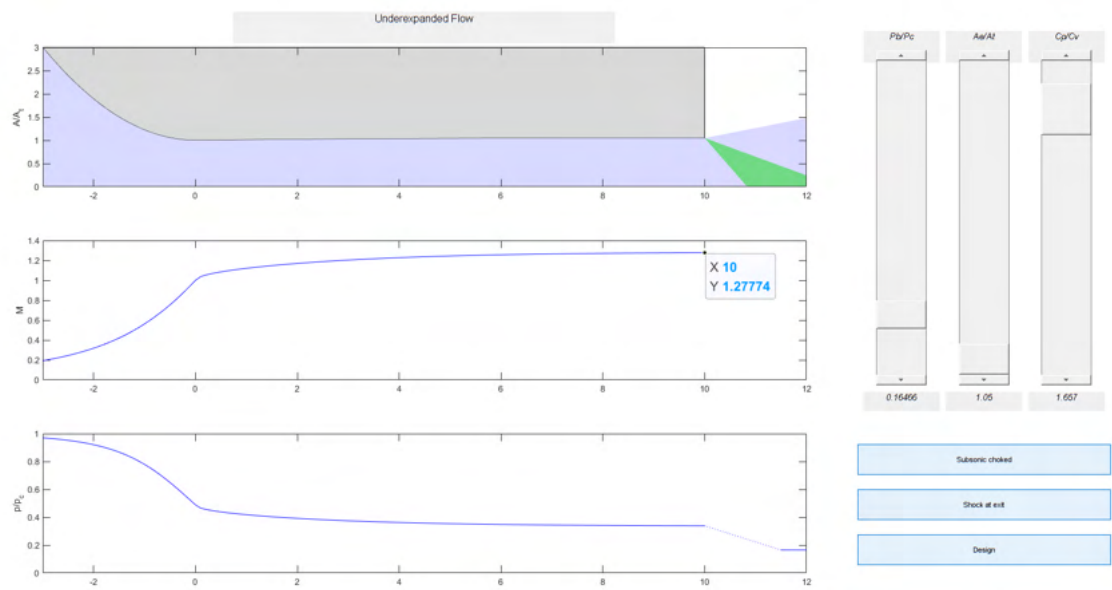
V5A CDN and 5-atm pressure difference



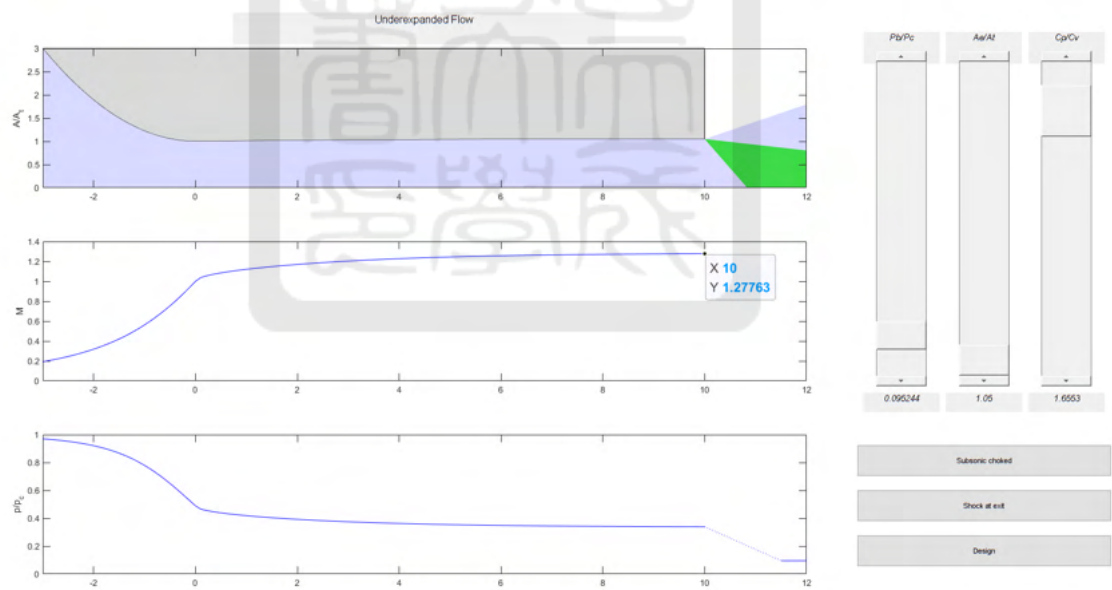
V5A CDN and 10-atm pressure difference



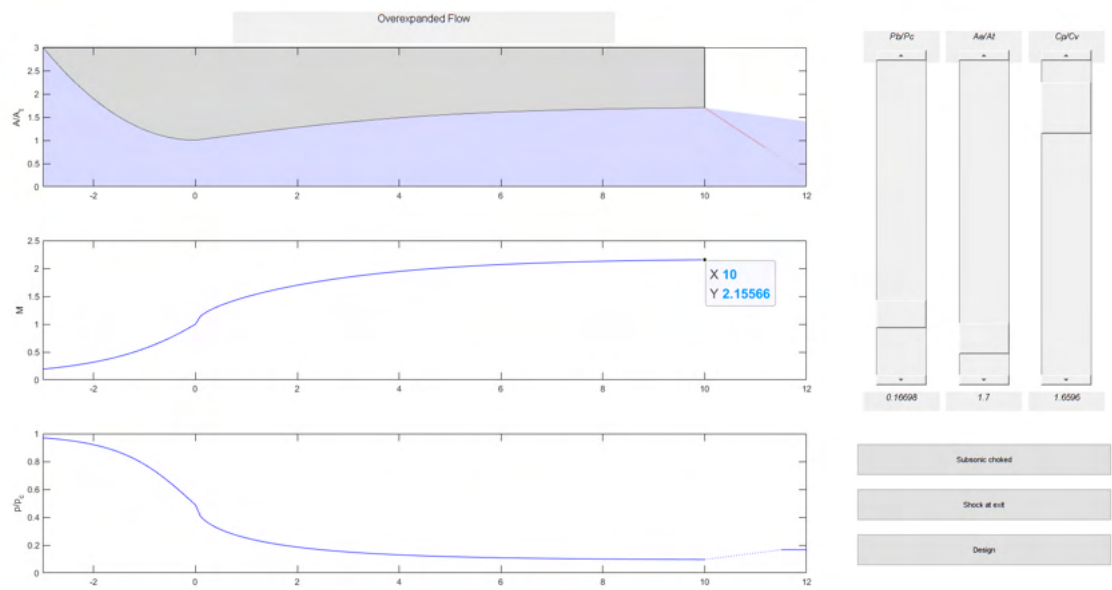
V5B CDN and 5-atm pressure difference



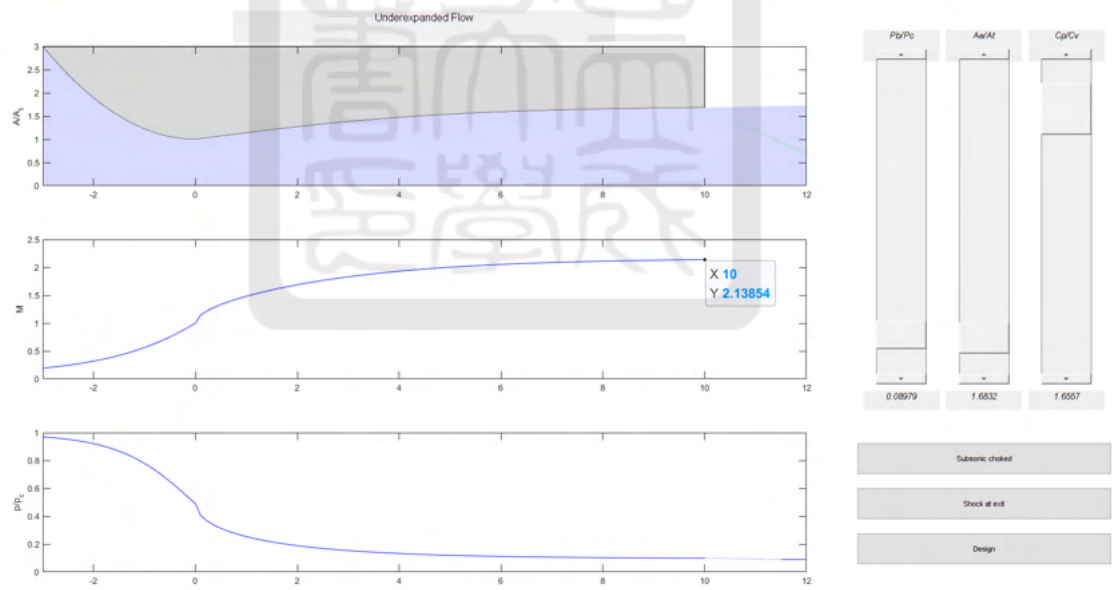
V5B CDN and 10-atm pressure difference



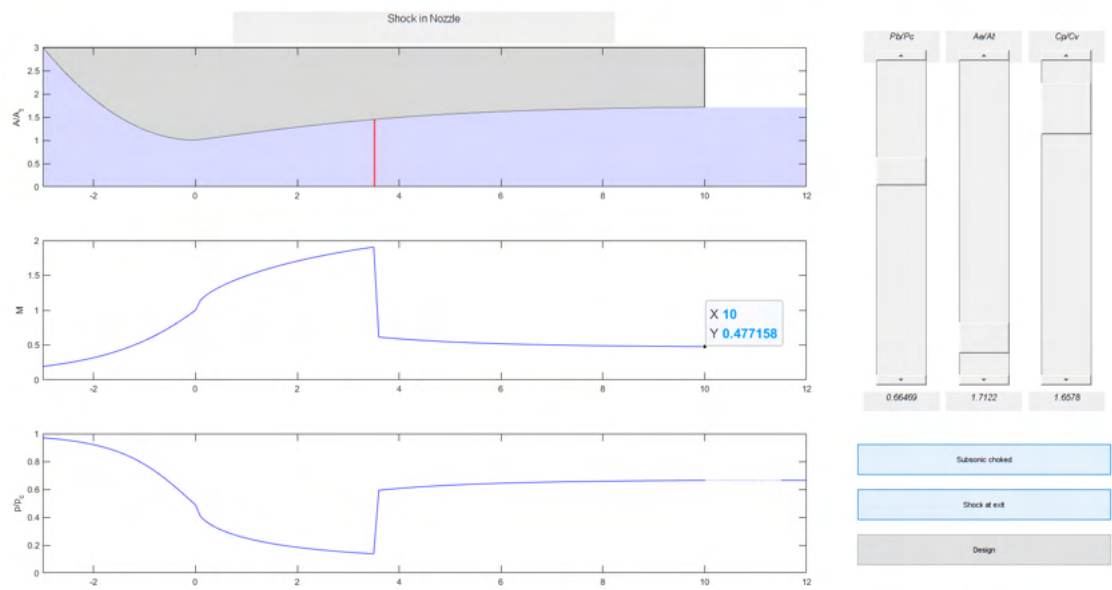
V6 CDN and 5-atm pressure difference



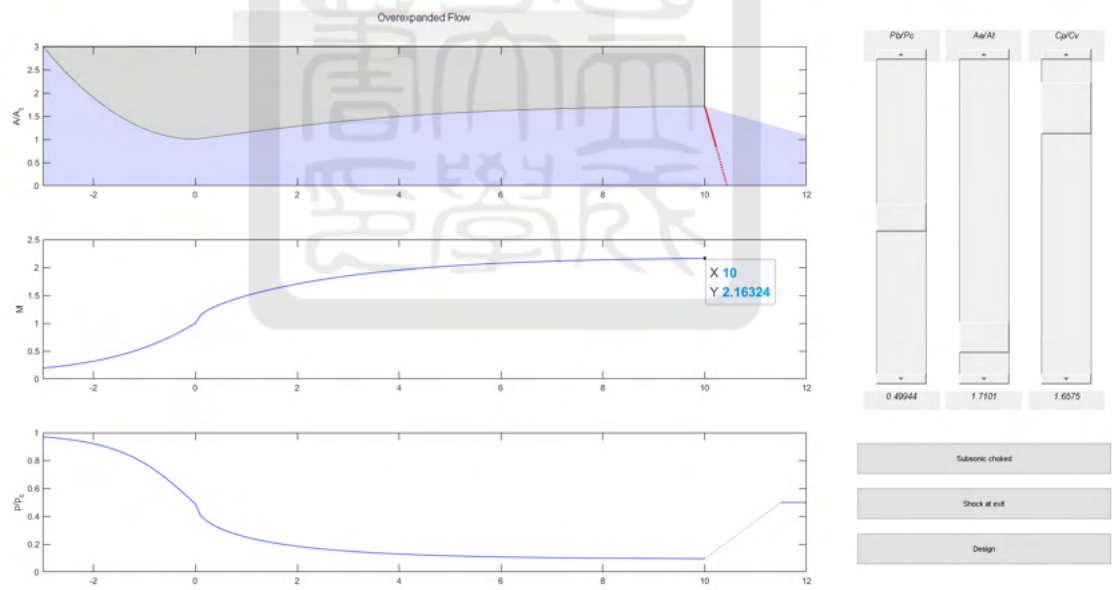
V6 CDN and 10-atm pressure difference



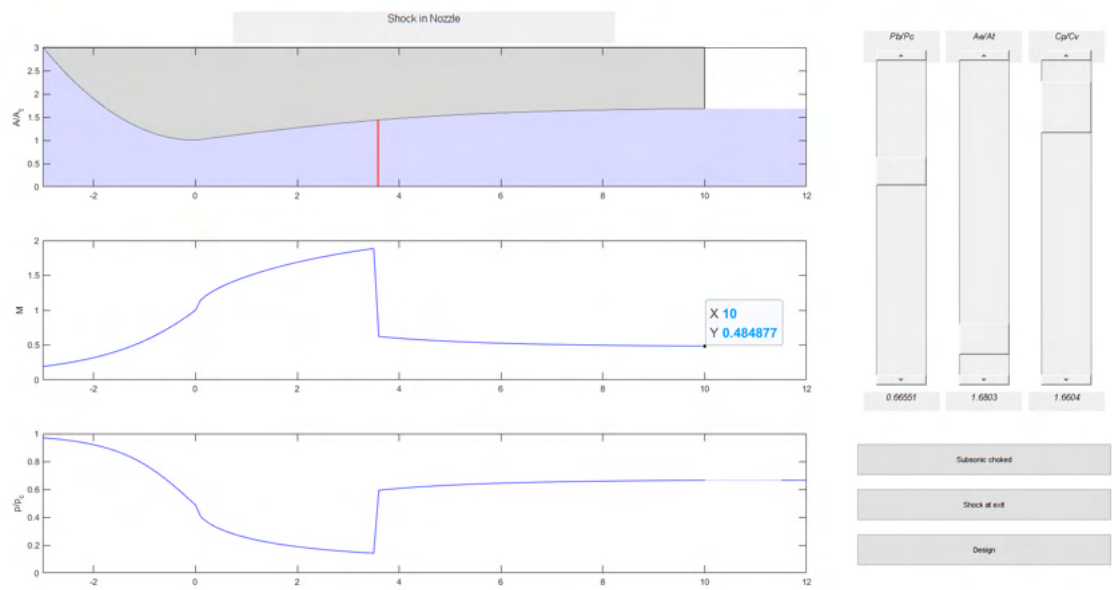
V7 CDN and 0.5-atm pressure difference



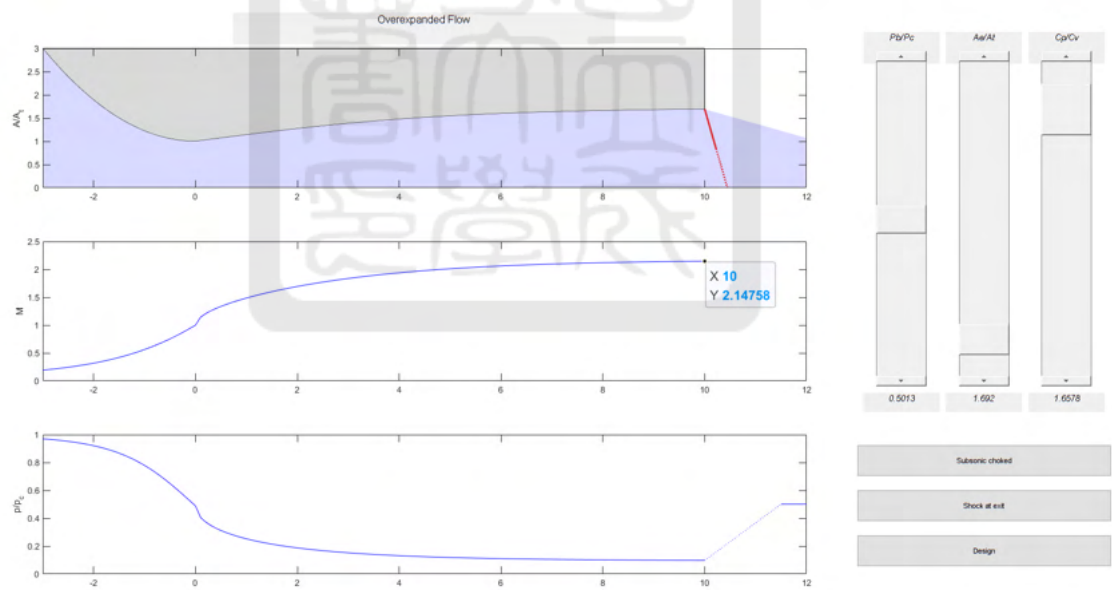
V7 CDN and 1-atm pressure difference



V8 CDN and 0.5-atm pressure difference

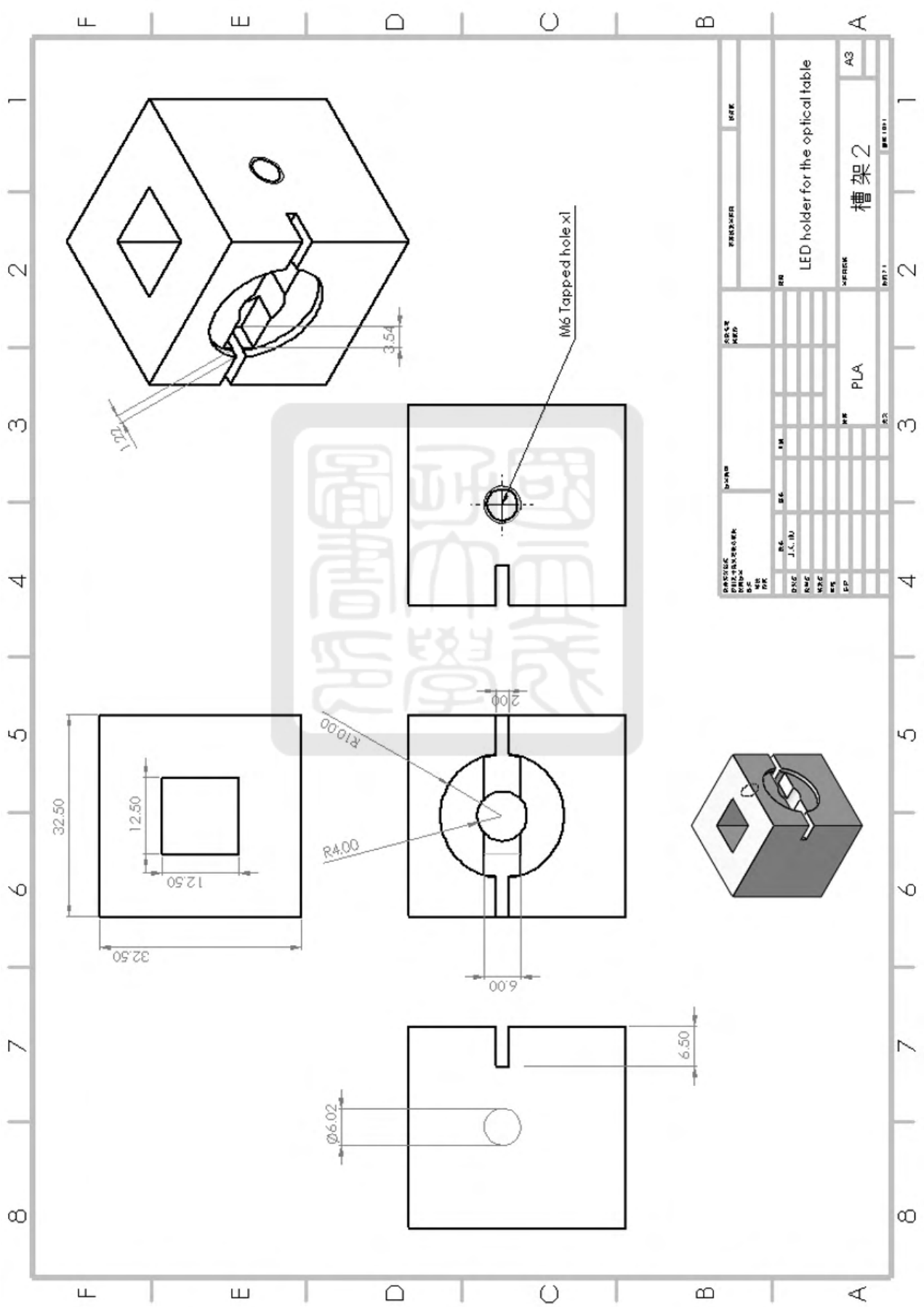


V8 CDN and 1-atm pressure difference

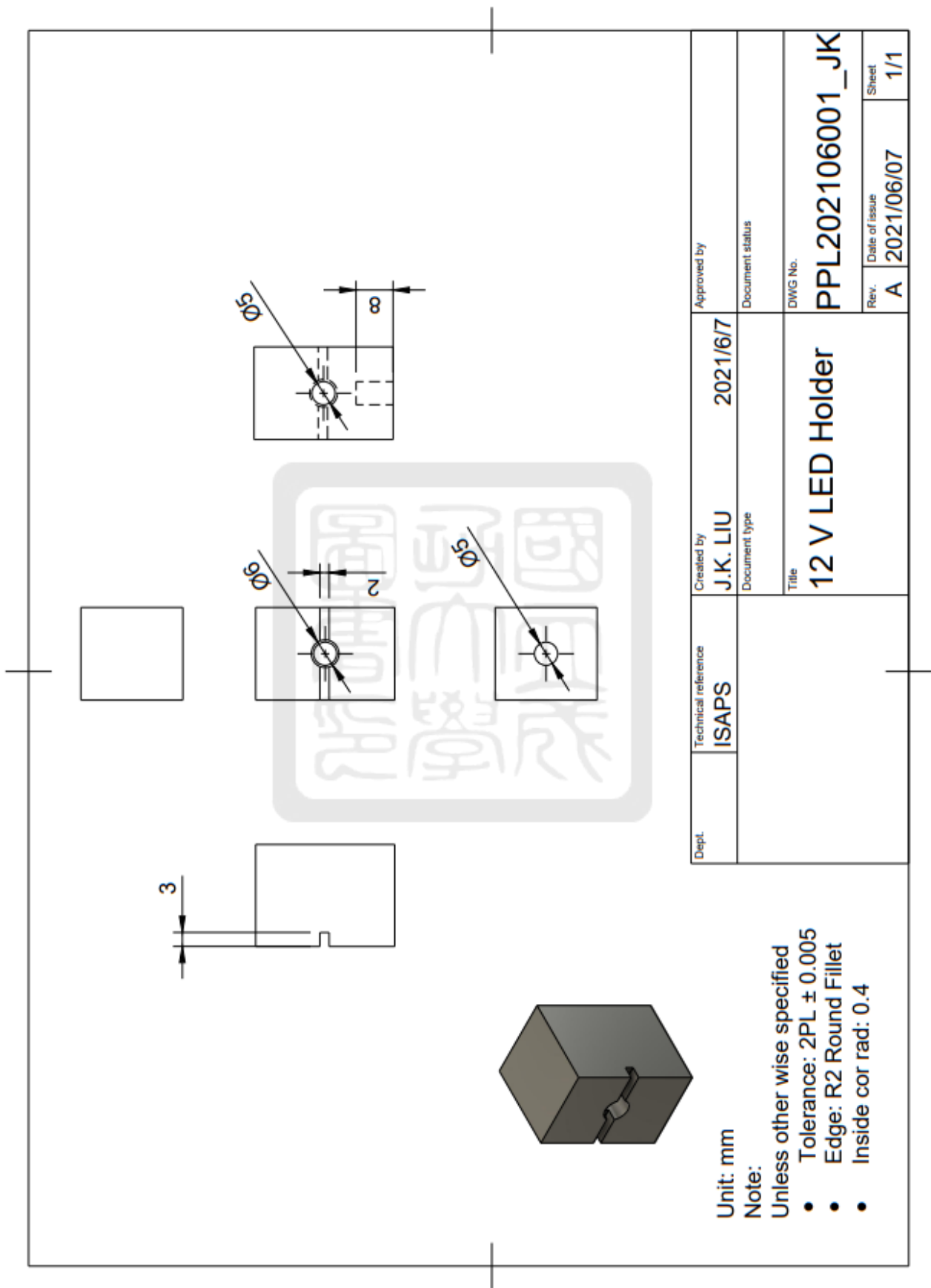


A.3 Schlieren system

A.3.1 The first version of the 12-V LED holder



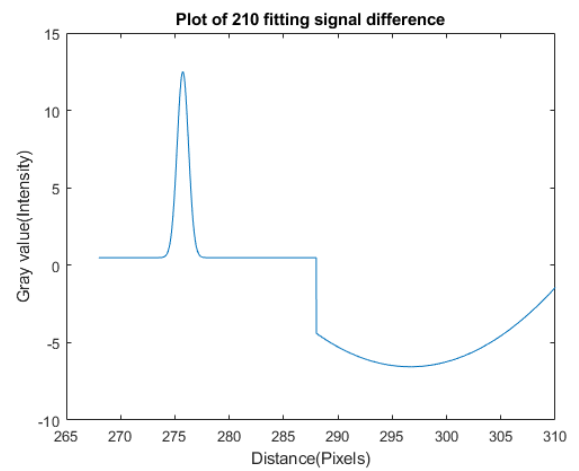
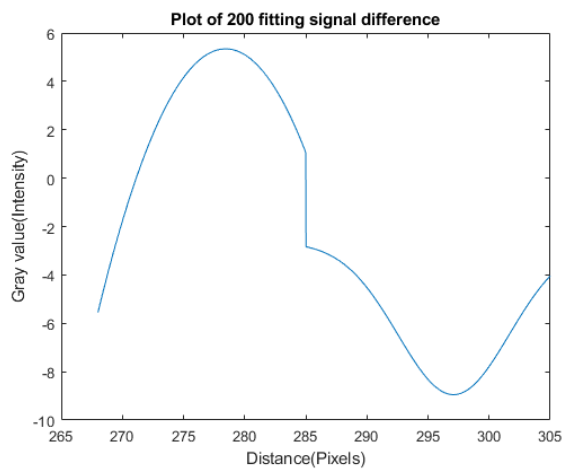
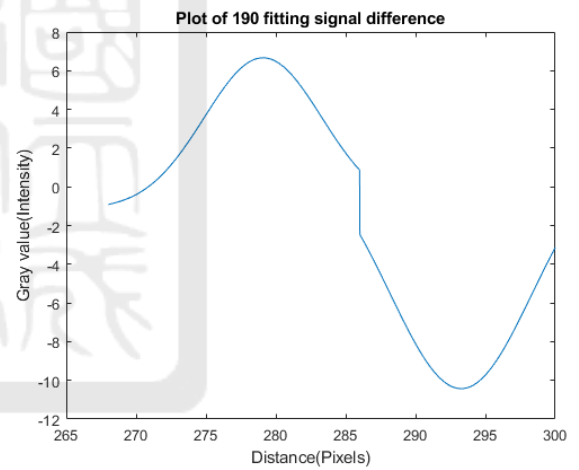
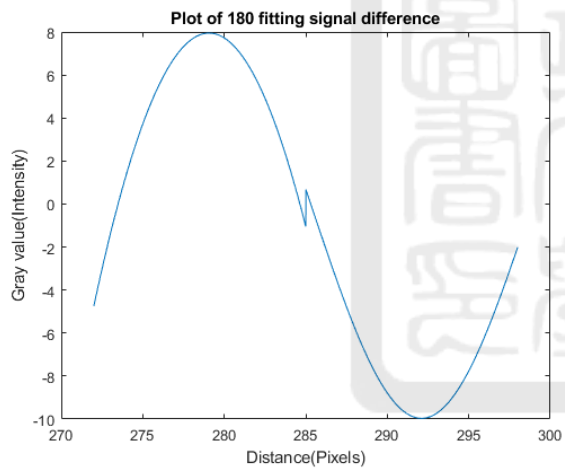
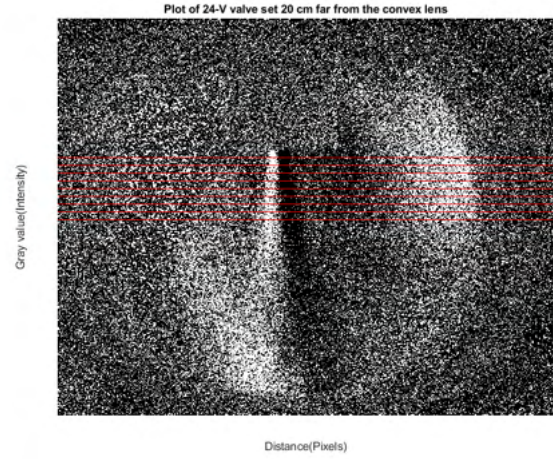
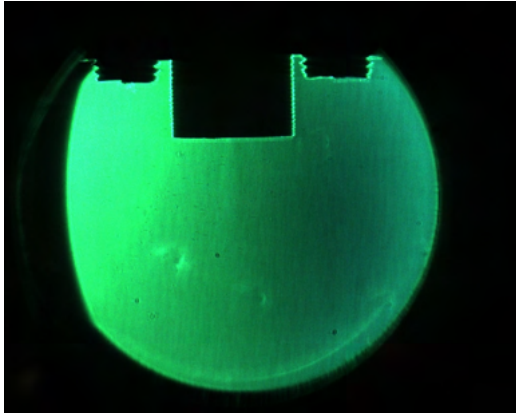
A.3.2 The second version of the 12-V LED holder

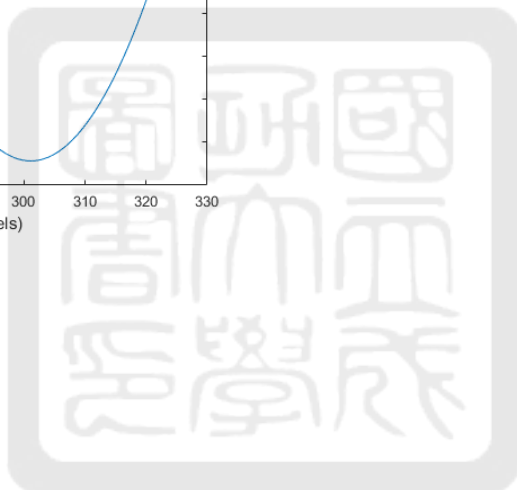
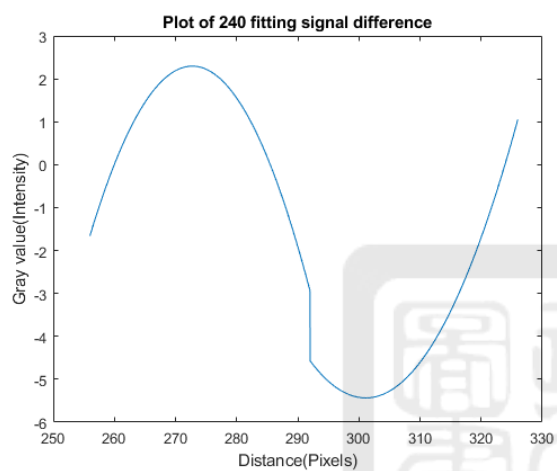
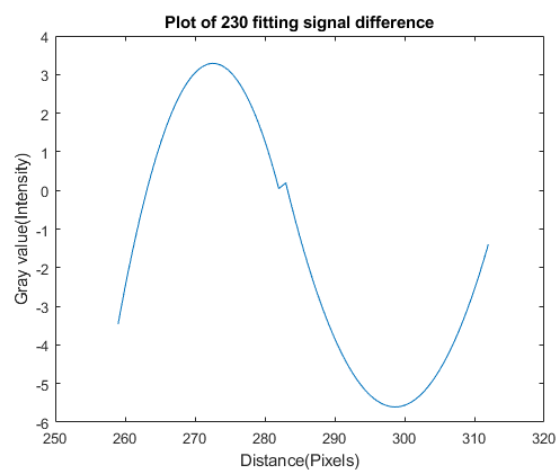
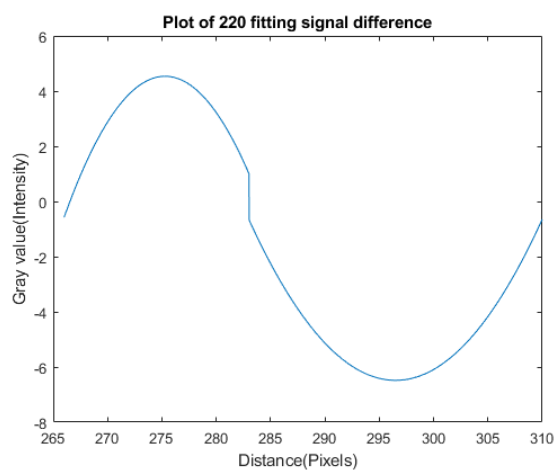


A.4 Experimental results

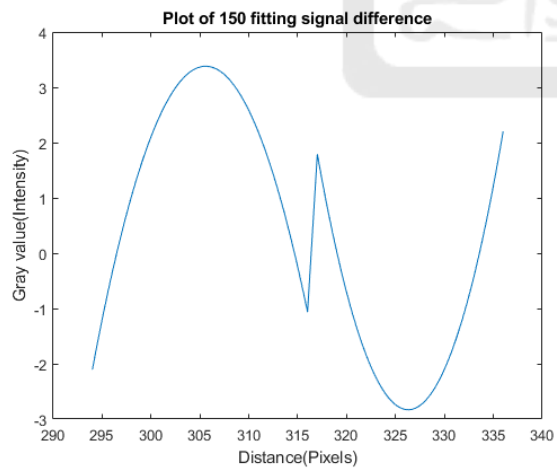
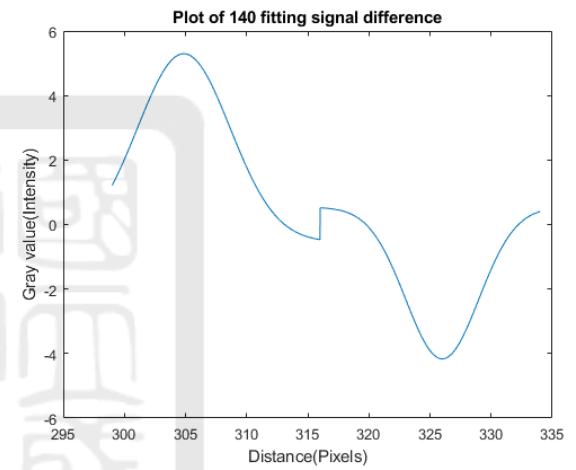
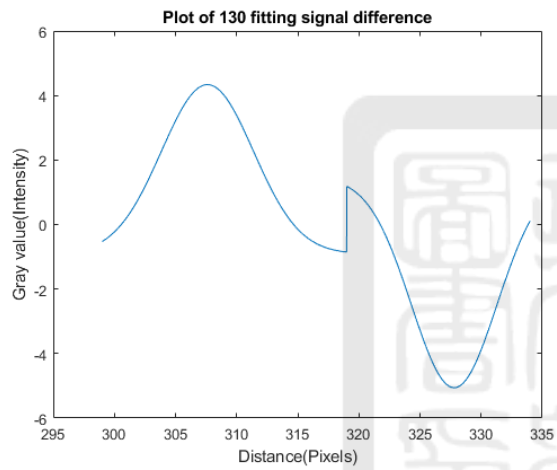
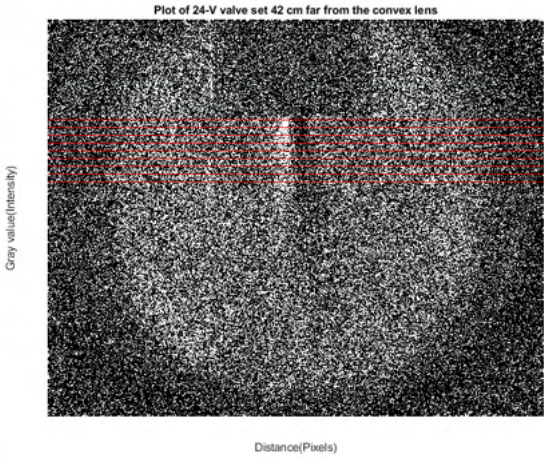
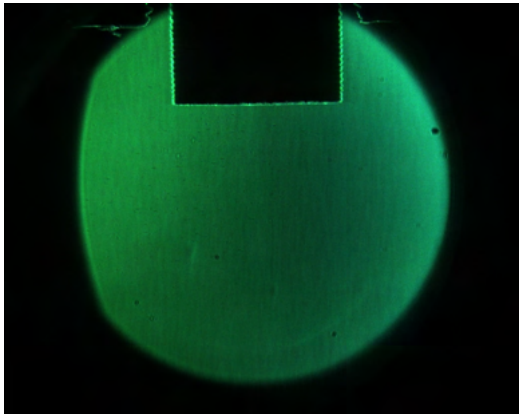
A.4.1 Different locations of the pulse valve setting

Set at 20 cm from the convex lens



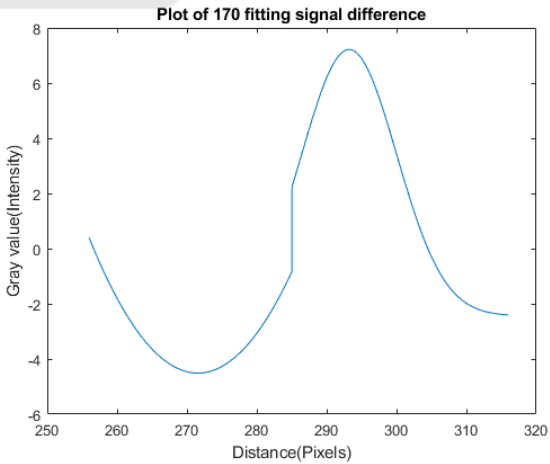
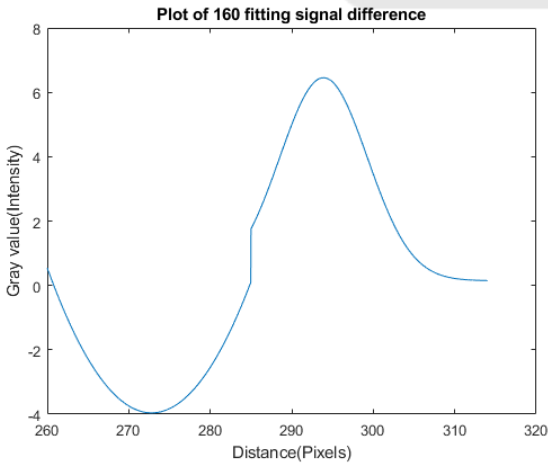
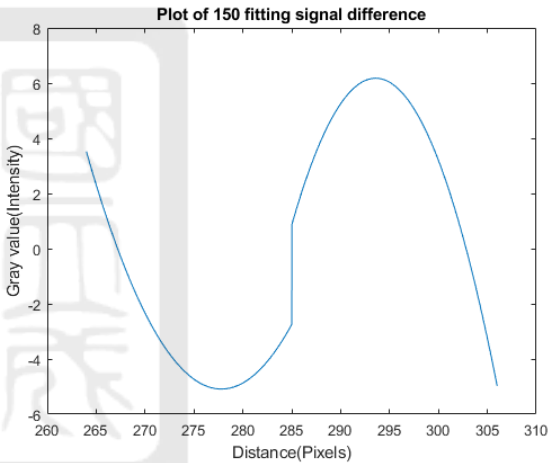
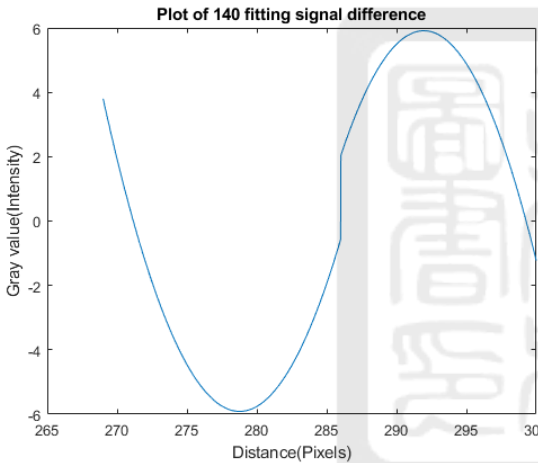
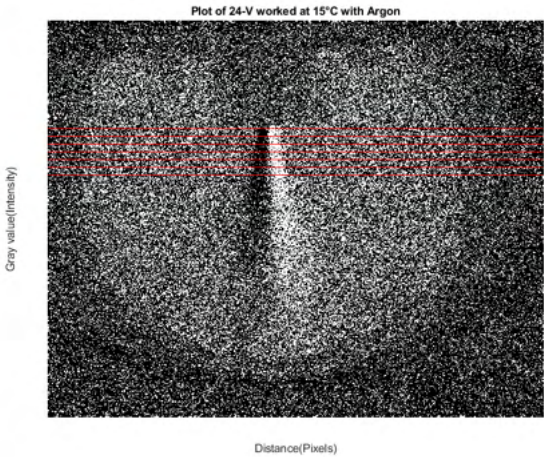
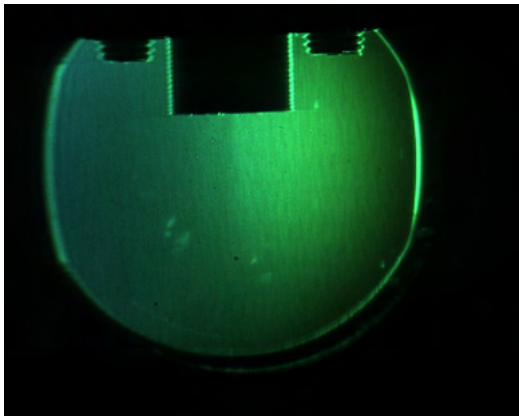


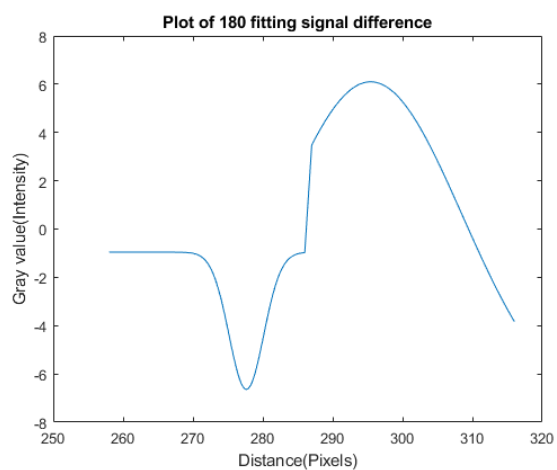
Set at 42 cm from the convex lens



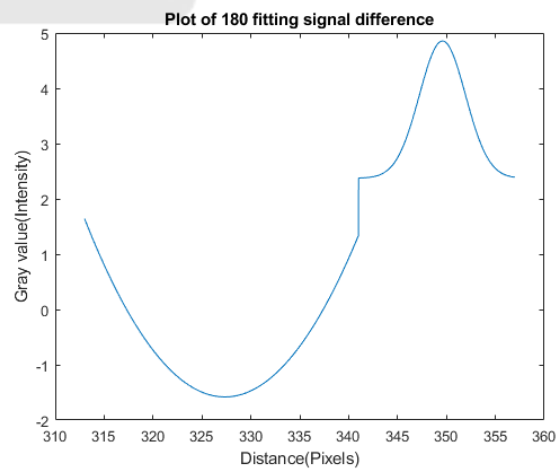
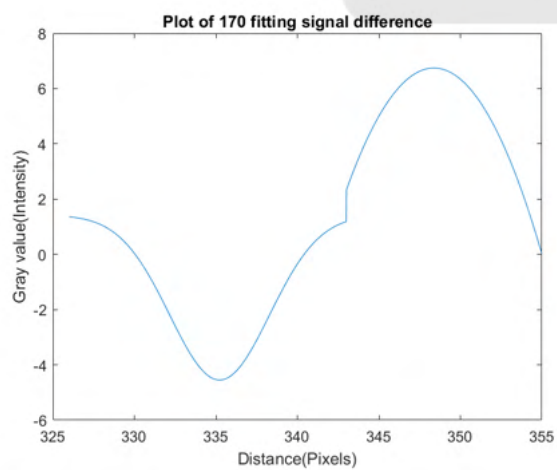
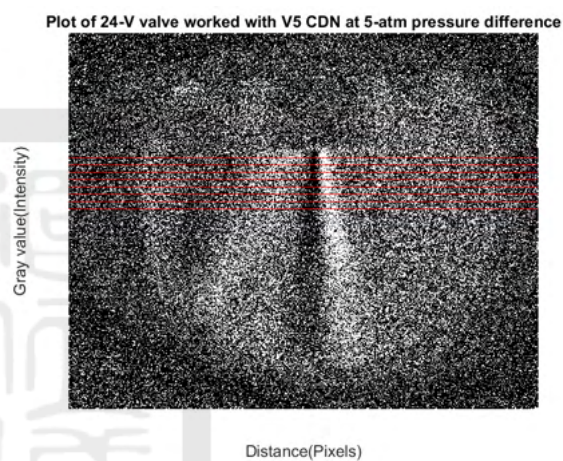
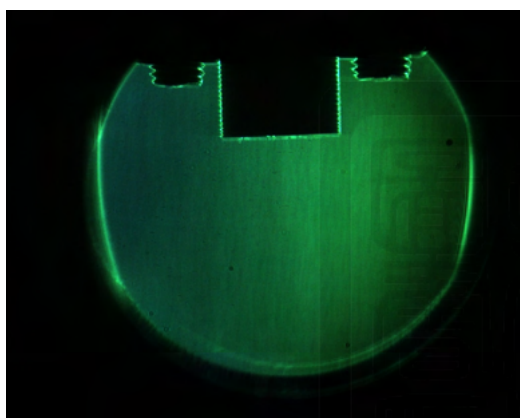
A.4.2 Different temperature of the gas puff

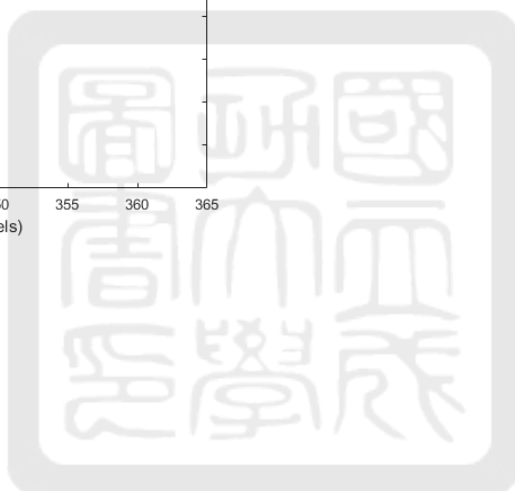
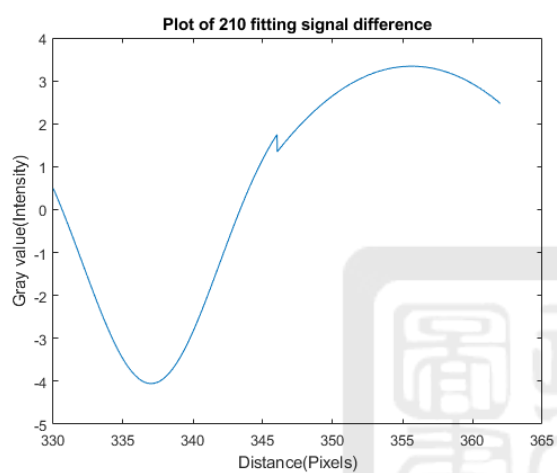
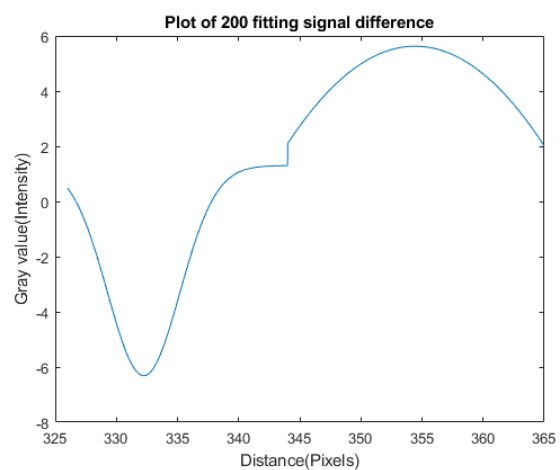
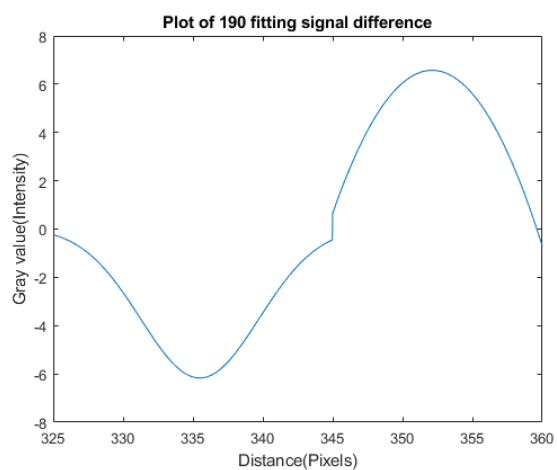
15°C





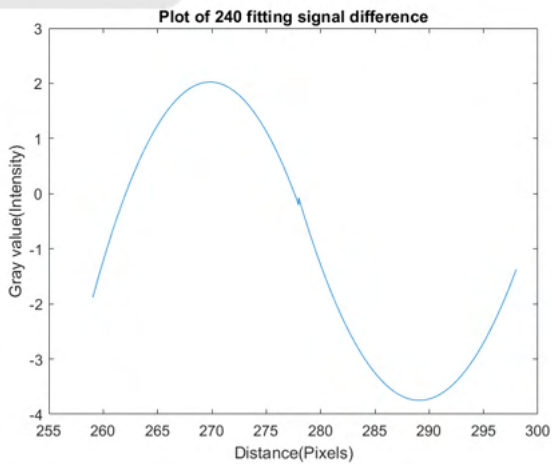
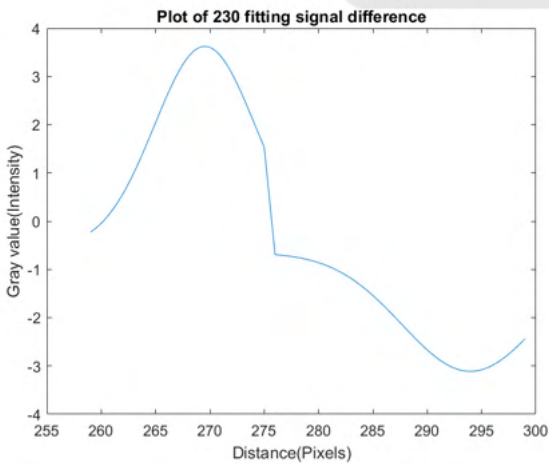
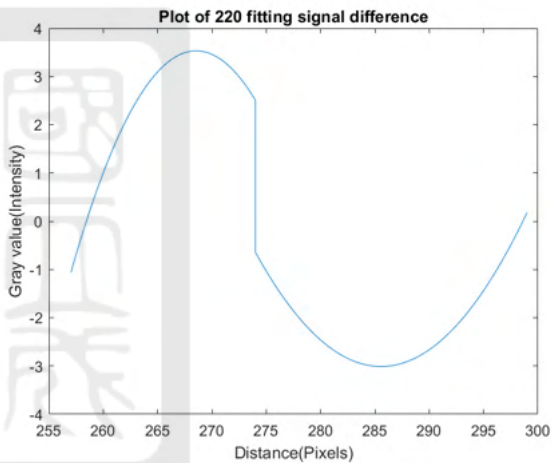
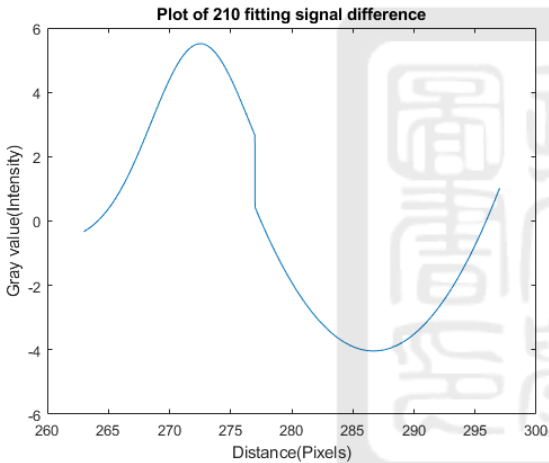
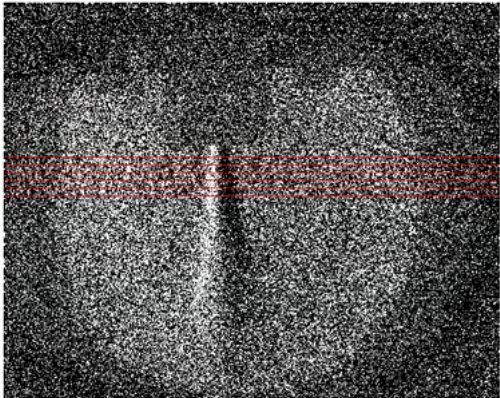
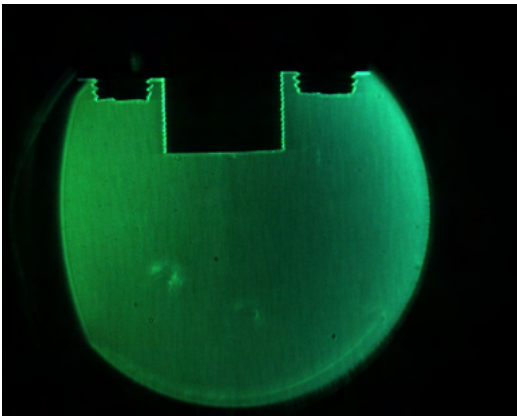
25°C

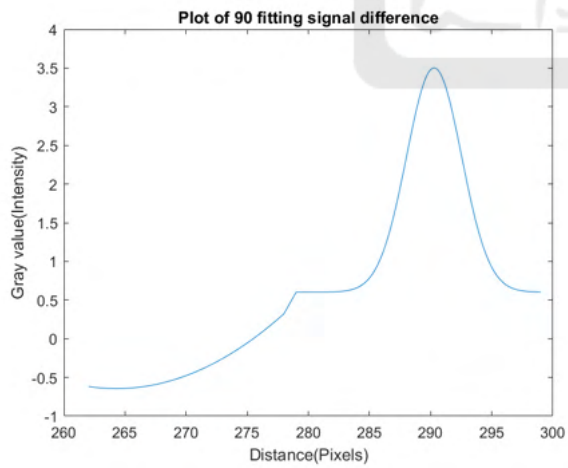
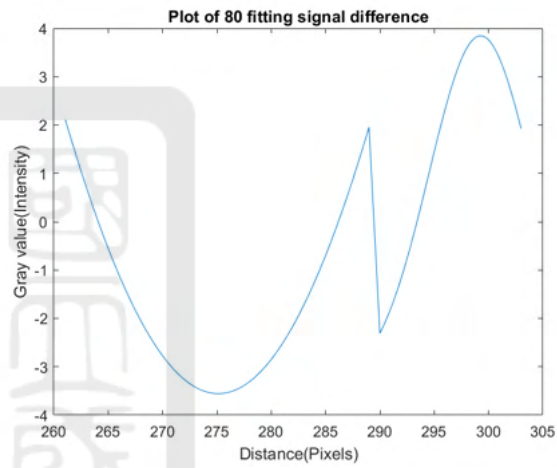
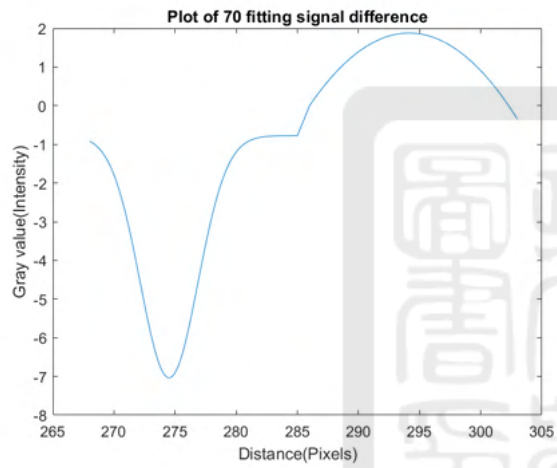
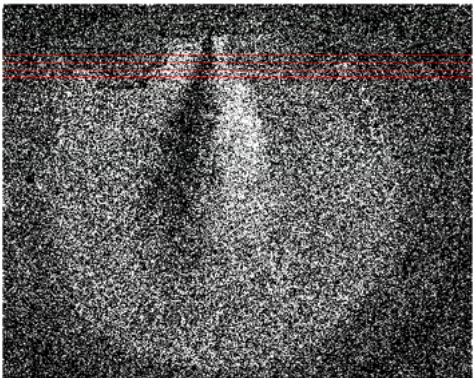
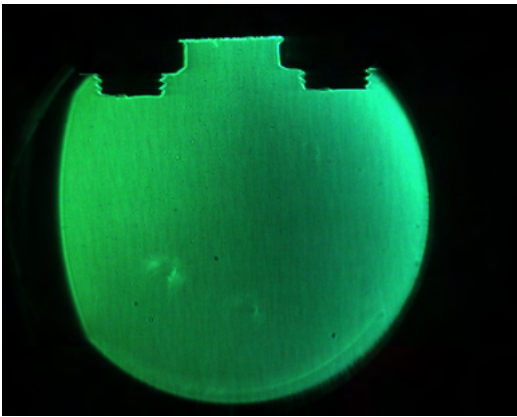


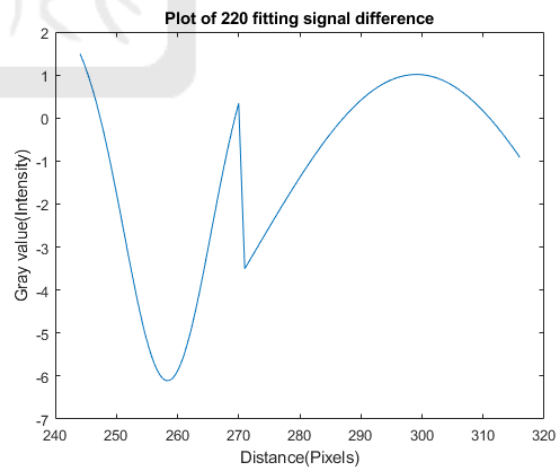
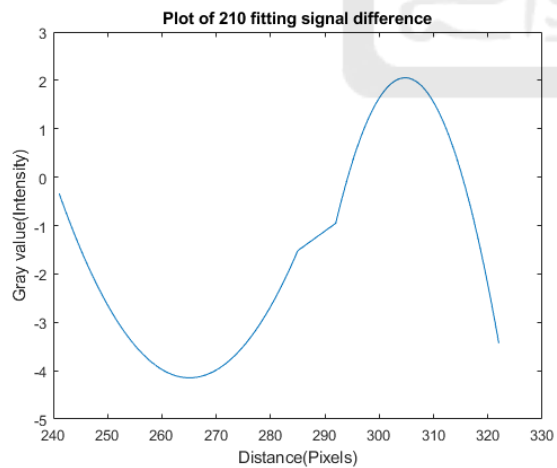
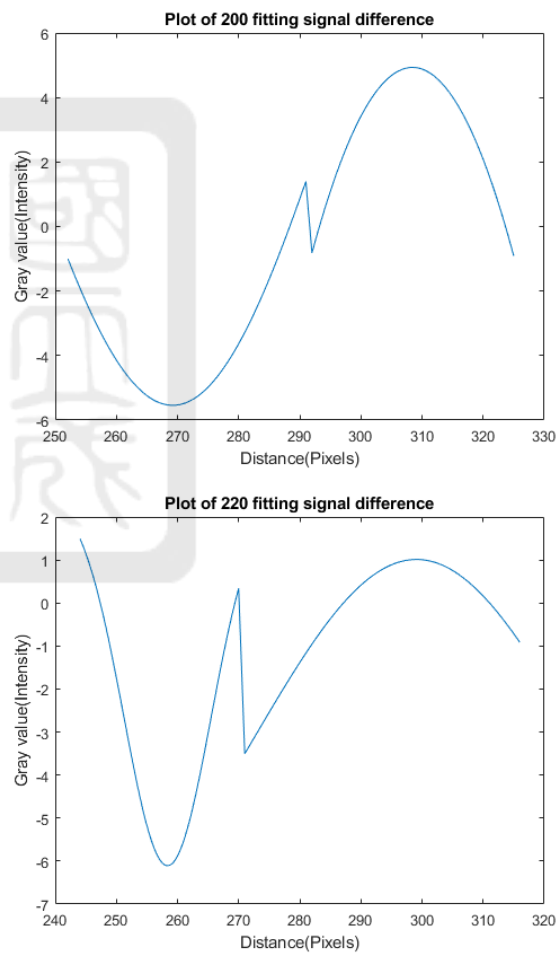
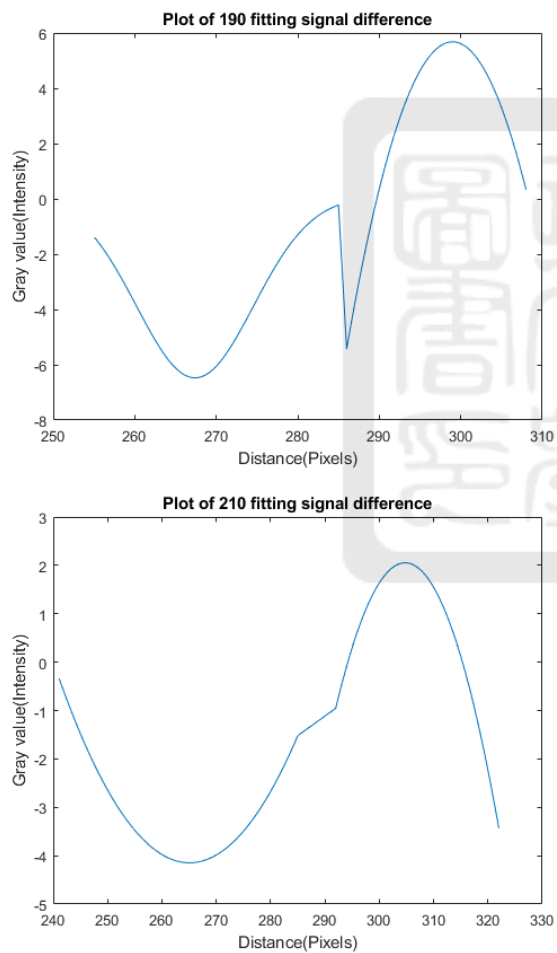
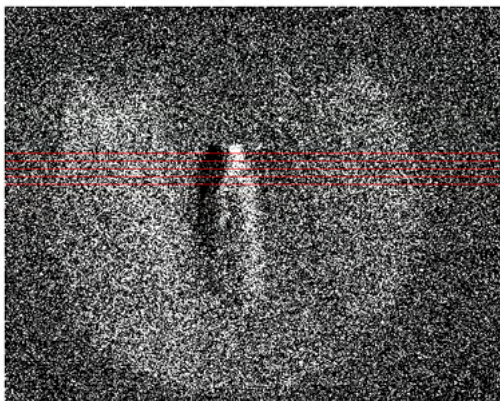
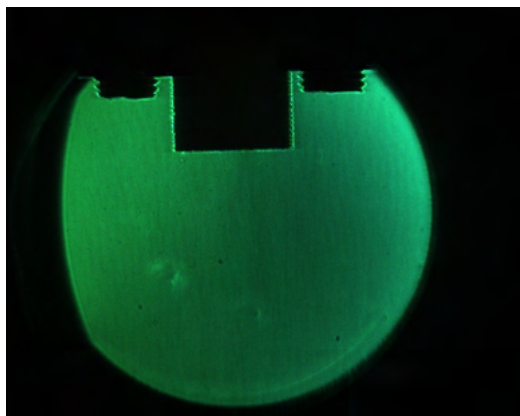


A.4.3 Different convergent-divergent nozzles (CDNs)

V5A CDN

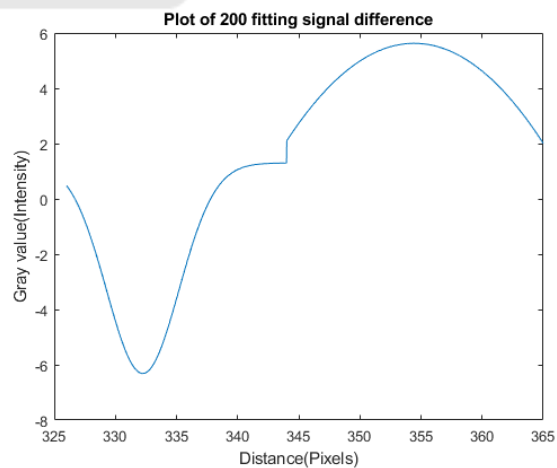
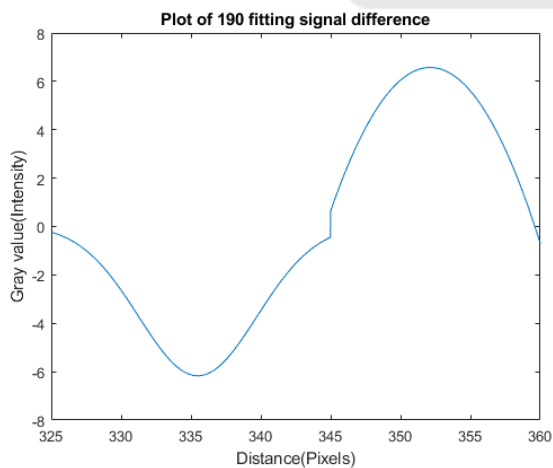
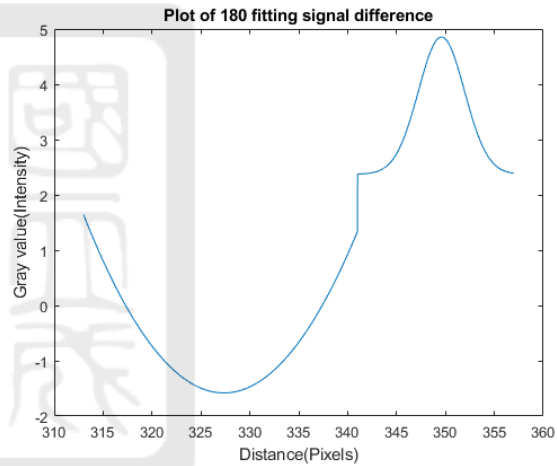
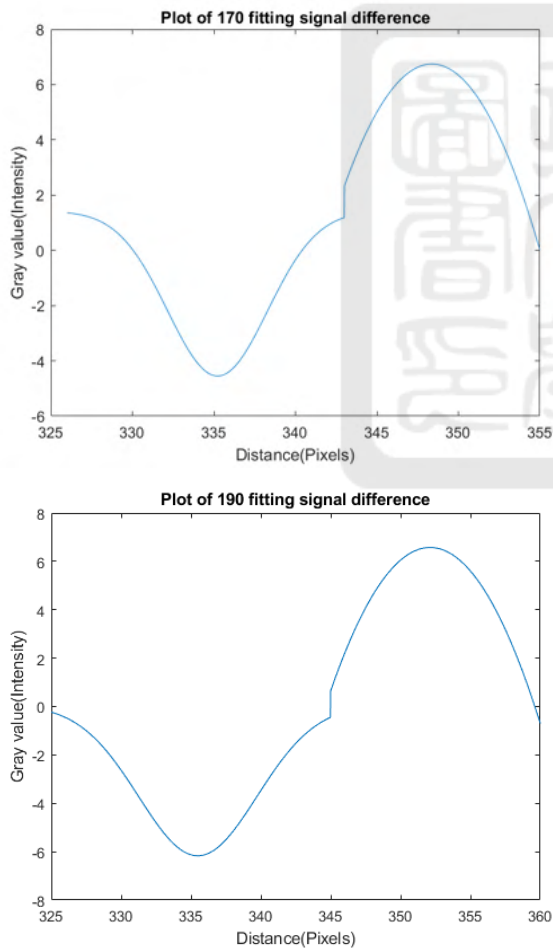
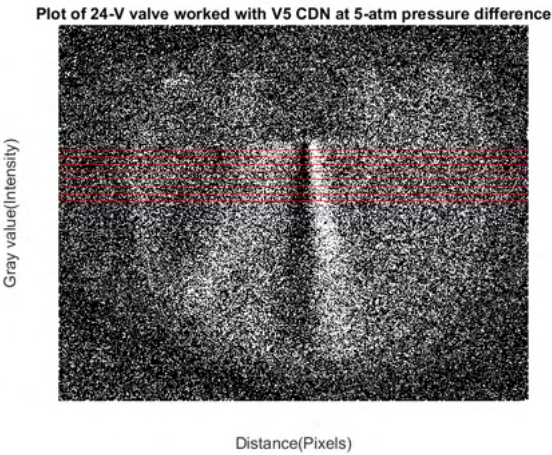
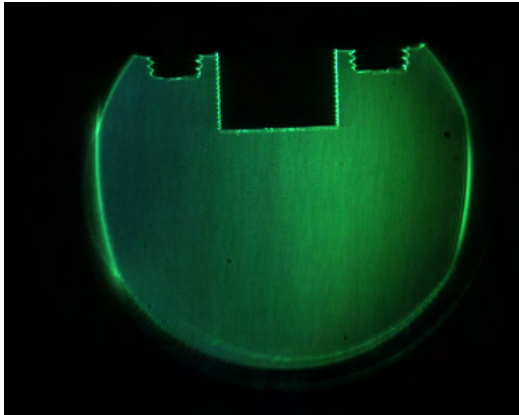


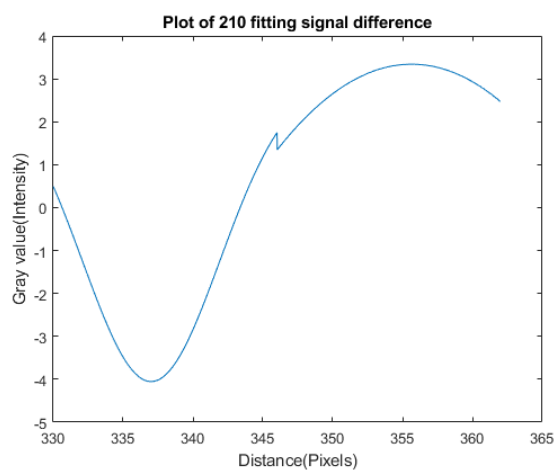




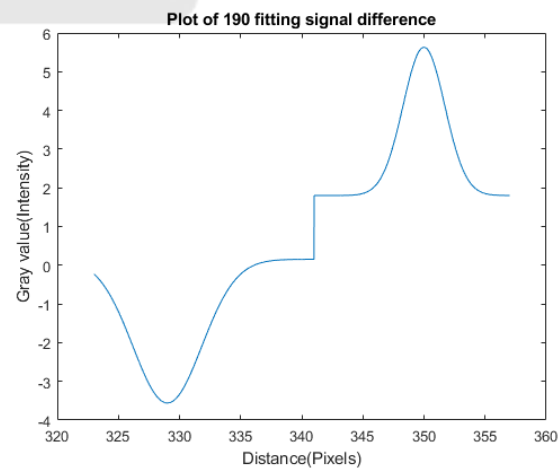
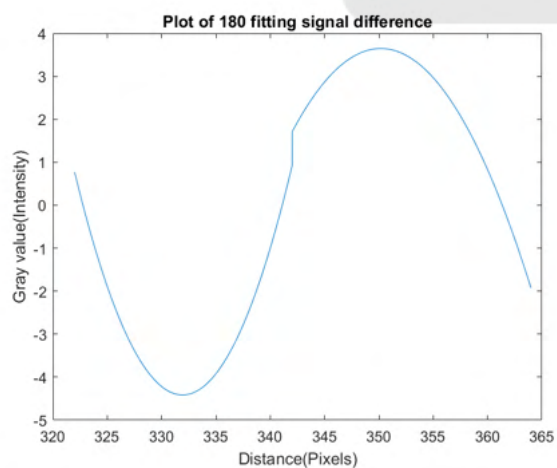
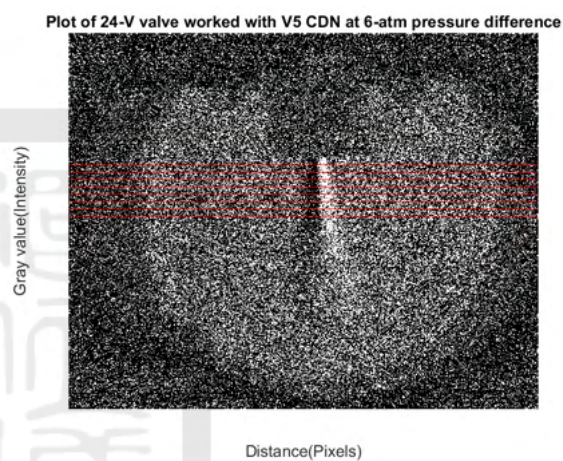
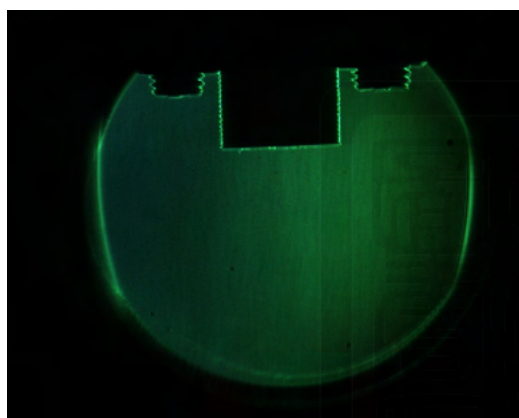
A.4.4 Different pressure of the argon gas

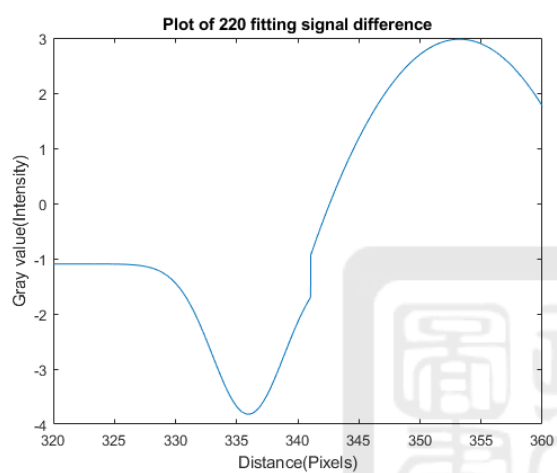
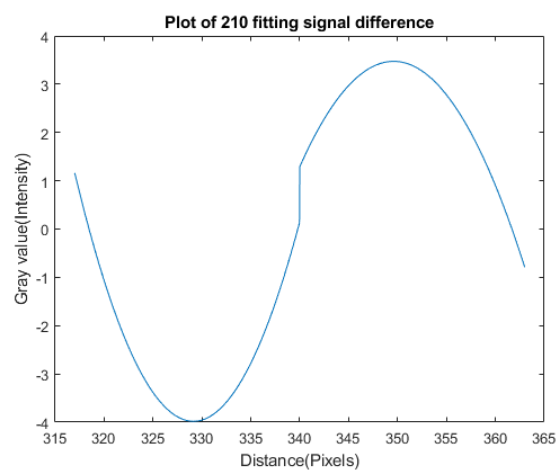
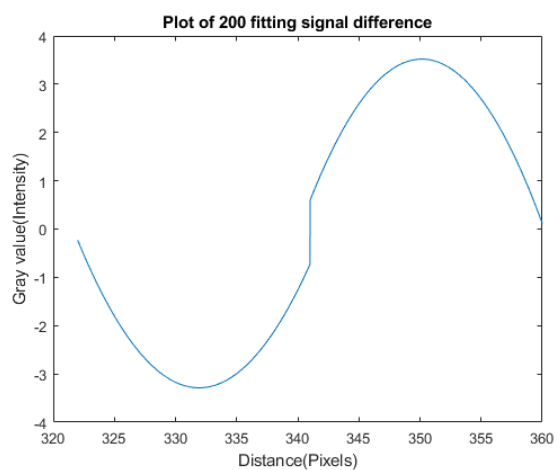
5 atm



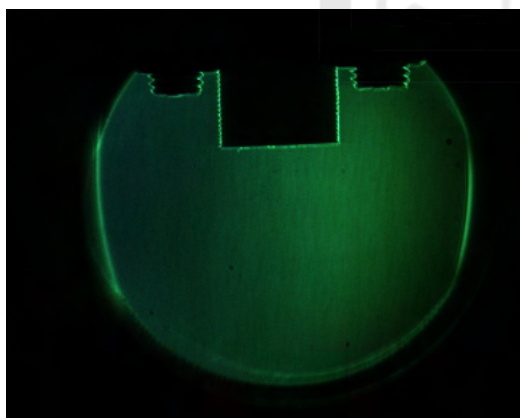


6 atm

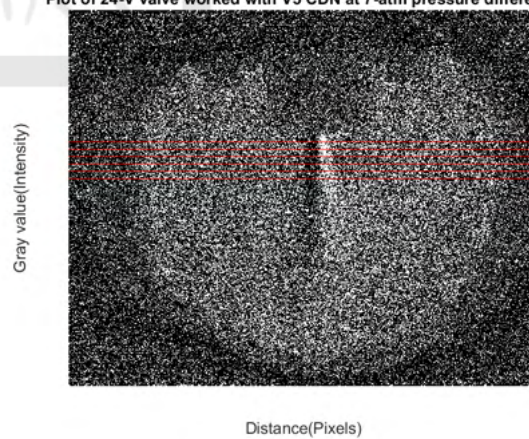


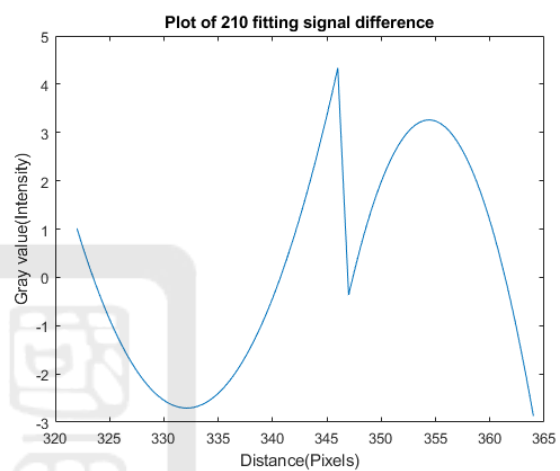
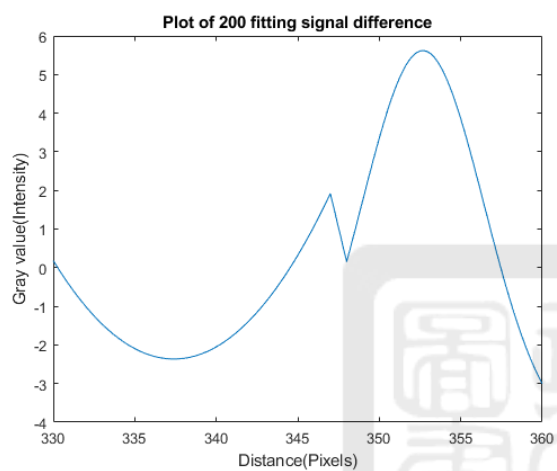
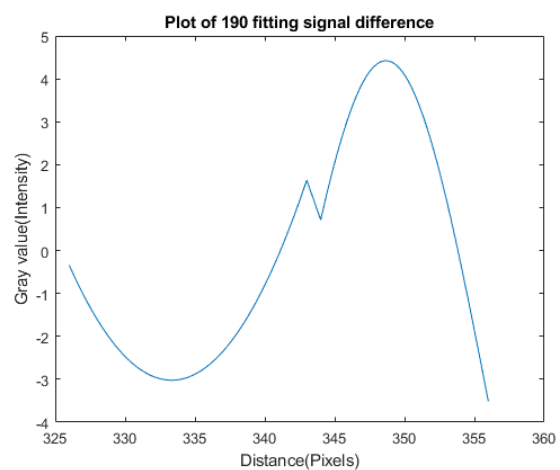
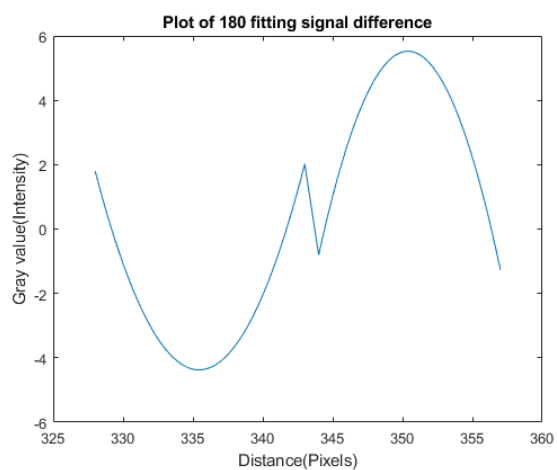


7 atm

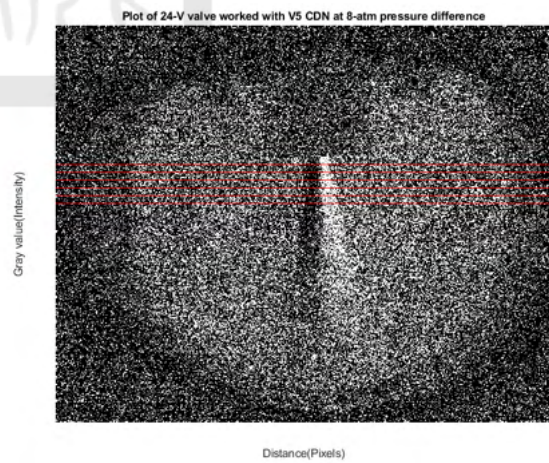
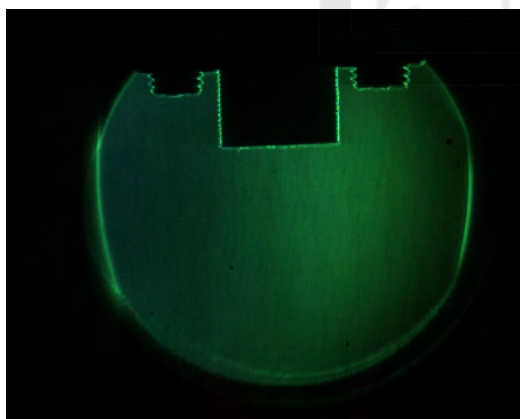


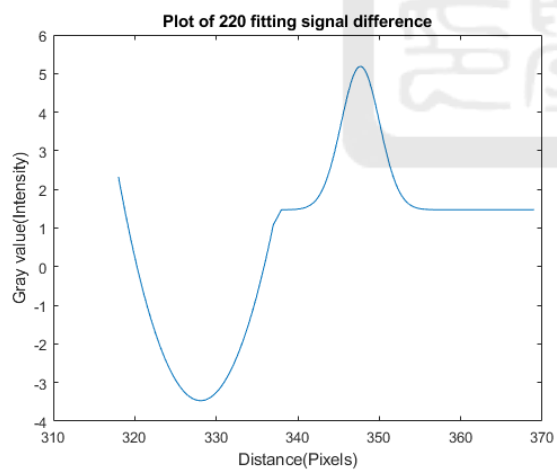
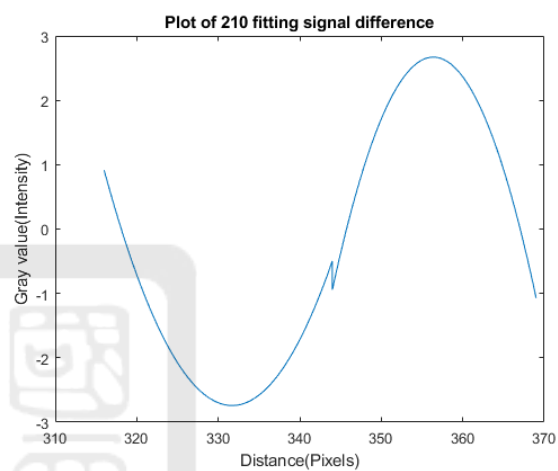
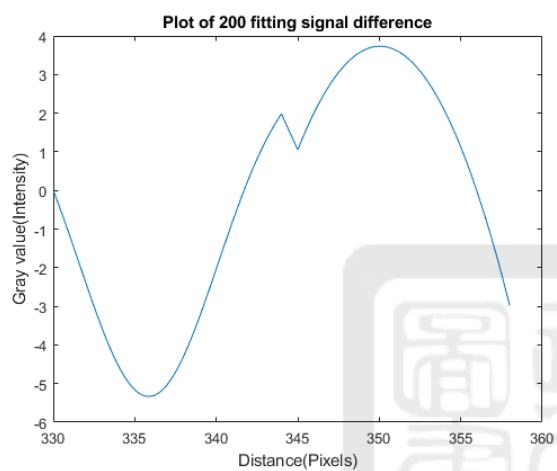
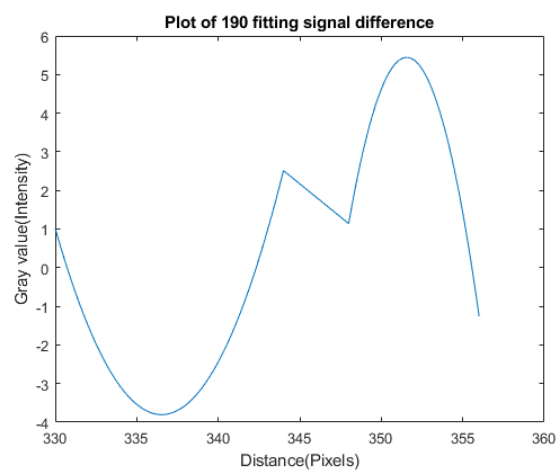
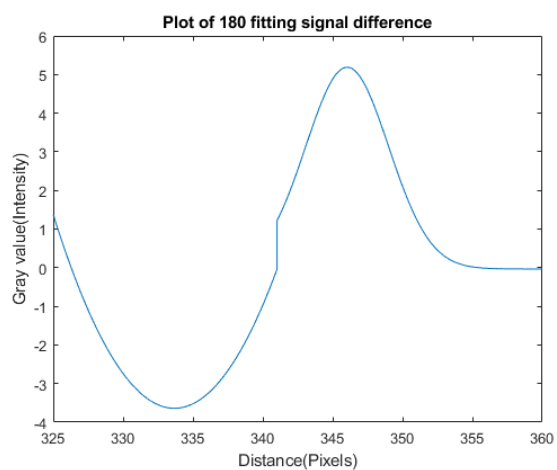
Plot of 24-V valve worked with V5 CDN at 7-atm pressure difference



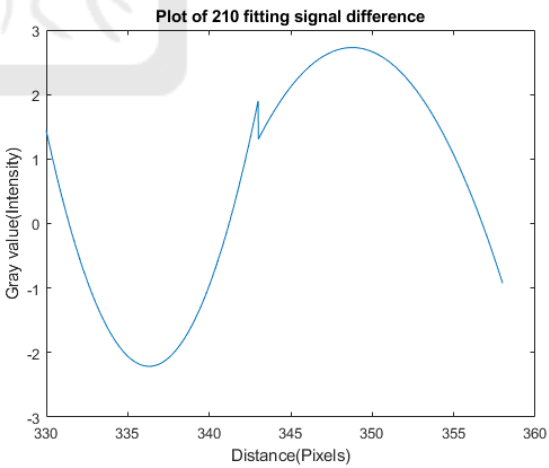
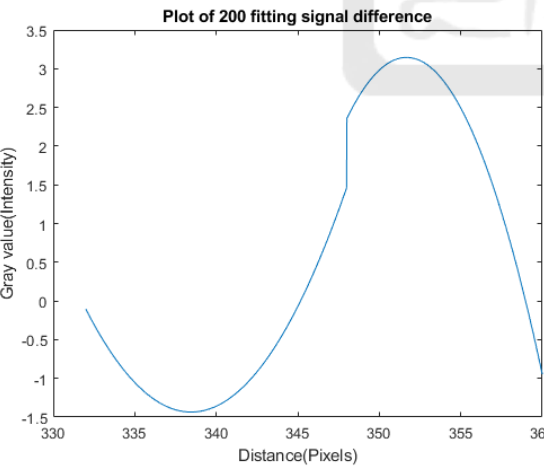
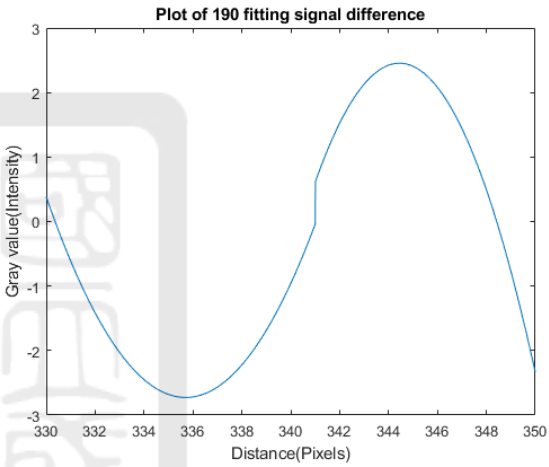
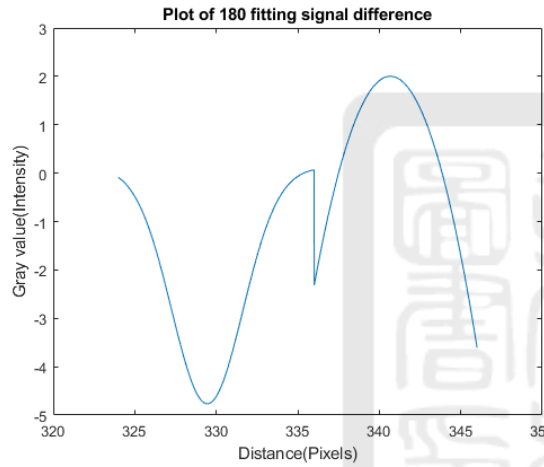
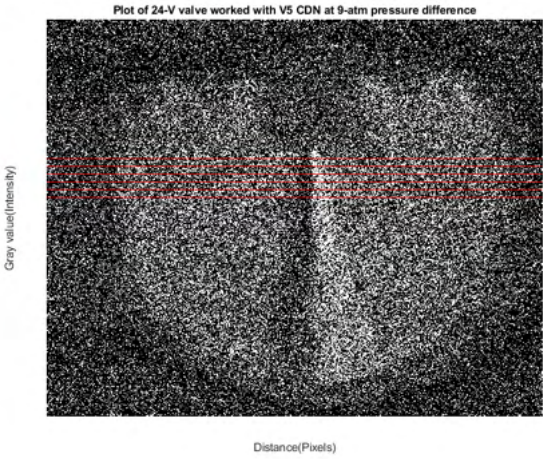
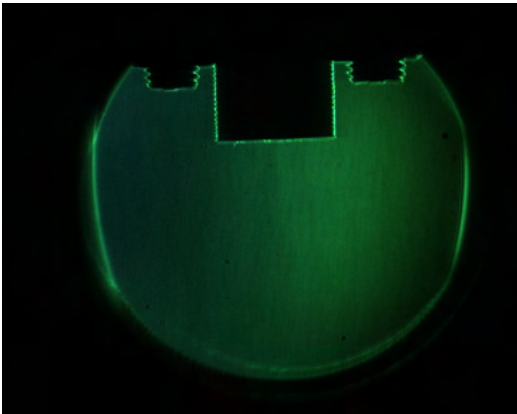


8 atm

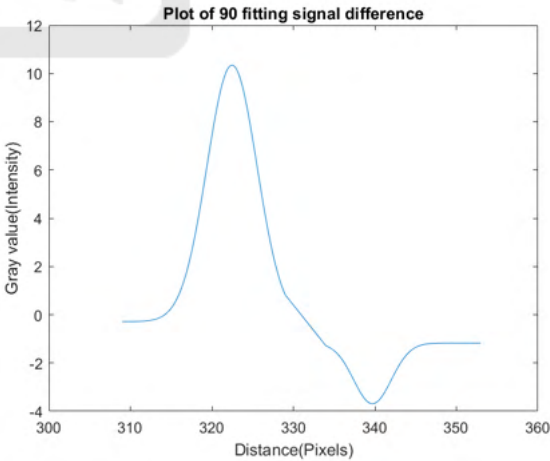
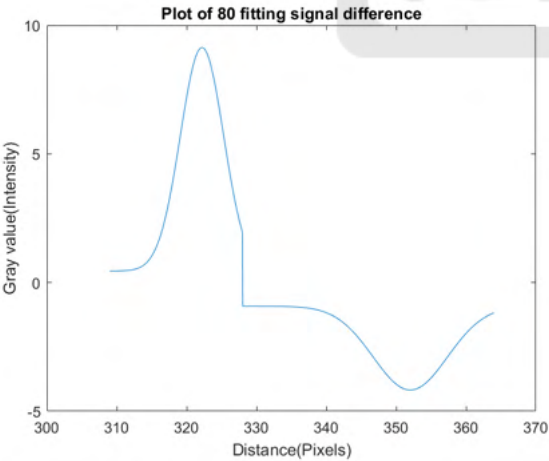
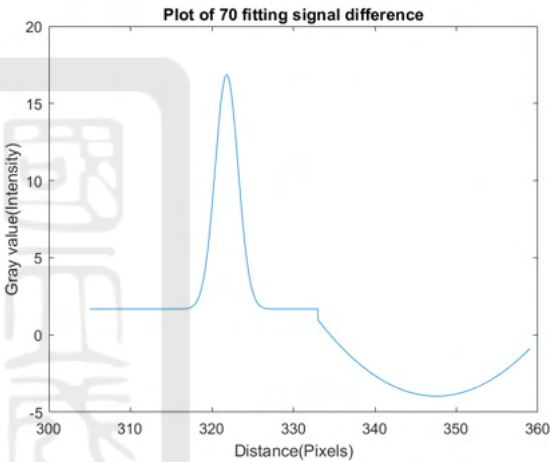
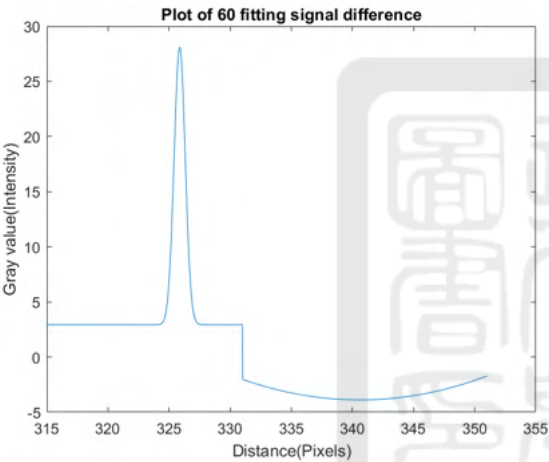
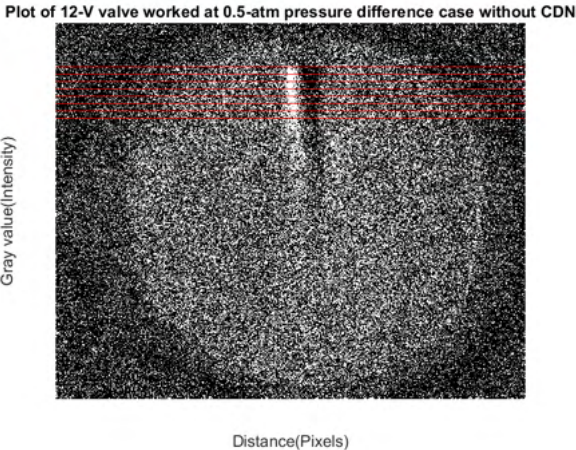
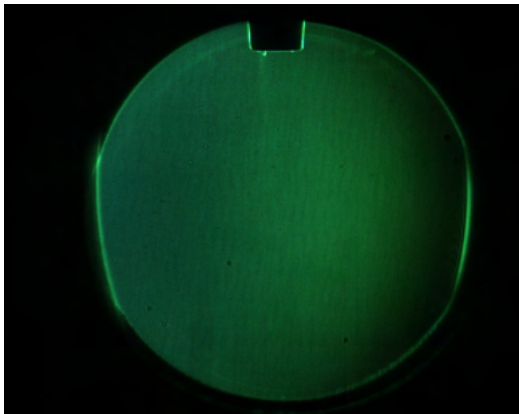


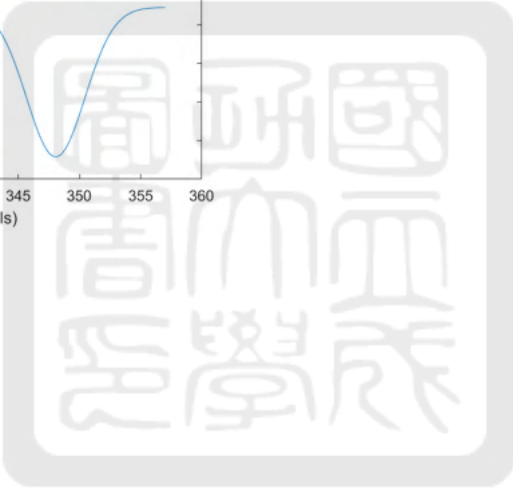
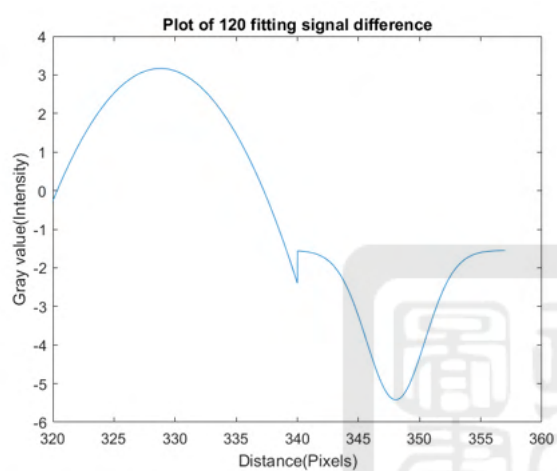
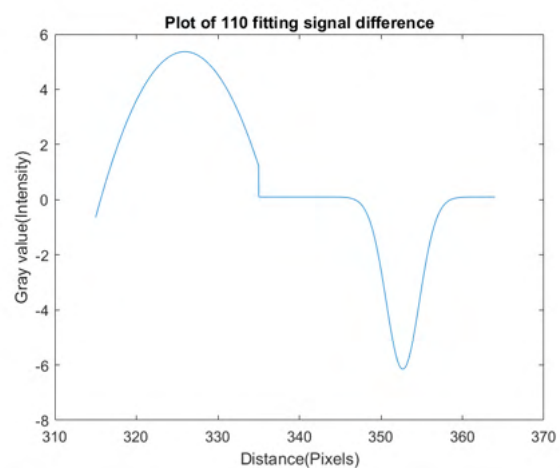
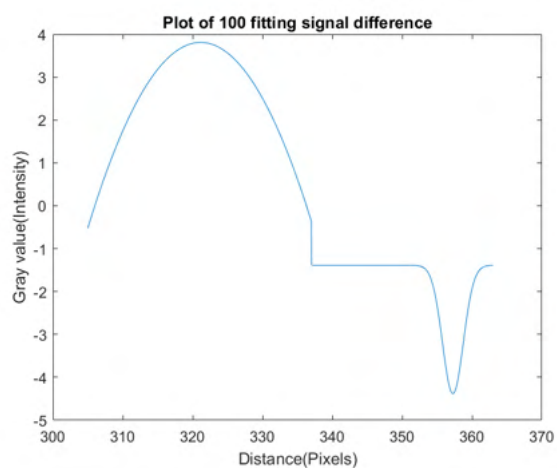


9 atm

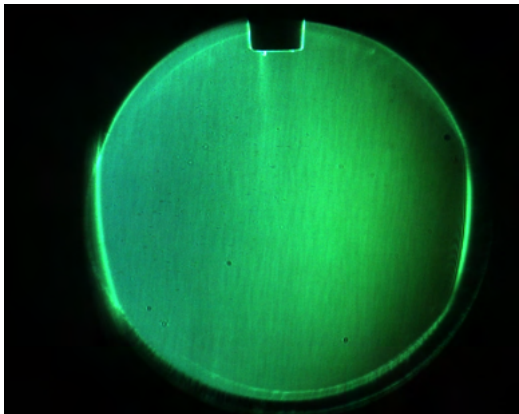


A.4.5 No CDN, 0.5-atm pressure difference

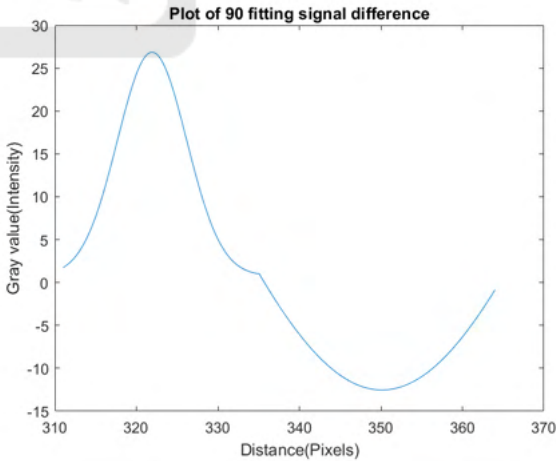
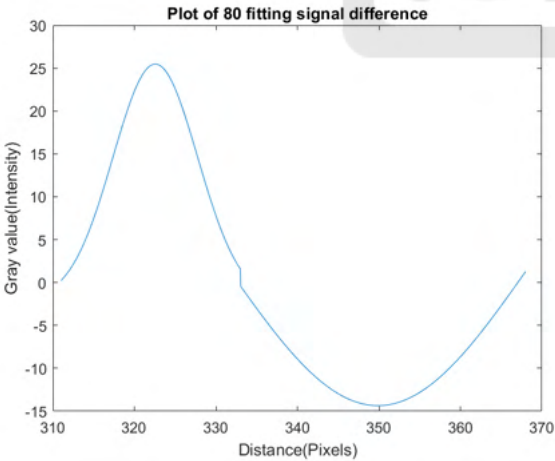
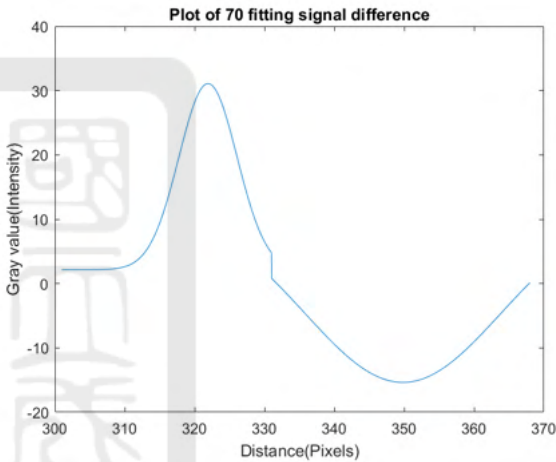
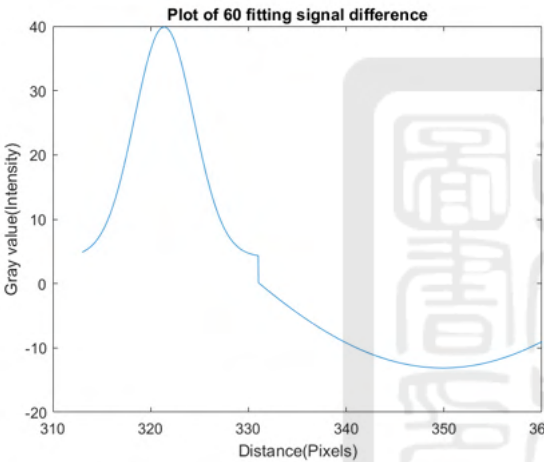
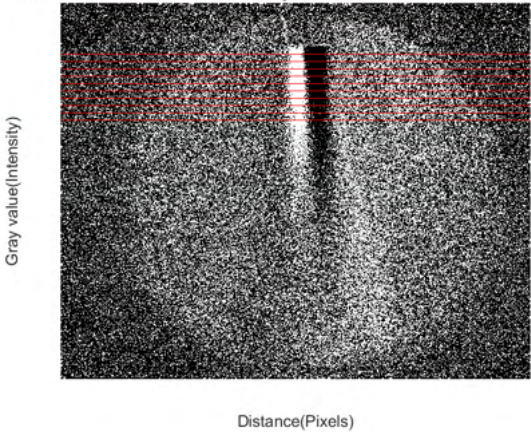


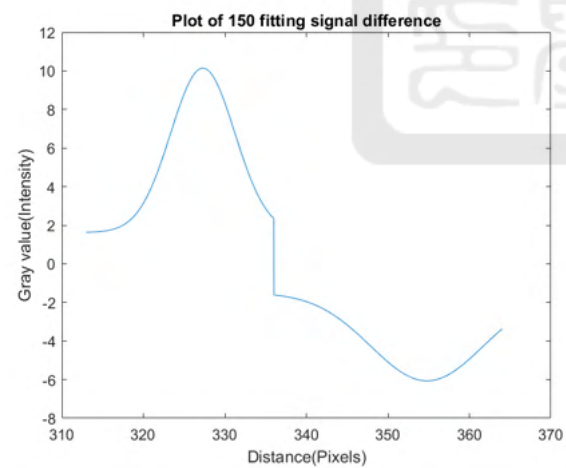
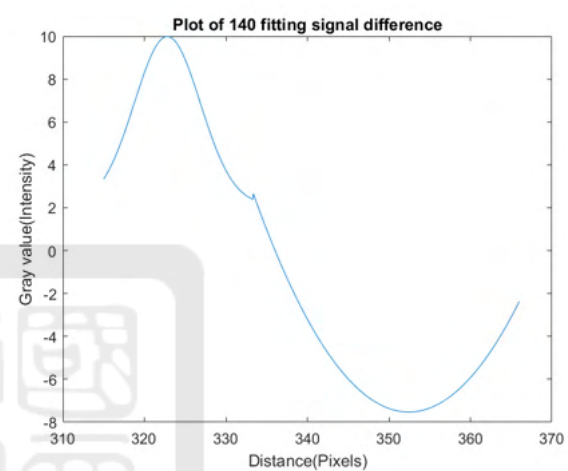
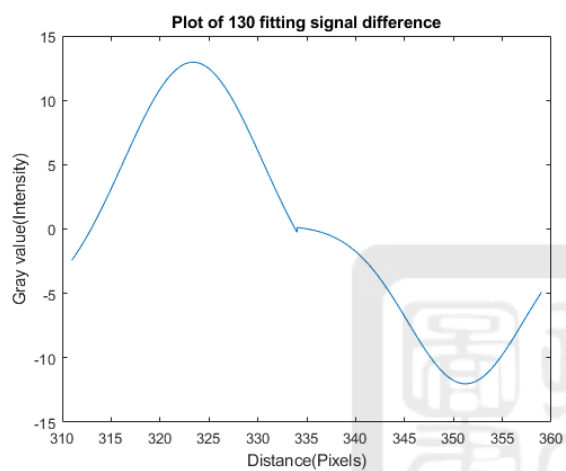
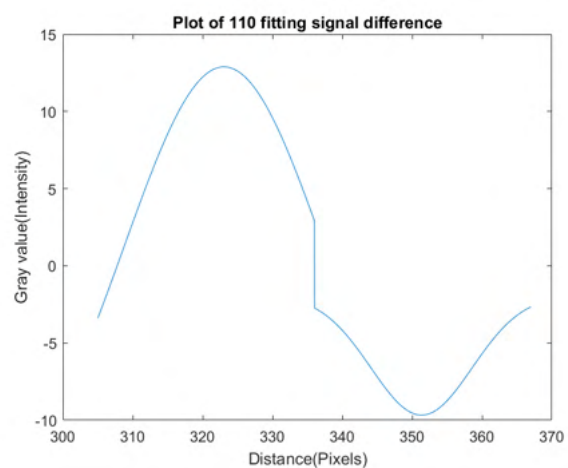
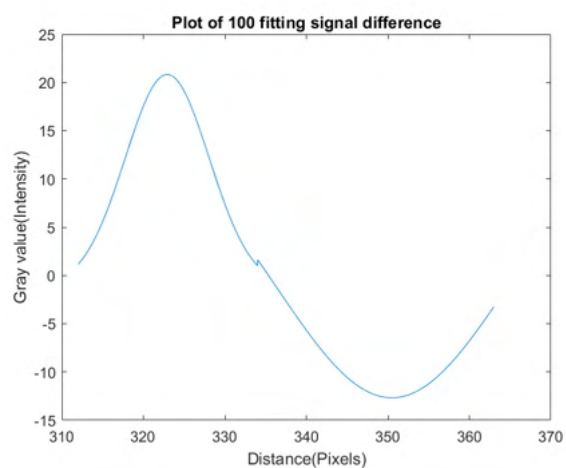


A.4.6 No CDN, 1-atm pressure difference

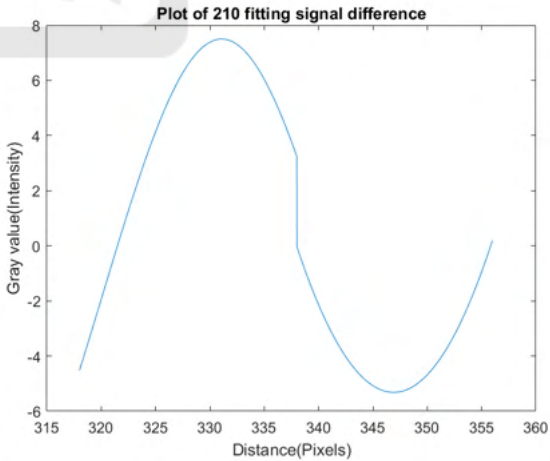
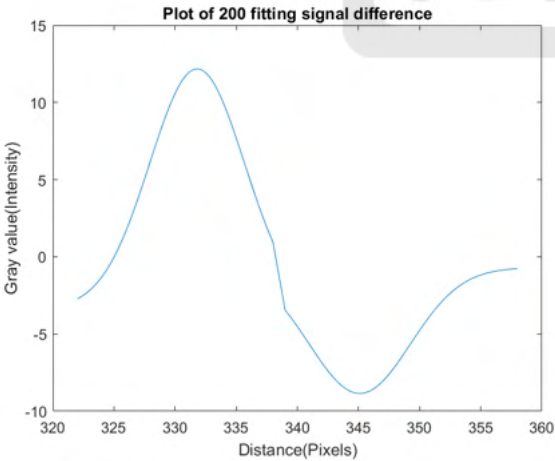
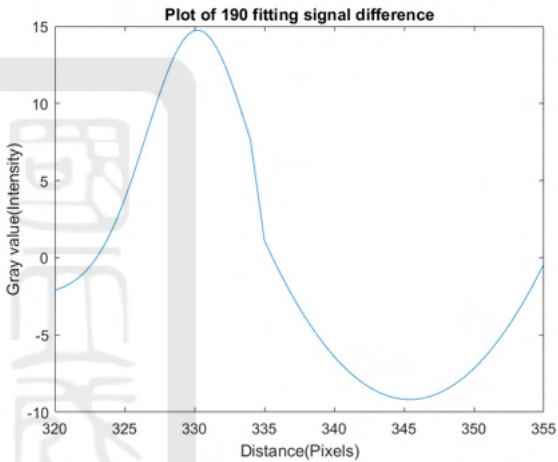
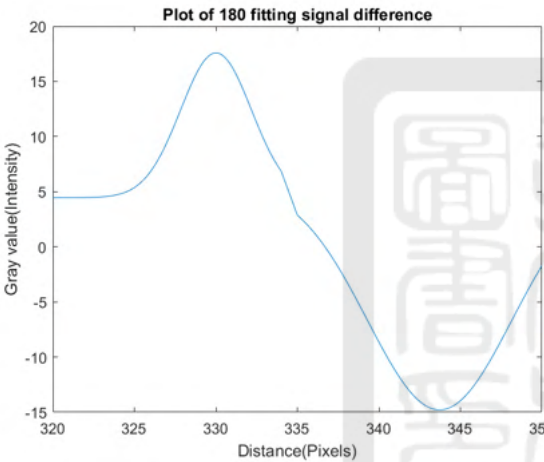
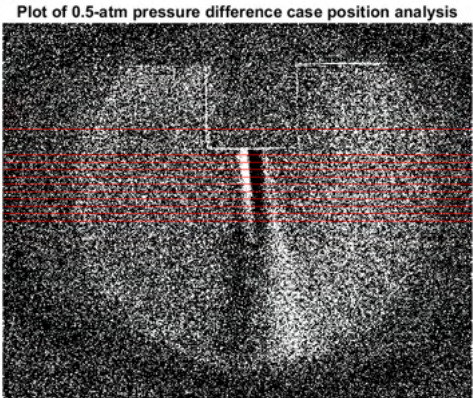
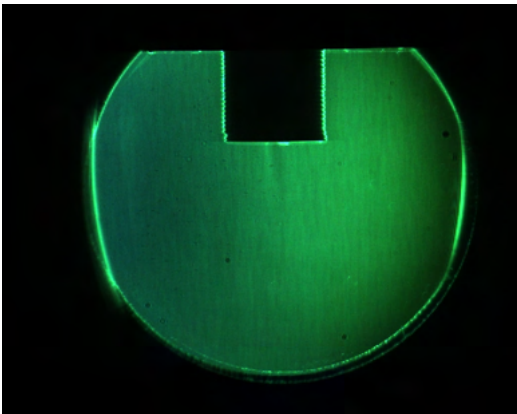


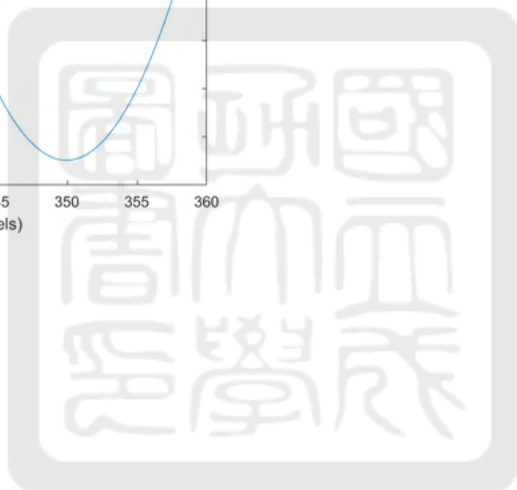
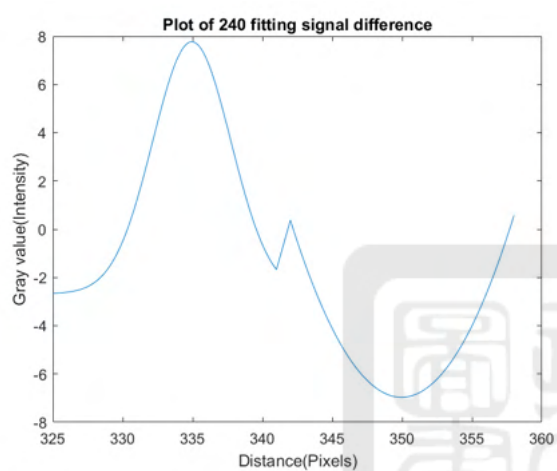
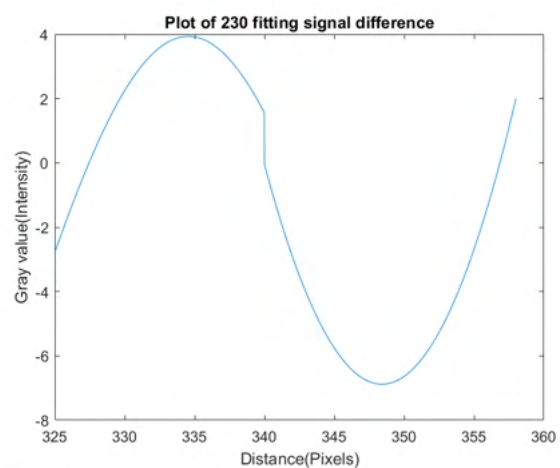
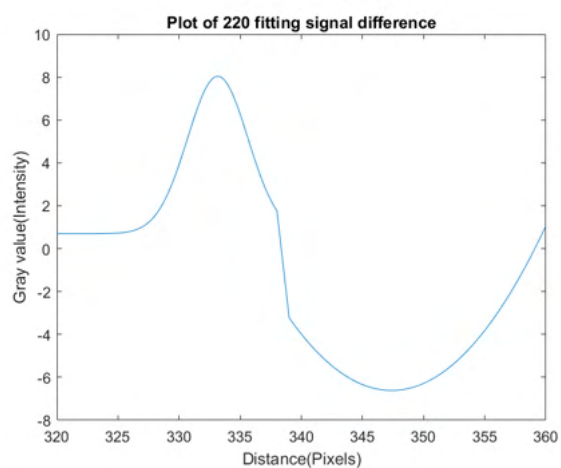
Plot of 12-V valve worked at 1-atm pressure difference case without CDN



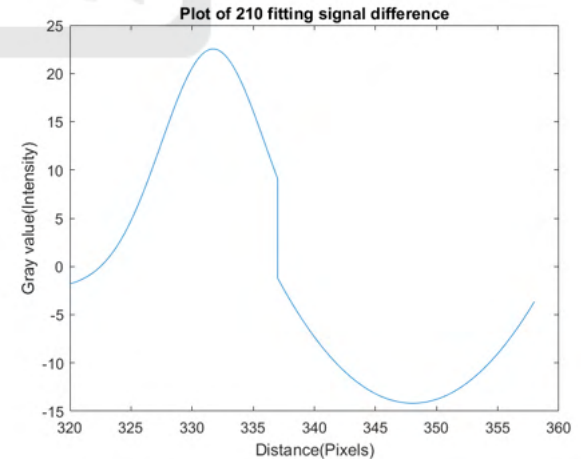
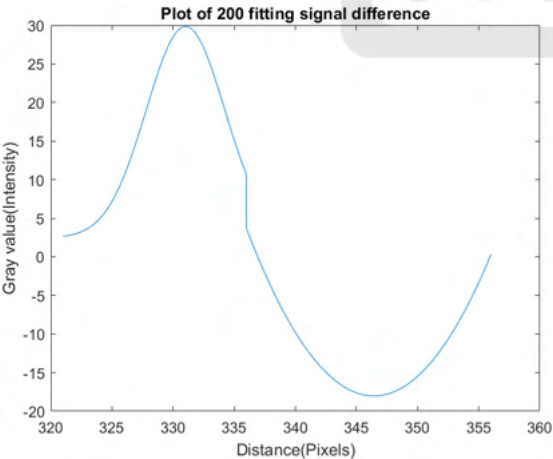
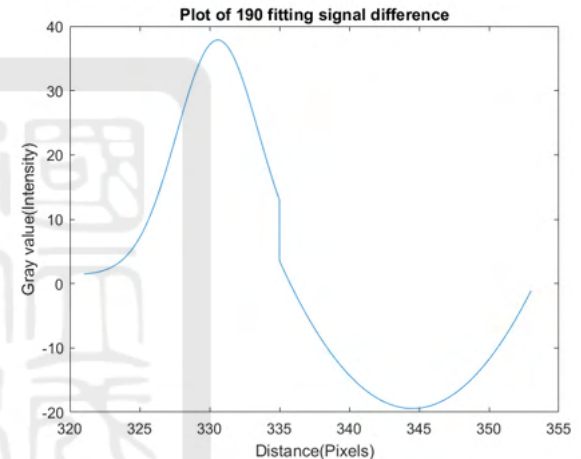
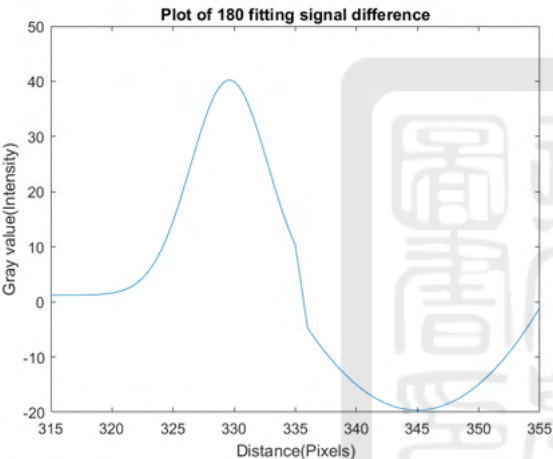
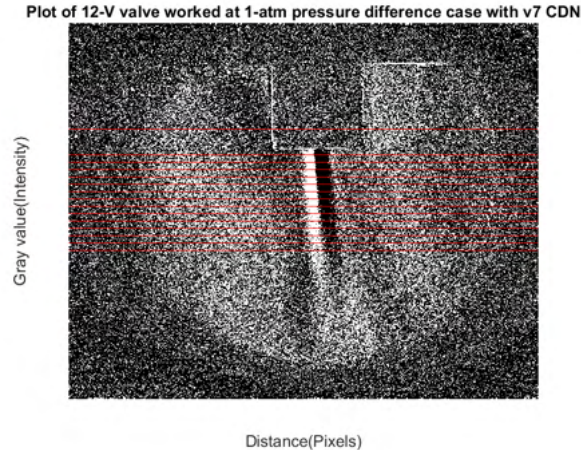
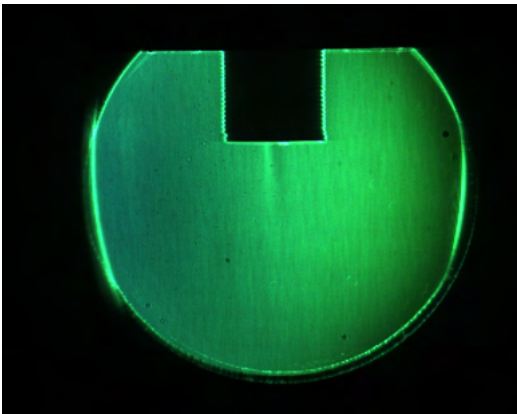


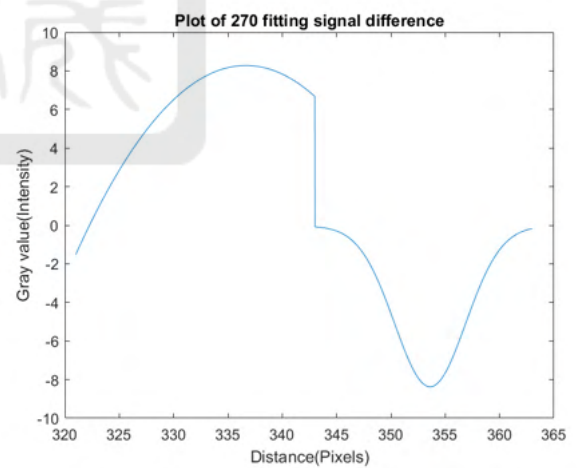
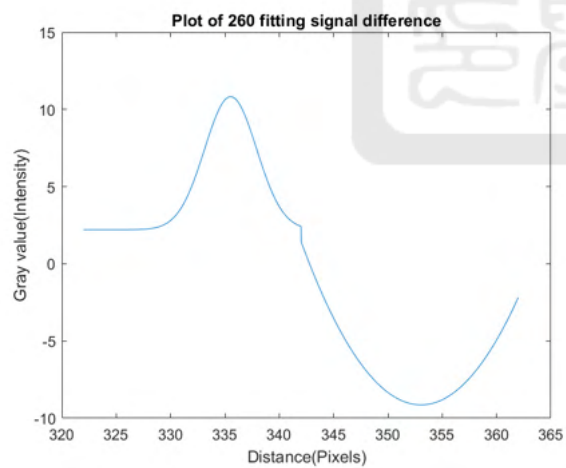
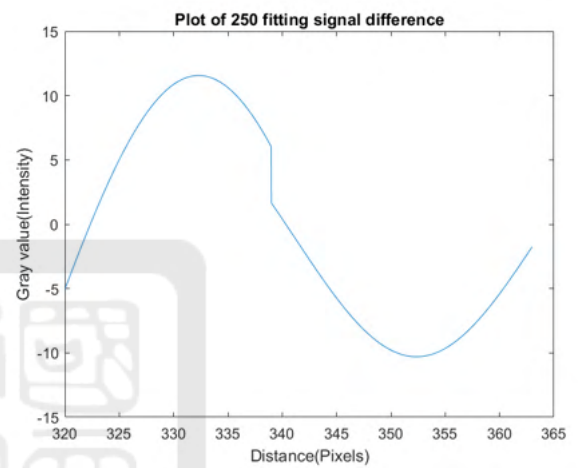
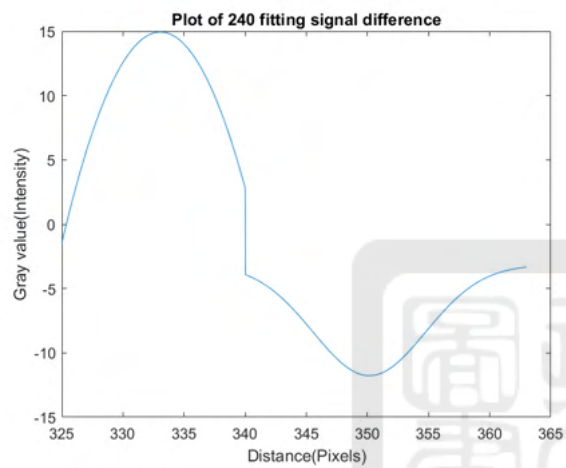
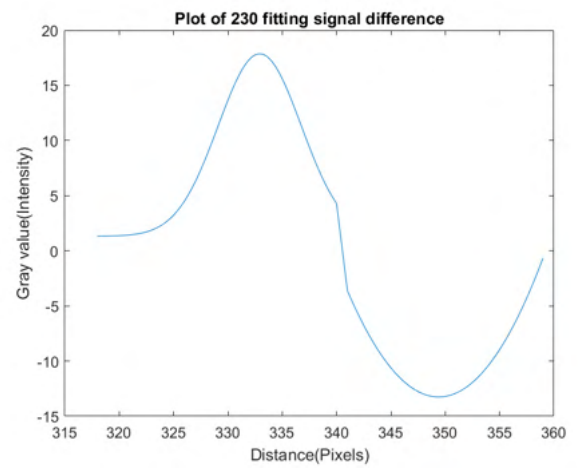
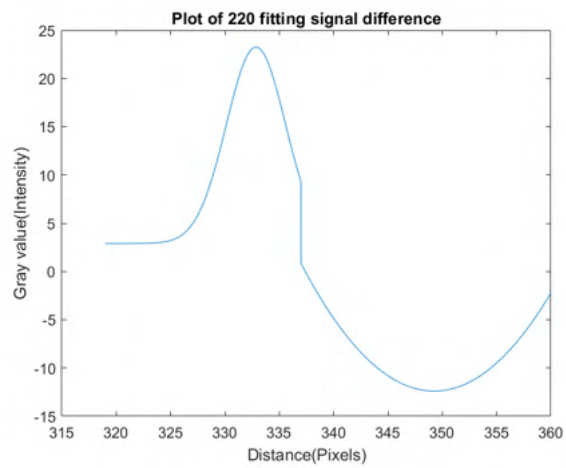
A.4.7 V7 CDN, 0.5-atm pressure difference

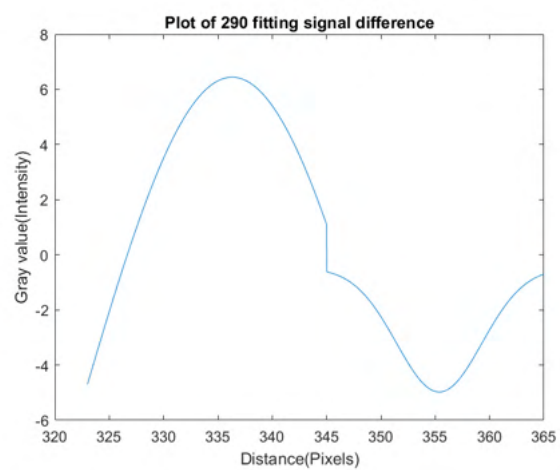
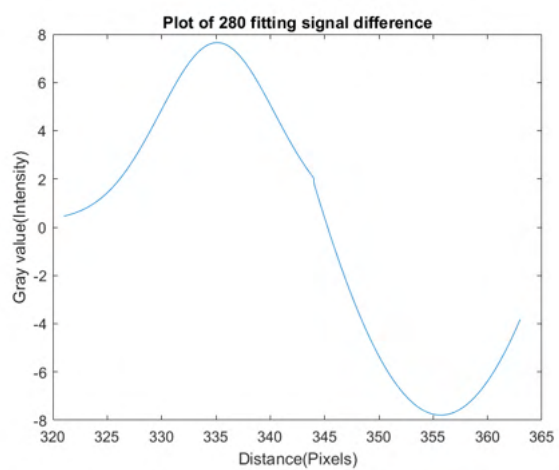




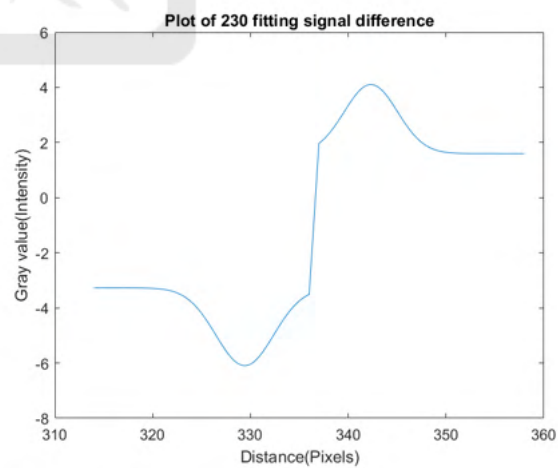
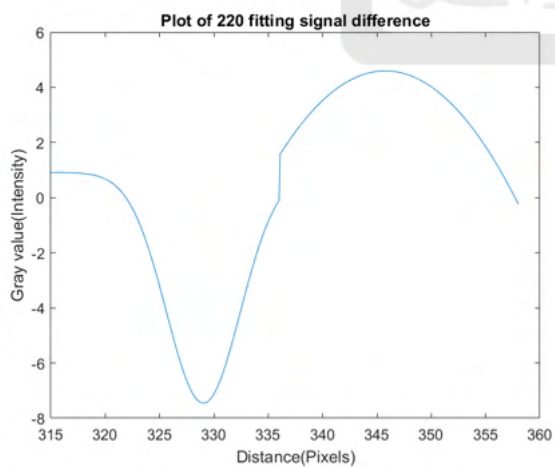
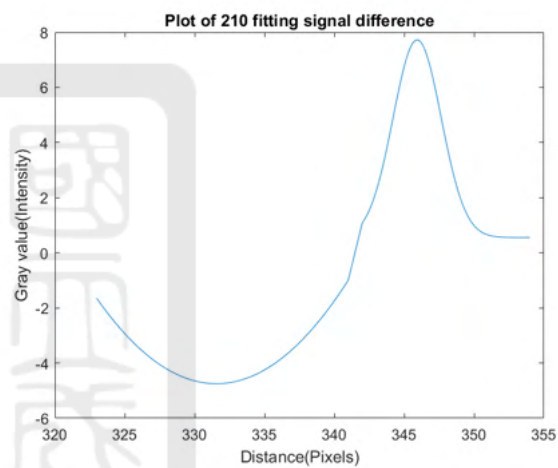
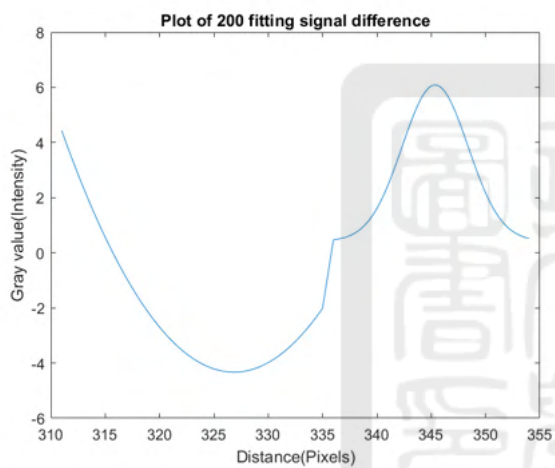
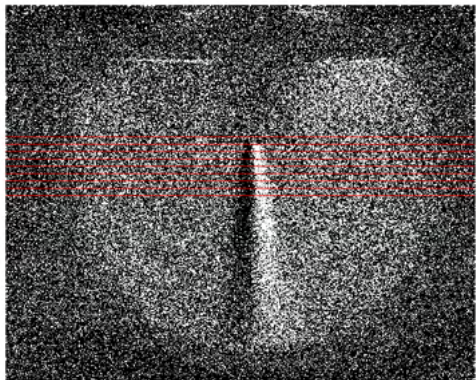
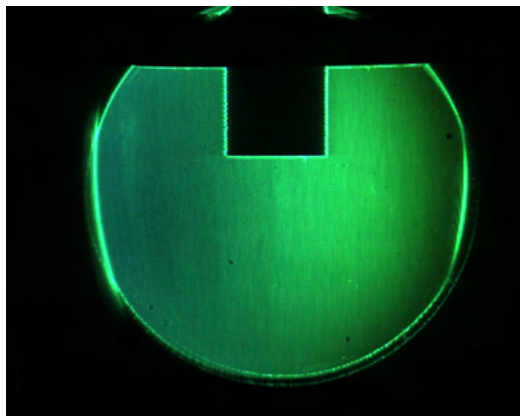
A.4.8 V7 CDN, 1-atm pressure difference

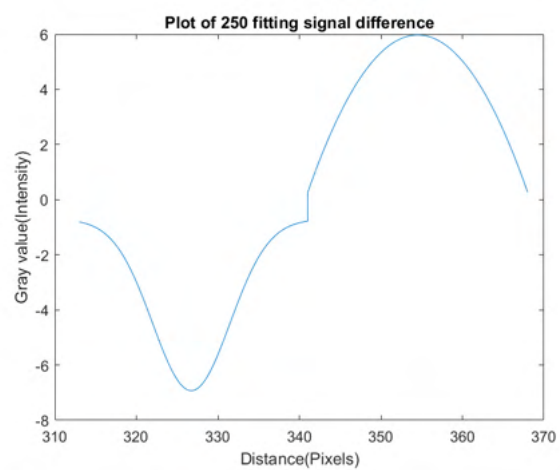
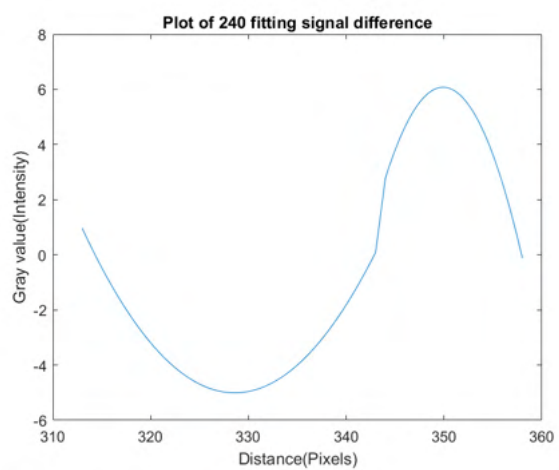




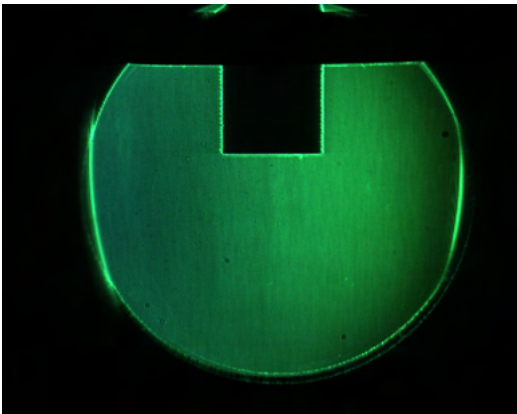


A.4.9 V8 CDN, 0.5-atm pressure difference

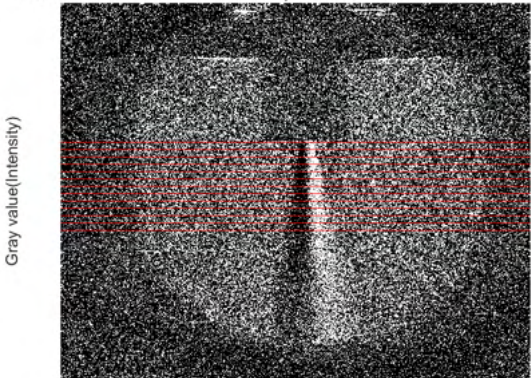




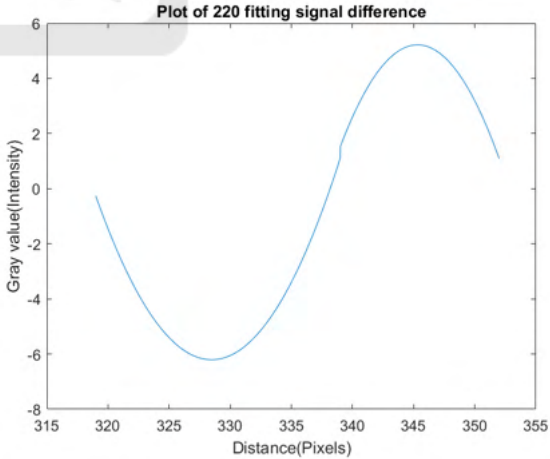
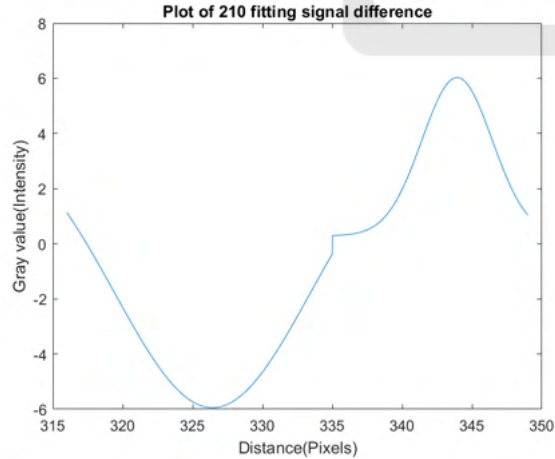
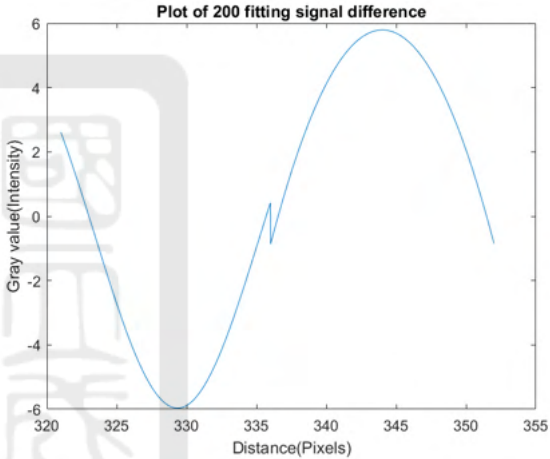
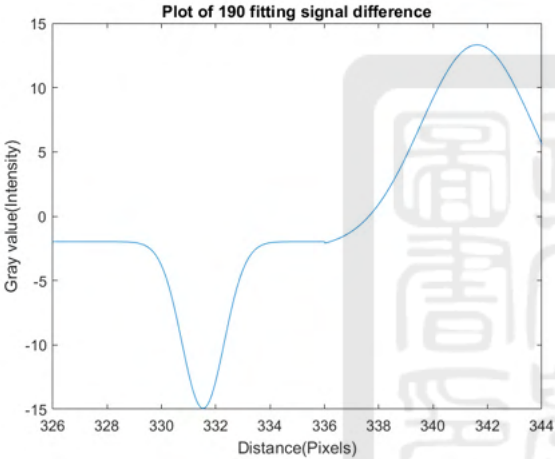
A.4.10 V8 CDN, 1-atm pressure difference

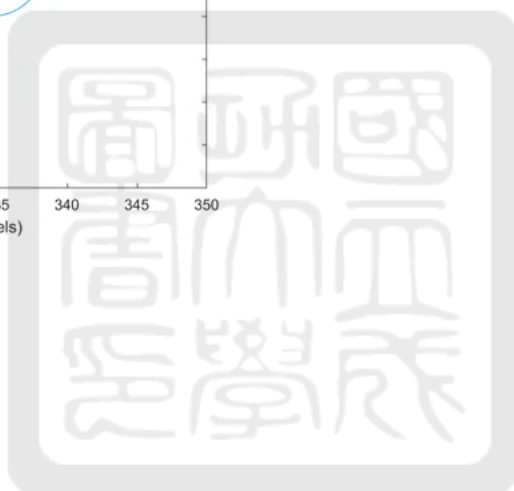
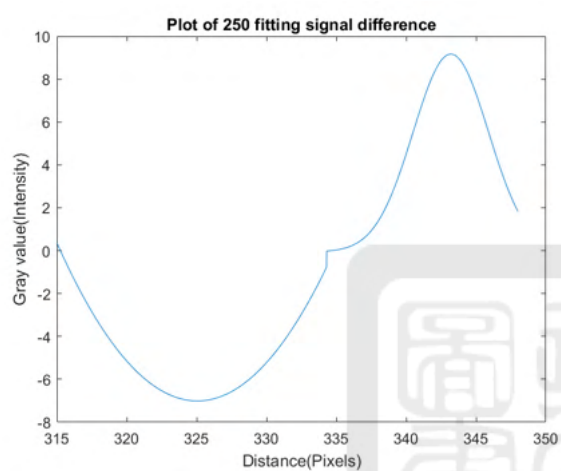
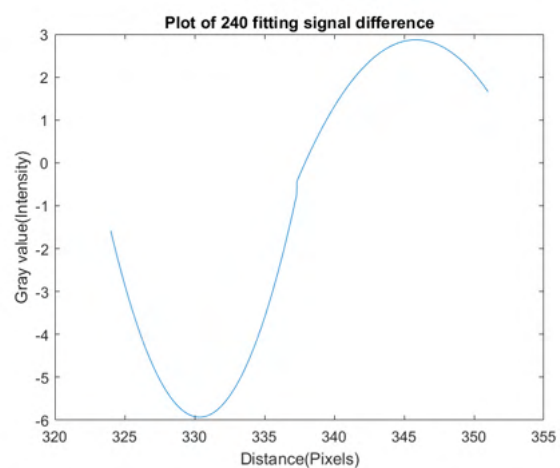
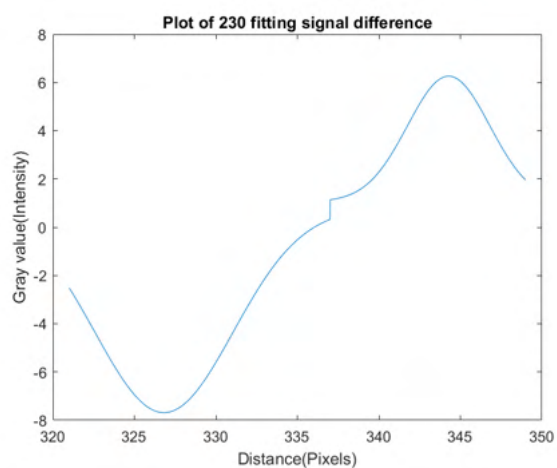


Plot of 12-V valve worked at 1-atm pressure difference case with v8 CDN



Distance(Pixels)





A.5 The venders of all components

Component	Vender	Note
Electronic components (電子材料)	南一電子 or RS	RS using PPL account
3D printer material (3D列印機)	紅蘋果科技	
Screws (螺絲)	鈺峰螺絲 or 永勝螺絲	
Aluminum plate (鋁板)	三川銅鋁	
Acrylic plate (壓克力材料)	長明壓克力	
Air compressor (空壓機配件)	三通行	
Quartz tube (玻璃管)	三美玻璃儀器行	
24-V pulse valve (脈衝氣閥)	Parker Company Ltd	
12-V pulse valve (電磁閥)	蝦皮-doublebuy1	
Optical chopper (截波器)	Scitec Instruments Ltd	
Optical components (光學儀器)	銓州光電	

A.6 Folder of data

- The experimental data is located in /Experiments/2019_jliu/items in the lab drive.
- The drawing is located in /Drawing/jkliu/items in the lab drive.
- The other informations are located in /Shares/J.K Liu/items in the lab drive.

